

Washington University in St. Louis

## Washington University Open Scholarship

---

Arts & Sciences Electronic Theses and  
Dissertations

Arts & Sciences

---

Winter 12-15-2021

### Probing New Physics Beyond the Standard Model via New Neutrino Interactions

Garv Chauhan

*Washington University in St. Louis*

Follow this and additional works at: [https://openscholarship.wustl.edu/art\\_sci\\_etds](https://openscholarship.wustl.edu/art_sci_etds)



Part of the [Physics Commons](#)

---

#### Recommended Citation

Chauhan, Garv, "Probing New Physics Beyond the Standard Model via New Neutrino Interactions" (2021).  
*Arts & Sciences Electronic Theses and Dissertations*. 2568.  
[https://openscholarship.wustl.edu/art\\_sci\\_etds/2568](https://openscholarship.wustl.edu/art_sci_etds/2568)

This Dissertation is brought to you for free and open access by the Arts & Sciences at Washington University Open Scholarship. It has been accepted for inclusion in Arts & Sciences Electronic Theses and Dissertations by an authorized administrator of Washington University Open Scholarship. For more information, please contact [digital@wumail.wustl.edu](mailto:digital@wumail.wustl.edu).

WASHINGTON UNIVERSITY IN ST. LOUIS  
DEPARTMENT OF PHYSICS

Dissertation Examination Committee:

Bhupal Dev, Chair

Soumendra Lahiri

Michael Ogilvie

Saori Pastore

Alexander Seidel

Probing New Physics Beyond the Standard Model via New Neutrino Interactions

by

Garv Chauhan

A dissertation presented to  
The Graduate School  
of Washington University in  
partial fulfillment of the  
requirements for the degree  
of Doctor of Philosophy

St. Louis, Missouri  
December, 2021

© 2021, Garv Chauhan

# Contents

<b>List of Figures</b> . . . . .	v
<b>List of Tables</b> . . . . .	ix
<b>Publications</b> . . . . .	xi
<b>Acknowledgements</b> . . . . .	xii
<b>Abstract</b> . . . . .	xvi
<b>1. Introduction</b> . . . . .	1
1.1 Standard Model of Particle Physics . . . . .	1
1.1.1 Electroweak Sector . . . . .	3
1.1.2 Quantum Chromodynamics . . . . .	3
1.1.3 Higgs Mechanism . . . . .	4
1.1.4 Yukawa sector . . . . .	5
1.2 Motivations for BSM Physics . . . . .	6
1.2.1 Experimental Motivations . . . . .	6
1.2.2 Theoretical Motivations . . . . .	10
1.3 Towards BSM Physics . . . . .	11
<b>2. Perturbativity and Unitarity in <math>U(1)_{B-L}</math> and Left-Right Model</b> . . . . .	13
2.1 Introduction . . . . .	13
2.2 Theoretical constraints . . . . .	16
2.3 $U(1)_{B-L}$ model . . . . .	18
2.4 The minimal left-right symmetric model . . . . .	23
2.4.1 Perturbativity constraints from the gauge sector . . . . .	25
2.4.2 Perturbativity constraints from the scalar sector . . . . .	30
2.5 Conclusion . . . . .	36
<b>3. Vacuum Stability and Symmetry Breaking in Left-Right Model</b> . . . . .	38
3.1 Introduction . . . . .	38
3.2 Boundedness . . . . .	39
3.2.1 Copositivity Criteria . . . . .	40
3.2.2 Gauge Orbit Spaces . . . . .	40
3.3 Left-Right Symmetric Model . . . . .	43

3.4	Vacuum Stability . . . . .	46
3.4.1	Bidoublet $\Phi$ : $\lambda$ Sector . . . . .	46
3.4.2	Triplets $\Delta_L$ and $\Delta_R$ : $\rho$ sector . . . . .	50
3.4.3	Dreaded Coupled Case: $\alpha_{1,3} \neq 0$ . . . . .	52
3.5	Symmetry Breaking and Desirable Vacuum . . . . .	60
3.6	Numerical Comparison . . . . .	68
3.7	Renormalization Group Equations Analysis . . . . .	69
3.7.1	Mass Spectrum & Unitarity Bounds . . . . .	69
3.7.2	Example Study . . . . .	71
3.8	Conclusion . . . . .	72
<b>4.</b>	<b>Scalar Non-standard Interactions of Neutrinos . . . . .</b>	<b>74</b>
4.1	Introduction . . . . .	74
4.2	Field theoretic origin of scalar NSI . . . . .	78
4.2.1	Neutrino self-energy from tadpole diagram . . . . .	80
4.2.2	Neutrino self-energy in a neutrino background . . . . .	82
4.3	Long-range force effects . . . . .	85
4.4	Experimental constraints on couplings . . . . .	88
4.4.1	Constraints on $y_e$ and $y_N$ . . . . .	89
4.4.2	Experimental Constraints on $y_\nu$ . . . . .	96
4.5	Thermal mass of scalar $\phi$ . . . . .	97
4.6	Quantum-mechanical bound on light scalar mass . . . . .	99
4.7	Numerical results . . . . .	102
4.7.1	Earth and Sun . . . . .	102
4.7.2	Supernovae . . . . .	105
4.8	UV-complete model for scalar NSI . . . . .	107
4.9	Conclusion . . . . .	110
<b>5.</b>	<b>Interactions of <math>\nu_R</math>-philic dark photon . . . . .</b>	<b>111</b>
5.1	Introduction . . . . .	111
5.2	Framework . . . . .	113
5.3	Loop-induced couplings of $Z'$ . . . . .	115
5.3.1	Example A: $1 \nu_L + 1 \nu_R$ . . . . .	118
5.3.2	Example B: $1 \nu_L + 2 \nu_R$ with opposite charges . . . . .	119
5.3.3	Example C: $3 \nu_L + 3 \nu_R$ with diagonal $M_R$ . . . . .	121
5.4	Dark photon masses and technical naturalness . . . . .	123
5.5	Phenomenology . . . . .	125
5.5.1	Experimental limits . . . . .	126
5.5.2	How dark is the $\nu_R$ -philic dark photon? . . . . .	131
5.6	Conclusion . . . . .	132
<b>6.</b>	<b>Resonant Leptogenesis in a Model of Discrete Flavor and CP Symmetries</b>	<b>134</b>
6.1	Introduction . . . . .	134
6.2	Framework . . . . .	136
6.3	Different Cases . . . . .	142

6.3.1	Case 1 . . . . .	142
6.3.2	Case 2 . . . . .	152
6.3.3	Case 3a and Case 3b.1 . . . . .	160
6.4	CP Asymmetries . . . . .	168
6.5	Decay of Heavy Neutrinos . . . . .	169
6.5.1	Decay Length . . . . .	170
6.5.2	Branching Ratios and Signals at MATHUSLA . . . . .	175
6.6	Collider Signals . . . . .	177
6.6.1	Production of Heavy Neutrinos at Colliders . . . . .	177
6.6.2	Same-Sign Dilepton Signals at LHC . . . . .	179
6.6.3	Correlation with Leptogenesis . . . . .	181
6.7	Correlation of Low Energy and High Energy CP Phases . . . . .	186
6.7.1	Case 1 . . . . .	188
6.7.2	Case 2 . . . . .	190
6.7.3	Case 3 a and 3b.1 . . . . .	191
6.8	Conclusion . . . . .	191
<b>7.</b>	<b>Conclusions . . . . .</b>	<b>193</b>
<b>A.</b>	<b>Two-loop RGEs for the minimal LRSM . . . . .</b>	<b>196</b>
<b>B.</b>	<b>Limiting cases for scalar NSI expression . . . . .</b>	<b>204</b>
B.1	Limiting cases for scalar NSI expression . . . . .	204
B.1.1	Case 1: $\mu > m_f \gg T$ . . . . .	204
B.1.2	Case 2: $T \ll \mu < m_f$ . . . . .	205
B.1.3	Case 3: $\mu < m_f \ll T$ . . . . .	206
B.2	Calculation of neutrino self-energy in neutrino background . . . . .	207
B.3	Examples for finite medium effects in relativistic cases . . . . .	209
B.3.1	Constant density distribution . . . . .	209
B.3.2	Exponential density distribution . . . . .	211
B.4	Calculation of thermal mass for the scalar field . . . . .	212
<b>C.</b>	<b>Explicit calculation of loop diagrams . . . . .</b>	<b>214</b>
C.1	Explicit calculation of loop diagrams . . . . .	214
C.1.1	The $Z$ diagram . . . . .	215
C.1.2	The $W$ diagram . . . . .	216
<b>D.</b>	<b>Group Theory of <math>\Delta(6n^2)</math> and Representation Matrices . . . . .</b>	<b>218</b>
D.1	Group Theory of $\Delta(6n^2)$ and Representation Matrices . . . . .	218
D.2	Form of the Representation Matrices for Residual Symmetries . . . . .	220
D.3	CP symmetries and form of CP transformations . . . . .	222
	<b>References . . . . .</b>	<b>224</b>

# List of Figures

1.1	Particle content of the Standard Model, . . . . .	2
2.1	Correlation of $g_{R,BL}(v_R)$ and $g_{R,BL}(M_{\text{GUT}})$ in the $U(1)_{B-L}$ model as functions of $r_g \equiv g_R/g_L$ at the $v_R$ scale (shown by the color coding). The horizontal shaded region is excluded by the perturbativity limit $g_{R,BL} < \sqrt{4\pi}$ . The vertical dotted and dashed lines respectively denote the lower and upper limits on the gauge couplings. Here we have chosen $v_R = 5$ TeV and $M_{\text{GUT}} = 10^{16}$ GeV. . . . .	20
2.2	Correlation of $g_R$ and $g_{BL}$ at the scale $v_R = 5$ TeV (red line) and the lower and upper bounds on the couplings $g_R$ and $g_{BL}$ , induced from the requirement of perturbativity up to the GUT scale in the $U(1)_{B-L}$ model. . . . .	21
2.3	Current LHC13 constraints on $Z_R$ mass in the $U(1)_{B-L}$ model (shaded orange) as function of $r_g = g_R/g_L$ , and future prospects at the HL-LHC 14 TeV with an integrated luminosity of $3000 \text{ fb}^{-1}$ (short-dashed red) and the 100 TeV collider FCC-hh with a luminosity of $30 \text{ ab}^{-1}$ (long-dashed red). The vertical shaded regions are excluded by the perturbativity constraints given in Eq. (2.9). The pink, green, blue and purple contours show the variation of the $Z_R$ mass with respect to $r_g$ , with the RH scale $v_R = 5, 10, 20, 50$ TeV, respectively. . . . .	22
2.4	Current lower bound on the $v_R$ scale in the $U(1)_{B-L}$ model, as functions of $r_g = g_R/g_L$ , from the searches of $Z_R$ in the dilepton channel at LHC 13 TeV (shaded orange), as well as the future limit from HL-LHC 14 TeV with an integrated luminosity of $3000 \text{ fb}^{-1}$ (short-dashed red) and the 100 TeV collider FCC-hh with a luminosity of $30 \text{ ab}^{-1}$ (long-dashed red). The vertical shaded regions are excluded by the perturbativity constraints given in Eq. (2.9). The pink, green, blue and purple contours show the variation of $v_R$ with respect to $r_g$ , with the $Z_R$ mass $M_{Z_R} = 5, 10, 20, 50$ TeV, respectively. . . . .	23
2.5	Correlation of $g_{R,BL}(v_R)$ and $g_{R,BL}(M_{\text{GUT}})$ in the minimal LRSM as functions of $r_g = g_R/g_L$ at the $v_R$ scale (as shown by the color coding). The shaded regions are excluded by the perturbativity limits $g_{R,BL} < \sqrt{4\pi}$ . The two stars correspond to the special case $g_R = g_L$ at the $v_R$ scale. The vertical dotted and dashed lines respectively denote the lower and upper limits on the gauge couplings. Here we have chosen $v_R = 10$ TeV and $M_{\text{GUT}} = 10^{16}$ GeV. . . . .	26
2.6	Correlation of $g_R$ and $g_{BL}$ in the minimal LRSM at the scale $v_R = 10$ TeV (red curve), along with the lower and upper bounds on the couplings $g_{R,BL}$ , induced from the requirement of perturbativity up to the GUT scale. The shaded region is excluded by the perturbativity limit $g_R < \sqrt{4\pi}$ . . . . .	27

2.7	Current LHC13 constraints on the $W_R$ (left) and $Z_R$ (right) masses in the minimal LRSM (shaded orange) as function of $r_g = g_R/g_L$ , and future prospects at the HL-LHC 14 TeV with an integrated luminosity of $3000 \text{ fb}^{-1}$ (short-dashed red) and the 100 TeV collider FCC-hh with a luminosity of $30 \text{ ab}^{-1}$ (long-dashed red). The pink, green, blue and purple lines are the $W_R/Z_R$ mass with the RH scale $v_R = 5, 10, 20, 50 \text{ TeV}$ , respectively. The shaded gray and brown regions are excluded respectively by the perturbative constraints from the gauge and scalar sectors up to the GUT scale. The dashed vertical line corresponds to the absolute theoretical bound in Eq. (2.6). . . . .	27
2.8	Lower bounds on the $v_R$ scale in the minimal LRSM, as functions of $r_g$ , from the direct searches of $W_R$ and $Z_R$ bosons at LHC 13 TeV (shaded orange), and future prospects at the HL-LHC 14 TeV with an integrated luminosity of $3000 \text{ fb}^{-1}$ (short-dashed red) and the 100 TeV collider FCC-hh with a luminosity of $30 \text{ ab}^{-1}$ (long-dashed red). The shaded gray regions are excluded by the perturbativity constraints up to the GUT scale, with the vertical dashed line corresponding to the absolute theoretical bound in Eq. (2.6). The shaded brown regions are excluded by the perturbativity limits from the scalar sector, discussed in Section 2.4.2. . . . .	30
2.9	RG running of the quartic couplings $\lambda_{1,2,3,4}$ (left), and $\rho_{1,2}, \alpha_{1,2,3}$ (right) in the scalar potential Eq. (2.17) of minimal LRSM from $v_R$ up to the GUT scale, with $r_g = 1.1$ and $v_R = 6 \text{ TeV}$ (upper panels), $v_R = 12 \text{ TeV}$ (lower panels). . . . .	34
3.1	Dependence of gauge orbit variable $\zeta_i$ on $\xi$ and $\eta_i$ . (Left) Scatter plot of $\zeta$ with respect to $\xi$ and $\eta$ . (Right) Plot of $\zeta$ as a function of $\xi$ and $\eta$ given in eq. (3.29). . . . .	54
3.2	Numerical minimization of the scalar potential of LRSM. The figures are plotted for different pair of quartic couplings with values ranging from $(-5, 5)$ and with grid pixel size of $0.1 \times 0.1$ , with other quartics being set according to benchmark in Sec 3.6. The yellow region indicates an unbounded potential. The green region indicates the existence of a global minimum but not with the required VEV structure. The blue region indicates the existence of a global minimum with the required VEV structure. . . . .	67
3.3	RG running of the quartic couplings for the benchmark in sec 3.7.2 from $v_R = 26.8 \text{ TeV}$ , with $r_g = \frac{g_R}{g_L} = 1.2$ . . . . .	71
4.1	Neutrino self-energy diagrams: (a) Tadpole with background of $f$ and $\nu$ , and (b) Self-energy in a neutrino background. . . . .	80
4.2	Feynman diagram responsible for the thermal mass of the scalar $\phi$ . . . . .	99
4.3	Different experimental constraints on Yukawa coupling of scalar to electron for the case of Dirac neutrinos. The shaded regions are excluded. Some representative values of scalar NSI in Earth, Sun and supernova are also shown.	103
4.4	Same as in Fig. 4.3, but for scalar coupling to nucleons. . . . .	103
4.5	Same as in Fig. 4.3, but for Majorana neutrinos. . . . .	104
4.6	Same as in Fig. 4.4, but for Majorana neutrinos. . . . .	104
4.7	Explicit models generating operators of Eq. (4.88). . . . .	109

5.1	Loop-induced $Z'$ couplings to charged fermions in the mass basis (upper panels) and in the chiral basis (lower panels). . . . .	115
5.2	The $\nu_R$ -philic dark photon confronted with known experimental constraints. Here $g_{\text{eff}}$ is the loop-induced coupling of $Z'$ to electrons. The quark couplings are of the same order of magnitude as $g_{\text{eff}}$ and we have ignored the difference between them when recasting constraints on quark couplings. The theoretically favored values of $g_{\text{eff}}$ are below the solid blue, orange, or green lines, assuming $U(1)_R$ breaks at the scale of $m_D = 246$ GeV, $M_R = 24.6$ TeV, or $M_R \sim 10^{14}$ GeV (Type I seesaw), respectively. The collider bound consists of BaBar, LHCb, LEP, and LHC 8 TeV limits—see the text or Fig. 5.3 for more details. . . . .	126
5.3	Sensitivity of future experiments (SHiP, FASER, Belle-II) on the $\nu_R$ -philic dark photon. Here $g_{\text{eff}}$ is the loop-induced coupling of $Z'$ to electrons. The quark couplings are of the same order of magnitude as $g_{\text{eff}}$ and we have ignored the difference between them when recasting constraints on quark couplings. The theoretically favored values of $g_{\text{eff}}$ is below the solid blue or orange lines, assuming $U(1)_R$ breaks at the scale of $m_D = 246$ GeV or $M_R = 24.6$ TeV, respectively. . . . .	127
6.1	Case 1 $N_{1,2,3}$ decay lengths plotted against $\theta_R$ for different values of RHN mass scale $M$ (upper Panels) and light neutrino mass $m_0$ (lower panels) for $M_{Z'} = 4$ TeV. . . . .	171
6.2	Case 2 $N_{1,2,3}$ decay lengths plotted against $\theta_R$ for different values of RHN mass scale $M$ (upper Panels) and light neutrino mass $m_0$ (lower panels) for $M_{Z'} = 4$ TeV. . . . .	172
6.3	$N_{1,2,3}$ decay lengths plotted against $\theta_R$ for different values of RHN mass scale $M$ for Case 3a (left panel) and for Case 3b.1 (right panel) with $M_{Z'} = 4$ TeV. . . . .	173
6.4	Case 1 $N_1$ decay branching ratios for $N_1 \rightarrow l_\alpha W$ , ( $\alpha = e, \mu, \tau$ ) as a function of $s/n$ for strong NO and strong IO with $M = 250$ GeV. . . . .	177
6.5	Case 1 $N_2$ decay branching ratios for $N_2 \rightarrow l_\alpha W$ , ( $\alpha = e, \mu, \tau$ ) as a function of $s/n$ for strong NO and strong IO with $M = 250$ GeV. . . . .	178
6.6	Case 1 $N_3$ decay branching ratios for $N_3 \rightarrow l_\alpha W$ , ( $\alpha = e, \mu, \tau$ ) as a function of $s/n$ for strong NO and strong IO with $M = 250$ GeV. . . . .	179
6.7	Case 2 $N_1$ decay branching ratios for $N_1 \rightarrow l_\alpha W$ , ( $\alpha = e, \mu, \tau$ ) as a function of $t/n$ for strong NO and strong IO with $M = 250$ GeV. . . . .	180
6.8	Case 2 $N_2$ decay branching ratios for $N_2 \rightarrow l_\alpha W$ , ( $\alpha = e, \mu, \tau$ ) as a function of $t/n$ for strong NO and strong IO with $M = 250$ GeV. . . . .	181
6.9	Case 2 $N_3$ decay branching ratios for $N_3 \rightarrow l_\alpha W$ , ( $\alpha = e, \mu, \tau$ ) as a function of $t/n$ for strong NO and strong IO with $M = 250$ GeV. . . . .	182
6.10	Case 3a $N_{1,2,3}$ decay branching ratios for $N_i \rightarrow l_\alpha W$ , ( $\alpha = e, \mu, \tau$ ) as a function of $s/n$ for strong NO, $m$ even, $s$ even with $M = 250$ GeV. . . . .	183
6.11	Case 3b.1 $N_{1,2,3}$ decay branching ratios for $N_i \rightarrow l_\alpha W$ , ( $\alpha = e, \mu, \tau$ ) as a function of $s/n$ for strong IO, $m$ even, $s$ even with $M = 250$ GeV. . . . .	184
6.12	lepton number violating (LNV) process $pp \rightarrow Z' \rightarrow N_i N_i \rightarrow \ell_\alpha^\pm \ell_\beta^\pm + 2W^\mp \rightarrow \ell_\alpha^\pm \ell_\beta^\pm + 4j$ (for $\alpha \neq \beta$ also violates lepton flavour) . . . . .	184

6.13	$pp \rightarrow Z' \rightarrow N_1 N_1$ production cross section as function of RHN mass scale $M_N$ at $\sqrt{s} = 14$ TeV LHC (solid lines) and $\sqrt{s} = 100$ TeV future collider (dotted lines) for $M_{Z'} = (4, 5, 6)$ TeV. . . . .	185
6.14	Production cross section for same-sign LNV dilepton signals (see Sec. 6.6.2) as function of RHN mass scale $M_N$ at $\sqrt{s} = 14$ TeV LHC for strong NO and strong IO for $M_{Z'} = 4$ TeV. . . . .	185
6.15	Case 1 : Prediction of the baryon asymmetry $\eta_B$ relative to the observed value $\eta_B^{\text{obs}}$ in the plane of the RH neutrino mass $M$ and the mass $M_{Z'}$ at $g_{B-L} = 0.1$ , $n = 26$ with $\vartheta_R$ being a point of ERS and $s$ set to 2(17) for strong NO (IO) in the left (right) panel. Red points correspond to $ \eta_B $ in the $5\sigma$ interval around $\eta_B^{\text{obs}}$ . The contours show $\sigma_{\text{prod}}$ at the $\sqrt{s} = 14$ TeV LHC (solid) and $\sqrt{s} = 100$ TeV future collider (dashed) in ab. . . . .	186
6.16	Case 2 : Prediction of the baryon asymmetry $\eta_B$ relative to the observed value $\eta_B^{\text{obs}}$ in the plane of the RH neutrino mass $M$ and the mass $M_{Z'}$ at $g_{B-L} = 0.1$ , $n = 14$ , $s = 1$ , $t = 2$ (i.e. $u = 2s - t = 0$ ) with $\vartheta_R$ being a point of ERS for strong NO (IO) in the left (right) panel. Red points correspond to $ \eta_B $ in the $5\sigma$ interval around $\eta_B^{\text{obs}}$ . The contours show $\sigma_{\text{prod}}$ at the $\sqrt{s} = 14$ TeV LHC (solid) and $\sqrt{s} = 100$ TeV future collider (dashed) in ab. . . . .	186
6.17	Case 3a (left panel) and Case 3b.1 (right panel) : Prediction of the baryon asymmetry $\eta_B$ relative to the observed value $\eta_B^{\text{obs}}$ in the plane of the RH neutrino mass $M$ and the mass $M_{Z'}$ at $g_{B-L} = 0.1$ , $n = 17(20)$ , $m = 16(10)$ with $\vartheta_R$ being a point of ERS and $s$ set to 10(2) for strong NO (IO) in the left (right) panel. Red points correspond to $ \eta_B $ in the $5\sigma$ interval around $\eta_B^{\text{obs}}$ . The contours show $\sigma_{\text{prod}}$ at the $\sqrt{s} = 14$ TeV LHC (solid) and $\sqrt{s} = 100$ TeV future collider (dashed) in ab. . . . .	187
6.18	Case 1 : Predictions for $\eta_B$ as a function of effective neutrino mass $m_{\beta\beta}$ for all values of $s$ for $n = 26$ , $M_N = 0.8(1.1)$ TeV with $M_{Z'} = 4.9(5.0)$ TeV for strong NO(IO) in the left(right) panel. The shaded region indicates the $m_{\beta\beta}$ range accessible to future $0\nu\beta\beta$ experiments, LEGEND200 (green) and nEXO (red). The blue shaded bar corresponds to $3\sigma$ interval around $\eta_B^{\text{obs}}$ . . . . .	188
6.19	Case 2 : Predictions for $\eta_B$ as a function of effective neutrino mass $m_{\beta\beta}$ for all values of $t$ for $u = 2s - t = 0$ , $n = 14$ , $M_N = 0.8(1.1)$ TeV with $M_{Z'} = 4.3(4.3)$ TeV for strong NO(IO) in the left(right) panel. The shaded region indicates the $m_{\beta\beta}$ range accessible to future $0\nu\beta\beta$ experiments, LEGEND200 (green) and nEXO (red). Red points correspond to $ \eta_B $ in the $5\sigma$ interval around $\eta_B^{\text{obs}}$ . . . . .	189
6.20	Case 3a (left panel) and Case 3b.1 (right panel) : Predictions for $\eta_B$ as a function of effective neutrino mass $m_{\beta\beta}$ for all even values of $s$ for $n = 17(20)$ , $m = 16(10)$ , $M_N = 2.8(1.2)$ TeV with $M_{Z'} = 5.8(5.6)$ TeV for strong NO(IO) in the left(right) panel. The shaded region indicates the $m_{\beta\beta}$ range accessible to future $0\nu\beta\beta$ experiments, LEGEND200 (green) and nEXO (red). Red points correspond to $ \eta_B $ in the $5\sigma$ interval around $\eta_B^{\text{obs}}$ . . . . .	190

# List of Tables

1.1	Gauge charge assignments for the particle content of the Standard Model, $\mathcal{G}_{SM} \equiv SU(3)_c \times SU(2)_L \times U(1)_Y$ . . . . .	2
2.1	Particle content of the $SU(2)_L \times U(1)_{I_{3R}} \times U(1)_{B-L}$ model. . . . .	18
2.2	The lower bounds on the $Z_R$ boson mass $M_{Z_R}$ and the $v_R$ scale in the $U(1)_{B-L}$ model from the current LHC13 data [1, 2] and the prospects at the HL-LHC 14 TeV with an integrated luminosity of $3000 \text{ fb}^{-1}$ [3, 4] and future 100 TeV collider FCC-hh with a luminosity of $30 \text{ ab}^{-1}$ [4, 5]. The range in each case corresponds to the allowed range of $r_g$ from perturbativity constraints, as given in Eq. (2.9). . . . .	21
2.3	Particle content of the minimal LRSM based on the gauge group $SU(2)_L \times SU(2)_R \times U(1)_{B-L}$ . . . . .	24
2.4	Lower bounds on the $W_R$ and $Z_R$ boson masses and the corresponding $v_R$ scale in the minimal LRSM from the current LHC13 data [6, 1, 2] and the prospects at the HL-LHC 14 TeV with an integrated luminosity of $3000 \text{ fb}^{-1}$ [7, 3, 4] and future 100 TeV collider FCC-hh with a luminosity of $30 \text{ ab}^{-1}$ [8, 4, 5], with both the gauge and scalar perturbativity limits up to the GUT scale taken into consideration. The range in each case corresponds to the allowed range of $r_g$ from perturbativity constraints, as given in Figs. 2.7 and 2.8. The missing entries mean that the corresponding maximum experimental reach has been excluded by the scalar perturbativity constraints. See text for more details. . . . .	35
3.1	Particle content of left-right symmetric model based on the gauge group $SU(3)_C \otimes SU(2)_L \otimes SU(2)_R \otimes U(1)_{B-L}$ . . . . .	45
4.1	The compositions of source and test masses used in the experiment listed and the corresponding values of ratio $\frac{Z_1}{A_1} \frac{Z_2}{A_2}$ . . . . .	91
4.2	The maximum allowed value of scalar NSI in different cases and domains with corresponding ranges for the scalar mass $\phi$ and the coupling strength $y_f$ , for a fixed $y_\nu$ as shown in Figures 4.3-4.6. . . . .	107
5.1	The values of $Q_Z^{(f)}$ used in this work. . . . .	117

- 6.1 Numerical example for mixing pattern of case 1). We choose  $n = 26$  and only display values of  $s$  for which  $\sin \alpha$  is different in magnitude and different from zero. The parameter  $k_1$  is always set as  $k_1 = 0$ . The sign of  $\sin \alpha$  can be changed by taking  $k_1 = 1$  or by choosing a different value of  $s$  than the displayed one. Remember  $s$  is constrained to be  $0 \leq s \leq n - 1 = 25$ . The given values for  $\sin \alpha$  are approximated. We use the formula in (6.46) for computing  $\sin \alpha$ . . . . . 150
- 6.2 Two examples for case 2) that fulfill all constraints on the index  $n$  and that can accommodate the lepton mixing angles well for some value of  $\theta$ , if  $u = 2s - t$  is properly chosen. Since the CP invariant  $I_1$  or better to say the Majorana phase  $\alpha$  depends on  $v = 3t$  only that can take a variety of values we discuss this Majorana phase and its different admitted values for  $n$  and  $u$  in the main text. As always we take  $k_1 = 0$  and  $k_2 = 0$ . . . . . 158
- 6.3 Example for mixing pattern of Case 3a. The parameters  $n$  and  $m$  are chosen as  $n = 17$  and  $m = 1$ . This entails as values for the reactor and the atmospheric mixing angles:  $\sin^2 \theta_{13} \approx 0.0225$  and  $\sin^2 \theta_{23} \approx 0.607$ . Note there are two different best fitting points for the choice  $s = 2$  that indeed lead to different results for the CP phases  $\delta$  and  $\beta$ . The Majorana phase  $\alpha$  only changes sign. The fact that there is only one value for  $s = 3$  is related to the question whether the solar mixing angle can be fitted to its experimental central value or not. If it cannot, then there is only one value of  $\theta_{\text{bf}}$  and it also entails that  $\sin \alpha$  vanishes exactly. For details see [9]. As in all other cases  $k_1 = k_2 = 0$ . . . 166
- 6.4 Example for mixing pattern of case 3 b.1). The parameters  $n$  and  $m$  are chosen as  $n = 8$  and  $m = 4$ . Note there are two different best fitting points for the choice  $s = 1$  and  $s = 4$ . As in all other cases  $k_1 = k_2 = 0$ . Due to that  $\sin \alpha$  and  $\sin \beta$  are not only coinciding in magnitude (coming from the choice  $m = n/2$ ), but also in sign. . . . . 167

# Publications

1. **Garv Chauhan**, P. S. Bhupal Dev, Rabindra N. Mohapatra and Y. Zhang, “Perturbativity constraints on  $U(1)_{B-L}$  and left-right models and implications for heavy gauge boson searches”, JHEP 01 (2019) 208 [arXiv: 1811.08789] [10].
2. **Garv Chauhan**, “Vacuum Stability and Symmetry Breaking in Left-Right Symmetric Model”, JHEP 12 (2019) 137 [arXiv: 1907.07153] [11].
3. K. S. Babu, **Garv Chauhan** and P. S. Bhupal Dev, “Neutrino nonstandard interactions via light scalars in the Earth, Sun, supernovae, and the early Universe”, Phys. Rev. D 101 (2020) 095029 [arXiv: 1912.13488] [12].
4. **Garv Chauhan** and Xun-Jie Xu, “How dark is the  $\nu_R$ -philic dark photon ?”, JHEP 04 (2021) 003 [arXiv: 2012.09980] [13].
5. **Garv Chauhan** and P. S. Bhupal Dev, “Resonant Leptogenesis, Neutrinoless Double Beta Decay and Collider Signals in a Model of Discrete Flavor and CP Symmetries”, [arXiv: 2110.abcde] (to be submitted).

# Acknowledgements

Science is a result of human endeavors, imagination, and creativity. For me, it is as much built on the shoulders of giants as well as on the support of family, friends and colleagues, who have helped me along the way. Completing five years of graduate school is not something I could have done alone, and I want to use this section to thank them.

First and foremost, I would like to thank the Department of Physics at Washington University in St. Louis (WashU), for giving a chance to pursue my dreams. It was during my undergraduate studies in electronics and communications engineering that I decided to pursue physics for my higher degree. WashU Physics gave me a chance to pursue a career in Physics inspite of my non-traditional background and I will be forever indebted to them.

I would also like to thank my thesis advisor Prof. P. S. Bhupal Dev for his valuable guidance over the last four years. He had joined the department a semester later than me. Before he came in, I was looking for an advisor and an area of interest suited for my skills. He introduced me to the centerpiece of this dissertation - problems in beyond the Standard Model physics specially the conundrum with neutrinos. He was always very welcoming and his command on the scientific literature in the field was very impressive to me. This was really fruitful while having discussions with him on varied sub-topics and ideas, which was tremendously useful. He guided me through the harder part of the projects while also letting me be independent when i was working. In addition to his great advises on physics and career, he always encouraged us to participate in conferences and helped me collaborate with several other physicists.

I am extremely grateful to the members of my committee - Michael Ogilvie, Alexander

Seidel, Saori Pastore and Soumendra Lahiri for reading and critiquing my thesis. In particular, I would like to thank Mike and Alex for their helpful suggestions and advises during all these years as my faculty mentoring committee members. I also want to thank Saori for always being a great mentor and friend to me.

I would also like to extend gratitude to all my collaborators, K.S. Babu, Rabindra Mohapatra, and Xun-Jie Xu from whom I have learned a lot of physics and research skills. Especially my deepest gratitude to K.S. Babu for his valuable scientific guidance during my Ph.D. and long discussions during our collaborations. I also thank Department of Physics at Oklahoma State University for their hospitality during my "Neutrino Theory Network" (NTN) visit. Also many thanks to my undergraduate advisor Harish Parthasarathy, whose monumental support and guidance helped me reach this platform. I would also like to acknowledge my fellow group members, Yongchao Zhang, Yicong Sui and Fang Xu for many fruitful discussions. Special thanks to Yicong for being a a great friend and travel buddy to conferences.

I cannot begin to express my thanks to the Pffeifer Physics library and Department of Physics staff for all the help over the years. I am also grateful to McDonnell Center for the Space Sciences and the Graduate School Arts & Sciences for travel support to conferences and seminars.

I also had great pleasure of sharing office space in Compton 375 "theoretical lab" with Sumanta, Steven, Yicong, Fang and Matheus. Thank you all for your great company, physics and other lively discussions that kept the working atmosphere vibrant.

I am extremely grateful to all of my friends in the Physics department for all the support and the fun times together. They are family to me and I have made unforgettable memories with them. I would like to specially thank my close friends Sayantan, Siera, Andrew (Diaz, West), Yuewen, Xia Ji, Elham and Jufri for their invaluable friendship and support in my Ph.D. life. I would like to express my loving and deep appreciation for Maryam, who has been there for me all the time in good and bad.

I am most thankful to my parents and my sister Deepanjali - for their love and constant support for all my decisions. I am specially grateful to my parents and deeply thoughtful for all their sacrifices over the years to provide me with a bright future.

Garv Chauhan

*Washington University in St. Louis*

*December, 2021*

Dedicated to the loving memory of my grandparents,  
Dayawati and Isam

## ABSTRACT OF THE DISSERTATION

Probing New Physics Beyond the Standard Model via New Neutrino Interactions

by

Garv Chauhan

Doctor of Philosophy in Physics

Washington University in St. Louis, 2021

Professor Bhupal Dev (Chair)

The Standard Model (SM) of Particle Physics provides a self-consistent quantum field theoretic framework to explain three of the four known fundamental forces (electromagnetic, weak, strong) along with classifying all known elementary particles. Since its conception in the 1960s, the SM has been one of the most tested theories of physics and has withstood all experimental batterings. In spite of these successes, there are compelling indications, both experimental and theoretical, that require us to expand our understanding of the nature beyond the SM (BSM). Arguably the most glaring indication of BSM physics is the observation of neutrino oscillations, which implies that neutrinos are massive. The underlying BSM physics responsible for neutrino mass must necessarily involve new BSM interactions of neutrinos. In this dissertation, we focus on some case studies of the theory and phenomenology of these new BSM neutrino interactions. On the theoretical side, we consider a class of BSM scenarios for neutrino masses with extra gauge groups, whose generators contribute to the electric charge, and studied the effect of perturbativity constraints on these models, assuming them to be valid up to higher energy scales. In particular, we have derived lower bounds on the new gauge bosons and their couplings from perturbativity considerations, which have important implications for future searches of these BSM particles. In our second work, we have developed analytic techniques to study the vacuum stability and spontaneous symmetry breaking for generic multi-Higgs potential, with application to the well-motivated Left-Right

Symmetric Model (LRSM) as an example study. We found that requiring vacuum stability in conjunction with other phenomenological constraints significantly reduces the available parameter space for low-scale LRSM. On a more phenomenological side, we study the effect of Non-standard interactions (NSI) of neutrinos with matter mediated by a scalar field. We develop general techniques to study matter effects and long-range force effects consistently in all media. We show that observable scalar NSI effects, although precluded in terrestrial experiments, are still possible in future solar and supernovae neutrino data, and in cosmological observations such as cosmic microwave background and big bang nucleosynthesis data. In another project, we study the experimental prospects for a scenario with neutrino interactions with right-handed neutrinos  $\nu_R$  charged under a hidden  $U(1)$  gauge group. We investigate the loop-induced couplings and find that the  $\nu_R$ -philic dark photon is not inaccessiblely dark and can be of potential importance to future dark photon searches. In our final project, we explore the production of baryon asymmetry through resonant leptogenesis and phenomenological signatures of the type-I seesaw scenario with a given flavor and CP symmetry group. We find that requiring successful baryon asymmetry generation via resonant leptogenesis imposes interesting constraints for the detection prospects of heavy neutrinos at colliders, as well as in future neutrinoless double beta decay experiments.

# Chapter 1

## Introduction

*"You take the blue pill...the story ends, you wake up in your bed and believe whatever you want to believe. You take the red pill...you stay in Wonderland, and I show you how deep the rabbit hole goes."*

- Morpheus, The Matrix (1999)

In ancient times, the world was believed to be composed of four basic elements - fire, earth, water, air. This understanding of physical world in those times came from the distillation of direct experiences with nature everyday. This was the ultimate scale that could be probed in those times. Since then the story has progressed a couple thousand pages. We can now probe nature at length scales of attometer<sup>1</sup> to billions of light-years<sup>2</sup> away.

In our current understanding of the entire observable natural world, simply referred to as "*The Universe*", composed of 17 fundamental particles and governed by four natural forces: electromagnetic force, weak nuclear force, strong nuclear force and gravity<sup>3</sup>.

### 1.1 Standard Model of Particle Physics

Standard Model (SM) of Particle Physics governs the physics in everyday life except gravity.

It was brought to life by Steven Weinberg in 1967 in his landmark paper, "A Model of

---

<sup>1</sup> 1 am =  $10^{-18}$  m

<sup>2</sup> 1 ly =  $9.4607 \times 10^{15}$  m

<sup>3</sup> The definition of what constitutes a fundamental force has delved into a fuzzy territory. More appropriately, it can be phrased mathematically as 3 fundamental gauge groups with addition of general relativity.

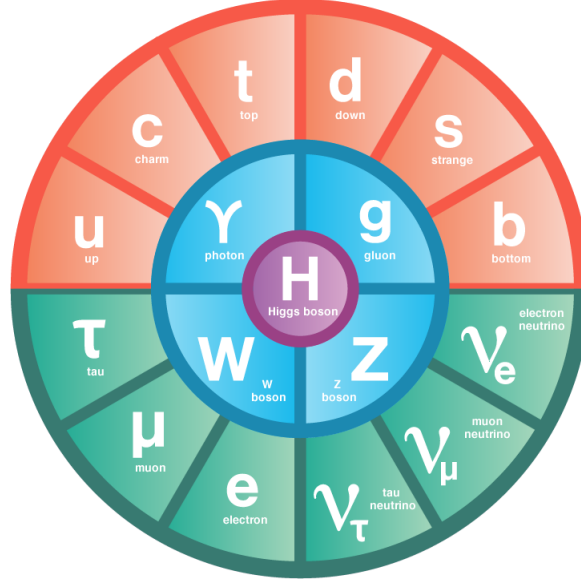


Fig. 1.1: Particle content of the Standard Model,

	$SU(3)_c$	$SU(2)_L$	$U(1)_Y$
$Q$	<b>3</b>	<b>2</b>	$\frac{1}{3}$
$u_R$	<b>3</b>	<b>1</b>	$\frac{2}{3}$
$d_R$	<b>3</b>	<b>1</b>	$-\frac{1}{3}$
$L$	<b>1</b>	<b>2</b>	$-\frac{1}{2}$
$e_R$	<b>1</b>	<b>1</b>	$-1$
$H$	<b>1</b>	<b>2</b>	$1$

Tab. 1.1: Gauge charge assignments for the particle content of the Standard Model,  $\mathcal{G}_{SM} \equiv SU(3)_c \times SU(2)_L \times U(1)_Y$

Leptons" [14]. Since then SM has been one of the most tested theories of physics and has withstood all experimental batterings. It can explain three of the four known fundamental forces (electromagnetic force, weak nuclear force, strong nuclear force) along with classifying all known elementary particles.

Standard Model is a non-abelian Yang-Mills gauge theory invariant under a local internal symmetry group :

$$SU(3)_C \times SU(2)_L \times U(1)_Y \tag{1.1}$$

where the conserved charge corresponding to  $SU(3)_c$  is the color charge, for  $SU(2)$  is the weak isospin and weak hypercharge for  $U(1)_Y$ . The particle content is detailed in Fig. 1.1.

### 1.1.1 Electroweak Sector

The symmetry group for the Electroweak (EW) sector is  $SU(2)_L \times U(1)_Y$ , where  $L$  denotes interactions only with left-handed fermions and  $Y$  denotes the weak hypercharge.

$$\mathcal{L}_{\text{EW}} = \sum_{\psi} \bar{\psi} \gamma^{\mu} D_{\mu} \psi - \frac{1}{4} W_a^{\mu\nu} W_{\mu\nu}^a - \frac{1}{4} B^{\mu\nu} B_{\mu\nu} \quad (1.2)$$

where the three contributions are the gauge-invariant kinetic terms for fermion field  $\psi$  and the gauge bosons ( $W_{\mu}, B_{\mu}$ ) and,

$$D_{\mu} = \left( i\partial_{\mu} - g' \frac{1}{2} Y_W B_{\mu} - g \frac{1}{2} \vec{\tau}_L \cdot \vec{W}_{\mu} \right) \quad (1.3)$$

denotes the covariant derivative that handles the gauge transformations of the fermionic fields.  $B_{\mu}$  is the  $U(1)_Y$  gauge field,  $W_{\mu}^a$  is the three component  $SU(2)$  gauge field (where  $a = (1, 2, 3)$ ),  $Y_W$  and  $\vec{\tau}_L$  are the group generators for  $U(1)_Y$  and  $SU(2)_L$  with coupling constants  $g'$  and  $g$  respectively. Note that in eq. 1.2 (and further in this section), Einstein summation convention is being followed and the variable  $a$  is summed over.

### 1.1.2 Quantum Chromodynamics

The symmetry group for the quantum chromodynamics (QCD) sector is  $SU(3)_c$ , where  $c$  denotes interactions only with particle species carrying the color charge.

$$\mathcal{L}_{\text{QCD}} = \sum_{\psi} \bar{\psi}_i \left( i\gamma^{\mu} (\partial_{\mu} \delta_{ij} - ig_s G_{\mu}^a T_{ij}^a) \right) \psi_j - \frac{1}{4} G_{\mu\nu}^a G_a^{\mu\nu} \quad (1.4)$$

where the two contributions are the gauge-invariant kinetic terms for fermion field  $\psi$  and the gauge bosons  $G_{\mu}^a$  (which denotes the 8 component  $SU(3)$  gauge field) and  $T_{ij}^a$  are  $3 \times 3$  Gell-Mann matrices which are the group generators for  $SU(3)_c$  with coupling constants  $g_s$ .

### 1.1.3 Higgs Mechanism

It is important to note that until now all the degrees of freedom in the gauge theory are massless, which is in conflict with the observations of the natural world. Therefore, we need a way to provide masses to particles in the theory, which is exactly what is accomplished by the addition of the Higgs mechanism<sup>4</sup>.

The Higgs mechanism is based on addition of a scalar Higgs field which undergoes spontaneous symmetry breaking. In the Standard model, the Higgs field is a complex scalar of the group  $SU(2)_L$ ,

$$\Phi = \begin{pmatrix} \phi^+ \\ \phi^0 \end{pmatrix} \quad (1.5)$$

with weak hypercharge  $Y = +1$  and no color charge. The gauge symmetry of the SM and renormalizability requires the Lagrangian for  $\Phi$  as follows :

$$\mathcal{L}_{\text{Higgs}} = (D_\mu \Phi)(D^\mu \Phi) + \frac{1}{2}\mu^2 \Phi\Phi - \frac{1}{4}\lambda_h(\Phi\Phi)^2 \quad (1.6)$$

If  $\mu^2 > 0$ , the scalar field  $\Phi$  develops a non-zero vacuum expectation value (VEV) which spontaneously breaks the symmetry. Since the electric charge should be conserved after breaking, only the neutral scalar field can develop a non-zero VEV.

$$\langle \Phi \rangle = \begin{pmatrix} 0 \\ \frac{1}{\sqrt{2}}v \end{pmatrix} \quad (1.7)$$

This leads to the breaking of the electroweak sector to electromagnetism, which is now the only remaining unbroken symmetry of the vacuum.

After SSB, three out of four scalar degrees of freedom acts as the longitudinal polarization

---

<sup>4</sup> More appropriately should be referred as "Anderson-Englert-Brout-Higgs-Guralnik-Hagen-Kibble" mechanism

for the three linear combinations of the gauge fields, hence making them massive.

$$W_\mu^\pm = \frac{W_\mu^1 \mp W_\mu^2}{\sqrt{2}}, \quad Z_\mu = \frac{gW_\mu^3 - g'B_\mu}{\sqrt{g^2 + g'^2}}, \quad A_\mu = \frac{gW_\mu^3 + g'B_\mu}{\sqrt{g^2 + g'^2}} \quad (1.8)$$

with masses given by :

$$m_{W^\pm} = \frac{gv}{2}, \quad m_Z = \frac{\sqrt{g^2 + g'^2}v}{2}, \quad m_A = 0 \quad (1.9)$$

The fourth leftover degree of freedom of the scalar Higgs field is identified as the Higgs boson  $h^5$ . In the unitary gauge, the scalar doublet is written as :

$$\Phi = \begin{pmatrix} 0 \\ \frac{1}{\sqrt{2}}v + h \end{pmatrix} \quad (1.10)$$

### 1.1.4 Yukawa sector

Now we can generate the masses for all the fermions with the VEV of a single Higgs doublet with use of  $\Phi$  and  $\tilde{\Phi}$ , where

$$\tilde{\Phi}_i = \epsilon_{ij}\Phi_j^*, \quad \langle \tilde{\Phi} \rangle = \begin{pmatrix} \frac{1}{\sqrt{2}}v \\ 0 \end{pmatrix} \quad (1.11)$$

To show how SSB generates fermion masses in the SM, we look at the first generation as an example :

$$\mathcal{L}_{\text{Yuk}} = f_e \bar{L} \Phi e_R + f_u \bar{q}_L \tilde{\Phi} u_R + f_d \bar{q}_L \Phi d_R + h.c. \quad (1.12)$$

After SSB, the Lagrangian takes the form :

$$\mathcal{L}_{\text{Yuk}} = \frac{f_e v}{\sqrt{2}}(\bar{e}_L e_R + \bar{e}_R e_L) + \frac{f_u v}{\sqrt{2}}(\bar{u}_L u_R + \bar{u}_R u_L) + \frac{f_d v}{\sqrt{2}}(\bar{d}_L d_R + \bar{d}_R d_L) \quad (1.13)$$

---

<sup>5</sup> It was Steven Weinberg who correctly incorporated the Higgs mechanism in the electroweak theory by identifying the Higgs field as a  $SU(2)_L$  doublet of the electroweak gauge group. For this reason, SM Higgs boson might also be referred as the "Weinberg" boson.

from which the fermion masses can be directly read off.

## 1.2 Motivations for BSM Physics

The successful experimental predictions of the SM places it on a grand pedestal as a powerful theory of nature. In spite of these successes, there are indeed few cracks through which we can gain insight to build further on. In this section, we discuss few of the most motivated theoretical and experimental hints for looking beyond the Standard Model (BSM). We discuss experimental motivations, for e.g. explanation for small neutrino masses, neutrino mass mechanism and generation of matter-antimatter asymmetry of the Universe. Few of the theoretical motivations include the issue of vacuum stability in SM and prospects of unification of the couplings at higher energies, for which we will look and offer theoretical guidance by analyzing the limits of our most motivated BSM models like Left-Right Symmetric Model and  $U(1)_{B-L}$  model.

### 1.2.1 Experimental Motivations

#### 1.2.1.1 Neutrino Oscillations and Masses

In the late 1960s, the solar neutrino problem arose from observations in Homestake Experiment led by Ray Davis and John Bahcall, in which there were a lot fewer neutrino events reported than expected theoretically assuming the standard solar model. This problem was only resolved later in around 2002 after measurements of other experiments involving solar, atmospheric and reactor neutrinos, which could be effectively explained if neutrinos of different flavors could change into each other. This mechanism for neutrino flavor conversion during propagation is now known as "Neutrino oscillations" . An important implication of neutrino oscillations is that neutrinos can only oscillate in vacuum if they have non-zero masses. Although the absolute mass scale is still unknown but the associated mass splittings have been measured to sub-eV precision along with the mixing angles. In addition, the

## Introduction

---

absolute sign for one of the mass splitting is unknown and this leads to two possible mass hierarchy for neutrinos : Normal ordering, NO ( $m_3 > m_2 > m_1$ ) and Inverted ordering, IO ( $m_2 > m_1 > m_3$ ).

For neutrinos following NO, the three masses  $m_i$  are parametrized as

$$m_1 = m_0 \quad , \quad m_2 = \sqrt{m_0^2 + \Delta m_{\text{sol}}^2} \quad , \quad m_3 = \sqrt{m_0^2 + \Delta m_{\text{atm}}^2} \quad (1.14)$$

with  $m_0$  denoting the lightest neutrino mass and from the global fit 2020 [15]

$$\begin{aligned} \Delta m_{\text{sol}}^2 = m_2^2 - m_1^2 &= \left(7.42_{-0.20}^{+0.21}\right) \times 10^{-5} \text{ eV}^2, & \Delta m_{\text{atm}}^2 = m_3^2 - m_1^2 &= \left(2.517_{-0.028}^{+0.026}\right) \times 10^{-3} \text{ eV}^2, \\ 6.82 \times 10^{-5} \text{ eV}^2 &\leq \Delta m_{\text{sol}}^2 \leq 8.04 \times 10^{-5} \text{ eV}^2, \\ 2.435 \times 10^{-3} \text{ eV}^2 &\leq \Delta m_{\text{atm}}^2 \leq 2.598 \times 10^{-3} \text{ eV}^2. \end{aligned} \quad (1.15)$$

at the  $3\sigma$  level.

For neutrino with IO, the masses  $m_i$  are written as

$$m_1 = \sqrt{m_0^2 + |\Delta m_{\text{atm}}^2| - \Delta m_{\text{sol}}^2}, \quad m_2 = \sqrt{m_0^2 + |\Delta m_{\text{atm}}^2|}, \quad m_3 = m_0 \quad (1.16)$$

where

$$\begin{aligned} \Delta m_{\text{sol}}^2 = m_2^2 - m_1^2 &= \left(7.42_{-0.20}^{+0.21}\right) \times 10^{-5} \text{ eV}^2, & \Delta m_{\text{atm}}^2 = m_3^2 - m_2^2 &= \left(-2.498_{-0.028}^{+0.028}\right) \times 10^{-3} \text{ eV}^2 \\ 6.82 \times 10^{-5} \text{ eV}^2 &\leq \Delta m_{\text{sol}}^2 \leq 8.04 \times 10^{-5} \text{ eV}^2, \\ -2.581 \times 10^{-3} \text{ eV}^2 &\leq \Delta m_{\text{atm}}^2 \leq -2.414 \times 10^{-3} \text{ eV}^2 \end{aligned} \quad (1.17)$$

at the  $3\sigma$  level.

The lepton flavor eigenstates of neutrino  $\nu_f$  ( $f = e, \mu, \tau$ ) can be written as a linear combination of the mass eigenstates  $\nu_i$  ( $i = 1, 2, 3$ ),

$$\nu_f = \sum_i U_{fi} \nu_i \quad (1.18)$$

## Introduction

---

where  $U$  is the  $3 \times 3$  unitary mixing matrix for neutrinos, known as Pontecorvo-Maki-Nakagawa-Sakata (PMNS) matrix.

As parametrization of the PMNS mixing matrix we take

$$U_{\text{PMNS}} = \begin{pmatrix} c_{12}c_{13} & s_{12}c_{13} & s_{13}e^{-i\delta} \\ -s_{12}c_{23} - c_{12}s_{23}s_{13}e^{i\delta} & c_{12}c_{23} - s_{12}s_{23}s_{13}e^{i\delta} & s_{23}c_{13} \\ s_{12}s_{23} - c_{12}c_{23}s_{13}e^{i\delta} & -c_{12}s_{23} - s_{12}c_{23}s_{13}e^{i\delta} & c_{23}c_{13} \end{pmatrix} \text{diag}(1, e^{i\alpha/2}, e^{i(\beta/2+\delta)}) \quad (1.19)$$

and  $s_{ij} = \sin \theta_{ij}$  and  $c_{ij} = \cos \theta_{ij}$ . The mixing angles  $\theta_{ij}$  range from 0 to  $\pi/2$ , while the Majorana phases  $\alpha, \beta$  as well as the Dirac phase  $\delta$  take values between 0 and  $2\pi$ . Note one of the Majorana phases becomes unphysical, if the lightest neutrino mass  $m_0$  vanishes.

As experimental constraints on the lepton mixing angles and the CP phase  $\delta$  we use the results from the global fit 2020 [15]. These read for NO (IO)

$$\begin{aligned} \sin^2 \theta_{13} &= 0.02219(38)_{-0.00063(2)}^{+0.00062(3)} & \text{and} & \quad 0.02032(52) \leq \sin^2 \theta_{13} \leq 0.02410(28) , \\ \sin^2 \theta_{12} &= 0.304_{-0.012}^{+0.012(3)} & \text{and} & \quad 0.269 \leq \sin^2 \theta_{12} \leq 0.343 , \\ \sin^2 \theta_{23} &= 0.573(5)_{-0.020(19)}^{+0.016(23)} & \text{and} & \quad 0.415(9) \leq \sin^2 \theta_{23} \leq 0.616(7) , \\ \delta &= 3.43(4.98)_{-0.42}^{+0.47} & \text{and} & \quad 2.09(3.36) \leq \delta \leq 6.44(15) \end{aligned} \quad (1.20)$$

for best fit value,  $1\sigma$  level and  $3\sigma$  range, respectively.

To sum up, SM neutrinos do not have a right-handed partner and hence are massless to all orders in perturbation theory. But the presence of oscillations between different flavors indicates massive neutrinos and hence directly points to physics beyond the SM.

### 1.2.1.2 Matter-Antimatter Asymmetry

One of the most important questions in physics is, why there is more matter than antimatter? This asymmetry between matter and antimatter can be precisely stated in terms of a ratio  $\eta_B$  defined as the number density of net baryons over photons. This ratio has been

determined experimentally using the abundance of light elements at the time of Big Bang Nucleosynthesis. Most recent precise measurement done by Planck Collaboration (2018) [16] sets the matter-antimatter asymmetry parameter  $\eta_B$

$$\eta_B = \frac{n_b - n_{\bar{b}}}{n_\gamma} = (6.12 \pm 0.08) \times 10^{-10} \quad (1.21)$$

This can be explained through the dynamical generation of baryon asymmetry for which required basic ingredients includes the 3 Sakharov conditions for a model: presence of C & CP violation, baryon number violation and departure from thermal equilibrium for the baryon number violating processes.

A very closely related idea for baryon asymmetry generation is the leptogenesis mechanism. The central idea of leptogenesis is the production of leptonic asymmetry in early Universe which is then converted to baryonic asymmetry of the Universe (BAU) through B-L conserving electroweak sphaleron interactions<sup>6</sup>. More details on the leptogenesis mechanism are covered in Chapter 6.

### 1.2.1.3 Dark Matter

In 1930s while observing the Coma Cluster, Swiss astrophysicist Fritz Zwicky noticed that the observed luminous mass of the cluster was less than then the mass inferred from the virial motion of the galaxies near the edge of the cluster<sup>7</sup> He inferred that most of the mass of the cluster is dark and called it “*dunkle Materie*” (‘dark matter’). A turning point in missing matter problem occurred in 1970-1980s. Vera Rubin along with Ken Ford measured the galactic rotation curves for numerous spiral galaxies. They found that rotation curves tend to flattening out at far enough distances from the center of the galaxy compared to the Newtonian expectation of gradual decrease in radial velocity at larger radii. They showed

---

<sup>6</sup> SM Sphaleron interactions are non-perturbative processes that violate net baryon + lepton  $B+L$  number but conserve the total  $B - L$  charge.

<sup>7</sup> Zwicky had estimated amount of missing matter to be 400 times more than luminous mass of the cluster. It is now known that his estimate was off by an order of magnitude mainly due to (then known) value of the Hubble constant.

that galaxies must contain six times more dark matter than luminous matter. These observations were monumental in convincing the larger community for the existence of Dark Matter (DM).

It has been shown through studies on Big Bang nucleosynthesis and gravitational lensing that bulk of the DM in the universe cannot be made up of currently known SM particles. Thus, presence of missing mass constitutes one of the most direct push for BSM physics. Although the experimental searches for various DM candidates have been done since late 1980s, all of these searches have turned empty handed. One of the most popular earlier choices for DM called Weakly Interacting Massive Particles (WIMPS) have been ruled out (although more convoluted models might still survive). For now this has motivated the search for light dark matter candidates such as axion-like particles (with SM axion being ruled out).

There is an another interesting class of DM candidates such as Bose-Einstein Condensate DM, fuzzy DM and Superfluid DM. In these scenarios, the point-particle behaviour of the DM is lost at short scales and instead manifests in form of a condensate (can be classical or quantum based on the model) at the galactic scales.

## 1.2.2 Theoretical Motivations

### 1.2.2.1 Vacuum Stability

An important problem with the SM is the stability of the scalar Higgs potential at high-energies. The condition for stability of the scalar potential in the SM is the positivity of the Higgs quartic coupling  $\lambda_h$  (see Eq. 1.6). However, renormalization group equation (RGE) analysis shows that  $\lambda_h$  becomes negative at a scale of around  $10^{10}$  GeV for experimentally measured value of the Higgs mass [17]. Thus, the potential in the SM is unbounded from below around this scale and makes the theory unstable<sup>8</sup>. This motivates us to look beyond

---

<sup>8</sup> Technically, the SM vacuum is metastable i.e. the average time to tunnel to true vacuum state is longer than the age of the Universe

the SM and also ensure to ensure the stability of the scalar Higgs potential in these candidate theories for physics beyond the SM.

### 1.2.2.2 GUT Unification

Motivated by the unification of electromagnetism and weak force as a two different manifestation of a single electroweak force, points to an obvious question : Can all of the fundamental forces in the SM be unified into one fundamental force ? This can more concretely be described in language of gauge groups : Does there exist a simplified gauge symmetry group structure that breaks down to SM at lower energies ? The coupling constants in any QFT depend on the energy scale and termed as "running" couplings. The unification at higher energies might be reflected indirectly if the gauge couplings of the SM unify at some higher scale, often dubbed as GUT scale where GUT stands for the Grand Unified Theory. Although the SM couplings do not unify exactly near GUT scale but this scenario might change with introduction of new particles/gauge symmetries at between TeV to GUT scale. The system of equations governing the running of the coupling constants are known as Renormalization Group Equations (RGEs).

## 1.3 Towards BSM Physics

In this dissertation, we explore the new physics beyond the SM motivated by the theoretical and experimental reasoning as described in the previous section.

In Chapter 2, we derive perturbativity constraints on beyond standard model scenarios with extra gauge groups, such as  $SU(2)$  or  $U(1)$ , whose generators contribute to the electric charge, and show that there are both upper and lower limits on the additional gauge couplings, from the requirement that the couplings remain perturbative up to the grand unification theory (GUT) scale. This leads to stringent constraints on the masses of the corresponding gauge bosons and their collider phenomenology.

In Chapter 3, we derive analytic necessary and sufficient conditions for the vacuum stability of the left-right symmetric model as an example by using the concepts of copositivity and gauge orbit spaces. We also derive the conditions sufficient for successful symmetry breaking and the existence of a correct vacuum. We also discuss the renormalization group analysis of the scalar quartic couplings through an example study that satisfies vacuum stability, perturbativity, unitarity and experimental bounds on the physical scalar masses.

BSM physics of neutrino masses entail new interactions and thus motivates to carefully study them for minute effects. In Chapter 4, we study the effect of Nonstandard interactions (NSI) of neutrinos with matter mediated by a scalar field. We develop general techniques to study matter effects and long range force effects consistently even in relativistic backgrounds, and discuss various limiting cases applicable to the neutrino propagation in different media, such as the Earth, Sun, supernovae and early Universe.

In Chapter 5, We consider a generic dark photon that arises from a hidden U(1) gauge symmetry imposed on right-handed neutrinos  $\nu_R$ . Such a  $\nu_R$ -philic dark photon is naturally dark due to the absence of tree-level couplings to normal matter. However, loop-induced couplings to charged leptons and quarks are inevitable, provided that  $\nu_R$  mix with left-handed neutrinos via Dirac mass terms. We investigate the loop-induced couplings and find that the  $\nu_R$ -philic dark photon is not inaccessibly dark, which could be of potential importance to future dark photon searches.

In Chapter 6, we discuss about the production of baryon asymmetry through resonant leptogenesis and phenomenological signatures of type-I seesaw scenario with a flavour and a CP symmetry that strongly constrain lepton mixing angles, and both low- and high-energy CP phases. We specially focus on the effect of these symmetries on the collider signals in minimal  $U(1)_{B-L}$  model and effective neutrino mass ( $m_{\beta\beta}$ ) in neutrinoless double beta decay ( $0\nu\beta\beta$ ), while also requiring production of the experimentally observed baryon asymmetry ( $\eta_B$ ).

We finally conclude in Chapter. 7.

## Chapter 2

# Perturbativity and Unitarity in $U(1)_{B-L}$ and Left-Right Model<sup>9</sup>

*"I don't want to believe. I want to know."*

- Carl Sagan

## 2.1 Introduction

BSM physics could of course be at any scale; however, from an experimental point of view, it is interesting if it is at the TeV scale so that it could be tested by current and planned experiments. Many TeV-scale BSM extensions proposed to remedy the above shortcomings of the SM introduce extended gauge groups, such as extra  $U(1)$  or  $SU(2) \times U(1)$  groups at the TeV scale, which are usually derived from a higher symmetry group, such as  $SO(10)$  [18, 19, 20, 21, 22] at the grand unification theory (GUT) scale. Such extensions broadly fall into two classes:

- (i) The generators of the extra gauge groups contribute to the electric charge [23, 24].

Two widely discussed examples are (a) the models based on the gauge group  $SU(2)_L \times U(1)_{I_{3R}} \times U(1)_{B-L}$  [25, 26] and (b) the left-right symmetric model (LRSM) based on the gauge group  $SU(2)_L \times SU(2)_R \times U(1)_{B-L}$  [27, 28, 29], both of which are useful

---

<sup>9</sup> This chapter is based on [10]

and motivated in order to understand neutrino masses via the seesaw mechanism [30, 31, 32, 33, 34].

- (ii) The extra gauge groups do not contribute to electric charge. Examples of this class are the dark photon [35, 36, 37],  $U(1)_{B-L}$  [38, 39], and more generic  $U(1)_X$  [40, 41, 42, 43] models, which have been discussed extensively in connection with dark matter [44] and collider signatures [45].

In both these classes of models, demanding that gauge couplings remain perturbative i.e.  $g_i < \sqrt{4\pi}$  up to the GUT or Planck scale imposes severe constraints on the allowed values of the extra gauge couplings, as well as on the masses of the additional gauge bosons. In case (i), where the additional group generators contribute to the electric charge, we find both upper and lower limits on the gauge couplings, whereas in case (ii), where the additional gauge couplings are not related to the electric charge, we only get upper limits and no lower limits. In this chapter, we only focus on the case (i) models and derive the perturbativity bounds on the gauge couplings  $g_R$  and  $g_{BL}$ , corresponding to the  $SU(2)_R$  (or  $U(1)_{I_{3R}}$ ) and  $U(1)_{B-L}$  gauge groups, respectively.

Our results have far-reaching implications for collider searches for extra gauge bosons. In particular, they have to be taken into consideration, while interpreting the current direct search constraints on the  $W_R$  [46, 6] and  $Z_R$  [1, 2] bosons from the Large Hadron Collider (LHC) data, or the prospects [7, 47, 8, 5, 48] at the High-Luminosity LHC (HL-LHC) and a future 100 TeV collider [49, 50]. In particular, if the measured gauge couplings fall outside the limits derived from perturbativity up to the GUT (or Planck) scale, that would imply that there is new physics at the TeV or intermediate scale which allows this to happen. That would have interesting implications for new BSM physics.

There is another important implication of our results for the LRSM. Due to the stringent flavor-changing neutral current (FCNC) constraints in the high-precision electroweak data such as  $K_0 - \bar{K}_0$ ,  $B_d - \bar{B}_d$  and  $B_s - \bar{B}_s$  mixings [51], the parity partner of the SM doublet

scalar is required to be very heavy, i.e.  $\gtrsim 10$  TeV [52, 53, 54, 55].<sup>10</sup> Then one of the quartic couplings ( $\alpha_3$ ) in the scalar potential [see Eq. (2.17)] is of order one, if the right-handed (RH) scale  $v_R$  lies in the few-TeV range. As a result, the perturbativity of the quartic couplings up to the GUT scale imposes a lower bound on the  $v_R$  scale, i.e.  $v_R \gtrsim 10$  TeV. The renormalization group (RG) running of  $\alpha_3$  and other quartic couplings involves the gauge couplings  $g_R$  and/or  $g_{BL}$ . Hence, the perturbativity constraints in the scalar sector of LRSM do not only narrow down significantly the allowed ranges for the gauge couplings  $g_R$  and  $g_{BL}$ , but also supersede the current  $W_R$  and  $Z_R$  mass limits from the LHC, and even rule out the possibility of finding them at the HL-LHC (see Fig. 2.7). Therefore, if a heavy  $W_R$  and/or  $Z_R$  boson was to be found at the later stages of LHC, then either it does not belong to the LRSM, or the minimal LRSM has to be further extended at the TeV-scale or a higher intermediate scale, such that all the gauge, scalar and Yukawa couplings are perturbative up to the GUT scale.

Though we focus on the minimal  $U(1)_{B-L}$  and LRSM gauge groups in this chapter, the basic arguments and main results could easily be generalized to other gauge groups at the TeV scale, such as the  $SU(3)_L \times U(1)_X$  [56, 57, 58, 59],  $SU(3)_L \times SU(3)_R \times U(1)_X$  [60, 61, 62, 63, 64], and alternative left-right models with universal seesaw mechanism for the SM quarks and charged leptons [65, 66, 67, 68, 69, 70, 71, 72, 73, 74] or with a stable right-handed neutrino (RHN) dark matter [75, 76]. However, our results do not apply to situations where the extra  $U(1)$  groups emerge out of non-Abelian groups at an intermediate scale, since they will completely alter the ultraviolet (UV) behavior of the TeV scale  $U(1)$  gauge couplings. String theories provide many examples where extra  $U(1)$ 's persist till the string scale without necessarily being embedded in intermediate scale non-Abelian groups [45, 77]. However, if the extra TeV-scale gauge group in question is valid up to the GUT scale, where it gets embedded into a non-Abelian GUT group,  $SO(10)$  [18, 19, 20, 21, 22] or higher rank groups, our results will be applicable and give useful information on the particle spectrum at the

---

<sup>10</sup> Due to sizable hadronic uncertainties, the FCNC constraints on the heavy bidoublet scalars might go up to  $\sim 25$  TeV.

TeV scale.

This chapter is organized as follows: In Section 2.2, we sketch the basic theoretical arguments behind the perturbativity constraints on the gauge couplings that contribute to the electric charge. The application to the  $SU(2)_L \times U(1)_{I_{3R}} \times U(1)_{B-L}$  gauge group is detailed in Section 2.3, along with the implications for searches of the heavy  $Z_R$  boson and the  $v_R$  scale at the LHC and future 100 TeV colliders. The analogous study for the LRSM gauge group  $SU(2)_L \times SU(2)_R \times U(1)_{B-L}$  is performed in Section 2.4, where we also include the phenomenological implications on the  $W_R, Z_R$  searches at colliders. We conclude in Section 2.5. The state-of-the-art two-loop RG equations for the gauge, quartic and Yukawa couplings in the LRSM are collected in Appendix A.

## 2.2 Theoretical constraints

Our basic strategy is as follows: In the SM, when the electroweak gauge group breaks down to the electromagnetic group, i.e.  $\mathcal{G}_{\text{SM}} \equiv SU(2)_L \times U(1)_Y \rightarrow U(1)_{\text{EM}}$ , the electric charge is given by

$$Q = I_{3L} + \frac{Y}{2}, \quad (2.1)$$

and we have the relation among the gauge couplings at the electroweak scale:

$$\frac{1}{e^2} = \frac{1}{g_L^2} + \frac{1}{g_Y^2}, \quad (2.2)$$

where  $g_L, g_Y, e$  are the gauge couplings for the  $SU(2)_L, U(1)_Y$  and  $U(1)_{\text{EM}}$  gauge groups, respectively. Current experiments completely determine these coupling values at the electroweak scale [51]:

$$e = 0.313 \pm 0.000022, \quad g_L = 0.652 \pm 0.00026, \quad g_Y = 0.357 \pm 0.000060. \quad (2.3)$$

When the SM is extended in the gauge sector, to the gauge group  $SU(2)_L \times U(1)_X \times U(1)_Z$ , such that the extra  $U(1)_{X,Z}$ 's both contribute to the electric charge, then the modified electric charge formula becomes

$$Q = I_{3L} + I_X + I_Z. \quad (2.4)$$

This is also true if we replace one of the  $U(1)_{X,Z}$ 's with an  $SU(2)$ . The corresponding relation involving the new gauge couplings become [78]:<sup>11</sup>

$$\frac{1}{g_Y^2} = \frac{1}{g_X^2} + \frac{1}{g_Z^2}, \quad (2.5)$$

where  $g_X$  and  $g_Z$  are the gauge couplings for the  $U(1)_X$  and  $U(1)_Z$  gauge groups, respectively. This relation holds at the scale  $v_X$ , where  $U(1)_X \times U(1)_Z$  breaks down to the SM  $U(1)_Y$  and correlates the couplings  $g_{X,Z}$  to  $g_Y$ . Since the value of  $g_Y$  is experimentally determined at any scale  $v_X$  (with the appropriate SM RG evolution), we must have  $g_{X,Z}$  bounded from below in order to satisfy Eq. (2.5). On the other hand, requiring that the gauge couplings  $g_{X,Z}$  remain perturbative till the GUT or Planck scale implies that  $g_{X,Z}$  must also be bounded from above at any given scale  $v_X$ . In other words, the couplings  $g_{X,Z}$  can neither be arbitrarily large nor arbitrarily small at the TeV-scale, allowing only a limited range for their values. This in turn constrains the mass of the extra heavy gauge boson  $Z'$ , which is given by  $M_{Z'}^2 \sim (g_X^2 + g_Z^2)v_X^2$ . Clearly this has implications for the production of  $Z'$  at colliders.

As an example, when the SM gauge group is extended to  $SU(2)_L \times U(1)_{I_{3R}} \times U(1)_{B-L}$  as in Section 2.3, or to  $SU(2)_L \times SU(2)_R \times U(1)_{B-L}$  as in Section 2.4, the gauge couplings  $g_{X,Z}$  are respectively  $g_R$  and  $g_{BL}$ , and  $v_R$  is the scale at which the extended gauge groups break down to the SM electroweak gauge group  $\mathcal{G}_{\text{SM}}$ . Eq. (2.5) then implies a *lower* bound

---

<sup>11</sup> Note that we are not using here any GUT normalizations for the  $U(1)$  couplings in Eq. (2.5). For normalized couplings, the relation has to be altered accordingly.

Tab. 2.1: Particle content of the  $SU(2)_L \times U(1)_{I_{3R}} \times U(1)_{B-L}$  model.

	$SU(2)_L$	$U(1)_{I_{3R}}$	$U(1)_{B-L}$
$Q$	<b>2</b>	0	$\frac{1}{3}$
$u_R$	<b>1</b>	$+\frac{1}{2}$	$\frac{1}{3}$
$d_R$	<b>1</b>	$-\frac{1}{2}$	$\frac{1}{3}$
$L$	<b>2</b>	0	-1
$N$	<b>1</b>	$+\frac{1}{2}$	-1
$e_R$	<b>1</b>	$-\frac{1}{2}$	-1
$H$	<b>2</b>	$-\frac{1}{2}$	0
$\Delta_R$	<b>1</b>	-1	2

on the coupling  $g_R$  [79]:

$$r_g \equiv \frac{g_R}{g_L} > \tan \theta_w \left( 1 - \frac{4\pi}{g_{BL}^2} \frac{\alpha_{EM}}{\cos^2 \theta_w} \right)^{-1/2}, \quad (2.6)$$

where  $\theta_w \equiv g_Y/g_L$  is the weak mixing angle, and  $\alpha_{EM} \equiv e^2/4\pi$  is the fine-structure constant. For a phenomenologically-preferred TeV-scale  $v_R$ , if  $g_{BL}$  is in the perturbative regime, we can set an *absolute* theoretical lower bound on  $r_g > \tan \theta_w \simeq 0.55$  [79, 80]. One should note that the lower bound on  $g_R$  depends on the  $v_R$  scale. This is before requiring the perturbativity to persist up to the GUT or Planck scale. When perturbativity constraints are imposed, the lower limit on  $g_R$  becomes more stringent, as we show below (see Figs. 2.3, 2.4, 2.7 and 2.8).

## 2.3 $U(1)_{B-L}$ model

The first case we focus on is the  $SU(2)_L \times U(1)_{I_{3R}} \times U(1)_{B-L}$  model [25, 26] which possesses two BSM  $U(1)$  gauge groups, i.e.  $U(1)_{I_{3R}} \times U(1)_{B-L}$ , which break down to the SM  $U(1)_Y$  at a scale  $v_R$ . Labeling the gauge couplings for the groups  $U(1)_{I_{3R}}$  and  $U(1)_{B-L}$  as  $g_R$  and  $g_{BL}$  respectively, we can set lower bounds on both  $g_R$  and  $g_{BL}$  at the  $v_R$  scale from the coupling relation (2.5), as well as upper bounds from the requirement that they remain perturbative up to the GUT scale, as argued in Section 2.2.

The particle content of this model [81, 82] is presented in Table 2.1. Freedom from

anomalies requires three RHNs which help to generate the tiny neutrino masses via the type-I seesaw mechanism [31]. In the scalar sector, one singlet  $\Delta_R$  is used to break the  $U(1)$  groups and generate the RHN masses, while the doublet  $H$  breaks the electroweak group, as in the SM. The one-loop renormalization group equations (RGEs) for the gauge couplings of the two  $U(1)$ 's are generated by the following  $\beta$ -functions:

$$16\pi^2\beta(g_{I_{3R}}) = \frac{9}{2}g_{I_{3R}}^3, \quad (2.7)$$

$$16\pi^2\beta(g_{BL}) = 3g_{BL}^3. \quad (2.8)$$

Note that we have not used GUT renormalized  $g_{BL}$ , since we are not considering coupling unification, but rather the implications for the heavy  $Z_R$  boson searches at colliders. This model could be viewed in some sense as an “effective” TeV-scale theory of LRSM with the  $SU(2)_R$ -breaking scale and the mass of the heavy  $W_R$  boson at the GUT scale [81, 82]. The  $U(1)_{B-L}$  model discussed in this section could also be the TeV-scale effective theory of some GUT that contains  $U(1)_{B-L}$  as a subgroup.

As an illustration, we set explicitly the RH scale  $v_R = 5$  TeV, and run the SM coupling  $g_Y$  from the electroweak scale  $M_Z$  up to the  $v_R$  scale, at which the couplings  $g_R$  and  $g_{BL}$  are related to  $g_Y$  as in Eq. (2.5) and can be expressed as functions of the ratio  $r_g \equiv g_R/g_L$ . Then we evolve the two couplings  $g_R$  and  $g_Y$  from the  $v_R$  scale up to the GUT scale, based on the  $\beta$ -functions in Eqs. (2.7) and (2.8). The correlations of  $g_{R,BL}$  at the RH scale  $v_R$  and GUT scale  $M_{\text{GUT}} = 10^{16}$  GeV are presented in Fig. 2.1, as functions of the ratio  $r_g$  at the  $v_R$  scale (as shown by the color coding). The horizontal shaded region is excluded by the perturbativity limit  $g_{R,BL} < \sqrt{4\pi}$ . The vertical dashed lines denote the upper limits on the gauge couplings, requiring them to stay below the perturbativity limit up to the GUT scale. On the other hand, the vertical dotted lines denote the lower limits on the gauge couplings, obtained from Eq. (2.5), which implies there is only one degree of freedom in the  $U(1)_{B-L}$  model, and the values of  $g_R$  and  $g_{BL}$  are correlated at the scale  $v_R$ , as shown by the red curve

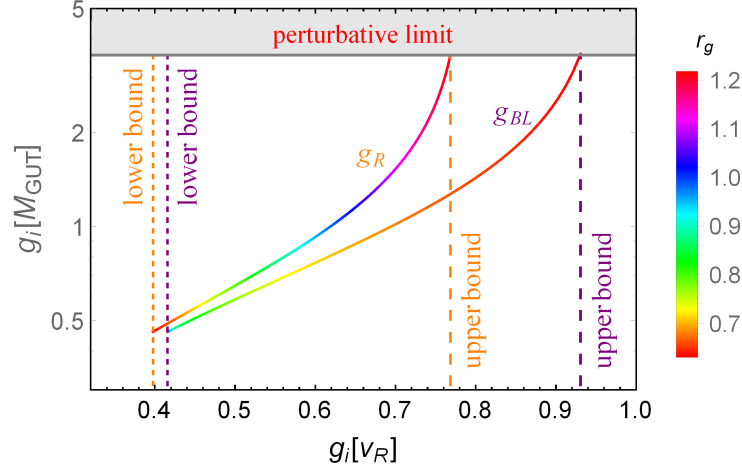


Fig. 2.1: Correlation of  $g_{R,BL}(v_R)$  and  $g_{R,BL}(M_{\text{GUT}})$  in the  $U(1)_{B-L}$  model as functions of  $r_g \equiv g_R/g_L$  at the  $v_R$  scale (shown by the color coding). The horizontal shaded region is excluded by the perturbativity limit  $g_{R,BL} < \sqrt{4\pi}$ . The vertical dotted and dashed lines respectively denote the lower and upper limits on the gauge couplings. Here we have chosen  $v_R = 5$  TeV and  $M_{\text{GUT}} = 10^{16}$  GeV.

in Fig. 2.2. In other words, a lower bound on  $g_R$  corresponds to an upper bound on  $g_{BL}$ , and vice versa. Numerically, the gauge couplings are found to be constrained to lie within a narrow window

$$0.398 < g_R < 0.768 \quad \text{and} \quad 0.416 < g_{BL} < 0.931, \quad \text{with} \quad 0.631 < r_g < 1.218 \quad (2.9)$$

at the  $v_R$  scale, as shown in Fig. 2.1.

The perturbativity constraints on the gauge couplings  $g_R$  and  $g_{BL}$  at the  $v_R$  scale have profound implications for the searches of the heavy  $Z_R$  boson, whose mass is given by

$$M_{Z_R}^2 \simeq 2(g_R^2 + g_{BL}^2)v_R^2. \quad (2.10)$$

The  $Z_R$  couplings to the chiral fermions  $f_{L,R}$  are respectively [82]

$$g_{Z_R f_L f_L} = \frac{e}{\cos \theta_w} (I_{3,f} - Q_f) \frac{\sin \phi}{\cos \phi}, \quad (2.11)$$

$$g_{Z_R f_R f_R} = \frac{e}{\cos \theta_w} (I_{3,f} - Q_f \sin^2 \phi) \frac{1}{\sin \phi \cos \phi} \quad (2.12)$$

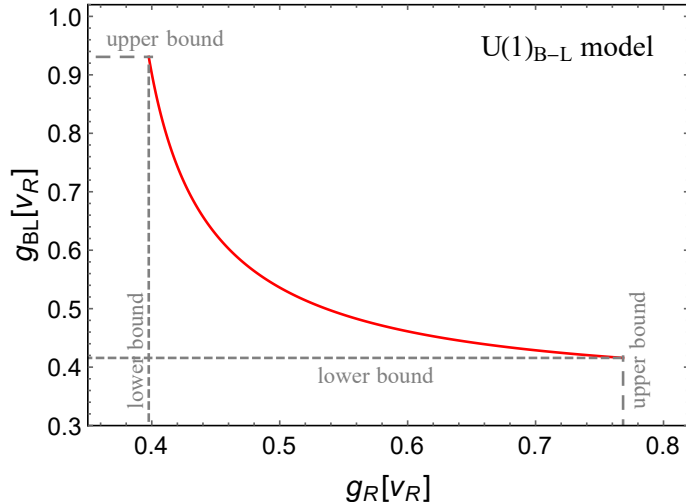


Fig. 2.2: Correlation of  $g_R$  and  $g_{BL}$  at the scale  $v_R = 5$  TeV (red line) and the lower and upper bounds on the couplings  $g_R$  and  $g_{BL}$ , induced from the requirement of perturbativity up to the GUT scale in the  $U(1)_{B-L}$  model.

Tab. 2.2: The lower bounds on the  $Z_R$  boson mass  $M_{Z_R}$  and the  $v_R$  scale in the  $U(1)_{B-L}$  model from the current LHC13 data [1, 2] and the prospects at the HL-LHC 14 TeV with an integrated luminosity of  $3000 \text{ fb}^{-1}$  [3, 4] and future 100 TeV collider FCC-hh with a luminosity of  $30 \text{ ab}^{-1}$  [4, 5]. The range in each case corresponds to the allowed range of  $r_g$  from perturbativity constraints, as given in Eq. (2.9).

collider	$M_{Z_R}$ [TeV]	$v_R$ [TeV]
LHC13	[3.6, 4.2]	[3.02, 3.57]
HL-LHC	[6.0, 6.6]	[4.60, 5.82]
FCC-hh	[27.9, 31.8]	[19.9, 26.8]

with  $Q_f$  the electric charge of fermion  $f$ ,  $I_{3,f}$  the third-component of isospin of that particle, and  $\tan \phi \equiv g_{BL}/g_R$  the RH gauge mixing angle.

For a TeV-scale  $v_R$ , the  $Z_R$  mass is stringently constrained by the dilepton data  $pp \rightarrow Z_R \rightarrow \ell^+\ell^-$  (with  $\ell = e, \mu$ ) at the LHC [83, 84]. For a sequential  $Z'$  boson, the current mass limit is 4.05 TeV at the 95% confidence level (CL) [1, 2]. The dilepton prospects of a sequential  $Z'$  boson have also been estimated at the HL-LHC [3, 4] and future 100 TeV colliders [4, 5], which are respectively 6.4 TeV and 30.7 TeV, for an integrated luminosity of  $3000 \text{ fb}^{-1}$ . Given a luminosity of 10 times larger at the 100 TeV collider, the dilepton prospects could be significantly enhanced, up to 43.7 TeV. The production cross section  $\sigma(pp \rightarrow Z_R \rightarrow \ell^+\ell^-)$  in the  $U(1)_{B-L}$  model can be obtained by rescaling that of a sequential

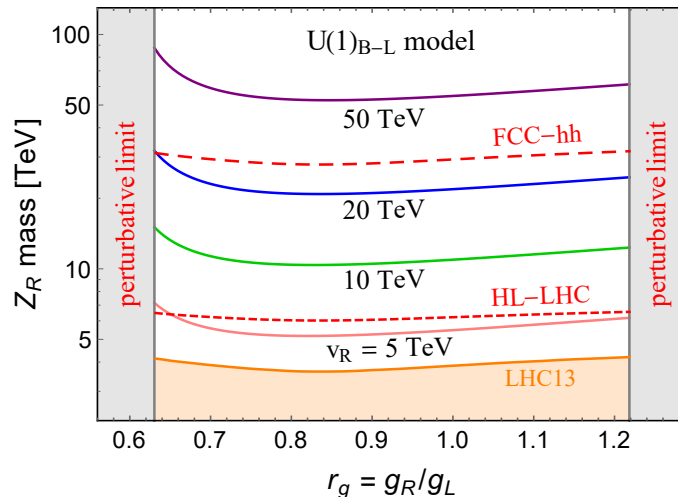


Fig. 2.3: Current LHC13 constraints on  $Z_R$  mass in the  $U(1)_{B-L}$  model (shaded orange) as function of  $r_g = g_R/g_L$ , and future prospects at the HL-LHC 14 TeV with an integrated luminosity of  $3000 \text{ fb}^{-1}$  (short-dashed red) and the 100 TeV collider FCC-hh with a luminosity of  $30 \text{ ab}^{-1}$  (long-dashed red). The vertical shaded regions are excluded by the perturbativity constraints given in Eq. (2.9). The pink, green, blue and purple contours show the variation of the  $Z_R$  mass with respect to  $r_g$ , with the RH scale  $v_R = 5, 10, 20, 50 \text{ TeV}$ , respectively.

heavy  $Z'$  boson, as function of  $r_g = g_R/g_L$ . The rescaled current mass limit and the expected limits at the HL-LHC and the future 100 TeV collider FCC-hh are presented in Fig. 2.3, as a function of  $r_g$ . The  $Z_R$  mass contours for  $v_R = 5, 10, 20$  and  $50 \text{ TeV}$  are also shown in Fig. 2.3 in the colors of pink, green, blue and purple, respectively. The vertical shaded regions are excluded by the perturbativity constraints given in Eq. (2.9).<sup>12</sup> Fig. 2.3 implies that the LHC13 lower limits, as well as the future HL-LHC and FCC-hh limits, on  $Z_R$  boson mass are in a narrow range, depending on the allowed values of  $r_g$ , as shown in Table 2.2. Thus, the perturbativity constraints restrict the accessible range of  $M_{Z_R}$  up to 6.6 TeV at the HL-LHC and 31.8 TeV at the FCC-hh. For the purpose of concreteness, we have assumed the decay  $Z_R \rightarrow N_i N_i$  is open, such that the  $\text{BR}(Z_R \rightarrow \ell^+ \ell^-)$  is slightly smaller than the case without the decaying of  $Z_R$  into RHNs and the dilepton limits in Fig. 2.3 are comparatively more conservative [75].

The dilepton constraints on the  $Z_R$  mass can be traded for the constraints on  $v_R$  scale

<sup>12</sup> When the  $v_R$  scale changes from 5 TeV, the perturbative constraints on  $r_g$  in Fig. 2.3 will change accordingly from those given below Eq. (2.9). However, this change is negligible for  $v_R$  up to 50 TeV.

using Eq. (2.10). This is shown in Fig. 2.4 and Table 2.2. The pink, green, blue and purple contours here show the variation of  $v_R$  with respect to  $r_g$ , with fixed  $Z_R$  mass of  $M_{Z_R} = 5, 10, 20, 50$  TeV, respectively. The perturbativity constraints given in Eq. (2.9) restrict the accessible range of  $v_R$  up to 5.8 TeV at the HL-LHC and 26.8 TeV at the FCC-hh.

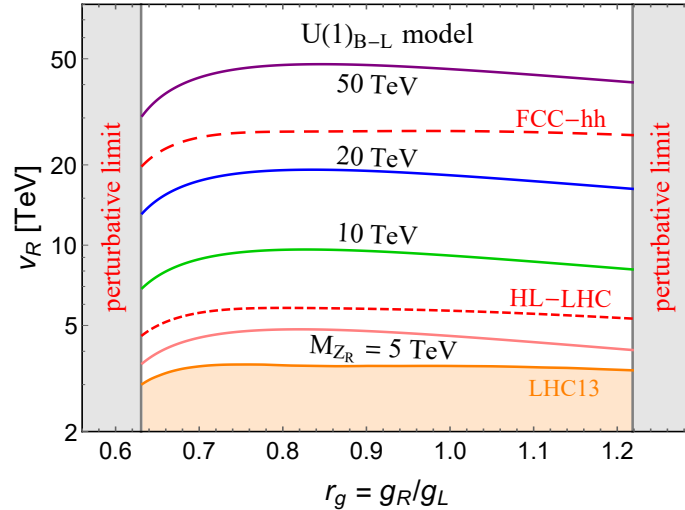


Fig. 2.4: Current lower bound on the  $v_R$  scale in the  $U(1)_{B-L}$  model, as functions of  $r_g = g_R/g_L$ , from the searches of  $Z_R$  in the dilepton channel at LHC 13 TeV (shaded orange), as well as the future limit from HL-LHC 14 TeV with an integrated luminosity of  $3000 \text{ fb}^{-1}$  (short-dashed red) and the 100 TeV collider FCC-hh with a luminosity of  $30 \text{ ab}^{-1}$  (long-dashed red). The vertical shaded regions are excluded by the perturbativity constraints given in Eq. (2.9). The pink, green, blue and purple contours show the variation of  $v_R$  with respect to  $r_g$ , with the  $Z_R$  mass  $M_{Z_R} = 5, 10, 20, 50$  TeV, respectively.

## 2.4 The minimal left-right symmetric model

We now consider the TeV-scale LRSM based on the gauge group  $SU(2)_L \times SU(2)_R \times U(1)_{B-L}$  [27, 28, 29]. Original aim of this model was to explain the asymmetric chiral structure of electroweak interactions in the SM. It was subsequently pointed out that it could account for the observed small neutrino masses via the type-I [30, 31, 32, 33, 34] and/or type-II [85, 86, 31, 87, 88, 89] seesaw mechanisms. In the “canonical” version of LRSM, it is always assumed that the gauge coupling  $g_R = g_L$  and the scalar content of the LRSM consists of one bidoublet  $\Phi$  and the left-handed ( $\Delta_L$ ) and right-handed ( $\Delta_R$ ) triplets.

Tab. 2.3: Particle content of the minimal LRSM based on the gauge group  $SU(2)_L \times SU(2)_R \times U(1)_{B-L}$ .

	$SU(2)_L$	$SU(2)_R$	$U(1)_{B-L}$
$Q_L \equiv \begin{pmatrix} u_L \\ d_L \end{pmatrix}$	<b>2</b>	<b>1</b>	$\frac{1}{3}$
$Q_R \equiv \begin{pmatrix} u_R \\ d_R \end{pmatrix}$	<b>1</b>	<b>2</b>	$\frac{1}{3}$
$\psi_L \equiv \begin{pmatrix} \nu_L \\ e_L \end{pmatrix}$	<b>2</b>	<b>1</b>	-1
$\psi_R \equiv \begin{pmatrix} N \\ e_R \end{pmatrix}$	<b>1</b>	<b>2</b>	-1
$\Phi = \begin{pmatrix} \phi_1^0 & \phi_2^+ \\ \phi_1^- & \phi_2^0 \end{pmatrix}$	<b>2</b>	<b>2</b>	0
$\Delta_R = \begin{pmatrix} \frac{1}{\sqrt{2}}\Delta_R^+ & \Delta_R^{++} \\ \Delta_R^0 & -\frac{1}{\sqrt{2}}\Delta_R^+ \end{pmatrix}$	<b>1</b>	<b>3</b>	2

As long as the RH scale  $v_R$  is at the few-TeV range, the values of  $g_R$  and  $g_{BL}$  and their RG running up to the GUT scale are almost fixed, at least at the one-loop level. However, the coupling  $g_R$  might be different from  $g_L$ , which generates very rich phenomenology in the LRSM, see e.g. [79, 75, 90, 80, 91]. Moreover, a free  $g_R$  not necessarily equal to  $g_L$  makes it possible to investigate the whole parameter space of perturbative constraints in the LRSM. In addition, the parity and  $SU(2)_R$  breaking scales might also be different such that the left-handed triplet  $\Delta_L$  decouples from the TeV-scale physics [92]. This also helps to avoid the unacceptably large type-II seesaw contribution to the neutrino masses and/or fine-tuning in the scalar sector. Based on these arguments, we will not consider the  $\Delta_L$  field in the low-energy LRSM. The matter content and the scalar fields in the minimal LRSM are collected in Table 2.3. Three RHNs  $N_{1,2,3}$  have been naturally introduced to form the RH lepton doublets  $\psi_R$  and accommodate the type-I seesaw mechanism. The perturbative constraints from the gauge and scalar sectors follow in the next two subsections.

### 2.4.1 Perturbativity constraints from the gauge sector

The perturbativity limits in the gauge sector are conceptually similar to the  $U(1)_{B-L}$  model in Section 2.3; the difference is mainly due to the  $\beta$ -function coefficients, which in this case are given by

$$16\pi^2\beta(g_R) = -\frac{7}{3}g_R^3, \quad (2.13)$$

$$16\pi^2\beta(g_{BL}) = \frac{11}{3}g_{BL}^3. \quad (2.14)$$

Note the change in sign for  $\beta(g_R)$ , as compared to Eq. (2.7), which is due to the non-Abelian nature of  $SU(2)_R$ . For completeness, we have also computed the two-loop RGEs using the code `PyR@TE` [93, 94] and list them in Appendix A, although it turns out that the two-loop corrections change the results only by a few per cent, as compared to the one-loop results presented here.

As the RH scale  $v_R = 5$  TeV (chosen in Section 2.3) is in tension with the stringent constraints from the scalar sector in LRSM (see Section 2.4.2 and Fig. 2.8), we set  $v_R = 10$  TeV as an illustrative example to evaluate the perturbative constraints on the gauge couplings  $g_R$  and  $g_{BL}$ . In fact, as long as the  $v_R$  scale is at the ballpark of few-TeV, the changes in the running of  $g_R$  and  $g_{BL}$  are mainly due to the initial values of  $g_{R,BL}$  at the  $v_R$  scale, and are negligibly small. As in the  $U(1)_{B-L}$  model in Section 2.3, the couplings  $g_R$  and  $g_{BL}$  are both functions of the ratio  $r_g = g_R/g_L$ . The correlations of  $g_{R,BL}$  at the  $v_R$  scale and the GUT scale are presented in Fig. 2.5, as functions of  $r_g$  (as shown by the color coding). The two stars in Fig. 2.5 correspond to the special case  $g_R = g_L$  at the  $v_R$  scale. As a result of non-Abelian nature of the  $SU(2)_R$  group,  $g_R$  is asymptotically free, i.e. it becomes smaller at higher energy scales. Thus  $g_R$  could go up to the perturbativity limit of  $\sqrt{4\pi}$  at the  $v_R$  scale (without considering the perturbativity limits from the scalar sector for the moment), which is very different from the  $U(1)_{B-L}$  model, where the  $g_R$  value is much more restricted at the

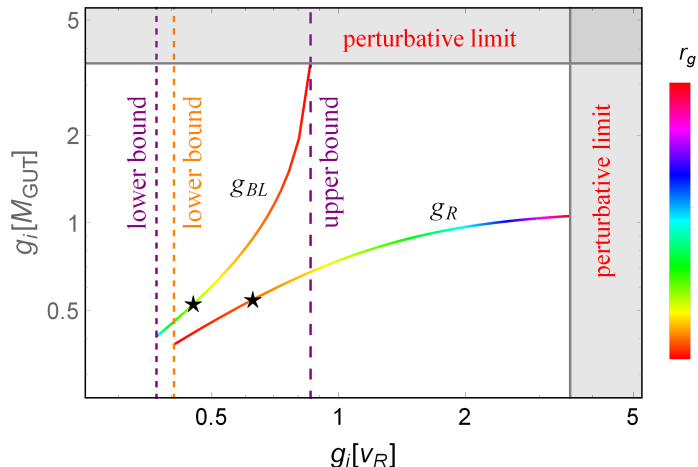


Fig. 2.5: Correlation of  $g_{R,BL}(v_R)$  and  $g_{R,BL}(M_{\text{GUT}})$  in the minimal LRSM as functions of  $r_g = g_R/g_L$  at the  $v_R$  scale (as shown by the color coding). The shaded regions are excluded by the perturbativity limits  $g_{R,BL} < \sqrt{4\pi}$ . The two stars correspond to the special case  $g_R = g_L$  at the  $v_R$  scale. The vertical dotted and dashed lines respectively denote the lower and upper limits on the gauge couplings. Here we have chosen  $v_R = 10$  TeV and  $M_{\text{GUT}} = 10^{16}$  GeV.

$v_R$  scale [cf. Fig. 2.1]. The allowed ranges of the gauge couplings in the minimal LRSM are

$$0.406 < g_R < \sqrt{4\pi} \quad \text{and} \quad 0.369 < g_{BL} < 0.857, \quad \text{with} \quad 0.648 < r_g < 5.65 \quad (2.15)$$

at the scale  $v_R$ , which is clearly shown in the correlation plot of  $g_R$  and  $g_{BL}$  in Fig. 2.6.

In the LRSM, the couplings of  $Z_R$  boson to the SM fermions and the heavy RHNs are the same as in the  $U(1)_{B-L}$  model in Section 2.3. Thus, the dilepton limits from current LHC 13 TeV data [1, 2] and the prospects at the HL-LHC [3, 4] and future 100 TeV colliders [4, 5] are also the same as in  $U(1)_{B-L}$  model, up to the different perturbative windows for the gauge couplings in Eqs. (2.9) and (2.15), respectively. The current LHC 13 TeV dilepton constraints on the  $Z_R$  mass in the minimal LRSM and the future prospects are shown in the right panel of Fig. 2.7, along with the contours for  $M_{Z_R}(r_g)$  with the RH scale  $v_R = 5, 10, 20$  and  $50$  TeV. In the plot we have also shown the absolute theoretical lower bound on  $r_g > \tan \theta_w$  from Eq. (2.6) as the dashed vertical line, which is weaker than the “real” lower bound from perturbativity up to the GUT scale shown in Figs. 2.5 and 2.6 (the solid vertical

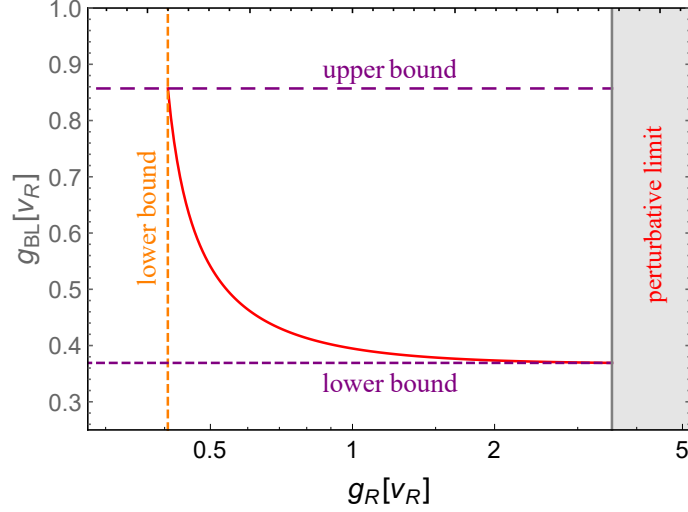


Fig. 2.6: Correlation of  $g_R$  and  $g_{BL}$  in the minimal LRSM at the scale  $v_R = 10$  TeV (red curve), along with the lower and upper bounds on the couplings  $g_{R,BL}$ , induced from the requirement of perturbativity up to the GUT scale. The shaded region is excluded by the perturbativity limit  $g_R < \sqrt{4\pi}$ .

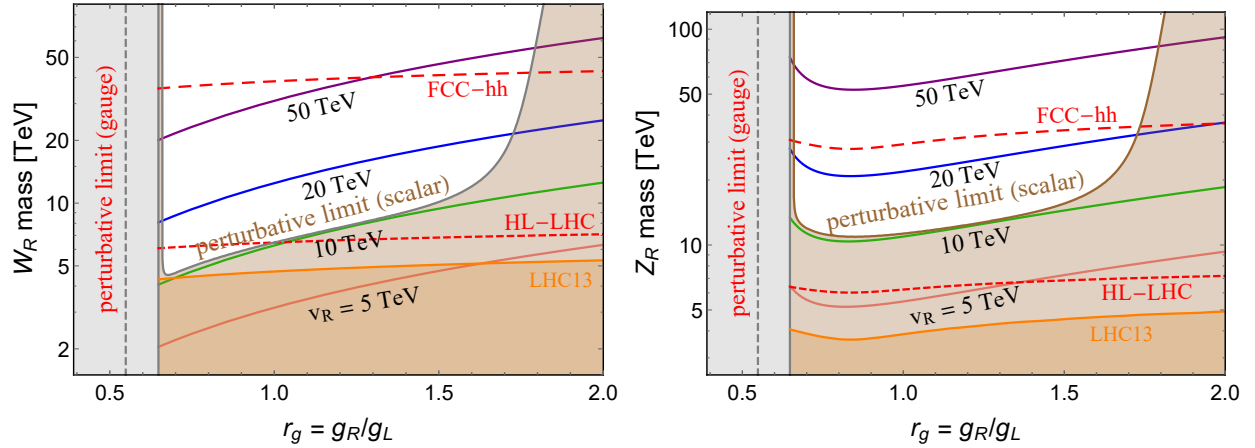


Fig. 2.7: Current LHC13 constraints on the  $W_R$  (left) and  $Z_R$  (right) masses in the minimal LRSM (shaded orange) as function of  $r_g = g_R/g_L$ , and future prospects at the HL-LHC 14 TeV with an integrated luminosity of  $3000 \text{ fb}^{-1}$  (short-dashed red) and the 100 TeV collider FCC-hh with a luminosity of  $30 \text{ ab}^{-1}$  (long-dashed red). The pink, green, blue and purple lines are the  $W_R/Z_R$  mass with the RH scale  $v_R = 5, 10, 20, 50$  TeV, respectively. The shaded gray and brown regions are excluded respectively by the perturbative constraints from the gauge and scalar sectors up to the GUT scale. The dashed vertical line corresponds to the absolute theoretical bound in Eq. (2.6).

gray line in Fig. 2.7). The scalar perturbativity limit shown in Fig. 2.7 will be discussed in Section 2.4.2.

As for the limits on  $W_R$  boson in the LRSM, due to the Majorana nature of the heavy

RHNs, the same-sign dilepton plus jets  $pp \rightarrow W_R \rightarrow \ell^\pm N \rightarrow \ell^\pm \ell^\pm jj$  is the “smoking-gun” signal from the production and decay of the heavy  $W_R$  boson at hadron colliders [95]. The associated searches of  $W_R$  and RHN have been performed at LHC 13 TeV [46, 6]. To be concrete, we fix the RHN mass  $M_N = 1$  TeV; for such a benchmark scenario, the current LHC data requires that the  $W_R$  mass  $M_{W_R} > 4.7$  TeV for  $g_R = g_L$  [6]. If  $g_R \neq g_L$ , we have to re-evaluate the dependence of the production of  $W_R$  and the subsequent decays  $W_R \rightarrow \ell^\pm N$  and  $N \rightarrow \ell^\pm \ell \ell$  on the gauge coupling  $g_R$ .<sup>13</sup> Specifically,

- The production of  $W_R$  at hadron colliders is proportional to the  $W_R$  couplings to the SM quarks, i.e.  $\sigma(pp \rightarrow W_R) \propto g_R^2$ .
- The  $W_R$  boson decays predominately into the SM quarks and the charged leptons and heavy RHNs, i.e.  $W_R \rightarrow \bar{q}_R q'_R, \ell_R N$ . All the partial widths are proportional to  $g_R^2$ , but not the branching fraction  $\text{BR}(W_R \rightarrow \ell N)$ .
- In the limit of vanishing  $W - W_R$  mixing and heavy-light neutrino mixing,  $N \rightarrow \ell jj$  is the dominant decay mode (assuming  $N$  here is the lightest RHN), whose branching fraction does not depend on  $g_R$ .

In short, the  $g_R$  dependence is only relevant to the production  $pp \rightarrow W_R$ . For fixed  $W_R$  mass, we need only to rescale the production cross section  $\sigma(pp \rightarrow W_R)$  by a factor of  $r_g^2 = (g_R/g_L)^2$ . The current LHC constraint on  $W_R$  mass is presented in the left panel of Fig. 2.7 as function of  $r_g$ , along with the contours of  $M_{W_R}$  for  $v_R = 5, 10, 20$  and 50 TeV.

It is a good approximation in the minimal LRSM that the right-handed quark mixing matrix is identical to the CKM matrix in the SM, up to some unambiguous signs [98]. Then the  $W_R$ -mediated right-handed currents contributes to the  $K_0 - \bar{K}_0$  and  $B - \bar{B}$  mixings, leading to strong constraints on the  $W_R$  mass,  $M_{W_R} \gtrsim 3$  TeV [99, 100, 101, 53]. This limit

---

<sup>13</sup> The  $W_R$  boson might also decay into  $WZ$  and  $Wh$ , with the branching fractions depending largely on the VEV  $\kappa'/\kappa$  [91]. This does not affect the dependence of  $W_R$  production on the gauge coupling  $g_R$ . For simplicity, we have also neglected the effect of the heavy-light neutrino mixing on the  $W_R$  decay [96], since this mixing is severely constrained for TeV-scale LRSM with type-I seesaw [97].

does not depend on the coupling  $g_R$ , as in the limit of  $m_{K,B} \ll M_{W_R}$  the  $g_R$  dependence of  $W_R$  coupling to the SM quarks is canceled out by the dependence of  $g_R$  in the  $W$  boson propagator. The  $W_R$  contribution is effectively suppressed by  $v_{EW}^2/v_R^2$ . As the quark flavor limits on  $W_R$  mass is significantly lower than that from the direct searches at the LHC for  $r_g \gtrsim 0.65$ , they are not shown in the left panel of Fig. 2.7. The  $W_R$  contributes also to neutrinoless double  $\beta$ -decays [102, 103, 104, 105, 106, 107, 108, 109, 110], which however depends on the masses of heavy RHNs and the doubly-charged scalars, and therefore, not included in Fig. 2.7.

The  $W_R$  could be probed up to 5.4 TeV at LHC 14 with a luminosity of  $300 \text{ fb}^{-1}$  [7, 111]. By rescaling the production cross section  $\sigma(pp \rightarrow W_R)$  using CalCHEP [112], the  $W_R$  prospects could go up to 6.5 TeV for  $g_R = g_L$  at the HL-LHC where the integrated luminosity is 10 times larger ( $3000 \text{ fb}^{-1}$ ). At future 100 TeV hadron colliders, for a relatively light RHN  $M_N \ll M_{W_R}$ , the decay products from the RHN tend to be highly-collimated and form fat jets. We adopt the analysis in Ref. [8] where  $M_N/M_{W_R}$  was taken to be 0.1. Given a luminosity of  $30 \text{ ab}^{-1}$  at 100 TeV hadron colliders, the  $W_R$  mass could be probed up to 38.4 TeV with  $g_R = g_L$ . The projected sensitivity of  $W_R$  mass for a relatively low  $M_N$  at the HL-LHC and future 100 TeV collider FCC-hh could also be generalized to the case with  $g_R \neq g_L$ , which are depicted in the left panel of Fig. 2.7 respectively as the short-dashed and long-dashed red curves.

With the heavy gauge boson masses in the minimal LRSM

$$M_{W_R}^2 \simeq g_R^2 v_R^2, \quad M_{Z_R}^2 \simeq 2(g_R^2 + g_{BL}^2)v_R^2, \quad (2.16)$$

the current direct search limits of the  $W_R$  and  $Z_R$  boson at LHC 13 TeV and the future prospects at the HL-LHC and FCC-hh can be translated into limits on the  $v_R$  scale (as in the  $U(1)_{B-L}$  model in Section 2.3), which are presented in Fig. 2.8. For illustration purpose, we have also shown the contours of  $M_{W_R}(M_{Z_R}) = 5, 10, 20$  and  $50$  TeV in the left (right)

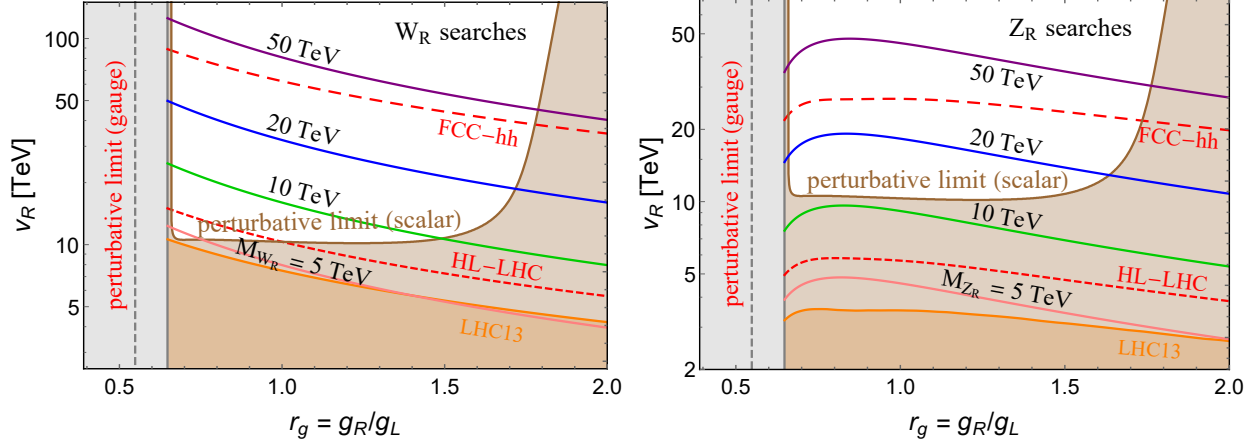


Fig. 2.8: Lower bounds on the  $v_R$  scale in the minimal LRSM, as functions of  $r_g$ , from the direct searches of  $W_R$  and  $Z_R$  bosons at LHC 13 TeV (shaded orange), and future prospects at the HL-LHC 14 TeV with an integrated luminosity of  $3000 \text{ fb}^{-1}$  (short-dashed red) and the 100 TeV collider FCC-hh with a luminosity of  $30 \text{ ab}^{-1}$  (long-dashed red). The shaded gray regions are excluded by the perturbativity constraints up to the GUT scale, with the vertical dashed line corresponding to the absolute theoretical bound in Eq. (2.6). The shaded brown regions are excluded by the perturbativity limits from the scalar sector, discussed in Section 2.4.2.

panel of Fig. 2.8, which are depicted respectively in pink, green, blue and purple. We find that the RH scale could be probed up to  $\simeq 87 \text{ TeV}$  in the searches of  $W_R$  boson and  $\sim 25 \text{ TeV}$  in the  $Z_R$  boson channel at the 100 TeV collider.

## 2.4.2 Perturbativity constraints from the scalar sector

The most general renormalizable scalar potential for the  $\Phi$  and  $\Delta_R$  fields is given by

$$\begin{aligned}
 \mathcal{V} = & -\mu_1^2 \text{Tr}(\Phi^\dagger \Phi) - \mu_2^2 [\text{Tr}(\tilde{\Phi} \Phi^\dagger) + \text{Tr}(\tilde{\Phi}^\dagger \Phi)] - \mu_3^2 \text{Tr}(\Delta_R \Delta_R^\dagger) \\
 & + \lambda_1 [\text{Tr}(\Phi^\dagger \Phi)]^2 + \lambda_2 \left\{ [\text{Tr}(\tilde{\Phi} \Phi^\dagger)]^2 + [\text{Tr}(\tilde{\Phi}^\dagger \Phi)]^2 \right\} \\
 & + \lambda_3 \text{Tr}(\tilde{\Phi} \Phi^\dagger) \text{Tr}(\tilde{\Phi}^\dagger \Phi) + \lambda_4 \text{Tr}(\Phi^\dagger \Phi) [\text{Tr}(\tilde{\Phi} \Phi^\dagger) + \text{Tr}(\tilde{\Phi}^\dagger \Phi)] \\
 & + \rho_1 [\text{Tr}(\Delta_R \Delta_R^\dagger)]^2 + \rho_2 \text{Tr}(\Delta_R \Delta_R) \text{Tr}(\Delta_R^\dagger \Delta_R^\dagger) \\
 & + \alpha_1 \text{Tr}(\Phi^\dagger \Phi) \text{Tr}(\Delta_R \Delta_R^\dagger) + [\alpha_2 e^{i\delta_2} \text{Tr}(\tilde{\Phi}^\dagger \Phi) \text{Tr}(\Delta_R \Delta_R^\dagger) + \text{H.c.}] + \alpha_3 \text{Tr}(\Phi^\dagger \Phi \Delta_R \Delta_R^\dagger).
 \end{aligned} \tag{2.17}$$

Due to the LR symmetry, all the 12 parameters  $\mu_{1,2,3}^2$ ,  $\lambda_{1,2,3,4}$ ,  $\rho_{1,2}$ ,  $\alpha_{1,2,3}$  are real, and the only CP-violating phase is  $\delta_2$  associated with the coupling  $\alpha_2$ , as explicitly shown in Eq. (2.17).<sup>14</sup> The neutral component of the triplet develops a non-vanishing vacuum expectation value (VEV)  $\langle \Delta_R^0 \rangle = v_R$ , which breaks the  $SU(2)_R \times U(1)_{B-L}$  down to the SM  $U(1)_Y$ , and generates masses for the heavy scalars, the  $W_R$  and  $Z_R$  bosons and the RHNs. The bidoublet VEVs  $\langle \phi_1^0 \rangle = \kappa$  and  $\langle \phi_2^0 \rangle = \kappa'$  are responsible for the electroweak symmetry breaking. Neglecting the CP violation and up to the leading order in the small parameters  $\epsilon = v_{EW}/v_R$  and  $\xi = \kappa'/\kappa$ , the physical scalar masses are respectively [79]

$$\begin{aligned} M_h^2 &\simeq 4\lambda_1 v_{EW}^2, & M_{H_1, A_1, H_1^\pm}^2 &\simeq \alpha_3 v_R^2, \\ M_{H_3}^2 &\simeq 4\rho_1 v_R^2, & M_{H_2^{\pm\pm}}^2 &\simeq 4\rho_2 v_R^2, \end{aligned} \quad (2.18)$$

where  $h$  is the SM Higgs,  $H_1$ ,  $A_1$  and  $H_1^\pm$  respectively the heavy CP-even and CP-odd neutral components and the singly-charged scalars from the bidoublet  $\Phi$ ,  $H_3$  and  $H_2^{\pm\pm}$  are the neutral and doubly-charged scalars from the triplet  $\Delta_R$ , following the convention of Ref. [79].

In the minimal LRSM, the heavy neutral scalars  $H_1$  and  $A_1$  have tree-level FCNC couplings to the SM quarks, which contribute to the  $K_0 - \bar{K}_0$ ,  $B_d - \bar{B}_d$  and  $B_s - \bar{B}_d$  mixings. Thus their masses are tightly constrained by the high-precision flavor data, i.e.  $M_H \gtrsim 10$  TeV [52, 53, 54]. For a few-TeV scale  $v_R$ , this implies that the quartic coupling  $\alpha_3 \simeq M_{H_1}^2/v_R^2$  is pretty large, typically of order one. The RG running of the quartic couplings in Eq. (2.17) are all entangled together, and a large  $\alpha_3$  is the main reason why the LRSM could easily hit a Landau pole at an energy scale that is much lower than the GUT scale [113, 114, 115, 116]. This could be alleviated if the  $v_R$  scale is higher and the coupling  $\alpha_3$  gets smaller. Therefore, the perturbativity of the quartic couplings in Eq. (2.17) up to the GUT scale could set a lower bound on the  $v_R$  scale, assuming there is no intermediate scales or particles in between

---

<sup>14</sup> This potential stems from the full LRSM at a higher energy scale in presence of the left-handed triplet  $\Delta_L$ . At the high scale, all but one of the couplings are real. At low scales there will be small phases in some couplings induced by radiative renormalization group effects. We ignore these small phases. Our main conclusions are not affected by this.

$v_R$  and the GUT scale.

A thorough analysis of the RG running of all the quartic couplings in Eq. (2.17) is rather complicated and it obfuscates the perturbativity limits on the  $v_R$  scale. While some of the quartic couplings could be tuned very small at the  $v_R$  scale as they only induce mixings among the scalars such as  $\alpha_{1,2}$  [79], there are only four quartic couplings, i.e. the  $\lambda_1$ ,  $\alpha_3$ ,  $\rho_1$  and  $\rho_2$  appearing in Eq. (2.18), that are responsible for the scalar masses at the tree level. Therefore, for the purpose of perturbativity limits in the scalar sector, we consider a simple scenario with only these four non-vanishing quartic couplings  $\lambda_1$ ,  $\alpha_3$ ,  $\rho_1$  and  $\rho_2$  at the  $v_R$  scale. In particular, we set the scalar masses to the following benchmark values:

$$\begin{aligned} M_h &= 125 \text{ GeV}, & M_{H_1, A_1, H_1^\pm} &= 10 \text{ TeV}, \\ M_{H_3} &= 100 \text{ GeV}, & M_{H_2^{\pm\pm}} &= 1 \text{ TeV}, \end{aligned} \quad (2.19)$$

from which one could obtain the values of  $\lambda_1$ ,  $\alpha_3$ ,  $\rho_1$  and  $\rho_2$  by using Eq. (2.18). All other quartic couplings  $\lambda_{2,3,4}$ ,  $\alpha_{1,2}$  are set to zero, and this corresponds to the limits without any tree-level scalar mixing at the  $v_R$  scale. In the limit of vanishing mixing between  $h$  and  $H_1$ , the neutral scalar  $H_3$  from the triplet  $\Delta_R$  is hadrophobic and the experimental constraints on  $H_3$  are rather weak [117, 81]. Thus we have set  $H_3$  to be light, at the 100 GeV scale, in Eq. (2.19). The smoking-gun signal of a doubly-charged scalar is the same-sign dilepton pairs  $H_2^{\pm\pm} \rightarrow \ell_\alpha^\pm \ell_\beta^\pm$  with  $\alpha, \beta = e, \mu, \tau$ , which is almost background free. The current most stringent limits are from the LHC 13 TeV data [118, 119], which requires that  $M_{H_2^{\pm\pm}} \gtrsim (271 - 760) \text{ GeV}$ , depending largely on the charged lepton flavors involved [120]. To be concrete, we have set the doubly-charged scalar mass at 1 TeV in Eq. (2.19), which easily satisfies the current LHC constraints. As for the bidoublet masses  $M_{H_1, A_1, H_1^\pm}$ , we have taken the minimum possible value allowed by FCNC constraints [53], whereas for the SM Higgs, we have taken the current best-fit value [121].

All the RGEs for the gauge couplings  $g_{L,R,BL}$  and the quartic couplings in the potential

in Eq. (2.17) are collected in Appendix A up to the two-loop level. To be self-consistent, we include also the RGE for the dominant Yukawa coupling  $h_t$  that is responsible for generation of the top quark mass at the electroweak scale. The Yukawa couplings for the bottom and tauon are comparatively much smaller and are neglected here. For a RH scale  $v_R \gtrsim 10$  TeV, the Yukawa coupling  $f_R$  of  $\Delta_R$  to the lepton doublets are also small if the masses of the three RHNs  $M_N \simeq \text{TeV}$ . For simplicity, the  $f_R$  terms in the  $\beta$ -functions are also neglected. See Appendix A for more details.

Given the scalar masses in Eq. (2.19), all the  $\beta$ -functions for the quartic couplings in Eq. (A.5) to (A.15) are dominated by the  $\alpha_3$  terms if the RH scale  $v_R$  is not too much higher than the TeV scale, i.e.

$$16\pi^2\beta(\lambda_1) = \frac{5}{4}\alpha_3^2 + \frac{3}{8}\left(3g_L^4 + 2g_L^2g_R^2 + 3g_R^4\right) - 6h_t^4 + \dots, \quad (2.20)$$

where the dots stand for the subleading terms. For a few-TeV  $v_R$  and  $\alpha_3 \gtrsim \mathcal{O}(1)$ , the quartic couplings rapidly blow up before reaching the GUT scale [113, 114, 115, 116]. An explicit example is shown in the two upper panels of Fig. 2.9, with  $r_g = g_R/g_L = 1.1$  and  $v_R = 6$  TeV, where the quartic couplings become non-perturbative at  $\sim 10^7$  GeV. When the RH scale  $v_R$  is higher, for a fixed mass  $M_{H_1} = 10$  TeV, the coupling  $\alpha_3 \simeq M_{H_1}^2/v_R^2$  is significantly smaller. As a result, in a large region of the parameter space, all the quartic couplings are perturbative up to the GUT scale, as exemplified in the two lower panels of Fig. 2.9 with  $r_g = g_R/g_L = 1.1$  and  $v_R = 12$  TeV. In both examples, the bounded-from-below conditions in the scalar sector are respected [115, 122].<sup>15</sup>

$$\lambda_1 \geq 0, \quad \rho_1 \geq 0, \quad \rho_1 + \rho_2 \geq 0, \quad \rho_1 + 2\rho_2 \geq 0. \quad (2.21)$$

One should note that the  $g_R$  and  $g_{BL}$  terms in the  $\beta$ -functions in Eqs. (A.5) to (A.15) might be unacceptably large. Thus the perturbativity limits in the scalar sector depend

---

<sup>15</sup> More generic vacuum stability criteria can be found, e.g., in Ref. [123].

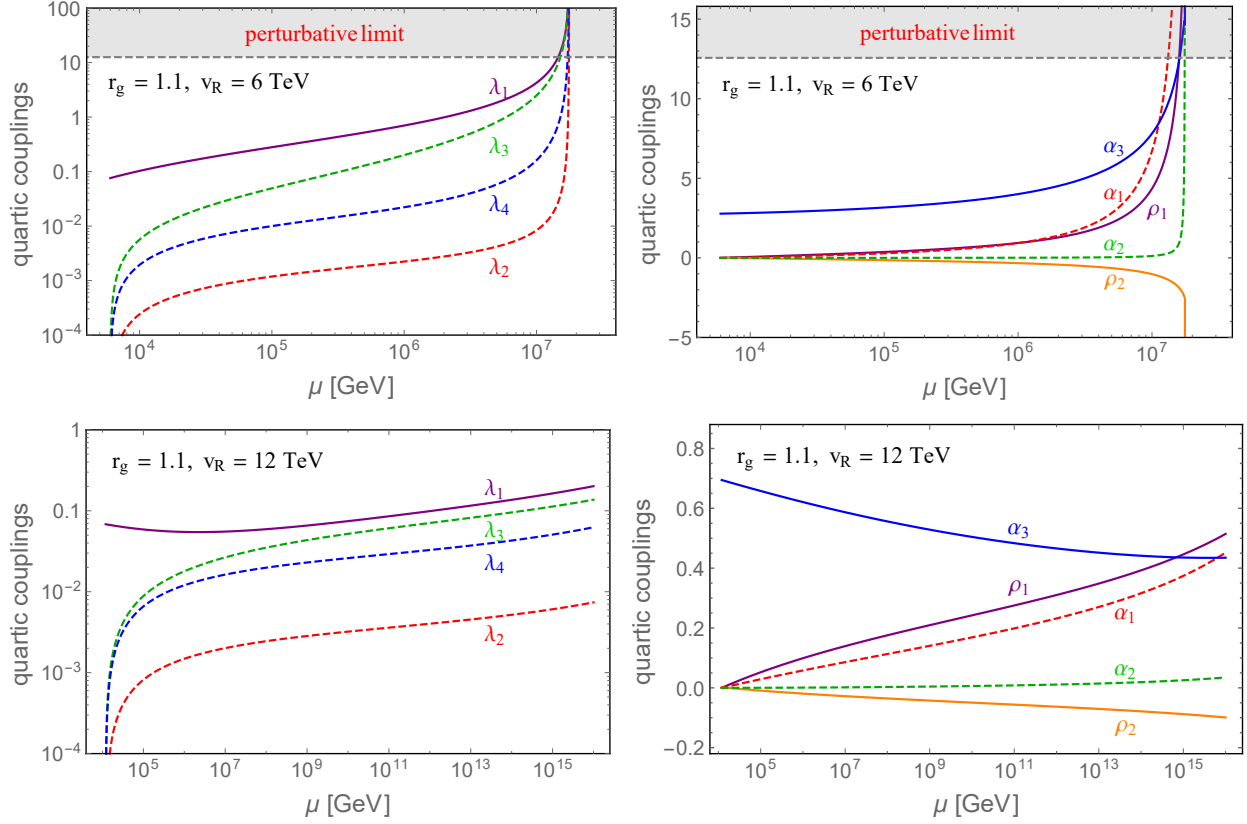


Fig. 2.9: RG running of the quartic couplings  $\lambda_{1,2,3,4}$  (left), and  $\rho_{1,2}$ ,  $\alpha_{1,2,3}$  (right) in the scalar potential Eq. (2.17) of minimal LRSM from  $v_R$  up to the GUT scale, with  $r_g = 1.1$  and  $v_R = 6$  TeV (upper panels),  $v_R = 12$  TeV (lower panels).

also on the gauge couplings  $g_R$  and  $g_{BL}$ , or equivalently the ratio  $r_g = g_R/g_L$ . As seen in Eq. (2.20), when  $g_R \gtrsim \mathcal{O}(1)$  [or  $g_{BL} \gtrsim \mathcal{O}(1)$ ], the constraints on the  $v_R$  scale and  $\alpha_3$  tend to be more stringent. The  $r_g$ -dependent scalar perturbativity constraints on  $v_R$  are shown in Fig. 2.8 as the shaded brown regions. Numerically, we find the requirement in the minimal LRSM that

$$v_R \gtrsim 10 \text{ TeV} \quad \text{for} \quad 0.65 \lesssim r_g \lesssim 1.6, \quad (2.22)$$

which makes the perturbativity constraints very stringent in the gauge sector (see Figs. 2.5 and 2.6). The quartic couplings blow up very quickly when  $r_g$  is out of this range unless  $v_R$  is much higher than 10 TeV, as  $g_R \gtrsim \mathcal{O}(1)$  or  $g_{BL} \gtrsim \mathcal{O}(1)$ .

Tab. 2.4: Lower bounds on the  $W_R$  and  $Z_R$  boson masses and the corresponding  $v_R$  scale in the minimal LRSM from the current LHC13 data [6, 1, 2] and the prospects at the HL-LHC 14 TeV with an integrated luminosity of  $3000 \text{ fb}^{-1}$  [7, 3, 4] and future 100 TeV collider FCC-hh with a luminosity of  $30 \text{ ab}^{-1}$  [8, 4, 5], with both the gauge and scalar perturbativity limits up to the GUT scale taken into consideration. The range in each case corresponds to the allowed range of  $r_g$  from perturbativity constraints, as given in Figs. 2.7 and 2.8. The missing entries mean that the corresponding maximum experimental reach has been excluded by the scalar perturbativity constraints. See text for more details.

collider	$W_R$ searches		$Z_R$ searches	
	$M_{W_R}$ [TeV]	$v_R$ [TeV]	$M_{Z_R}$ [TeV]	$v_R$ [TeV]
LHC13	–	–	–	–
HL-LHC	[6.09, 6.47]	[10.3, 14.8]	–	–
FCC-hh	[35.6, 42.2]	[38.3, 87.5]	[27.9, 35.4]	[21.8, 26.8]

It is remarkable that the perturbativity constraints from the scalar sector supersede the current LHC constraints on the  $W_R$  and  $Z_R$  bosons in the minimal LRSM, and even the projected  $Z_R$  sensitivity at the HL-LHC, leaving only a very narrow window for  $W_R$ , as shown in Fig. 2.7. Fortunately, future 100 TeV colliders could probe a much larger parameter space. All the numerical ranges of the maximum  $W_R$  and  $Z_R$  mass reach and the corresponding  $v_R$  scales at future hadron colliders are collected in Table 2.4, with both the gauge and scalar perturbativity constraints taken into consideration. Finding a heavy  $W_R$  and/or  $Z_R$  boson at the HL-LHC, would have strong implications for the interpretation in the minimal LRSM. For instance, if a  $Z_R$  boson was to be found at the LHC, then it does not belong to the minimal LRSM. It could still be accommodated in the LRSM framework by introducing some exotic particles or an intermediate scale, e.g. at  $\sim 10^6 \text{ GeV}$ , to the minimal LRSM to keep all the gauge, Yukawa and quartic couplings perturbative up to the GUT scale.

It should be emphasized that the perturbative constraints on the  $W_R$  and  $Z_R$  masses and the  $v_R$  scale from the scalar sector shown in Figs. 2.7 and 2.8 are based on the assumptions of the scalar masses in Eq. (2.19) and the vanishing quartic couplings  $\lambda_{2,3,4}, \alpha_{1,2}$ . In light of the stringent flavor constraints on the bidoublet scalars  $H_1, A_1$  and  $H_1^\pm$ , the dilepton constraints on the doubly-charged scalar  $H_2^{\pm\pm}$  and the flavor constraints on the neutral scalar  $H_3$ , the masses in Eq. (2.19) are almost the most optimistic values allowed by the current data that

could give us the most conservative perturbativity constraints. If the BSM Higgs masses get larger (especially in the bidoublet sector), the corresponding quartic couplings  $\alpha_3$ ,  $\rho_1$  and  $\rho_2$  will be accordingly enhanced by  $M^2/v_R^2$  at the  $v_R$  scale (with  $M$  standing for the generic BSM scalar mass), and the scalar perturbativity limits on the  $v_R$  scale would be more stringent. Furthermore, if the couplings  $\lambda_{2,3,4}$ ,  $\alpha_{1,2}$  are not zero at the  $v_R$  scale, the quartic couplings tend to hit the Landau pole at a lower scale.

We have also checked also the two-loop corrections to the scalar perturbativity limits by deriving all the two-loop RGEs using the code `PyR@TE` [93, 94], as collected in Eqs. (A.1) to (A.16). It turns out that the two-loop corrections only amount to less than 3% different for the scalar perturbativity limits on  $v_R$  and the heavy gauge boson masses, as compared to the one-loop results presented in this section.

In the limit of small scalar mixing, just as we have assumed above,  $\lambda_1$  can be identified as the SM quartic coupling. As a byproduct, the extra scalars in the LRSM contribute positively to the  $\beta(\lambda_1)$  in Eq. (A.5) in a larger region of parameter space, which helps to stabilize the SM vacuum up to the GUT scale or even up to the Planck scale. The full analysis of the stability of the scalar potential is beyond the main scope of this chapter. See Ref. [122] for a recent analysis in this direction.

## 2.5 Conclusion

In conclusion, we find that in the extensions of the electroweak gauge group to either  $SU(2)_L \times U(1)_{I_{3R}} \times U(1)_{B-L}$  or the left-right symmetric group  $SU(2)_L \times SU(2)_R \times U(1)_{B-L}$ , both of which contribute to the electric charge, there are strong limits on the new gauge couplings  $g_R$  and  $g_{BL}$  from the requirement that the couplings remain perturbative till the GUT scale. We obtain those limits for the minimal versions of these models and study their implications for collider phenomenology. We find in particular that the ratio  $r_g \equiv g_R/g_L$ , or effectively the gauge couplings  $g_R$  and  $g_{BL}$ , are limited to a very narrow range at the

TeV scale, as seen in Figs. 2.2 and 2.6. Inclusion of the scalar sector in the minimal LRSM implies that the RH symmetry breaking scale in LRSM must have a lower bound of about 10 TeV for a limited coupling range  $0.65 \lesssim r_g \lesssim 1.6$ . The gauge (and scalar) perturbative constraints have rich implications for the searches of  $Z_R$  (and  $W_R$ ) bosons in these models at the HL-LHC and future 100 TeV colliders. All the direct search constraints on the  $W_R$  and  $Z_R$  masses from LHC 13 TeV, as well as the future prospects at HL-LHC and 100 TeV colliders, depend on the BSM gauge couplings  $g_R$  and  $g_{BL}$  (or effectively the ratio  $r_g$ ). All the  $Z_R$  (and  $W_R$ ) mass ranges and the corresponding  $v_R$  scales are collected in Figs. 2.3, 2.4 and Table 2.2 for the  $U(1)_{B-L}$  model, and Figs. 2.7, 2.8 and Table 2.4 for the LRSM. One of the most striking results we find is that the perturbativity constraints already exclude the possibility of finding the  $Z_R$  boson belonging to the minimal LRSM at the HL-LHC, and leave only a narrow window for the  $W_R$  boson. We hope this serves as an additional motivation for the 100 TeV collider, where a much broader parameter space can be probed.

## Chapter 3

# Vacuum Stability and Symmetry

## Breaking in Left-Right Model<sup>16</sup>

*"It is not that I'm so smart. But I stay with the questions much longer"*

- Albert Einstein

### 3.1 Introduction

Left-Right Symmetric Model (LRSM) is the simplest extension of the SM with modified electroweak gauge group:  $SU(2)_L \otimes SU(2)_R \otimes U(1)_{B-L}$  [27, 28, 29, 124]. It features heavy Majorana right-handed neutrinos and can naturally explain the small masses of left-handed neutrinos through see-saw mechanism [30, 125, 32, 33, 34]. It explains the asymmetric chiral structure of SM through restoration of parity symmetry at high energies.

Scalar sector of LRSM features an  $SU(2)$  bi-doublet, left and right-handed weak isospin triplets. Such an extended scalar sector leads to a complicated form of the potential which contains 17 free parameters (3 negative mass squares and 14 scalar quartic couplings). Analytical study of vacuum stability and desired minimum for the entire scalar potential is an arduous task. There has been some work in this direction [123, 122] but the results only hold for a small parameter space with most of the quartic couplings set to zero. Moreover, just

---

<sup>16</sup> This chapter is based on [11]

ensuring vacuum stability does not yield the desirable vacuum expectation values (VEVs) to ensure correct spontaneous symmetry breaking to SM [122]. In this work, we have derived most general conditions sufficient<sup>17</sup> to obtain the correct symmetry breaking and ensure vacuum stability of the LRSM. As we show later, it is necessary to obtain conditions for vacuum stability of the general scalar potential before requiring the correct VEV alignment at the minimum. The procedure outlined here for finding conditions for correct symmetry breaking is general in nature and can be applied to different theories with varied forms of the scalar sector.

This chapter is organised as follows. In section 3.2, concepts of copositivity and gauge orbit spaces are presented in context of vacuum stability. In section 3.3, we review the model details of LRSM. In section 3.4, we derive the necessary and sufficient conditions for the boundedness of scalar potential of the LRSM. In section 3.5, we derive conditions sufficient for scalar parameters to lead to spontaneous symmetry breaking (SSB) to the correct global minimum. In section 3.6, we compare the results from numerical minimization of the potential with those from the derived conditions. In section 3.7, we present an example study to use these conditions and other theoretical constraints (unitarity, scalar mass spectrum, perturbativity) on the quartic couplings to study the stability of the vacuum at high energies and agreement with current experimental limits on scalar mass spectrum. Finally, we conclude in section 3.8.

### 3.2 Boundedness

For the stability of the vacuum state, the potential should be bounded in all field directions. In the large-field limit, terms with dimension  $d < 4$  can be ignored as they are negligible in comparison to the quartic terms (denoted by  $V_4(\phi_i)$ ) in the potential. Thus, requiring  $V_4(\phi_i) > 0$  as field values  $\phi_i \rightarrow \infty$  is a strong condition for boundedness. This criterion is termed as Bounded From Below (BFB) condition.

---

<sup>17</sup> We have set only few of the couplings ( $\alpha_2, \beta_i$ 's) to zero.

For obtaining conditions for vacuum stability of a scalar potential using BFB criterion, concepts of copositivity criteria and gauge orbit spaces can help greatly simplify the analysis.

### 3.2.1 Copositivity Criteria

Given a condition of the form:

$$ax^2 + bx + c > 0 \tag{3.1}$$

where  $x \in \mathbb{R}$ , the conditions for it to be positive-definite are very well known. If  $x \in \mathbb{R}^+$ , then the requirement that eq. (3.1) holds is termed as copositivity. The conditions for copositivity are given below:

$$a > 0, c > 0, b + 2\sqrt{ac} > 0$$

The quartic part of the vacuum potential is bounded from below if it satisfies the copositivity conditions. The criteria of copositivity has been applied to numerous models in literature to obtain vacuum stability conditions [126, 123, 127, 128]. The difficulty to solve these conditions based solely on copositive criteria is a formidable task. Usually it involves checking copositivity in all n-field directions to obtain an exhaustive list of conditions for vacuum stability .

In sec. 3.4.1 and 3.4.2, copositive criteria is used in conjunction with suitable parametrization of gauge orbit parameters to yield results easily. In the coupled case (Sec. 3.4.3), when mixed field terms are present<sup>18</sup>, we observe that exact values of minima are required and copositivity isn't helpful as it yields results only upto a multiplicative constant.

### 3.2.2 Gauge Orbit Spaces

Due to the gauge freedom of the theory, different values of the fields can lead to same value of the potential. These field values connected through gauge transformations collectively form

---

<sup>18</sup> i.e  $\alpha$ 's  $\neq 0$

a gauge orbit. Minimization of the Higgs potentials in orbit spaces has been extensively studied in context of grand unified theories in the 1980's [129, 130, 131, 132, 133, 134]. Here, we present the method of orbit spaces for the two higgs fields case [129]. This is an extension of the one-field treatment as presented in ref.[129, 127].

Consider the scalar potential of a theory with two higgs fields  $\phi$  and  $\pi$  charged under non-abelian gauge groups  $G$  and  $G'$  respectively, with the following form :

$$\begin{aligned}
 V(\phi, \pi) = & -\mu_1^2(\phi_i^* \phi_i) - \mu_2^2(\pi_i^* \pi_i) + \lambda_1(\phi_i^* \phi_i)^2 + \lambda_2 f_{ijkl} \phi_i^* \phi_j \phi_k^* \phi_l + \dots & (3.2) \\
 & + \rho_1(\pi_i^* \pi_i)^2 + \rho_2 g_{ijkl} \pi_i^* \pi_j \pi_k^* \pi_l + \dots \\
 & + \alpha_1(\phi_i^* \phi_i)(\pi_j^* \pi_j) + \dots \text{(other terms coupling } (\phi, \pi))
 \end{aligned}$$

where  $V(\phi, \pi)$  remains invariant under the action of the group elements of  $G$  and  $G'$ . Field  $\phi(\pi)$  (with components denoted by  $\phi_i(\pi_i)$ ) live in the representation  $\mathbf{R}(\mathbf{R}')$  of group  $G(G')$ .

The group elements of  $G$  rotate a field into other field values on the same orbit space. It can be shown that all the fields  $\psi_i$  on the orbit respect the same group, called the little group. If their action on the fields is unitary, the norm of the field value  $\phi_i^* \phi_i$  is preserved. This similarly holds for field  $\pi$ . Several different orbits respect the same group and form a set. The set of these orbits is called the stratum of the little group. Thus, we need to find the gauge orbit that minimizes the potential.

The dimensionless ratios of invariants called orbit space parameters specifies a strata as follows:

$$A_n(\hat{\phi}) = \frac{f_{ijkl} \phi_i^* \phi_j \phi_k^* \phi_l}{(\phi_i^* \phi_i)^2} \quad B_n(\hat{\pi}) = \frac{g_{ijkl} \pi_i^* \pi_j \pi_k^* \pi_l}{(\pi_j^* \pi_j)^2}$$

Similarly, for coupled terms  $C_n(\hat{\phi}, \hat{\pi})$  can be defined but normalized by  $\phi_i^* \phi_i \pi_j^* \pi_j$ . Orbit space parameters greatly reduce the number of parameters and contain all the directional

information required for the minimization. Defining orbit space parameters for eq. (3.2),

$$\begin{aligned}
 V(\phi, \pi) &= -\mu_1^2|\phi|^2 - \mu_2^2|\pi|^2 + |\phi|^4(\lambda_1 + \lambda_2 A_1(\hat{\phi}) + \lambda_3 A_2(\hat{\phi}) + \dots) \\
 &\quad + |\pi|^4(\rho_1 + \rho_2 B_1(\hat{\pi}) + \rho_3 B_2(\hat{\pi}) + \dots) \\
 &\quad + |\phi|^2|\pi|^2(\alpha_1 + \alpha_2 C_1(\hat{\phi}, \hat{\pi}) + \dots) \\
 &\equiv -\mu_1^2|\phi|^2 - \mu_2^2|\pi|^2 + |\phi|^4 A(\lambda, \hat{\phi}) + |\pi|^4 B(\rho, \hat{\pi}) + |\phi|^2|\pi|^2 C(\alpha, \hat{\phi}, \hat{\pi}) \quad (3.3)
 \end{aligned}$$

where

$$\begin{aligned}
 |\phi|^2 &= \phi_i^* \phi_i, \quad |\pi|^2 = \pi_i^* \pi_i, \quad \hat{\phi} = \frac{\phi}{|\phi|}, \quad \hat{\pi} = \frac{\pi}{|\pi|} \\
 A(\lambda, \hat{\phi}) &= \lambda_1 + \lambda_2 A_1(\hat{\phi}) + \lambda_3 A_2(\hat{\phi}) + \dots \\
 B(\rho, \hat{\pi}) &= \rho_1 + \rho_2 B_1(\hat{\pi}) + \rho_3 B_2(\hat{\pi}) + \dots \\
 C(\alpha, \hat{\phi}, \hat{\pi}) &= \alpha_1 + \alpha_2 C_1(\hat{\phi}, \hat{\pi}) + \dots
 \end{aligned}$$

Note that we have assumed terms like  $|\phi|^3|\pi|$  and  $|\phi||\pi|^3$  to be absent from the expression for  $V(\phi, \pi)$ . This is particularly true if the higgs potential is invariant under a reflection symmetry for  $\phi$  and  $\pi$ . Requiring boundedness and applying copositivity criterion, we get the following conditions for the stability of the potential,

$$\begin{aligned}
 |\phi|^4 A(\lambda, \hat{\phi}) + |\pi|^4 B(\rho, \hat{\pi}) + |\phi|^2|\pi|^2 C(\alpha, \hat{\phi}, \hat{\pi}) &> 0 \quad \forall A(\lambda, \hat{\phi}), B(\rho, \hat{\pi}), C(\alpha, \hat{\phi}, \hat{\pi}) \\
 \implies A > 0, B > 0, C + 2\sqrt{AB} > 0 &\quad (3.4)
 \end{aligned}$$

Treatment in ref.[129] assumes the monotonicity of the orbit space parameters in the potential and thus minimization of these parameters are not required. Our treatment for the left-right model differs here due to the presence of non-linearity in orbit space parameters. It should be noted that eq. (3.4) must also be minimized over all orbit space parameters. We also

study the VEV structure of the scalar fields in the theory. Thus, minimizing  $V$  w.r.t to  $|\phi|$  and  $|\pi|$  yields,

$$\begin{aligned}\frac{\partial V}{\partial |\phi|} &= 2|\phi| \left( -\mu_1^2 + 2|\phi|^2 A + |\pi|^2 C \right) = 0 \\ \frac{\partial V}{\partial |\pi|} &= 2|\pi| \left( -\mu_2^2 + 2|\pi|^2 B + |\phi|^2 C \right) = 0\end{aligned}$$

Since, field value should be non-zero, the minimum occurs at:

$$|\phi_0|^2 = \frac{2B\mu_1^2 - C\mu_2^2}{4AB - C^2} \quad |\pi_0|^2 = \frac{2A\mu_2^2 - C\mu_1^2}{4AB - C^2} \quad (3.5)$$

Using second derivative analysis for  $\phi$  and  $\pi$ , it can be proved that field values in eq. (3.5) leads to a minimum of the potential if and only if following conditions are satisfied.

$$2B\mu_1^2 - C\mu_2^2 > 0 \quad (3.6)$$

$$2A\mu_2^2 - C\mu_1^2 > 0 \quad (3.7)$$

$$4AB - C^2 > 0 \quad (3.8)$$

Plugging obtained field values at the minimum in eq. (3.3), we get

$$V_0(\phi) = -\frac{B\mu_1^4 - C\mu_1^2\mu_2^2 + A\mu_2^4}{4AB - C^2} \quad (3.9)$$

It can be shown using conditions obtained above that this minimum is guaranteed to be the global minimum of the potential.

### 3.3 Left-Right Symmetric Model

Left-Right Symmetric model (LRSM) is a gauge extension of the Standard Model (SM), which restores parity symmetry at high-energies [27, 28, 29]. It treats left and right handed

chiralities of fermions equally prior to spontaneous symmetry breaking. It features heavy right-handed Majorana neutrinos, and thus explains small masses of left-handed neutrinos via the see-saw mechanism [30, 125, 32]. The extended gauge group for this model :  $SU(3)_C \otimes SU(2)_L \otimes SU(2)_R \otimes U(1)_{B-L}$ . The particle content and their irreducible representations under the gauge group is given in table 3.1. The spontaneous symmetry breaking (SSB) of LRSM proceeds in two steps. First, the electrically neutral component of  $\Delta_R$  acquires a VEV  $v_R$  and breaks the gauge group from  $SU(2)_R \otimes U(1)_{B-L}$  to  $U(1)_Y$ . Finally, the VEV of bidoublet  $\Phi$  breaks the symmetry down to  $U(1)_Q$  [135, 136]. The VEV structure of the scalar fields is

$$\Phi = \frac{1}{\sqrt{2}} \begin{pmatrix} \kappa_1 & 0 \\ 0 & \kappa_2 e^{i\theta_2} \end{pmatrix}, \quad \Delta_L = \frac{1}{\sqrt{2}} \begin{pmatrix} 0 & 0 \\ v_L e^{i\theta_L} & 0 \end{pmatrix}, \quad \Delta_R = \frac{1}{\sqrt{2}} \begin{pmatrix} 0 & 0 \\ v_R & 0 \end{pmatrix} \quad (3.10)$$

Note that only the neutral components acquire VEV so that  $U(1)_{EM}$  does not break. Using the gauge transformations, two of the phases in  $\kappa_1$  and  $v_R$  have been rotated away. It is required that the VEV's respect the following hierarchy for correct phenomenology:

$$v_L \ll \kappa_{1,2} \ll v_R$$

The electric charge formula takes the form:

$$Q = T_{3L} + T_{3R} + \frac{B-L}{2}$$

where  $T_{3X}$ ,  $X = (L, R)$  is the third generator of the group  $SU(2)_X$  and  $B-L$  is the baryon minus lepton number, the charge for group  $U(1)_{B-L}$  [23, 24]. The most general renormalizable scalar potential for LRSM contains 17 independent terms [136, 122]:

	$SU(3)_C$	$SU(2)_L$	$SU(2)_R$	$U(1)_{B-L}$
$Q_L \equiv \begin{pmatrix} u_L \\ d_L \end{pmatrix}$	<b>3</b>	<b>2</b>	<b>1</b>	$\frac{1}{3}$
$Q_R \equiv \begin{pmatrix} u_R \\ d_R \end{pmatrix}$	<b>3</b>	<b>1</b>	<b>2</b>	$\frac{1}{3}$
$\psi_L \equiv \begin{pmatrix} \nu_L \\ e_L \end{pmatrix}$	<b>1</b>	<b>2</b>	<b>1</b>	-1
$\psi_R \equiv \begin{pmatrix} N \\ e_R \end{pmatrix}$	<b>1</b>	<b>1</b>	<b>2</b>	-1
$\Phi = \begin{pmatrix} \phi_1^0 & \phi_2^+ \\ \phi_1^- & \phi_2^0 \end{pmatrix}$	<b>1</b>	<b>2</b>	<b>2</b>	0
$\Delta_L = \begin{pmatrix} \frac{1}{\sqrt{2}}\Delta_L^+ & \Delta_L^{++} \\ \Delta_L^0 & -\frac{1}{\sqrt{2}}\Delta_L^+ \end{pmatrix}$	<b>1</b>	<b>3</b>	<b>1</b>	2
$\Delta_R = \begin{pmatrix} \frac{1}{\sqrt{2}}\Delta_R^+ & \Delta_R^{++} \\ \Delta_R^0 & -\frac{1}{\sqrt{2}}\Delta_R^+ \end{pmatrix}$	<b>1</b>	<b>1</b>	<b>3</b>	2

Tab. 3.1: Particle content of left-right symmetric model based on the gauge group  $SU(3)_C \otimes SU(2)_L \otimes SU(2)_R \otimes U(1)_{B-L}$ .

$$\begin{aligned}
 V = & -\mu_1^2 \text{Tr}[\Phi^\dagger \Phi] - \mu_2^2 \left( \text{Tr}[\tilde{\Phi} \Phi^\dagger] + \text{Tr}[\tilde{\Phi}^\dagger \Phi] \right) - \mu_3^2 \left( \text{Tr}[\Delta_L \Delta_L^\dagger] + \text{Tr}[\Delta_R \Delta_R^\dagger] \right) + \lambda_1 \text{Tr}[\Phi^\dagger \Phi]^2 \\
 & + \lambda_2 \left( \text{Tr}[\tilde{\Phi} \Phi^\dagger]^2 + \text{Tr}[\tilde{\Phi}^\dagger \Phi]^2 \right) + \lambda_3 \text{Tr}[\tilde{\Phi} \Phi^\dagger] \text{Tr}[\tilde{\Phi}^\dagger \Phi] + \lambda_4 \text{Tr}[\Phi^\dagger \Phi] \left( \text{Tr}[\tilde{\Phi} \Phi^\dagger] + \text{Tr}[\tilde{\Phi}^\dagger \Phi] \right) \\
 & + \rho_1 \left( \text{Tr}[\Delta_L \Delta_L^\dagger]^2 + \text{Tr}[\Delta_R \Delta_R^\dagger]^2 \right) + \rho_2 \left( \text{Tr}[\Delta_L \Delta_L] \text{Tr}[\Delta_L^\dagger \Delta_L^\dagger] + \text{Tr}[\Delta_R \Delta_R] \text{Tr}[\Delta_R^\dagger \Delta_R^\dagger] \right) \\
 & + \rho_3 \text{Tr}[\Delta_L \Delta_L^\dagger] \text{Tr}[\Delta_R \Delta_R^\dagger] + \rho_4 \left( \text{Tr}[\Delta_L \Delta_L] \text{Tr}[\Delta_R^\dagger \Delta_R^\dagger] + \text{Tr}[\Delta_L^\dagger \Delta_L^\dagger] \text{Tr}[\Delta_R \Delta_R] \right) \quad (3.11) \\
 & + \alpha_1 \text{Tr}[\Phi^\dagger \Phi] \left( \text{Tr}[\Delta_L \Delta_L^\dagger] + \text{Tr}[\Delta_R \Delta_R^\dagger] \right) + \alpha_3 \left( \text{Tr}[\Phi \Phi^\dagger \Delta_L \Delta_L^\dagger] + \text{Tr}[\Phi^\dagger \Phi \Delta_R \Delta_R^\dagger] \right) \\
 & + \alpha_2 \left( \text{Tr}[\Delta_L \Delta_L^\dagger] \text{Tr}[\tilde{\Phi} \Phi^\dagger] + \text{Tr}[\Delta_R \Delta_R^\dagger] \text{Tr}[\tilde{\Phi}^\dagger \Phi] + \text{H.c.} \right) \\
 & + \beta_1 \left( \text{Tr}[\Phi \Delta_R \Phi^\dagger \Delta_L^\dagger] + \text{Tr}[\Phi^\dagger \Delta_L \Phi \Delta_R^\dagger] \right) + \beta_2 \left( \text{Tr}[\tilde{\Phi} \Delta_R \Phi^\dagger \Delta_L^\dagger] + \text{Tr}[\tilde{\Phi}^\dagger \Delta_L \Phi \Delta_R^\dagger] \right) \\
 & + \beta_3 \left( \text{Tr}[\Phi \Delta_R \tilde{\Phi}^\dagger \Delta_L^\dagger] + \text{Tr}[\Phi^\dagger \Delta_L \tilde{\Phi} \Delta_R^\dagger] \right)
 \end{aligned}$$

where all couplings are assumed real. Here,  $\tilde{\Phi} = \sigma_2 \Phi^* \sigma_2$ , where  $\sigma_2$  is the 2nd Pauli matrix.  $\tilde{\Phi}$  transforms the same way as  $\Phi$  does.

Assume that after the SSB, the vacuum state of the potential is stable and has the form

of VEV structure eq. (3.10). We can then minimize the potential w.r.t the VEV parameters,

$$\frac{\partial V}{\partial \kappa_1} = \frac{\partial V}{\partial \kappa_2} = \frac{\partial V}{\partial \theta_2} = \frac{\partial V}{\partial v_L} = \frac{\partial V}{\partial \theta_L} = \frac{\partial V}{\partial v_R} = 0$$

This yields a set of 6 equations which can be solved to yield the famous VEV see-saw relation [122].

$$\beta_1 \cos(\theta_2 - \theta_L) \kappa_2 \kappa_1 + \beta_2 \kappa_1^2 \cos \theta_L + \beta_3 \cos(2\theta_2 - \theta_L) \kappa_2^2 = (2\rho_1 - \rho_3) v_L v_R \quad (3.12)$$

Note if  $\beta_{1,2,3} = 0$  and since phenomenologically  $v_R \neq 0$ , this implies  $v_L = 0$ .

## 3.4 Vacuum Stability

Quartic terms containing only the scalar bidoublet Higgs field constitutes the  $\lambda$  sector and those containing only left and right-handed triplet Higgs fields constitutes the  $\rho$  sector. It should be noted that mixing terms (i.e. involving  $\alpha$ 's and  $\beta$ 's) complicate the analysis for boundedness. We first look at bidoublet and triplets part of the potential separately to understand the procedure of minimization and useful parametrization to obtain BFB conditions. We then analyze the BFB condition for the potential in presence of non-zero quartic terms that couple bidoublet and triplet fields together in Sec 3.4.3.

### 3.4.1 Bidoublet $\Phi$ : $\lambda$ Sector

As the potential should be bounded in all field directions, we first choose to find conditions for  $\lambda$  sector containing the bidoublet  $\Phi$ . Considering only the quartic part, we require

$$\begin{aligned} V_4^\lambda &= \lambda_1 \text{Tr}[\Phi^\dagger \Phi]^2 + \lambda_2 \left( \text{Tr}[\tilde{\Phi} \Phi^\dagger]^2 + \text{Tr}[\tilde{\Phi}^\dagger \Phi]^2 \right) + \lambda_3 \text{Tr}[\tilde{\Phi} \Phi^\dagger] \text{Tr}[\tilde{\Phi}^\dagger \Phi] \\ &+ \lambda_4 \text{Tr}[\Phi^\dagger \Phi] \left( \text{Tr}[\tilde{\Phi} \Phi^\dagger] + \text{Tr}[\tilde{\Phi}^\dagger \Phi] \right) > 0 \quad \forall \Phi \end{aligned} \quad (3.13)$$

To obtain the conditions to be BFB, we parametrize  $V_4^\lambda$  as follows:

$$\begin{aligned}\text{Tr}[\Phi^\dagger\Phi] &\equiv r^2 \\ \text{Tr}[\tilde{\Phi}\Phi^\dagger]/\text{Tr}[\Phi^\dagger\Phi] &\equiv \xi e^{i\omega} \\ \text{Tr}[\tilde{\Phi}^\dagger\Phi]/\text{Tr}[\Phi^\dagger\Phi] &\equiv \xi e^{-i\omega}\end{aligned}$$

where  $r > 0$ ,  $\xi \in [0, 1]$  and  $\omega \in [0, 2\pi]$ . Quartic field terms present in the potential are normalized with the norm of the bidoublet  $\Phi$  as discussed in sec 3.2.2. The complex product  $\text{Tr}[\tilde{\Phi}\Phi^\dagger]/\text{Tr}[\Phi^\dagger\Phi]$  between two unit spinors will be a complex number and hence has been parametrized accordingly. This approach to parametrization has been earlier used for obtaining boundedness criteria in two-Higgs-doublet Model [137, 138] and doublet-triplet-Higgs Model [139].

Substituting above in eq. (3.13),

$$V_4^\lambda = r^4 \left( \lambda_1 + 2\lambda_2 \xi^2 \cos 2\omega + \lambda_3 \xi^2 + 2\lambda_4 \xi \cos \omega \right) \equiv r^4 f(\lambda, \xi, \omega) \quad (3.14)$$

We know from the extremum value theorem, the minimum of  $V_4^\lambda$  must exist in/on the closed boundary defined by the disk. Furthermore, it should either exist inside the bounded region or on the boundary. We first minimize  $V_4^\lambda$  inside the boundary w.r.t  $\xi$  and  $\omega$ .

$$\begin{aligned}f_\xi = \frac{\partial f}{\partial \xi} &= 4\lambda_2 \xi \cos 2\omega + 2\lambda_3 \xi + 2\lambda_4 \cos \omega = 0 \\ f_\omega = \frac{\partial f}{\partial \omega} &= -4\lambda_2 \xi^2 \sin 2\omega - 2\lambda_4 \xi \sin \omega = -2\xi \sin \omega (4\lambda_2 \xi \cos \omega + \lambda_4) = 0\end{aligned}$$

Here, we denote  $\frac{\partial f}{\partial x}$  as  $f_x$  and continue using this notation for conciseness. Solving the above two equations simultaneously, we get three critical points. Only the first two critical points are valid solutions of these pair of equations.

$$f_\omega = 0 \implies \xi = 0, \sin \omega = 0 \text{ or } \cos \omega = -\frac{\lambda_4}{4\lambda_2\xi}$$

**Case 1:**  $\xi = 0$

$$f_\xi = 2\lambda_4 \cos \omega = 0$$

$$\implies \cos \omega = 0$$

Using this  $\xi$  and  $\cos \omega$  in (3.14), we obtain the trivial condition for boundedness

$$\lambda_1 > 0 \tag{3.15}$$

**Case 2:**  $\sin \omega = 0$

Notice,  $\sin \omega = 0 \implies \cos \omega = \pm 1$ . From eq. (3.14), we notice this minimum value of  $\cos \omega$  depends on the sign on  $\lambda_4$ .

$$\cos \omega = -\text{sgn}(\lambda_4)$$

Here,  $\text{sgn}(x)$  is the signum function. Thus, the relevant equation for minimum can be written as:

$$f_\xi = 4\lambda_2\xi + 2\lambda_3\xi - 2|\lambda_4| = 0$$

$$\implies \xi = \frac{|\lambda_4|}{2\lambda_2 + \lambda_3}$$

Inserting these values in  $f$  requiring  $V_4^\lambda > 0$ , we get

$$\lambda_1 + (2\lambda_2 + \lambda_3) \left( \frac{|\lambda_4|}{2\lambda_2 + \lambda_3} \right)^2 - 2|\lambda_4| \frac{|\lambda_4|}{2\lambda_2 + \lambda_3} > 0$$

Thus, we get second condition as requirement:

$$\lambda_1 - \frac{\lambda_4^2}{2\lambda_2 + \lambda_3} > 0 \iff 2\lambda_2 + \lambda_3 > |\lambda_4| \quad (3.16)$$

**Case 3:**  $\cos \omega = -\frac{\lambda_4}{4\lambda_2\xi}$

$$4\lambda_2\xi \left( 2 \left( \frac{\lambda_4}{4\lambda_2\xi} \right)^2 - 1 \right) + 2\lambda_3\xi - 2\lambda_4 \left( \frac{\lambda_4}{4\lambda_2\xi} \right) = -2\lambda_3\xi = 0$$

The solution for above is  $\xi = 0$  but  $\cos \omega$  is not defined for this value. Thus, this is not a valid solution. Now, we try to minimize  $f$  on the boundary w.r.t to  $\omega$  by setting  $\xi = 1$ .

$$f_\omega = -4\lambda_2 \sin 2\omega - 2\lambda_4 \sin \omega = -2 \sin \omega (4\lambda_2 \cos \omega + \lambda_4) = 0$$

**Case 4:**  $\xi = 1, \sin \omega = 0 \implies \cos \omega = -\text{sgn}(\lambda_4), \cos 2\omega = 1$  Using this we have the condition,

$$\lambda_1 + \lambda_3 + 2(\lambda_2 - |\lambda_4|) > 0 \quad (3.17)$$

**Case 5:**  $\xi = 1, \cos \omega = -\frac{\lambda_4}{4\lambda_2}$

$$\lambda_1 + 2\lambda_2 \left( 2 \left( \frac{\lambda_4}{4\lambda_2} \right)^2 - 1 \right) + \lambda_3 - 2\lambda_4 \left( \frac{\lambda_4}{4\lambda_2} \right) > 0$$

The final condition can be written as:

$$\lambda_1 + \lambda_3 - 2\lambda_2 - \frac{\lambda_4^2}{4\lambda_2} > 0 \iff \left| \frac{\lambda_4}{4\lambda_2} \right| < 1 \quad (3.18)$$

Thus, equations (3.15), (3.16), (3.17) and (3.18) collectively form the required bounded from below (BFB) conditions for  $\lambda$  sector.

Now, we'll remark on the behaviour of these conditions to understand their characteristics in the plots. The condition with the minimum value dominates the boundedness of the potential. All conditions dominate in different regions of the parameter space and controls the boundedness of the potential. For instance, the condition from inside the boundary eq. (3.16) dominates over other conditions if  $2\lambda_2 + \lambda_3 > |\lambda_4|$  is satisfied. It can also be shown that eq. (3.18) dominates when  $\lambda_2 > 0$  otherwise eq. (3.17) is valid.

### 3.4.2 Triplets $\Delta_L$ and $\Delta_R$ : $\rho$ sector

The quartic part of the potential with  $\rho_i$ 's is :

$$\begin{aligned}
 V_4^\rho = & \rho_1 \left( \text{Tr}[\Delta_L \Delta_L^\dagger]^2 + \text{Tr}[\Delta_R \Delta_R^\dagger]^2 \right) + \rho_2 \left( \text{Tr}[\Delta_L \Delta_L] \text{Tr}[\Delta_L^\dagger \Delta_L^\dagger] + \text{Tr}[\Delta_R \Delta_R] \text{Tr}[\Delta_R^\dagger \Delta_R^\dagger] \right) \\
 & + \rho_3 \text{Tr}[\Delta_L \Delta_L^\dagger] \text{Tr}[\Delta_R \Delta_R^\dagger] + \rho_4 \left( \text{Tr}[\Delta_L \Delta_L] \text{Tr}[\Delta_R^\dagger \Delta_R^\dagger] + \text{Tr}[\Delta_L^\dagger \Delta_L^\dagger] \text{Tr}[\Delta_R \Delta_R] \right)
 \end{aligned} \tag{3.19}$$

To obtain the conditions for BFB, we parametrize  $V_4^\rho$  similar to sec 3.4.1 :

$$\begin{aligned}
 \text{Tr}[\Delta_L \Delta_L^\dagger] + \text{Tr}[\Delta_R \Delta_R^\dagger] & \equiv r^2 \\
 \text{Tr}[\Delta_L \Delta_L^\dagger] & \equiv r^2 \sin^2 \gamma \\
 \text{Tr}[\Delta_R \Delta_R^\dagger] & \equiv r^2 \cos^2 \gamma \\
 \text{Tr}[\Delta_L \Delta_L] / \text{Tr}[\Delta_L \Delta_L^\dagger] & \equiv \eta_1 e^{i\theta_1} \\
 \text{Tr}[\Delta_L^\dagger \Delta_L^\dagger] / \text{Tr}[\Delta_L \Delta_L^\dagger] & \equiv \eta_1 e^{-i\theta_1} \\
 \text{Tr}[\Delta_R \Delta_R] / \text{Tr}[\Delta_R \Delta_R^\dagger] & \equiv \eta_2 e^{i\theta_2} \\
 \text{Tr}[\Delta_R^\dagger \Delta_R^\dagger] / \text{Tr}[\Delta_R \Delta_R^\dagger] & \equiv \eta_2 e^{-i\theta_2}
 \end{aligned}$$

where  $r > 0$ ,  $\gamma \in [0, \frac{\pi}{2}]$ ,  $\eta_1, \eta_2 \in [0, 1]$  and  $\theta_1, \theta_2 \in [0, 2\pi]$ . Substituting above in eq. (3.19),

$$V_4^p = r^4(\rho_1(\cos^4 \gamma + \sin^4 \gamma) + \rho_2(\eta_1^2 \sin^4 \gamma + \eta_2^2 \cos^4 \gamma) + \rho_3 \cos^2 \gamma \sin^2 \gamma + 2\rho_4 \eta_1 \eta_2 \cos(\theta_1 - \theta_2) \cos^2 \gamma \sin^2 \gamma) \equiv g(\rho, \gamma, \eta_{1,2}, \theta_{1,2}) \quad (3.20)$$

For minimum w.r.t to  $\theta_1, \theta_2$  and taking in account sign of  $\rho_4$ , this can be rewritten as:

$$V_4^p = \frac{r^4}{(1 + \tan^2 \gamma)^2} \left( \tan^4 \gamma (\rho_1 + \rho_2 \eta_1^2) + \tan^2 \gamma (\rho_3 - 2|\rho_4| \eta_1 \eta_2) + \rho_1 + \rho_2 \eta_2^2 \right)$$

Requiring the above expression to be positive for all values of  $\tan \gamma$  can be translated to  $V_4^p$  being copositive for variable  $\tan^2 \gamma$ . Thus, we have following requirements for  $V_4^p$  to be bounded from below :

$$\rho_1 + \rho_2 \eta_1^2 > 0 \quad (3.21)$$

$$\rho_1 + \rho_2 \eta_2^2 > 0 \quad (3.22)$$

$$\mathcal{G}(\rho, \eta_{1,2}) \equiv \rho_3 - 2|\rho_4| \eta_1 \eta_2 + 2\sqrt{(\rho_1 + \rho_2 \eta_1^2)(\rho_1 + \rho_2 \eta_2^2)} > 0 \quad (3.23)$$

in regions  $\eta_1, \eta_2 \in [0, 1]$ .

Eq. (3.21) is equivalent to (3.22) as they are uncoupled in the constraint variable. Minimum value for the expression occurs at the endpoint as its monotonic in the quantity  $\eta_i^2$ , which ranges from  $[0, 1]$ . Plugging the end points of the range of  $\eta_i^2$ ,

$$\rho_1 > 0 \quad (3.24)$$

$$\rho_1 + \rho_2 > 0 \quad (3.25)$$

We can first minimize  $\mathcal{G}$  inside the boundary of square formed by  $\eta_1$  and  $\eta_2$ . By minimizing

the condition w.r.t to  $\eta$ 's,

$$\mathcal{G}_{\eta_1} \equiv 2\eta_1\rho_2 \frac{\sqrt{(\rho_1 + \rho_2\eta_2^2)}}{\sqrt{(\rho_1 + \rho_2\eta_1^2)}} - 2\eta_2|\rho_4| = 0$$

$$\mathcal{G}_{\eta_2} \equiv 2\eta_2\rho_2 \frac{\sqrt{(\rho_1 + \rho_2\eta_1^2)}}{\sqrt{(\rho_1 + \rho_2\eta_2^2)}} - 2\eta_1|\rho_4| = 0$$

Solving the above two equations, we get

$$(\eta_1, \eta_2) = (0, 0)$$

Plugging it back in  $\mathcal{G}$ ,

$$\rho_3 + 2\rho_1 > 0 \tag{3.26}$$

For minimizing  $\mathcal{G}$  on the boundary, we set  $\eta_1 = \eta_2 = 1$ . We obtain the condition

$$\rho_3 - 2|\rho_4| + 2(\rho_1 + \rho_2) > 0 \tag{3.27}$$

It can be proved that condition obtained by setting  $\eta_1 = 0, \eta_2 = 1$  or vice-versa, always lies between the above two conditions and need not be checked for boundedness. Thus, conditions (3.24), (3.25), (3.26) and (3.27) collectively form the required conditions for BFB  $\rho$  sector.

### 3.4.3 Dreaded Coupled Case: $\alpha_{1,3} \neq 0$

This section outlines the procedure to find boundedness in presence of terms that couple the bidoublet and the triplet Higgs fields. For VEV see-saw relation to work naturally, we assume  $\beta_i = 0$  [116]. This would imply  $v_L = 0$  and a non-zero  $v_R$ . Also  $\alpha_2$  does not explicitly appears in the expressions for scalar mass spectrum. This gives us the freedom to set it to 0 for our analysis [79]. Thus, only  $\alpha_1$  and  $\alpha_3$  are assumed to be non-zero as they contribute

to the scalar masses and have lower bounds on them from experimental constraints. The quartic part of the potential is given below:

$$\begin{aligned}
 V_4 = & \lambda_1 \text{Tr}[\Phi^\dagger \Phi]^2 + \lambda_2 \left( \text{Tr}[\tilde{\Phi} \Phi^\dagger]^2 + \text{Tr}[\tilde{\Phi}^\dagger \Phi]^2 \right) + \lambda_3 \text{Tr}[\tilde{\Phi} \Phi^\dagger] \text{Tr}[\tilde{\Phi}^\dagger \Phi] + \lambda_4 \text{Tr}[\Phi^\dagger \Phi] \left( \text{Tr}[\tilde{\Phi} \Phi^\dagger] + \text{Tr}[\tilde{\Phi}^\dagger \Phi] \right) \\
 & + \rho_1 \left( \text{Tr}[\Delta_L \Delta_L^\dagger]^2 + \text{Tr}[\Delta_R \Delta_R^\dagger]^2 \right) + \rho_2 \left( \text{Tr}[\Delta_L \Delta_L] \text{Tr}[\Delta_L^\dagger \Delta_L^\dagger] + \text{Tr}[\Delta_R \Delta_R] \text{Tr}[\Delta_R^\dagger \Delta_R^\dagger] \right) \\
 & + \rho_3 \text{Tr}[\Delta_L \Delta_L^\dagger] \text{Tr}[\Delta_R \Delta_R^\dagger] + \rho_4 \left( \text{Tr}[\Delta_L \Delta_L] \text{Tr}[\Delta_R^\dagger \Delta_R^\dagger] + \text{Tr}[\Delta_L^\dagger \Delta_L^\dagger] \text{Tr}[\Delta_R \Delta_R] \right) \\
 & + \alpha_1 \text{Tr}[\Phi^\dagger \Phi] \left( \text{Tr}[\Delta_L \Delta_L^\dagger] + \text{Tr}[\Delta_R \Delta_R^\dagger] \right) + \alpha_3 \left( \text{Tr}[\Phi \Phi^\dagger \Delta_L \Delta_L^\dagger] + \text{Tr}[\Phi^\dagger \Phi \Delta_R \Delta_R^\dagger] \right)
 \end{aligned} \tag{3.28}$$

The parametrization in this case follows similarly as before. This has 3 different field directions and therefore can be parametrized on a sphere.

$$\begin{aligned}
 \text{Tr}[\Phi^\dagger \Phi] + \text{Tr}[\Delta_L \Delta_L^\dagger] + \text{Tr}[\Delta_R \Delta_R^\dagger] & \equiv r^2 \\
 \text{Tr}[\Phi^\dagger \Phi] & \equiv r^2 \cos^2 \theta \\
 \text{Tr}[\Delta_L \Delta_L^\dagger] & \equiv r^2 \sin^2 \gamma \sin^2 \theta \\
 \text{Tr}[\Delta_R \Delta_R^\dagger] & \equiv r^2 \cos^2 \gamma \sin^2 \theta \\
 \text{Tr}[\tilde{\Phi} \Phi^\dagger] / \text{Tr}[\Phi^\dagger \Phi] & \equiv \xi e^{i\omega} \\
 \text{Tr}[\tilde{\Phi}^\dagger \Phi] / \text{Tr}[\Phi^\dagger \Phi] & \equiv \xi e^{-i\omega} \\
 \text{Tr}[\Delta_L \Delta_L] / \text{Tr}[\Delta_L \Delta_L^\dagger] & \equiv \eta_1 e^{i\theta_1} \\
 \text{Tr}[\Delta_L^\dagger \Delta_L^\dagger] / \text{Tr}[\Delta_L \Delta_L^\dagger] & \equiv \eta_1 e^{-i\theta_1} \\
 \text{Tr}[\Delta_R \Delta_R] / \text{Tr}[\Delta_R \Delta_R^\dagger] & \equiv \eta_2 e^{i\theta_2} \\
 \text{Tr}[\Delta_R^\dagger \Delta_R^\dagger] / \text{Tr}[\Delta_R \Delta_R^\dagger] & \equiv \eta_2 e^{-i\theta_2} \\
 \text{Tr}[\Phi \Phi^\dagger \Delta_L \Delta_L^\dagger] / \text{Tr}[\Phi^\dagger \Phi] \text{Tr}[\Delta_L \Delta_L^\dagger] & \equiv \zeta_1 \\
 \text{Tr}[\Phi^\dagger \Phi \Delta_R \Delta_R^\dagger] / \text{Tr}[\Phi^\dagger \Phi] \text{Tr}[\Delta_R \Delta_R^\dagger] & \equiv \zeta_2
 \end{aligned}$$

with  $r > 0$ ,  $|\xi| \leq 1$ ,  $\theta \in [0, \frac{\pi}{2}]$ ,  $\gamma \in [0, \frac{\pi}{2}]$ ,  $\eta_1, \eta_2 \in [0, 1]$ ,  $\theta_1, \theta_2 \in [0, 2\pi]$

Naively, it might be expected that  $\zeta_1, \zeta_2 \in [0, 1]$  [140]. However, as can be seen from the

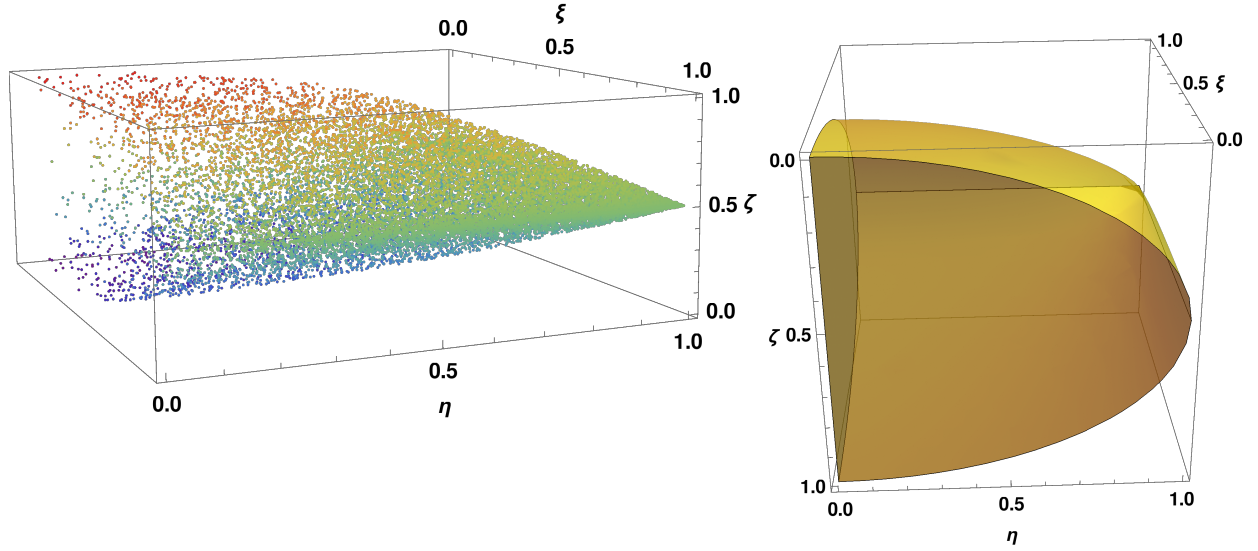


Fig. 3.1: Dependence of gauge orbit variable  $\zeta_i$  on  $\xi$  and  $\eta_i$ . (Left) Scatter plot of  $\zeta$  with respect to  $\xi$  and  $\eta$ . (Right) Plot of  $\zeta$  as a function of  $\xi$  and  $\eta$  given in eq. (3.29).

scatter plot in Fig 3.1,  $\zeta_i$  depends on  $\xi_i$  and  $\eta_i$ . In fact, it can be shown that value of  $\zeta_i$  is bounded from above and below given by,

$$\frac{1}{2} \left( 1 - \sqrt{1 - \xi^2} \sqrt{1 - \eta_i^2} \right) \leq \zeta_i \leq \frac{1}{2} \left( 1 + \sqrt{1 - \xi^2} \sqrt{1 - \eta_i^2} \right) \quad (3.29)$$

where  $i \in \{1, 2\}$ ,  $|\xi| \leq 1$  and  $\eta_i \in [0, 1]$ . As can be seen in Fig 3.1, the dependence of  $\zeta_i$  on  $\xi$  and  $\eta_i$  depicted in the scatter plot is captured exactly in eq. (3.29). Substituting the

above defined gauge orbit variables in eq. (3.28),

$$\begin{aligned}
 V_4 &= r^4 \cos^4 \theta \left( \lambda_1 + 2\lambda_2 \xi^2 \cos 2\omega + \lambda_3 \xi^2 + 2\lambda_4 \xi \cos \omega \right) \\
 &\quad + r^4 \sin^4 \theta \left( \rho_1 \left( \cos^4 \gamma + \sin^4 \gamma \right) + \rho_2 \left( \eta_1^2 \sin^4 \gamma + \eta_2^2 \cos^4 \gamma \right) \right. \\
 &\quad + \rho_3 \cos^2 \gamma \sin^2 \gamma + 2\rho_4 \eta_1 \eta_2 \cos(\theta_1 - \theta_2) \cos^2 \gamma \sin^2 \gamma \left. \right) \\
 &\quad + \left( \alpha_1 + \alpha_3 (\zeta_1 \cos^2 \gamma + \zeta_2 \sin^2 \gamma) \right) r^4 \cos^2 \theta \sin^2 \theta \\
 &\equiv r^4 \left( \cos^4 \theta f(\lambda, \xi, \omega) + \sin^4 \theta g(\rho, \gamma, \eta_{1,2}, \theta_{1,2}) + h(\alpha, \gamma, \zeta_{1,2}) \cos^2 \theta \sin^2 \theta \right) \quad (3.30)
 \end{aligned}$$

From copositivity criteria, it implies :

$$f(\lambda, \xi, \omega) > 0$$

$$g(\rho, \gamma, \eta_{1,2}, \theta_{1,2}) > 0$$

$$h(\alpha, \gamma, \zeta_{1,2}) + 2\sqrt{f(\lambda, \xi, \omega) g(\rho, \gamma, \eta_{1,2}, \theta_{1,2})} > 0$$

These conditions should hold for all values of  $(\xi, \omega, \gamma, \eta_{1,2}, \theta_{1,2}, \zeta_{1,2})$ . First two conditions are (3.14) and (3.20), evaluated in previous sections. For 2nd and 3rd condition, minimum of  $\theta_{1,2}$  can again be absorbed in the sign of  $\lambda_4$ .

$$\alpha_1 + \alpha_3 (\zeta_1 \cos^2 \gamma + \zeta_2 \sin^2 \gamma) + \sqrt{f(\lambda, \xi, \omega) g(\rho, \gamma, \eta_{1,2})} > 0 \quad (3.31)$$

where  $f$  and  $g$  can be written as :

$$f \equiv \lambda_1 + 2\lambda_2 \xi^2 \cos 2\omega + \lambda_3 \xi^2 + 2\lambda_4 \xi \cos \omega$$

$$g \equiv \frac{1}{(1 + \tan^2 \gamma)^2} \left( \tan^4 \gamma (\rho_1 + \rho_2 \eta_2^2) + \tan^2 \gamma (\rho_3 - 2|\rho_4| \eta_1 \eta_2) + \rho_1 + \rho_2 \eta_1^2 \right) \quad (3.32)$$

We now turn to symmetries to simplify further and reduce minimizing variables. We first

try to minimize condition  $g(\rho, \gamma, \eta_{1,2})$  again but using symmetry arguments as an example. Note that  $g$  is symmetric under the following operation:

$$\cos \gamma \leftrightarrow \sin \gamma, \quad \eta_1 \leftrightarrow \eta_2$$

Thus, the minimum occurs at  $\cos \gamma = \sin \gamma$  and  $\eta_1 = \eta_2$ , which yields :

$$g \equiv \frac{\rho_3 + 2\rho_1 + 2(\rho_2 - |\rho_4|)\eta_1^2}{4}$$

Plugging in the endpoints for  $\eta_1$ , we obtain two conditions :

$$g = \left\{ \frac{\rho_3 + 2\rho_1}{4}, \frac{\rho_3 + 2\rho_1 + 2(\rho_2 - |\rho_4|)}{4} \right\}$$

Previously, we minimized the condition for  $\cos \gamma = \sin \gamma$  i.e.  $\tan \gamma = 1$ . Now, we will minimize  $g$  for the endpoint,  $\tan \gamma = 0$ . Using the symmetry operations used above, it can be shown that minimizing the condition for other endpoint  $\tan \gamma = \infty$  is equivalent to case for  $\tan \gamma = 0$ . For this case, condition takes the form:

$$g \equiv \rho_1 + 2\rho_2\eta_1^2$$

Again plugging in the endpoints for  $\eta_1$ , we obtain two conditions. We obtain a total of 4 conditions for minimizing  $g$ , which exactly matches the conditions derived in sec. 3.4.2.

$$g : \left\{ \rho_1, \rho_1 + \rho_2, \frac{\rho_3 + 2\rho_1}{4}, \frac{\rho_3 - 2|\rho_4| + 2(\rho_1 + \rho_2)}{4} \right\} \quad (3.33)$$

Note that the 3rd condition is symmetric under the following operation:

$$\zeta_1 \leftrightarrow \zeta_2, \quad \cos \gamma \leftrightarrow \sin \gamma, \quad \eta_1 \leftrightarrow \eta_2$$

Thus, the function takes its minimum value inside the gauge orbit space when:

$$\zeta_1 = \zeta_2, \quad \cos \gamma = \sin \gamma, \quad \eta_1 = \eta_2$$

Using the above symmetry arguments, the form of the 3rd condition is :

$$\alpha_1 + \alpha_3 \zeta_1 + \sqrt{f(\lambda, \xi, \omega) (\rho_3 + 2\rho_1 + 2(\rho_2 - |\rho_4|)\eta_1^2)} > 0 \quad (3.34)$$

For this case, the condition is monotonic in  $\zeta_1$  &  $\eta_1^2$  and are trivially minimized at endpoints of their range. This implies for  $\alpha_3 < 0$ , the most constraining condition corresponds to  $\zeta_1 = \zeta_1^{max}$  and  $\zeta_1 = \zeta_1^{min}$  for  $\alpha_3 > 0$ .

$$\zeta_i^{max} = \frac{1}{2} \left( 1 + \sqrt{1 - \xi^2} \sqrt{1 - \eta_i^2} \right), \quad \zeta_i^{min} = \frac{1}{2} \left( 1 - \sqrt{1 - \xi^2} \sqrt{1 - \eta_i^2} \right)$$

The minimum of  $f$  has been evaluated in a previous section. This also yields corresponding value of  $\xi$  and  $\eta_1$  that determines the value of  $\zeta_i^{max}$  and  $\zeta_i^{min}$ . This yields a set of 10 different conditions.

Consider an example for above discussion. Let us assume  $f(\lambda, \xi, \omega)$  minimizes for  $\xi = \frac{|\lambda_4|}{2\lambda_2 + \lambda_3}$  and  $\eta_1 = 0$ , then  $\zeta_1$  is given by :

$$\Rightarrow \zeta_1 = \frac{1}{2} \left( 1 \pm \sqrt{1 - \left( \frac{|\lambda_4|}{2\lambda_2 + \lambda_3} \right)^2} \right)$$

then the required inequality to be checked for vacuum stability becomes :

$$\alpha_1 + \frac{\alpha_3}{2} \left( 1 \pm \sqrt{1 - \frac{\lambda_4^2}{(2\lambda_2 + \lambda_3)^2}} \right) + \sqrt{\left( \lambda_1 - \frac{\lambda_4^2}{2\lambda_2 + \lambda_3} \right) (\rho_3 + 2\rho_1)} > 0$$

We also need to minimize the 3rd condition for the edge surface of  $\tan \gamma$ . For the case

$\tan \gamma = 0$ , 3rd condition takes the form:

$$\alpha_1 + \alpha_3 \zeta_1 + 2\sqrt{f(\lambda, \xi, \omega) (\rho_1 + \rho_2 \eta_1^2)} > 0$$

The above condition can be minimized similarly as in case of  $\tan \gamma = 1$ , yielding a total of another 10 conditions.

Thus, minimizing the 3rd condition yields a set of 20 inequalities to be checked. We have finally derived all conditions required for the vacuum stability of the LRSM. The complete set of these necessary and sufficient conditions are collected below :

## Analytic Conditions for Vacuum Stability in LRSM

$$\begin{aligned}
 f > 0 : & \begin{cases} \lambda_1 \\ \left( \lambda_1 - \frac{\lambda_4^2}{2\lambda_2 + \lambda_3} \right) \iff 2\lambda_2 + \lambda_3 > |\lambda_4| \\ (\lambda_1 + \lambda_3 + 2(\lambda_2 - |\lambda_4|)) \\ \left( \lambda_1 + \lambda_3 - 2\lambda_2 - \frac{\lambda_4^2}{4\lambda_2} \right) \iff |4\lambda_2| > |\lambda_4| \end{cases} \\
 g > 0 : & \left\{ \rho_1, \rho_1 + \rho_2, \frac{\rho_3 + 2\rho_1}{4}, \frac{\rho_3 - 2|\rho_4| + 2(\rho_1 + \rho_2)}{4} \right\} \quad (3.35) \\
 & \alpha_1 + 2\sqrt{\lambda_1\rho_1} > 0 \\
 & \alpha_1 + \alpha_3 + 2\sqrt{\lambda_1\rho_1} > 0 \\
 & \alpha_1 + \frac{\alpha_3}{2} + 2\sqrt{\lambda_1(\rho_1 + \rho_2)} > 0 \\
 & \alpha_1 + \sqrt{\lambda_1(\rho_3 + 2\rho_1)} > 0 \\
 & \alpha_1 + \alpha_3 + \sqrt{\lambda_1(\rho_3 + 2\rho_1)} > 0 \\
 & \alpha_1 + \frac{\alpha_3}{2} + \sqrt{\lambda_1(\rho_3 - 2|\rho_4| + 2(\rho_1 + \rho_2))} > 0 \\
 & \alpha_1 + \frac{\alpha_3}{2} \left( 1 \pm \sqrt{1 - \frac{\lambda_4^2}{(2\lambda_2 + \lambda_3)^2}} \right) + 2\sqrt{\left( \lambda_1 - \frac{\lambda_4^2}{2\lambda_2 + \lambda_3} \right) \rho_1} > 0 \\
 & \alpha_1 + \frac{\alpha_3}{2} + 2\sqrt{\left( \lambda_1 - \frac{\lambda_4^2}{2\lambda_2 + \lambda_3} \right) (\rho_1 + \rho_2)} > 0 \\
 & \alpha_1 + \frac{\alpha_3}{2} \left( 1 \pm \sqrt{1 - \frac{\lambda_4^2}{(2\lambda_2 + \lambda_3)^2}} \right) + \sqrt{\left( \lambda_1 - \frac{\lambda_4^2}{2\lambda_2 + \lambda_3} \right) (\rho_3 + 2\rho_1)} > 0 \\
 & \alpha_1 + \frac{\alpha_3}{2} + \sqrt{\left( \lambda_1 - \frac{\lambda_4^2}{2\lambda_2 + \lambda_3} \right) (\rho_3 - 2|\rho_4| + 2(\rho_1 + \rho_2))} > 0 \\
 & \alpha_1 + \frac{\alpha_3}{2} + 2\sqrt{\left( \lambda_1 + \lambda_3 - 2\lambda_2 - \frac{\lambda_4^2}{4\lambda_2} \right) \mathbf{Min}(g)} > 0 \\
 & \alpha_1 + \frac{\alpha_3}{2} + 2\sqrt{(\lambda_1 + \lambda_3 + 2(\lambda_2 - |\lambda_4|)) \mathbf{Min}(g)} > 0
 \end{aligned}$$

For using these conditions, we first ensure  $f$  and  $g$  should be strictly positive at all minima.

For some conditions in  $f$ , we have the following structure  $p \iff q$ . This implies condition  $p$  only needs to be checked if and only if condition  $q$  is true. We then check rest of the conditions based on minimum value of  $f$  and  $g$ .

### 3.5 Symmetry Breaking and Desirable Vacuum

A BFB potential does not necessarily leads to correct symmetry breaking yielding the correct ground state of the Higgs potential. Recently, some useful conditions (though not necessary) for a good vacuum in the left-right model were derived for a limited parameter space in [122]. Gauge-independent criteria to obtain a good vacuum was also proposed.

$$\langle \Phi \rangle \neq 0$$

$$\det \langle \Delta_R \rangle = \det \langle \Delta_L \rangle = 0$$

$$\langle \Delta_R \rangle \neq \langle \Delta_L \rangle$$

The first condition leads to non-zero expectation for Higgs VEV in the Standard Model. The second condition is required for  $U(1)_{em}$  not to be broken. The third condition is required for broken parity at low energies. Although reference [122] specifies 4 conditions for a good vacuum but effectively only 3 conditions are required. As their condition  $\langle \Delta_R \rangle \neq 0$  or  $\langle \Delta_L \rangle \neq 0$  for good vacuum is contained in  $\langle \Delta_R \rangle \neq \langle \Delta_L \rangle$ .

In this section, we derive some useful conditions for scalar potential to exhibit correct spontaneous symmetry breaking (SSB) and specify the gauge-independent criteria for correct vacuum in more general form. Using the VEV structure of the scalar fields eq. (3.10) in the

general scalar potential eq. (3.11),

$$\begin{aligned}
 V = & -\frac{(\kappa_1^2 + \kappa_2^2)}{2}\mu_1^2 - 2\kappa_1\kappa_2\mu_2^2 \cos(\theta_2) - \mu_3^2 (v_L^2 + v_R^2) + \frac{(\kappa_1^2 + \kappa_2^2)^2}{4}\lambda_1 \\
 & + 2\kappa_1^2\kappa_2^2\lambda_2 \cos(2\theta_2) + \kappa_1\kappa_2 (\kappa_1^2 + \kappa_2^2) \lambda_4 \cos(\theta_2) + \kappa_1^2\kappa_2^2\lambda_3 \\
 & + \rho_1 (v_L^4 + v_R^4) + \rho_3 v_L^2 v_R^2 \\
 & + \alpha_1 \frac{(\kappa_1^2 + \kappa_2^2)}{2} (v_L^2 + v_R^2) + \alpha_3 \frac{\kappa_2^2}{2} (v_L^2 + v_R^2)
 \end{aligned} \quad (3.36)$$

For boundedness, the quartic part of the potential can be written as:

$$V_4 \equiv r^4 \left( f_{SSB}(\lambda, \xi, \omega) \cos^4 \theta + g_{SSB}(\rho, \gamma, \theta_{1,2}) \sin^4 \theta + h_{SSB}(\alpha, \gamma, \zeta_{1,2}) \cos^2 \theta \sin^2 \theta \right) \quad (3.37)$$

where parametrizing variables are defined in accordance with section 3.4.3. To obtain necessary and sufficient conditions for correct symmetry breaking, the minimum from the potential  $V_{SSB}$  should be deeper than the one obtained from the general potential. Using eq. (3.9), the required condition can be written as :

$$-\frac{g\mu_1^4 - h\mu_1^2\mu_2^2 + f\mu_2^4}{4fg - h^2} > -\frac{g_{SSB}\mu_1^4 - h_{SSB}\mu_1^2\mu_2^2 + f_{SSB}\mu_2^4}{4f_{SSB}g_{SSB} - h_{SSB}^2} \quad (3.38)$$

The above relation needs to be minimized for the entire gauge orbit parameter space. Due to the non-linearity of the orbit variables, this is not analytically tractable.

The important observation in this work is that the conditions sufficient for a general potential to lead to a good vacuum after SSB can be obtained by requiring VEV aligned scalar potential to dominate the general scalar potential i.e.  $V \geq V_{SSB}$ . This is a stronger condition than eq. (3.38) and using eq. (3.30), (3.37) can be written as :

$$(f - f_{SSB}) \cos^4 \theta + (g - g_{SSB}) \sin^4 \theta + (h - h_{SSB}) \cos^2 \theta \sin^2 \theta \geq 0 \quad (3.39)$$

Thus, for VEV structure in eq. (3.10) to be the global minima of the theory, following

conditions are required :

$$f \geq f_{SSB}, \quad g \geq g_{SSB} \quad (3.40)$$

$$h - h_{SSB} + 2\sqrt{(f - f_{SSB})(g - g_{SSB})} \geq 0 \quad (3.41)$$

It is also required that  $V_{SSB}$  exhibits stable vacuum, which implies :

$$f_{SSB} > 0, \quad g_{SSB} > 0, \quad h_{SSB} + 2\sqrt{f_{SSB} g_{SSB}} > 0 \quad (3.42)$$

We begin by noticing that in eq. (3.36),  $f_{SSB}$  takes the same form as  $f(\lambda, \xi, \omega)$  for the general potential. VEV condition  $\langle \Phi \rangle \neq 0$  translates to  $r \cos \theta \neq 0$ . It is satisfied as long as  $\lambda$  sector is bounded from below. This implies all the conditions found for  $\lambda$  sector are required for existence of a good vacuum. It also implies  $f = f_{SSB}$  trivially satisfies condition for correct symmetry breaking. On the other hand,  $g_{SSB}$  has  $\eta_{1,2} = 0$ .

$$\text{Tr}[\langle \Delta_L \rangle \langle \Delta_L \rangle] = 0 \quad \implies \quad \eta_1 = 0$$

$$\text{Tr}[\langle \Delta_R \rangle \langle \Delta_R \rangle] = 0 \quad \implies \quad \eta_2 = 0$$

Therefore, coefficients of  $\rho_2$  and  $\rho_4$  vanish leading to following form of  $g$  (See eq. (3.32)):

$$g_{SSB} \equiv \frac{1}{(1 + \tan^2 \gamma)^2} (\rho_1 \tan^4 \gamma + \rho_3 \tan^2 \gamma + \rho_1)$$

The minimum for this expression occurs at  $\tan^2 \gamma = 0$  or  $1$ . We require  $\langle \Delta_L \rangle < \langle \Delta_R \rangle$  which can be easily shown equivalent to :

$$\text{Tr}[\langle \Delta_L \rangle \langle \Delta_L^\dagger \rangle] < \text{Tr}[\langle \Delta_R \rangle \langle \Delta_R^\dagger \rangle]$$

So according to the chosen parametrization, the preferred minima is  $\tan^2 \gamma = 0$ . We know from sec. 3.2.2, condition with less positive value dominates the minima. Thus, this condition should dominate over the other minima i.e  $\tan^2 \gamma = 1$  in  $g_{SSB}$ . Thus, we require

$$\frac{\rho_3 + 2\rho_1}{4} \geq \rho_1 \implies \rho_3 - 2\rho_1 \geq 0$$

After requiring the internal structure of the VEV alignment, we want eq. (3.40) to hold i.e.  $g \geq g_{SSB}$  should hold. The minimum of  $g_{SSB}$  occurs for  $\rho_1 > 0$ . This condition should dominate other possible minima of the general potential. Using minimum conditions from eq. (3.33),

$$\rho_1 + \rho_2 \geq \rho_1 \implies \rho_2 \geq 0$$

$$\frac{\rho_3 + 2\rho_1}{4} \geq \rho_1 \implies \rho_3 - 2\rho_1 \geq 0$$

$$\frac{\rho_3 - 2|\rho_4| + 2(\rho_1 + \rho_2)}{4} \geq \rho_1 \implies |\rho_4| \leq \frac{\rho_3 - 2\rho_1}{2} + \rho_2$$

Since  $f = f_{SSB}$ , eq. (3.41) implies  $h \geq h_{SSB}$ .

$$\alpha_1 + \alpha_3(\zeta_1 \cos^2 \gamma + \zeta_2 \sin^2 \gamma) \geq \alpha_1 + \alpha_3(\zeta_1^{SSB} \cos^2 \gamma + \zeta_2^{SSB} \sin^2 \gamma)$$

Note that since  $\eta_i = 0$  for  $V_{SSB}$ ,  $\zeta_i \neq \zeta_i^{SSB}$ . The condition above is monotonic in  $\zeta$ 's and the endpoints of their range can be substituted depending on the sign of  $\alpha_3$ .

$$\frac{\alpha_3}{2} \left( 1 - \mathbf{Sgn}(\alpha_3) \sqrt{1 - \xi^2} \sqrt{1 - \eta_i^2} \right) \geq \frac{\alpha_3}{2} \left( 1 - \mathbf{Sgn}(\alpha_3) \sqrt{1 - \xi^2} \right)$$

As can be seen directly, the above condition holds true for all  $\xi$ ,  $\eta$  and  $\alpha_3$ . Similarly, for vacuum stability condition to hold true, we require :

$$\alpha_1 + \frac{\alpha_3}{2} \zeta + 2\sqrt{f(\lambda, \xi, \omega)} \rho_1 > 0 \tag{3.43}$$

where,  $\zeta = (1 - \text{Sgn}(\alpha_3)\sqrt{1 - \xi_*^2})$  and  $\xi_*$  equals the value of  $\xi$  that minimizes  $f(\lambda, \xi, \omega)$ . The minimization of  $f$  has been covered in sec. 3.4.1.

For non-zero field values to be the global minimum (refer sec. 3.2.2), we also require eq. (3.6),(3.7) and (3.8) to hold. For non-zero  $\langle \Phi \rangle$  and  $\langle \Delta_R \rangle$ , we require :

$$\begin{aligned} 2 \text{Min}[f_{SSB}]\mu_3^2 - \text{Min}[h_{SSB}]\bar{\mu}_1^2 &> 0 \\ 2 \text{Min}[g_{SSB}]\bar{\mu}_1^2 - \text{Min}[h_{SSB}]\mu_3^2 &> 0 \end{aligned} \quad (3.44)$$

where,

$$\bar{\mu}_1^2 = \mu_1^2 + 2\sigma\mu_2^2, \quad \sigma = \xi \cos \omega$$

and

$$2\sqrt{\text{Min}[f_{SSB}] \text{Min}[g_{SSB}]} - \|\text{Min}[h_{SSB}]\| > 0$$

Here, expression for  $\bar{\mu}_1^2$  has been obtained by using parametrization from sec. (3.4.1) to relevant mass-squared terms in the scalar potential. Thus, the complete set of conditions sufficient to obtain a correct vacuum after SSB in left-right symmetric model are stated below:

## Analytic Conditions for Symmetry Breaking to Correct Vacuum

$$f_{SSB} > 0 : \begin{cases} \lambda_1 > 0, \quad \xi = \sigma = 0, \\ \left(\lambda_1 - \frac{\lambda_4^2}{2\lambda_2 + \lambda_3}\right) > 0 \iff 0 < \xi = \frac{|\lambda_4|}{2\lambda_2 + \lambda_3} < 1, \quad \sigma = -\frac{\lambda_4}{2\lambda_2 + \lambda_3}, \\ (\lambda_1 + \lambda_3 + 2(\lambda_2 - |\lambda_4|)) > 0, \quad \xi = 1, \quad \sigma = -\mathbf{Sgn}(\lambda_4), \\ \left(\lambda_1 + \lambda_3 - 2\lambda_2 - \frac{\lambda_4^2}{4\lambda_2}\right) > 0 \iff |4\lambda_2| > |\lambda_4|, \quad \xi = 1, \quad \sigma = -\frac{\lambda_4}{4\lambda_2}, \end{cases}$$

$$\rho_1 > 0, \quad \rho_2 > 0, \quad \rho_3 > 2\rho_1, \quad |\rho_4| < \frac{\rho_3 - 2\rho_1}{2} + \rho_2$$

$$\alpha_1 + 2\sqrt{\lambda_1\rho_1} > 0$$

$$\alpha_1 + \alpha_3 + 2\sqrt{\lambda_1\rho_1} > 0$$

$$\alpha_1 + \frac{\alpha_3}{2} \left(1 \pm \sqrt{1 - \frac{\lambda_4^2}{(2\lambda_2 + \lambda_3)^2}}\right) + 2\sqrt{\left(\lambda_1 - \frac{\lambda_4^2}{2\lambda_2 + \lambda_3}\right)\rho_1} > 0$$

$$\alpha_1 + \frac{\alpha_3}{2} + 2\sqrt{\left(\lambda_1 + \lambda_3 - 2\lambda_2 - \frac{\lambda_4^2}{4\lambda_2}\right)\rho_1} > 0$$

$$\alpha_1 + \frac{\alpha_3}{2} + 2\sqrt{(\lambda_1 + \lambda_3 + 2(\lambda_2 - |\lambda_4|))\rho_1} > 0$$

$$\bar{\mu}_1^2 = \mu_1^2 + 2\sigma\mu_2^2$$

$$2\sqrt{\mathbf{Min}[f_{SSB}]\rho_1} - \left\| \alpha_1 + \frac{\alpha_3}{2} \left(1 - \mathbf{Sgn}(\alpha_3)\sqrt{1 - \xi^2}\right) \right\| > 0$$

$$2\mathbf{Min}[f_{SSB}]\mu_3^2 - \left[ \alpha_1 + \frac{\alpha_3}{2} \left(1 - \mathbf{Sgn}(\alpha_3)\sqrt{1 - \xi^2}\right) \right] \bar{\mu}_1^2 > 0$$

$$2\rho_1\bar{\mu}_1^2 - \left[ \alpha_1 + \frac{\alpha_3}{2} \left(1 - \mathbf{Sgn}(\alpha_3)\sqrt{1 - \xi^2}\right) \right] \mu_3^2 > 0$$

For using these conditions, we first ensure  $f_{SSB}$  should be strictly positive at all minima. For some conditions in  $f$ , we have the following structure  $p \Leftarrow q$ ,  $\xi = \text{value1}$ ,  $\sigma = \text{value2}$ . This implies condition  $p$  only needs to be checked if and only if condition  $q$  is true. It also yields a corresponding values of  $\xi$  and  $\sigma$  to be used in the last three conditions. We then check rest of the conditions based on minimum value of  $f_{SSB}$ .

We would like to assert the usefulness of these conditions. Using the above conditions not only ensures the boundedness of the potential but also gives the minimum with desired VEV alignment. The results derived here are general in nature and reduce to those obtained in [122] for their choice of parameters<sup>19</sup>. In [122], their derived conditions for good vacuum are asserted to be only sufficient but not necessary and same holds for our case. Even with good vacuum conditions, they do not get a correct vacuum in their numerical study at all times. This possibly happens due to the parameter range of non-zero  $\alpha_i$ 's in their numerical analysis that leads to the violation of condition on mass-squares  $\mu^2$  derived in this work.

Given the treatment here, we can also generalize the gauge-independent conditions for correct vacuum in the left-right symmetric model as:

$$\begin{aligned}
 \text{Tr}[\langle\Phi\rangle\langle\Phi\rangle] &\neq 0 \\
 \text{Tr}[\langle\Delta_L\rangle\langle\Delta_L\rangle] &= \text{Tr}[\langle\Delta_R\rangle\langle\Delta_R\rangle] = 0 \\
 \text{Tr}[\langle\Delta_L\rangle\langle\Delta_L^\dagger\rangle] &< \text{Tr}[\langle\Delta_R\rangle\langle\Delta_R^\dagger\rangle]
 \end{aligned} \tag{3.45}$$

---

<sup>19</sup> Setting  $\lambda_{2,4}$ ,  $\rho_4$ ,  $\alpha_i$ 's and  $\beta_i$ 's to 0

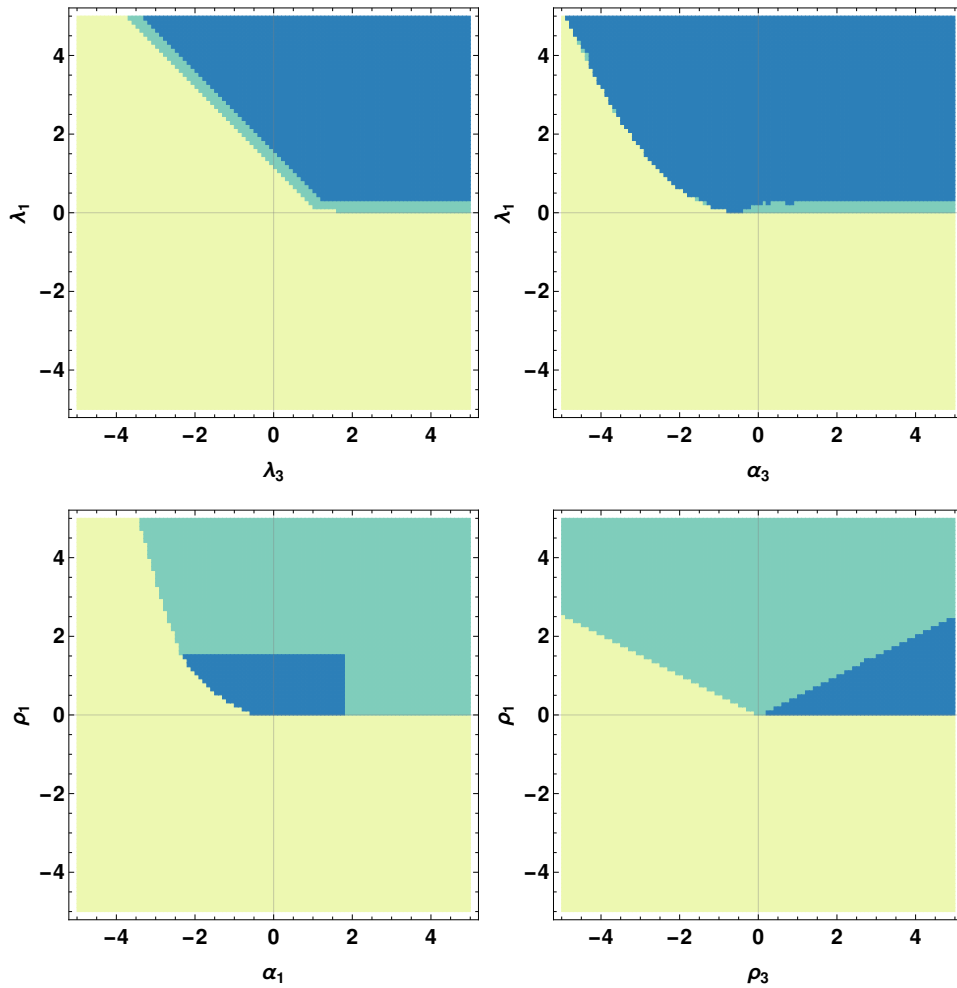


Fig. 3.2: Numerical minimization of the scalar potential of LRSM. The figures are plotted for different pair of quartic couplings with values ranging from  $(-5, 5)$  and with grid pixel size of  $0.1 \times 0.1$ , with other quartics being set according to benchmark in Sec 3.6. The yellow region indicates an unbounded potential. The green region indicates the existence of a global minimum but not with the required VEV structure. The blue region indicates the existence of a global minimum with the required VEV structure.

## 3.6 Numerical Comparison

We use the following benchmark values to study the numerical minimization of the potential and its agreement with the conditions obtained in this work.

$$\begin{aligned}\mu_1^2, \mu_2^2, \mu_3^2 &\equiv (1, 0.25, 1) \text{ TeV}^2 \\ \lambda_1, \lambda_2, \lambda_3, \lambda_4 &\equiv (1, 0.5, 3, -0.5) \\ \rho_1, \rho_2, \rho_3, \rho_4 &\equiv (1, 0.5, 3, -0.5) \\ \alpha_1, \alpha_2, \alpha_3 &\equiv (0.5, 0, 0.5) \\ \beta_1, \beta_2, \beta_3 &\equiv (0, 0, 0)\end{aligned}$$

In fig 3.2, the potential is minimized for a pair of quartics with other couplings set according to the benchmark values. The minimization was performed with the `NMinimize` function with `NelderMead`, `DifferentialEvolution` and `SimulatedAnnealing` method in `Mathematica`. The pixel size of the grid is  $0.1 \times 0.1$ . With each parameter running from  $(-5, 5)$  yields a  $50 \times 50$  matrix. The yellow region has unbounded minima that violates the BFB conditions. The green region is bounded and has a global minimum but with an incorrect VEV alignment. In blue region, the potential undergoes correct sponataneous symmetry breaking to the desired VEV structure of the vacuum. This vacuum is stable and is phenomenologically viable.

We would like to assert that the results shown in fig 3.2 are in complete agreement with the vacuum stability and correct vacuum conditions obtained in this work. It should also be noted that although conditions to exhibit SSB to correct vaccum were derived using a stronger condition, they match results from numerical minimization remarkably.

## 3.7 Renormalization Group Equations Analysis

In a general case of randomly selected initial values, the evolution of quartic couplings according to the renormalization group equations (RGEs) for the model can lead to their running outside the allowed parameter space. Constraining the running of the quartic couplings to satisfy the vacuum stability conditions upto a certain high energy scale ensures the boundedness of the potential. In this section, we discuss some more constraints on the quartic couplings before we present an example study to demonstrate the usefulness of the conditions derived earlier.

### 3.7.1 Mass Spectrum & Unitarity Bounds

Along with BFB conditions and correct symmetry breaking, it's necessary to check that the potential exhibits a physical scalar mass spectrum. The scalar mass spectrum of the LRSM has 14 physical particles. It includes 8 electrically neutral<sup>20</sup>, four singly-charged and four doubly-charged Higgs bosons. The scalar mass spectrum for LRSM is given below[141, 115]:

$$\begin{aligned}
 M_{H_0^0}^2 &= 2 \left( \lambda_1 - \frac{\alpha_1^2}{4\rho_1} \right) \kappa_+^2, \\
 M_{H_2^\pm}^2 \simeq M_{A_1^0}^2 \simeq M_{H_1^0}^2 &= \frac{1}{2} \alpha_3 v_R^2, \\
 M_{H_2^0}^2 &= 2\rho_1 v_R^2, \\
 M_{H_1^{\pm\pm}}^2 \simeq M_{H_1^\pm}^2 \simeq M_{A_2^0}^2 = M_{H_3^0}^2 &= \frac{1}{2} (\rho_3 - 2\rho_1) v_R^2, \\
 M_{H_2^{\pm\pm}}^2 &= 2\rho_2 v_R^2 + \frac{1}{2} \alpha_3 \kappa_+^2
 \end{aligned}$$

where  $\kappa_+^2 = \kappa_1^2 + \kappa_2^2$ . The lightest neutral scalar  $M_{H_0^0}$  that only depends on the VEV of bidoublet  $\Phi$  is identified as the SM Higgs boson. We have taken the best fit value of  $M_{H_0^0} = m_h = 125$  GeV [121].  $H_1^0$ ,  $A_1^0$  and  $H_2^\pm$  are the CP-even and CP-odd neutral components and the two singly-charged scalars respectively from the bidoublet  $\Phi$ .  $H_2^0$ ,  $H_3^0$ ,  $A_2^0$ ,  $H_1^\pm$ ,  $H_1^{\pm\pm}$

<sup>20</sup> It contains two massless neutral degrees of freedom absorbed as the longitudinal polarization modes of physical gauge bosons.

and  $H_2^{\pm\pm}$  are the two CP-even and one CP-odd neutral components, 2 singly-charged and 4 doubly-charged scalars respectively from the triplets  $\Delta_L$  and  $\Delta_R$ .

There are strong experimental bounds on most scalar masses in LRSM. This places lower bounds on the allowed values of corresponding quartic couplings in the potential as a function of the breaking scale. The heavy neutral scalars  $H_1^0, A_1^0$  can contribute to  $B_d - \bar{B}_d, B_s - \bar{B}_d$  and  $K_0 - \bar{K}_0$  mixings due to presence of tree-level FCNC couplings to the SM quarks in LRSM. Thus, there are stringent limits on their masses from the FCNC constraints [52, 53, 54].

$$M_{H_1^0, A_1^0} > 15 \text{ TeV}$$

The cleanest detection channel for doubly-charged Higgs bosons is its decay to same-sign charged dilepton pairs. The current bounds on mass limits are from LHC 13 TeV run data [118, 142], which largely depends on charged lepton flavors involved in the decay process :

$$M_{H_1^{\pm\pm}} \gtrsim (770 - 870) \text{ GeV} \quad M_{H_2^{\pm\pm}} \gtrsim (660 - 760) \text{ GeV}$$

Parameter space for quartic couplings can be further squeezed by requiring tree-level unitarity to be preserved in a variety of scattering process. We consider the unitarity bounds only from 2-body scalar scattering processes [115], given below :

$$\begin{aligned} \lambda_1 &< 4\pi/3, \quad (\lambda_1 + 4\lambda_2 + 2\lambda_3) < 4\pi, \\ (\lambda_1 - 4\lambda_2 + 2\lambda_3) &< 4\pi, \\ \lambda_4 &< 4\pi/3, \\ \alpha_1 &< 8\pi, \quad \alpha_2 < 4\pi, \quad (\alpha_1 + \alpha_3) < 8\pi, \\ \rho_1 &< 4\pi/3, \quad (\rho_1 + \rho_2) < 2\pi, \quad \rho_2 < 2\sqrt{2}\pi, \\ \rho_3 &< 8\pi, \quad \rho_4 < 2\sqrt{2}\pi \end{aligned}$$

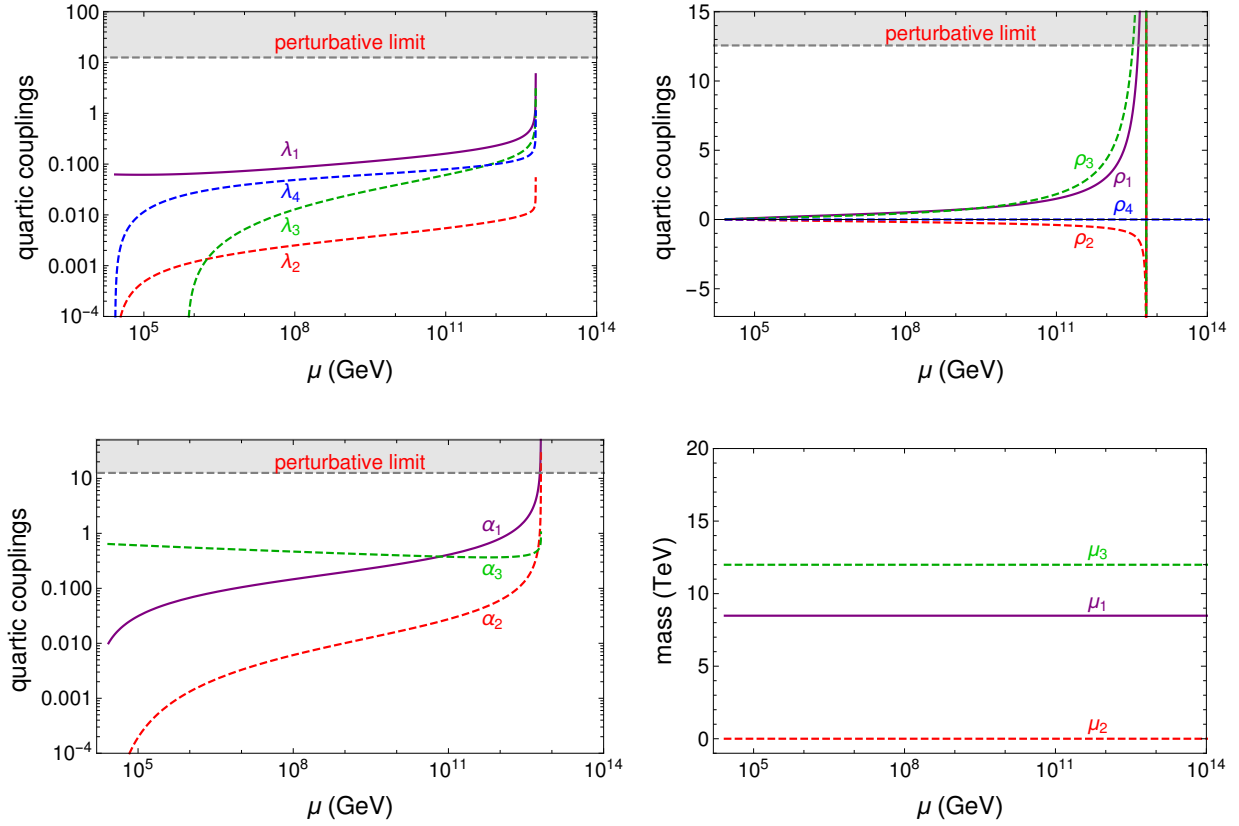


Fig. 3.3: RG running of the quartic couplings for the benchmark in sec 3.7.2 from  $v_R = 26.8$  TeV, with  $r_g = \frac{g_R}{g_L} = 1.2$ .

### 3.7.2 Example Study

We use the following benchmark values for RGE running of the quartic couplings.

$$\begin{aligned}
 \mu_1^2, \mu_2^2, \mu_3^2 &\equiv ((8.48)^2, 0, (11.99)^2) \text{ TeV}^2 \\
 \lambda_1, \lambda_2, \lambda_3, \lambda_4 &\equiv (0.0625, 0, 0, 0) \\
 \rho_1, \rho_2, \rho_3, \rho_4 &\equiv (0.01, 0.0005, 0.0226, 0) \\
 \alpha_1, \alpha_2, \alpha_3 &\equiv (0.01, 0, 0.64) \\
 \beta_1, \beta_2, \beta_3 &\equiv (0, 0, 0)
 \end{aligned} \tag{3.46}$$

The above benchmark is in complete agreement with the current experimental bounds on the scalar masses at the breaking scale.

$$\kappa_+ = \sqrt{\kappa_1^2 + \kappa_2^2} = 246 \text{ GeV}, \quad v_L = 0 \text{ TeV}, \quad v_R = 26.8 \text{ TeV}$$

Most importantly the ground state of the potential exhibits correct VEV structure of the theory at the right-handed breaking scale  $v_R$ . This is evident as the benchmark eq. (3.46) satisfies conditions derived for SSB to correct vacuum.

We now have a complete set of initial values and the system of RGE's at one-loop level for the LRSM [143, 115, 10, 144]. We run the system from the breaking scale  $v_R$  to the GUT scale while checking vacuum stability, perturbativity and unitarity bounds [114, 10]. The results are shown in fig 3.3. It can be seen that quartic couplings hit the Landau pole at a scale lower than GUT scale  $10^{12}$  GeV. Although the quartic couplings respects the vacuum stability conditions and unitarity bounds nearly upto the scale just before violating the perturbativity. We observe that most quartic couplings except  $\rho_4$  acquire non-zero values even if set to zero at the breaking scale.  $\rho_2$  is the only quartic that is observed to run to negative values although initialized at a positive value. Also notice that mass-squares  $\mu^2$  don't run appreciably once set at the breaking scale.

It should be mentioned that value of  $r_g = \frac{g_R}{g_L}$  is also crucial to the system of RGEs. Lower values of  $r_g$  for the benchmark in consideration leads to violation of vacuum stability conditions and hence an unbounded potential at high-energies.

## 3.8 Conclusion

We develop a method to extract necessary and sufficient conditions to ensure vacuum stability in LRSM by using the application of gauge orbit parameters in two-Higgs fields case. We also show application of copositivity criteria and its usefulness in simplifying the analysis for vacuum stability.

As it was asserted earlier, only requiring vacuum stability does not ensure SSB to a vacuum which reproduces SM at low-energies. For this purpose, we extend the vacuum stability analysis to help yield conditions sufficient to achieve SSB to the correct vacuum which should be charge conserving and also parity violating at low-energies. These analytic techniques can also be extended to analyze metastability of the vacuum and one-loop effective potentials.

We also compared our analytic results from those generated by numerical minimization of the potential. It is observed that the derived conditions are in excellent agreement with the numerical results. We also show that vacuum stability constraints along with other theoretical constraints (perturbativity, unitarity, scalar mass spectrum) coupled with RGE analysis can help us narrow down the allowed parameter space for the quartic couplings in the potential. A comprehensive study is required to explore the existence of sets of quartic and gauge couplings that obey these combined bounds. This is beyond the scope of this chapter and can be another viable future direction for investigation.

## Chapter 4

# Scalar Non-standard Interactions of Neutrinos<sup>21</sup>

*Young Monk: “Do not try and bend the spoon—that’s impossible.*

*Instead, only try to realize the truth.”*

*Neo: “What truth?”*

*Young Monk: “There is no spoon.”*

- The Matrix (1999)

### 4.1 Introduction

The discovery of neutrino oscillations implies that at least two of the three neutrinos must have small but non-zero masses [51]. The global neutrino oscillation program is now entering a new era, where the known mixing angles and mass-squared differences are being measured with an ever-increasing accuracy. Next-generation of long-baseline oscillation experiments like DUNE are poised to resolve the sub-dominant effects in oscillation data sensitive to the currently unknown oscillation parameters, namely the Dirac  $CP$  phase, sign of the atmospheric mass-squared difference and the octant of the atmospheric mixing angle. These analyses are usually performed within the  $3 \times 3$  neutrino mixing scheme under the assumption that neutrinos interact with matter only through the weak interactions mediated by Stan-

---

<sup>21</sup> This chapter is based on [12]

Standard Model (SM)  $W$  and  $Z$  bosons. On the other hand, the origin of neutrino mass clearly requires some new physics beyond the SM, which often comes with additional non-standard interactions (NSI) of neutrinos with matter fermions (i.e. electrons and/or nucleons). Allowing for these NSI in neutrino production, propagation and/or detection can in principle change the whole picture and crucially affect the interpretation of the experimental data in terms of the relevant  $3 \times 3$  oscillation parameters. It is, therefore, of paramount importance to understand all possible kinds of NSI effects, and to see how large these effects could be, while being consistent with other theoretical and experimental constraints. The study of NSI also opens up the possibility of using neutrino oscillations to probe the origin of neutrino mass.

Following the SM interactions of neutrinos with matter via either charged-current (CC) or neutral-current (NC), which can be written in the form  $(\bar{\nu}_\alpha \gamma^\mu P_L \nu_\alpha)(\bar{f} \gamma_\mu P f)$  after Fierz transformation (with  $f, f' \in \{e, u, d\}$  the matter fermions and  $P \in \{P_L, P_R\}$  the chirality projection operators), NSI induced by either a vector or charged-scalar mediator can be parametrized in terms of vector and axial-vector currents [145]:

$$\mathcal{L}_{\text{eff}}^{\text{V,NC}} = -2\sqrt{2}G_F \sum_{f,P,\alpha,\beta} \varepsilon_{\alpha\beta}^{f,P} (\bar{\nu}_\alpha \gamma^\mu P_L \nu_\beta)(\bar{f} \gamma_\mu P f), \quad (4.1)$$

$$\mathcal{L}_{\text{eff}}^{\text{V,CC}} = -2\sqrt{2}G_F \sum_{f,P,\alpha,\beta} \varepsilon_{\alpha\beta}^{f,P} (\bar{\nu}_\alpha \gamma^\mu P_L \ell_\beta)(\bar{f} \gamma_\mu P f'), \quad (4.2)$$

where  $G_F$  is Fermi's constant and the  $\varepsilon$  terms quantify the size of the new interactions. The vector components of NSI given by Eq. (4.1) and (4.2) affect neutrino oscillations during propagation in matter by providing a new flavor-dependent matter potential. The size of vector NSI is governed by the parameter  $\varepsilon \sim g_X^2 m_W^2 / (g^2 m_X^2)$ , where  $g_X$  and  $m_X$  are respectively the coupling and mass of the mediator  $X$ , and  $g$  is the  $SU(2)_L$  gauge coupling. There are two possibilities to realize experimentally observable vector NSI, which require  $\varepsilon_{\alpha\beta} \gtrsim 10^{-2}$  [146, 147]: (i) heavy mediator case with  $m_X \sim \mathcal{O}(100)$  GeV and  $g_X \sim \mathcal{O}(1)$ ; and (ii) light mediator case with  $m_X \ll m_W$  and  $g_X \ll 1$  such that  $g_X^2/m_X^2 \sim G_F$ , while

evading the low-energy experimental constraints. For concrete ultraviolet (UV)-complete model realizations, see e.g. Ref. [146] for the heavy mediator case and Refs. [148, 149, 150] for the light mediator case. For a recent review on different aspects of vector NSI, see Ref. [151]. For the current global status of the constraints on  $\varepsilon$ , see Ref. [147].

On the other hand, NSI induced by a neutral scalar mediator is no longer composed of vector current as in Eq. (4.1) or (4.2), but a scalar interaction for Dirac neutrinos given by [152]

$$\mathcal{L}_{\text{eff}}^{\text{S}} = \frac{y_f y_{\alpha\beta}}{m_\phi^2} (\bar{\nu}_\alpha \nu_\beta) (\bar{f} f), \quad (4.3)$$

where  $y_f$  and  $y_{\alpha\beta}$  are respectively the Yukawa couplings of the matter fermion and neutrinos to the scalar mediator  $\phi$ . This cannot be converted to vector currents, and hence, does not contribute to the matter potential.<sup>22</sup> Instead, it appears as a medium-dependent correction to the neutrino mass term, with the correction factor  $\Delta m_{\nu,\alpha\beta}$  being inversely proportional to the square of the mediator mass. As we will explicitly show below, large enough scalar NSI effect is possible only for a sufficiently light scalar mediator,<sup>23</sup> since we need  $G_{\text{eff}} \equiv y_f y_{\alpha\beta} / m_\phi^2 \sim 10^{10} G_F$  to have any observable effect for neutrino propagating in Earth with  $\Delta m_\nu \sim \mathcal{O}(0.1 m_\nu)$ . Nevertheless, this could potentially lead to significantly different phenomenological consequences in reactor, solar, atmospheric and accelerator neutrino oscillations, as well as for supernovae and early-universe neutrino interactions.

In this chapter, we derive a general formula for evaluating the scalar NSI of the neutrinos which is applicable to different environments. We perform a systematic study of the scalar NSI in presence of a light scalar mediator  $\phi$ . We consider both Dirac and Majorana neutrino possibilities. The main objective of this chapter is to provide a general field-theoretic derivation of the scalar NSI effect at finite temperature and density, which can be applied to different environments, such as Earth, Sun, supernovae and early Universe. Then we go

---

<sup>22</sup> The same is true for tensor NSI of the form  $(\bar{\nu}_\alpha \sigma^{\mu\nu} \nu_\beta) (\bar{f} \sigma_{\mu\nu} f)$ .

<sup>23</sup> Eq. (4.3) is equally applicable for both light and heavy mediator, since we are dealing with coherent forward scattering of neutrinos with  $q^2 \rightarrow 0$ .

on to derive various constraints on the couplings in Eq. (4.3) as a function of the mediator mass  $m_\phi$  from fifth force experiments, solar and supernova neutrino data, stellar cooling constraints from red giants (RG) and horizontal branch (HB) stars, and big bang nucleosynthesis (BBN). We have considered scalar interactions with electrons and nucleons separately to show the differences in the constraints. We find that the fifth force experiments constrain masses of  $\phi$  below 0.1 eV and couplings up to  $10^{-24}$ . RG/HB stars constrain couplings up to  $10^{-12}$  for nucleons and up to  $10^{-16}$  for electrons coupling to  $\phi$ . Bounds from BBN constrain couplings up to  $10^{-9}$  for the light scalar mediators. After taking into account all these constraints, we conclude that any prospects of observing scalar NSI in Earth matter have been ruled out, while these effects are still measurable with future solar neutrino data, supernova neutrino bursts or in cosmological observations of extra relativistic degrees of freedom.

The rest of the chapter is organized as follows: In Sec. 4.2, we present a general field-theoretic derivation of scalar NSI and discuss various limiting cases that are applicable to Earth, Sun, supernovae and early Universe. In Sec. 4.3, we discuss the long-range force effects of a light scalar. In Sec. 4.4, we summarize the current experimental constraints on the Yukawa couplings relevant for scalar NSI as a function of the mediator mass. In Sec. 4.5, we discuss the thermal mass of the mediator. In Sec. 4.6, we derive a quantum-mechanical bound on the effective in-medium mediator mass. In Sec. 4.7, we present our main results and discussions. In Sec. 4.8, we present a UV-complete model for scalar NSI. Our conclusions are given in Sec. 4.9. In Appendix B.1, we give the detailed derivation of various limiting cases for the scalar NSI discussed in Sec. 4.2. In Appendix B.2, we provide details of the calculation of the neutrino self-energy in neutrino background. In Appendix B.4, we present the calculation for thermal mass of the scalar mediator.

## 4.2 Field theoretic origin of scalar NSI

In this section, we derive expressions for medium-dependent neutrino mass and energy when the neutrinos have scalar NSI with matter fermions in the propagating medium. The results derived here are equally applicable for Dirac and Majorana neutrinos. As we will see later, for observable scalar NSI it will be required that the scalar field is very light, which we assume here. Consider the interaction of fermions  $f$  and Dirac neutrinos  $\nu$  with a light scalar  $\phi$ , with the relevant interaction terms given by the Lagrangian:

$$\mathcal{L} \supset -y_{\alpha\beta}\bar{\nu}_\alpha\phi\nu_\beta - y_f\bar{f}\phi f - m_{\alpha\beta}\bar{\nu}_\alpha\nu_\beta - \frac{m_\phi^2}{2}\phi^2. \quad (4.4)$$

In the case of Majorana neutrinos, the relevant Lagrangian has the form:

$$\mathcal{L} \supset -\frac{y_{\alpha\beta}}{2}\bar{\nu}_\alpha^c\phi\nu_\beta - y_f\bar{f}\phi f - \frac{m_{\alpha\beta}}{2}\bar{\nu}_\alpha^c\nu_\beta - \frac{m_\phi^2}{2}\phi^2. \quad (4.5)$$

We shall focus primarily on the Dirac neutrinos, but essentially all of our results will apply for Majorana neutrinos as well, provided that the normalization of couplings is as in Eq. (4.5). We shall comment on differences when they arise between the two cases.

A neutrino with four-momentum  $p^\mu$  propagating through matter obeys the Dirac equation given by:

$$[\not{p} - \Sigma(p)]\psi = 0. \quad (4.6)$$

In a general medium, the self energy  $\Sigma$  of the neutrino gets modified. We apply real time formalism of field theory at finite temperature and density in our derivations, which is manifestly Lorentz covariant [153]. With pure scalar interactions of the type given in Eqs. (4.4) and (4.5), the neutrino self-energy takes the general form

$$\Sigma(p) = m - (\hat{a}\not{p} + \hat{b}\not{\psi} + \hat{d}[\not{p}, \not{\psi}]), \quad (4.7)$$

where  $m$  is the neutrino mass inside the medium,  $u^\mu$  is the four-velocity of the medium and  $\hat{a}$ ,  $\hat{b}$ ,  $\hat{d}$  are functions of only two Lorentz scalars, viz.,  $p^2$  and  $p.u$ . In a Lorentz covariant description of field theory at finite temperature and density, one introduces a medium four-velocity vector  $u^\mu$  as in Eq. (4.7) obeying  $u^2 = 1$ . In real time formalism of thermal field theory, the finite temperature and density correction to self-energy of a fermion can be calculated with the help of finite temperature Green's function for a free Dirac field [153] (for applications to neutrino propagation in matter see Refs. [154, 155, 156]):

$$S_f(p) = (\not{p} + m_f) \left[ \frac{1}{p^2 - m_f^2 + i\epsilon} + i\Gamma_f(p) \right] \quad (4.8)$$

where

$$\Gamma_f(p) = 2\pi\delta(p^2 - m_f^2)[n_f(p)\Theta(p_0) + n_{\bar{f}}(p)\Theta(-p_0)] . \quad (4.9)$$

Here  $\Theta$  is the Heaviside step function and  $n_f$  ( $n_{\bar{f}}$ ) is the Fermi-Dirac distribution function for the fermion (anti-fermion) occupation number of the medium given by

$$n_f(p) = \frac{1}{e^{(|p.u|-\mu)/T} + 1}, \quad n_{\bar{f}}(p) = \frac{1}{e^{(|p.u|+\mu)/T} + 1}, \quad (4.10)$$

where  $\mu$  is the chemical potential and  $T$  is the temperature. Integrating the occupation number over all possible momentum states yields the total number density of the fermions (or anti-fermions) in the medium:

$$N_{f(\bar{f})} = g_f \int \frac{d^3p}{(2\pi)^3} n_{f(\bar{f})}(p) . \quad (4.11)$$

Here  $g_f$  denotes the number of internal degrees of freedom and is equal to two for electrons, nucleons and neutrinos for the two different spin states.

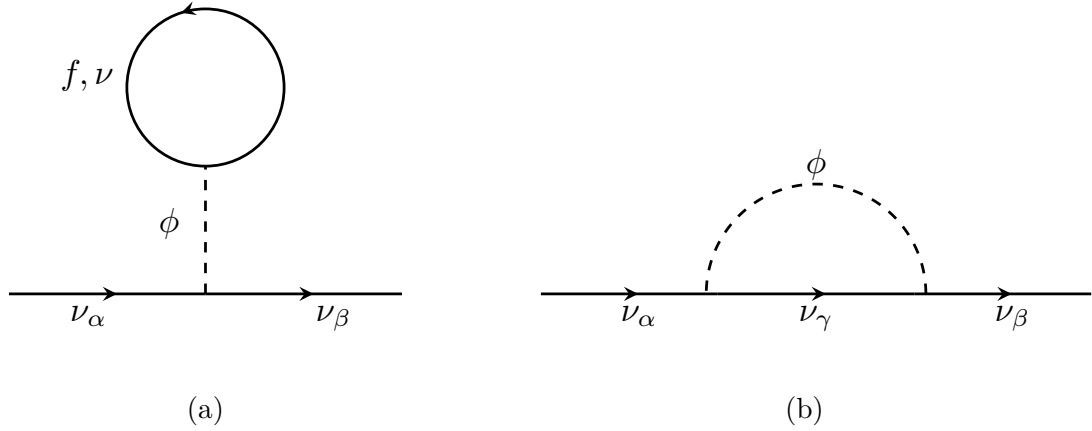


Fig. 4.1: Neutrino self-energy diagrams: (a) Tadpole with background of  $f$  and  $\nu$ , and (b) Self-energy in a neutrino background.

### 4.2.1 Neutrino self-energy from tadpole diagram

The one-loop thermal self energy corrections for the neutrinos arising from Eq. (4.4) or Eq. (4.5) are shown in Fig. 4.1. We first compute the one-loop neutrino thermal mass correction induced by the tadpole diagram in Fig. 4.1a. The Lorentz-invariant form of  $\Sigma$  as given in Eq. (4.7) can be conveniently evaluated by going to the rest frame of the medium, where the amplitude takes a simple form:

$$-i\Sigma_{\alpha\beta} = iy_{\alpha\beta} \frac{i}{q^2 - m_\phi^2} \int \frac{d^4k}{(2\pi)^4} \text{Tr} [iy_f iS_f(k)] . \quad (4.12)$$

In Eq. (4.12), we can set  $q^2 = 0$  for the momentum transfer because we are only interested in the coherent forward scattering of neutrinos in matter for the NSI effect. Only retaining the finite temperature and density part of the self-energy, we obtain

$$\Sigma_{\alpha\beta} = \frac{y_{\alpha\beta} y_f m_f}{\pi^2 m_\phi^2} \int_0^\infty dk_0 \int_0^\infty dk^2 k \delta(k^2 - k_0^2 + m_f^2) [n_f(k_0) + n_{\bar{f}}(-k_0)] . \quad (4.13)$$

Integrating over  $k^2$  using the delta function yields the final result:

$$\Sigma_{\alpha\beta} = \frac{y_{\alpha\beta}y_f m_f}{\pi^2 m_\phi^2} \int_{m_f}^{\infty} dk_0 \sqrt{k_0^2 - m_f^2} [n_f(k_0) + n_{\bar{f}}(k_0)] \equiv \Delta m_{\nu,\alpha\beta} . \quad (4.14)$$

While deriving Eq. (4.14), it has been assumed that the background medium contains both fermions and anti-fermions. Thus, Eq. (4.14) is the complete expression for scalar NSI of neutrinos at any finite temperature and density in a background without neutrinos. We have provided details of evaluating the integral of Eq. (4.14) in various useful limits in Appendix B.1.

Note that the scalar NSI of Eq. (4.14) appears as a medium-dependent mass of the neutrino. The relevant integral can be evaluated analytically in the high temperature as well as low temperature regimes. We find:

$$\Delta m_{\nu,\alpha\beta} = \begin{cases} \frac{y_f y_{\alpha\beta}}{m_\phi^2} (N_f + N_{\bar{f}}) & (\mu, T \ll m_f) & (4.15) \\ \frac{y_f y_{\alpha\beta} m_f}{m_\phi^2} \frac{1}{2} \left(\frac{3}{\pi}\right)^{\frac{2}{3}} (N_f^{2/3} + N_{\bar{f}}^{2/3}) & (\mu > m_f \gg T) & (4.16) \\ \frac{y_f y_{\alpha\beta} m_f}{3 m_\phi^2} \left(\frac{\pi^2}{12 \zeta(3)}\right)^{\frac{2}{3}} (N_f^{2/3} + N_{\bar{f}}^{2/3}) & (\mu < m_f \ll T) . & (4.17) \end{cases}$$

If the medium does not contain either fermions or anti-fermions of a certain type, the corresponding number density should be set to zero in the final result. If the background has more than one type of fermion, the various contributions should be added. Eq. (4.15) for  $\mu, T \ll m_f$  is the non-relativistic limit for the scalar NSI expression and matches the result stated in Ref. [152]. It is most useful in case of the Earth and Sun. The limiting case Eq. (4.16) is useful for relativistic medium backgrounds as with electrons in supernovae. For effect of scalar NSI in the early Universe, Eq. (4.17) is the most relevant. Detailed application of these results is carried out in Sec. 4.7.

### 4.2.2 Neutrino self-energy in a neutrino background

There is another important diagram that might contribute to the effect of neutrino propagation in a medium, as shown in Fig. 4.1b. This diagram contributes to neutrino self-energy only in media with a neutrino or an anti-neutrino background. This situation is realized in supernovae and early Universe cosmology. Here we derive the contribution of Fig. 4.1b in such backgrounds. Again using the real-time formalism of thermal field theory, we can write this contribution for a Dirac neutrino as:

$$\Sigma_{\alpha\beta}^{\nu} = -y_{\beta\gamma}y_{\gamma\alpha} \int \frac{d^4k}{(2\pi)^4} \left( \not{k} + \frac{\not{p}}{2} + m_{\nu} \right) \left[ \frac{\Gamma_{\phi} \left( k - \frac{p}{2} \right)}{\left( k + \frac{p}{2} \right)^2 - m_{\nu}^2} + \frac{\Gamma_{\nu} \left( k + \frac{p}{2} \right)}{\left( k - \frac{p}{2} \right)^2 - m_{\phi}^2} \right], \quad (4.18)$$

where  $\Gamma_{\nu}$  is defined in Eq. (4.9) and for  $\Gamma_{\phi}$ , we have used the finite temperature Green's function for a free bosonic field given by:

$$S_b(p) = \left[ \frac{1}{p^2 - m_b^2 + i\epsilon} - i\Gamma_b(p) \right] \quad (4.19)$$

where

$$\Gamma_b(p) = 2\pi\delta(p^2 - m_b^2)n_b(p)\Theta(p_0), \quad (4.20)$$

with the Bose-Einstein distribution function given by

$$n_b(p) = \frac{1}{e^{(|p.u|)/T} - 1}, \quad (4.21)$$

noting that the chemical potential of the real scalar field  $\phi$  is zero. We have carried out the evaluation of the self energy integral of Eq. (4.18) in Appendix B.2; here we summarize our main results. The contribution of Eq. (4.18) can be written as

$$\Sigma_{\alpha\beta}^{\nu} = -\frac{y_{\beta\gamma}y_{\gamma\alpha}}{8\pi^2|\mathbf{p}|} J, \quad (4.22)$$

with  $J$  identified as the integral of Eq. (4.18), except for an overall factor, and can be decomposed as

$$J = a\not{p} + b\not{\psi} + c + d[\not{p}, \not{\psi}] . \quad (4.23)$$

By taking traces of the integral in Eq. (4.18) multiplied by  $(1, \not{p}, \not{\psi}, \not{p}\not{\psi})$ , we can solve for the Lorentz scalars  $(a, b, c, d)$ . Defining

$$J_p = \text{Tr}(J\not{p}), \quad J_u = \text{Tr}(J\not{\psi}), \quad \text{and} \quad J_m = \text{Tr}(J), \quad (4.24)$$

we find

$$a = \frac{J_u(p.u) - J_p}{4[(p.u)^2 - p^2]}, \quad b = \frac{J_p(p.u) - J_u p^2}{4[(p.u)^2 - p^2]}, \quad c = \frac{J_m}{4}, \quad \text{and} \quad d = 0 . \quad (4.25)$$

It is clear that the coefficient  $c$  contributes to the neutrino mass in the medium [cf. Eq. (4.7)]. But this effect is negligible in our case, because there is no  $1/m_\phi^2$  enhancement.

There is also a matter potential that is caused by the neutrino self-interactions. To arrive at it we examine the pole in the neutrino propagator:

$$iS_\nu^{-1}(p) = i(\not{p} - \Sigma^\nu) = i[\not{p}(1 - A) - B\not{\psi}] , \quad (4.26)$$

where  $A$  and  $B$  are matrices in flavor-space, with elements given by

$$A_{\alpha\beta} = -\frac{y_{\beta\gamma}y_{\gamma\alpha}}{8\pi^2|\mathbf{p}|}a, \quad B_{\alpha\beta} = -\frac{y_{\beta\gamma}y_{\gamma\alpha}}{8\pi^2|\mathbf{p}|}b . \quad (4.27)$$

Since  $A$  and  $B$  commute,  $S_\nu$  can be obtained in terms of  $A$  and  $B$  as

$$iS_\nu(p) = i \frac{[(1 - A)\not{p} - B\not{\psi}]}{\{(1 - A)p - Bu\}^2} . \quad (4.28)$$

We define energy and momentum of the neutrino (in the massless limit) in the rest frame of

the medium as [155]

$$\mathcal{E} = p.u, \quad \mathcal{P} = \sqrt{\mathcal{E}^2 - p^2} . \quad (4.29)$$

The pole in the neutrino propagator of Eq. (4.28) occurs at energy values given by

$$\mathcal{E}_i = \frac{B_i}{1 - A_i} \pm \mathcal{P} . \quad (4.30)$$

This leads to the modified dispersion relation  $\mathcal{E} = U\mathcal{E}_iU^\dagger$  (where  $U$  is the unitary matrix that diagonalizes  $A$  and  $B$ ). The energy shift for neutrinos is thus  $B/(1 - A)$ , while the shift in antineutrino energy is  $-B/(1 - A)$ , which are both non-diagonal in the flavor basis [cf. Eq. (4.27)].

For significant regions of the Yukawa couplings  $y_{\alpha\beta}$  and  $y_f$ , the scalar  $\phi$  does not get thermalized. In this case, there is no  $\phi$  background and the term proportional to  $\Gamma_\phi(k - p/2)$  should be set to zero. We present our results here in this case first. The contribution from  $\Sigma_{\alpha\beta}^\nu$  can then be written as:

$$\Sigma_{\alpha\beta}^\nu = -y_{\alpha\gamma}y_{\gamma\beta} \int_{\frac{-p_0}{2}}^{\infty} dk_0 \int \frac{d^3k}{(2\pi)^3} \frac{(\not{k} + \frac{\not{p}}{2} + m_\nu)}{\left(k - \frac{p}{2}\right)^2 - m_\phi^2} \delta\left[\left(k + \frac{p}{2}\right)^2 - m_\nu^2\right] n_\nu\left(k_0 + \frac{p_0}{2}\right) . \quad (4.31)$$

We defer the details of evaluating this integral to Appendix B.2. Here we present the results in the high temperature limit, assuming that the chemical potential is vanishing. This condition is generally true in the early Universe when neutrinos propagate in a background of neutrinos. Furthermore, we set the neutrino mass to be zero, which is a consistent approximation as the medium-induced  $m_\nu$  is proportional to the original  $m_\nu$ . In the absence of neutrino mass, we can set  $p_0^2 - |\mathbf{p}|^2 = 0$ . Under these conditions, our results are as follows (see Appendix B.2 for details):

$$\begin{aligned} a &= -\frac{\pi^2 T^2}{24|\mathbf{p}|} \left[ 2 - 12\zeta'(-1) - \ln\left(\frac{16\pi|\mathbf{p}|T}{m_\phi^2}\right) \right] - \frac{T}{4} \ln 2 \ln\left(\frac{2\sqrt{2}|\mathbf{p}|T}{m_\phi^2}\right) , \\ b &= \frac{\pi^2 T^2}{12} . \end{aligned} \quad (4.32)$$

Here  $\zeta'(-1) = -0.165421$  is the derivative of Riemann zeta function evaluated at argument equal to  $-1$ . Using these results along with Eq. (4.30), we arrive at the energy shift experienced by the neutrino in a background of neutrinos:

$$\begin{aligned} \Delta\mathcal{E}_{+,\alpha\beta} = & -\frac{T^2}{96|\mathbf{p}|} \left[ yy^\dagger \left( 1 - yy^\dagger \frac{T^2}{192|\mathbf{p}|^2} \left\{ 2 - 12\zeta'(-1) - \ln \left( \frac{16\pi|\mathbf{p}|T}{m_\phi^2} \right) \right\} \right. \right. \\ & \left. \left. - yy^\dagger \frac{T}{32\pi^2|\mathbf{p}|} \ln 2 \ln \left( \frac{2\sqrt{2}|\mathbf{p}|T}{m_\phi^2} \right) \right)^{-1} \right]_{\alpha\beta}. \end{aligned} \quad (4.33)$$

Here we have made use of the fact that  $yy^\dagger = UDU^\dagger$ , where  $D$  is a diagonal matrix and  $U$  is unitary, obtained the poles in the neutrino propagators in the diagonal basis, and reinserted the unitary matrix in writing Eq. (4.33). While we do not use these results explicitly in our analyses, these are part of the neutrino scalar NSI which may find use in early Universe cosmology where there is a thermal background of neutrinos.

If the scalar field  $\phi$  is also in thermal equilibrium, a similar analysis goes through albeit with some replacements, as can be seen from Eq. (4.18):  $\Gamma_\nu \rightarrow \Gamma_\phi$ ,  $p \rightarrow -p$ , with a change in sign of  $\not{p}$  in the numerator and change of  $m_\phi \rightarrow m_\nu$  only in the denominator. These thermal  $\phi$  contributions will add to the neutrino self-energy contribution to  $J$  given in Eq. (4.23). In particular, the coefficients  $J_p$ ,  $J_u$ ,  $J_m$  of Eq. (4.24) will become  $J_p + J_p^\phi$ ,  $J_u + J_u^\phi$ ,  $J_m + J_m^\phi$ , where the new contributions are given in Appendix B.2.

### 4.3 Long-range force effects

A light scalar coupling to fermions can lead to long-range forces. This applies to charged fermions as well as neutrinos propagating through a medium. Even when the neutrino propagates outside of the medium, such long-range forces can affect its propagation. Thus, calculating the neutrino energy using point interactions with a very light mediator does not provide a complete picture. In this section, we sketch a heuristic derivation to account for these long-range force effects. Long range effects in non-relativistic media have been studied

in Refs. [157, 158]. Here, we have extended the analysis for all background media, i.e. both non-relativistic and relativistic cases. This will be especially useful in relativistic media such as in supernovae and in early Universe.

We use the Euler-Lagrange equations for the Lagrangian in Eq. (4.4) to obtain equations of motion for  $\nu$  and  $\phi$ :

$$(i\not{\partial} - m_{\alpha\beta} - y_{\alpha\beta}\phi)\nu_{\beta} = 0 \quad (4.34)$$

$$(\partial^2 + m_{\phi}^2)\phi - y_{\alpha\beta}\bar{\nu}_{\alpha}\nu_{\beta} - y_f\bar{f}f = 0. \quad (4.35)$$

As can be seen from Eq. (4.34), the interaction vertex  $y_{\alpha\beta}\bar{\nu}_{\alpha}\phi\nu_{\beta}$  leads to an extra contribution to neutrino mass:

$$\Delta m_{\nu,\alpha\beta} = y_{\alpha\beta} \langle \phi \rangle_{\text{medium}}. \quad (4.36)$$

To calculate the mass correction for a neutrino propagating in a medium, we will need to calculate the expectation value of the operators at finite temperature and density, appearing in Eqs. (4.34) and (4.35).

For a medium in thermal equilibrium with fermion number density  $N_f$  and anti-fermion number density  $N_{\bar{f}}$  can be represented as a Fock state  $|\Psi\rangle$ . This state contains information about particle and anti-particle distribution in different momentum states. Since the system is assumed to be in thermal equilibrium, the fermion and anti-fermion density in each momentum state does not change in time. Thus, we can set  $t = 0$  and the state  $|\Psi\rangle$  is normalized, i.e,  $\langle \Psi|\Psi\rangle = 1$ . The field operators for the fermion and anti-fermion fields can be written as [159]:

$$f(x) = \int \frac{d^3p}{(2\pi)^3} \frac{1}{\sqrt{2E_{\mathbf{p}}}} \sum_s \left[ a_{\mathbf{p}}^s u^s(p) e^{-ip \cdot x} + b_{\mathbf{p}}^{s\dagger} v^s(p) e^{ip \cdot x} \right], \quad (4.37)$$

$$\bar{f}(x) = \int \frac{d^3p}{(2\pi)^3} \frac{1}{\sqrt{2E_{\mathbf{p}}}} \sum_s \left[ b_{\mathbf{p}}^s \bar{v}^s(p) e^{-ip \cdot x} + a_{\mathbf{p}}^{s\dagger} \bar{u}^s(p) e^{ip \cdot x} \right]. \quad (4.38)$$

We need to calculate the expectation value of the operator  $\bar{f}f$ . While trying to interpret these quantities classically, we first need to normal order the product of the quantum fields:

$$\begin{aligned} \langle : \bar{f}f : \rangle &= \langle \Psi | : \bar{f}f : | \Psi \rangle = \int \frac{d^3 p_1}{(2\pi)^3} \int \frac{d^3 p_2}{(2\pi)^3} \frac{1}{\sqrt{2E_{\mathbf{p}_1}}} \frac{1}{\sqrt{2E_{\mathbf{p}_2}}} \\ &\times \sum_{s,s'} \left[ \langle a_{\mathbf{p}_1}^{s\dagger} a_{\mathbf{p}_2}^{s'} \rangle \bar{u}^s(p_1) u^{s'}(p_2) e^{-i(\mathbf{p}_1 - \mathbf{p}_2) \cdot \mathbf{x}} + \langle a_{\mathbf{p}_1}^{s\dagger} b_{\mathbf{p}_2}^{s'\dagger} \rangle \bar{u}^s(p_1) v^{s'}(p_2) e^{-i(\mathbf{p}_1 + \mathbf{p}_2) \cdot \mathbf{x}} \right. \\ &\left. + \langle b_{\mathbf{p}_1}^s a_{\mathbf{p}_2}^{s'} \rangle \bar{v}^s(p_1) u^{s'}(p_2) e^{i(\mathbf{p}_1 + \mathbf{p}_2) \cdot \mathbf{x}} + \langle b_{\mathbf{p}_2}^{s'\dagger} b_{\mathbf{p}_1}^s \rangle \bar{v}^s(p_1) v^{s'}(p_2) e^{i(\mathbf{p}_1 - \mathbf{p}_2) \cdot \mathbf{x}} \right], \end{aligned} \quad (4.39)$$

where we have used  $\langle A \rangle = \langle \Psi | A | \Psi \rangle$  for brevity and the symbol  $: :$  signifies normal ordering of the product. In Eq. (4.39), terms like  $a^\dagger b^\dagger$  and  $ab$  vanish, since they cannot be contracted because they act on different subspaces. It is well known from quantum field theory at zero temperature that  $a^\dagger a$  and  $b^\dagger b$  are the number density operators for fermions and anti-fermions respectively. This can be generalized to finite temperature and density using the Fermi-Dirac distribution:

$$\langle \Psi | a_{\mathbf{p}_1}^{s\dagger} a_{\mathbf{p}_2}^{s'} | \Psi \rangle = n_f(\mathbf{p}_1) \delta(\mathbf{p}_1 - \mathbf{p}_2) \delta_{s,s'}, \quad (4.40)$$

$$\langle \Psi | b_{\mathbf{p}_1}^{s\dagger} b_{\mathbf{p}_2}^{s'} | \Psi \rangle = n_{\bar{f}}(\mathbf{p}_1) \delta(\mathbf{p}_1 - \mathbf{p}_2) \delta_{s,s'}. \quad (4.41)$$

Eq. (4.40) can be understood by integrating it over all momentum states which yields the total number density  $N_f$ :

$$\int \frac{d^3 p_1}{(2\pi)^3} \int \frac{d^3 p_2}{(2\pi)^3} \langle \Psi | a_{\mathbf{p}_1}^{s\dagger} a_{\mathbf{p}_2}^{s'} | \Psi \rangle = N_f. \quad (4.42)$$

Using the normalization of states  $\bar{u}^s(p) u^s(p) = 2m_f$ , we obtain:

$$\langle \bar{f}f \rangle \equiv \langle \Psi | \bar{f}f | \Psi \rangle = g_f \int \frac{d^3 p}{(2\pi)^3} \frac{m_f}{E_{\mathbf{p}}} \left[ n_f(\mathbf{p}) + n_{\bar{f}}(\mathbf{p}) \right]. \quad (4.43)$$

Converting Eq. (4.43) into an energy integral, we have:

$$\langle \bar{f}f \rangle = \frac{g_f m_f}{2\pi} \int_{m_f}^{\infty} dk_0 \sqrt{k_0^2 - m_f^2} [n_f(k_0) + n_{\bar{f}}(k_0)] . \quad (4.44)$$

Notice that the integral form of Eq. (4.44) matches Eq. (4.14) except for the pre-factors. This implies that generalizing the limiting cases for Eq. (4.44) is straightforward.

Now to calculate  $\Delta m_{\nu, \alpha\beta}$  in Eq. (4.36), we need to solve Eq. (4.35) for  $\phi$ . Considering  $y_f \bar{f}f$  as a source term and neglecting the second term assuming low neutrino number density, we can write the solution as:

$$\langle \phi \rangle(\mathbf{x}) = -y_f \int d^3 \mathbf{x}' \frac{\langle \bar{f}f \rangle(\mathbf{x}')}{4\pi |\mathbf{x} - \mathbf{x}'|} e^{-m_\phi(|\mathbf{x} - \mathbf{x}'|)} . \quad (4.45)$$

Under assumptions of spherical symmetry of the medium, integrating over the angular variables yields the solution of the form:

$$\Delta m_{\nu, \alpha\beta}(r) = \frac{y_f y_{\alpha\beta}}{m_\phi r} \left( e^{-m_\phi r} \int_0^r x \langle \bar{f}f \rangle \sinh(m_\phi x) dx + \sinh(m_\phi r) \int_r^\infty x \langle \bar{f}f \rangle e^{-m_\phi x} dx \right) . \quad (4.46)$$

We have worked out Eq. (4.46) in the relativistic limit for two different density profile distributions in Appendix B.3. While we do not use these analytic results in our numerical analysis, these special cases can give insight for general situations. We use actual density profiles of the Sun and supernovae in our numerical calculations, integrating the relevant integrals exactly.

## 4.4 Experimental constraints on couplings

In this section we explore two specific scenarios:

- (i) scalar  $\phi$  coupling only to electrons and neutrinos, and
- (ii) scalar  $\phi$  coupling only to nucleons and neutrinos.

Here neutrinos can be either Dirac or Majorana in nature. In this section, we discuss experimental constraints on the couplings and mass of  $\phi$  in the aforementioned scenarios.

In accordance to Eq. (4.4), the scalar coupling to electron is denoted by  $y_e$ . On the other hand, the scalar coupling to quark cannot be probed directly but only measurable through their effect with scalar-nucleon interaction. Thus, we present the experimental constraints on scalar-nucleon coupling labeled as  $y_N$ . The conversion from quark level couplings  $y_q$  to  $y_N$  is discussed later in Sec. 4.4.1.4.

#### 4.4.1 Constraints on $y_e$ and $y_N$

##### 4.4.1.1 Anomalous electron magnetic moment

A scalar coupling with the electrons will contribute to the electron anomalous magnetic moment  $(g - 2)_e$  given by [160]:

$$\Delta a_e = \frac{1}{8\pi^2} \int_0^1 dx \frac{(1-x)^2(1+x)y_e^2}{(1-x)^2 + x(m_\phi/m_e)^2}. \quad (4.47)$$

There is currently a  $2.4\sigma$  discrepancy between the experimentally inferred value and SM prediction for  $\Delta a_e = a_e^{\text{exp}} - a_e^{\text{SM}} = (-88 \pm 36) \times 10^{-14}$  [51]. A light scalar can potentially make this discrepancy worse, as it gives a positive contribution, and thus provides a useful limit on scalar NSI parameters. Using the  $3\sigma$  value for the  $\Delta a_e$ , the allowed region in the  $y_e - m_\phi$  plane is obtained. This constraint is shown in Figs. 4.3 and 4.5, labeled as  $(g - 2)_e$ . This constraint yields an almost constant upper bound of  $y_e < 3.4 \times 10^{-6}$  for light scalar mediators.

##### 4.4.1.2 Fifth force experiments

These experiments measure the presence of fifth forces as deviation from the Newtonian gravitational potential between a given source mass and a test mass, which is parametrized

as follows:

$$V(r) = -\frac{Gm_1m_2}{r} \left(1 + \alpha e^{-r/\lambda}\right). \quad (4.48)$$

Given an interaction vertex of the form  $y_f \bar{f} \phi f$  as in Eqs. (4.4) and (4.5), consider the scattering of two distinguishable fermions in the non-relativistic limit. The corresponding Yukawa potential for the interaction is given by (see Sec. 4.7 of Ref. [159]):

$$V(r) = -\frac{y_f^2}{4\pi r} e^{-m_\phi r}, \quad (4.49)$$

where  $r$  is the distance between the scattering particles.

For experiments detailed in Refs. [161, 162, 163, 164, 165, 166] in the range  $\lambda = 10^{-6}$  to  $10^2$  m, the constraints provided on  $\alpha$  in Eq. (4.48) are not directly applicable to  $y_f$  in Eq. (4.49). Therefore, we will translate the constraints on  $\alpha$  to those on  $y_f$  for our case. Assuming a particle (e.g. lepton, quark) couples to the scalar mediator with strength  $q$  and each interacting body contains  $N$  number of these particles, the potential between two extended bodies can be written as:

$$V_\phi(r) = -\frac{N_1 q_1 N_2 q_2}{4\pi r} e^{-m_\phi r}. \quad (4.50)$$

We identify the inverse of the length scale  $\lambda$  as mass of the scalar particle  $\phi$ . Thus, we have:

$$\alpha = \frac{N_1 q_1 N_2 q_2}{4\pi G m_1 m_2} = \frac{q_1 q_2}{4\pi G A_1 A_2 u^2} = \frac{1}{4\pi G u^2} \frac{q_1}{A_1} \frac{q_2}{A_2}, \quad (4.51)$$

where we have used the relation  $m = N A u$  ( $A$ = mass number,  $u = 1$  atomic mass unit) and  $G$  is the gravitational constant. For bounds on  $y_e$ , the coupling strength will be proportional to the lepton number ( $L$ ), which is identical to atomic number ( $Z$ ) for a given material, i.e.,  $q = Z y_e$ , leading to

$$\alpha = \frac{y_e^2}{4\pi G u^2} \frac{Z_1 Z_2}{A_1 A_2}. \quad (4.52)$$

Values for charge to mass number ratio for test and source masses can be obtained from

Label	References	Source Mass Composition	Test Mass Composition	$\frac{Z_1}{A_1} \frac{Z_2}{A_2}$
I	Stanford [164]	Gold, Silicon	Gold	0.1804
II	Colorado [162]	Tungsten	Tungsten	0.1621
III	Eot-Wash'07 [163]	Molybdenum, Tantalum	Molybdenum	0.1839
IV	HUST'12 [165]	Tungsten	Tungsten	0.1621
V	HUST+ '16 [166]	Tungsten	Tungsten	0.1621
VI	Irvine A [161]	Copper	Copper	0.2159
VII	Irvine B [161]	Stainless Steel	Copper	0.2116

Tab. 4.1: The compositions of source and test masses used in the experiment listed and the corresponding values of ratio  $\frac{Z_1}{A_1} \frac{Z_2}{A_2}$ .

the experimental setups as given in Table 4.1. These are shown in Figs. 4.3 and 4.5 by the labels I to VII. Similar results follow for coupling to the nucleons  $y_N$  by replacing the atomic numbers ( $Z$ ) by mass numbers ( $A$ ) in Eq. (4.52). This implies that constraints on  $y_N$  will be independent of the material used in the experiment. These limits are shown in Figs. 4.4 and 4.6.

Additional constraints on  $y_e$  and  $y_N$  can be directly obtained from Ref. [167] which used experiments in the range  $\lambda = 10^{-1}$  to  $10^{13}$  m and the corresponding limits on

$$\tilde{\alpha} = \frac{y_{e(N)}^2}{4\pi G u^2}. \quad (4.53)$$

This constraint is labeled as ‘‘Torsional Balances’’ in Fig. 4.3, 4.4, 4.5, and 4.6. It can be seen from these figures that fifth-force experiments constrain both couplings  $y_e$  and  $y_N$  with an upper bound in the range  $10^{-25} - 10^{-15}$  for  $m_\phi < 0.1$  eV.

#### 4.4.1.3 Constraints from Stellar and Supernova Cooling

**$\phi - e$  coupling:** The production of the light scalar  $\phi$  in stellar bodies can lead to a new channel for energy loss leading to rapid cooling. This can help severely constrain the interaction of a scalar with electrons. The dominant production of this scalar is via its resonant mixing with the longitudinal component of the photon in the plasma [168]. The extra energy loss processes in red giants (RG) can delay their onset of helium ignition and can change

the helium-burning lifetime of the horizontal branch (HB) stars, in disagreement with the stellar models that match observations. For bounds from supernova, the energy loss from production of a scalar is required to be less than that of SN1987A neutrino burst. The energy loss rate from resonant production of a scalar with a plasmon is given by [168, 169]

$$Q_{\text{res}} \simeq \frac{\omega_L}{4\pi} \left( \frac{\omega_L}{m_\phi} \Pi^{\phi L} \right) \frac{1}{e^{\frac{\omega_L}{T}} - 1}, \quad (4.54)$$

where  $\omega_L$  is the resonant frequency and  $\Pi^{\phi L}$  is the mixing of the scalar with the longitudinal component of the photon in the medium, given by

$$\Pi^{\phi L} \simeq \frac{y_e e m_e^{\text{eff}} m_\phi}{\pi^2 k} \int_0^\infty dp v^2 [n_e(E_p) + n_{\bar{e}}(E_p)] \left[ \frac{\omega_L}{v k} \log \left( \frac{\omega_L + vk}{\omega_L - vk} \right) - \frac{2m_\phi^2}{\omega_L^2 - k^2 v^2} \right], \quad (4.55)$$

where  $v = p/E_p$  is the electron velocity,  $m_e^{\text{eff}}$  is the effective thermal mass of the electron and  $k = \sqrt{\omega_L^2 - m_\phi^2}$  is the 3-momentum of the scalar mediator  $\phi$ , where  $E_\phi = \omega_L$  due to the resonant production of scalar. Ref. [169] considers the resonant production process as dominant over the Compton scattering or electron-ion interactions.

For large values of the coupling, the scalar can get trapped inside the star/supernova. This capture would help alleviate the stringent upper bound on the coupling  $y_e$ . To derive the trapping limit, the detailed balance of production and absorption rates is used, i.e.,

$$\Gamma_{\text{prod}}(E_\phi) = e^{-\frac{E_\phi}{T}} \Gamma_{\text{abs}}(E_\phi). \quad (4.56)$$

Since we are only interested in ultra-light mediators with  $m_\phi < 1$  MeV, the absorption through the decay channel  $\phi \rightarrow e^+e^-$  is absent for our purposes. Thus, the absorption rate from the resonant mixing yields a mean free path length  $\lambda$  given by:

$$\lambda = \frac{1}{\Gamma_{\text{abs}}(E_\phi)} \sim \frac{E_\phi^4}{Q_{\text{res}}}. \quad (4.57)$$

By requiring the mean free path to be shorter than  $R = 10$  km, which is the typical size of a supernova core, we derive a bound on the coupling  $y_e$ , as shown in Figs. 4.3 and 4.5, labeled “SN1987A”.

In case of SN1987A, constraints on  $y_e$  range from  $10^{-9}$  to  $10^{-7}$  for scalar mediators lighter than the electron. Even stronger constraints are obtained from HB/RG stars with an upper bound of  $y_e \sim 10^{-15}$  for light scalar mediators.

**$\phi - N$  coupling :** The constraints are similar to the  $\phi - e$  coupling case. In HB and RG stars with typical temperatures of 10 keV, the main constraints for scalar coupling to nucleon in the literature are derived using Compton scattering,  $\gamma + \text{He} \rightarrow \text{He} + \phi$ , as the dominant process. It is required that the new energy loss per unit mass should be less than  $\epsilon < 10$  erg/g/s [170]. As shown in Ref. [168], resonant production through  $\phi$  mixing with a photon can increase the energy loss for low scalar masses and therefore the  $\phi$  coupling to nucleon is highly constrained.

The constraints from a supernova comes from scalar production through bremsstrahlung process  $N + N \rightarrow N + N + \phi$  [171]. Bounds on the coupling can be obtained by requiring the energy loss to be less than the energy contained in the neutrino burst, i.e.,  $\epsilon < 10^{19}$  erg/g/s [170]. Similarly, the trapping regime of the scalar being reabsorbed can be derived using the detailed balance between the absorption and production rates. Requiring the mean free path  $\lambda \propto \epsilon\rho/T^4$  to be smaller than 10 km yields the constraint on  $y_N$  [169], as shown in Figs. 4.4 and 4.6.

In case of SN1987A, constraints on  $y_N$  range from  $10^{-10}$  to  $10^{-7}$  for scalar mediators lighter than electron. Similar to  $y_e$ , stronger constraints are obtained from HB/RG stars with an upper bound of  $y_N \sim 10^{-12}$  for light scalar mediators.

#### 4.4.1.4 Meson decays

A light scalar coupling to nucleons can be produced in meson decays. The only process of interest in this case is a charged Kaon decay to a charged pion and the scalar:  $K^+ \rightarrow \pi^+ \phi$ .

This production cross section is highly constrained from the measurement of branching ratios from charged Kaon decay :  $\text{Br}(K^+ \rightarrow \pi^+ \bar{\nu} \nu) < 1.7 \times 10^{-10}$  [51].

Using the low-energy effective Lagrangian formalism presented in Ref. [172], the branching ratio for the process in consideration is given by

$$\text{BR}(K^+ \rightarrow \pi^+ \phi) = \frac{(3y_u G_F f_\pi f_K B)^2}{32\pi m_{K^+} \Gamma_{K^+}} |V_{ud} V_{us}|^2 \lambda^{1/2} \left( 1, \frac{m_\phi^2}{m_{K^+}^2}, \frac{m_{\pi^+}^2}{m_{K^+}^2} \right), \quad (4.58)$$

where  $B = \frac{m_\pi^2}{m_u + m_d}$  and  $\lambda(a, b, c) = a^2 + b^2 + c^2 - 2ab - 2bc - 2ac$ . Matching the nucleon level interaction to the effective Lagrangian:

$$\mathcal{L} \supset y_N \bar{N} N \phi, \quad (4.59)$$

where  $N = p, n$ , the nucleon coupling  $y_N$  can be written in terms of fundamental quark-level couplings  $y_u(y_d)$  as :

$$y_N = \sum_q y_q g_S^q, \quad (4.60)$$

where  $g_S^q$  is the nucleon scalar charge. We assume that the scalar couples equally to the up and down quark i.e.  $y_u = y_d$ . The effective nucleon couplings to a scalar is then given by

$$y_N = y_u (g_S^u + g_S^d) \simeq 9.47 y_u, \quad (4.61)$$

where we have used  $g_S^u = 5.20$  and  $g_S^d = 4.27$  [173]. This constraint is labeled as " $K^+ \rightarrow \pi^+ \phi$ " in Figs. 4.4 and 4.6. It yields an almost constant upper bound of  $y_N \sim 2.3 \times 10^{-5}$  for light scalar mediators.

#### 4.4.1.5 Big Bang Nucleosynthesis

**$\phi - e$  coupling:** In early Universe, the scalar mediator  $\phi$  can be in thermal equilibrium with the SM particles through annihilation ( $e^+ e^- \rightarrow \gamma \phi$ ) and Compton scattering ( $e^- \gamma \rightarrow e^- \phi$ ).

In the limit  $s \gg m_\phi^2, m_e^2$ , the cross sections for these processes are [169]

$$\sigma_{e\gamma \rightarrow e\phi} \approx \frac{\alpha_e y_e^2}{s} \left[ \log \left( \frac{s}{m_e^2 + m_\phi^2} \right) + \frac{5}{2} \right], \quad (4.62)$$

$$\sigma_{ee \rightarrow \gamma\phi} \approx \frac{2\alpha_e y_e^2}{s} \log \left( \frac{s}{4m_e^2} \right), \quad (4.63)$$

where  $\alpha_e \equiv e^2/4\pi$  is the fine-structure constant. The thermally averaged cross section for these two processes are given below:

$$\langle \sigma_{e\gamma \rightarrow e\phi} v \rangle = \frac{1}{16m_e^2 T^3 K_2(m_e/T)} \int_{m_e^2}^{\infty} ds \sigma(s - m_e^2) \sqrt{s} K_1 \left( \frac{\sqrt{s}}{T} \right), \quad (4.64)$$

$$\langle \sigma_{ee \rightarrow \gamma\phi} v \rangle = \frac{1}{8m_e^4 T (K_2(m_e/T))^2} \int_{4m_e^2}^{\infty} ds \sigma(s - 4m_e^2) \sqrt{s} K_1 \left( \frac{\sqrt{s}}{T} \right). \quad (4.65)$$

If  $\phi$  enters equilibrium with electrons before  $T \sim 1$  MeV, it can decrease the deuterium abundance which is in conflict with observations [169]. In our case, the mediator thermalizes if the thermally averaged cross section exceeds the Hubble expansion rate  $H(T) \sim 1.66\sqrt{g_*}T^2/M_{\text{Pl}}$  (where  $g_*$  is the number of relativistic degrees of freedom and  $M_{\text{Pl}}$  is the Planck mass) at  $T = 1$  MeV. This yields an upper bound of  $y_e = 5 \times 10^{-10}$  for ultra-light scalar mediators, independent of  $m_\phi$ .

Note that LEP measurements of the Bhabha scattering cross-section ( $e^+e^- \rightarrow e^+e^-$ ) can also constrain the coupling  $y_e$  through  $s$  and  $t$ -channel  $\phi$  exchange, but we estimate it to be only at  $\mathcal{O}(0.1)$  level [174, 146].

**$\phi - N$  coupling :** In this case, we require that the scalar  $\phi$  thermalizes around the QCD phase transition temperature. This will help dilute the relativistic degrees of freedom ( $N_{\text{eff}}$ ) until the nucleosynthesis phase is reached. Otherwise, the scalar  $\phi$  will be in equilibrium with SM and will have a significant contribution to relativistic degrees of freedom ( $\Delta N_{\text{eff}} = 4/7$ ) at the time of BBN, in tension with the current measurements from Planck [16]. Thus, we require that the interaction rate should be lower than the Hubble rate at  $T = 200$  MeV.

We can estimate the rate of  $\phi$  production from the processes like  $u\bar{u} \rightarrow \phi$  (and  $d\bar{d} \rightarrow \phi$ ) as  $\Gamma_\phi \sim y_u^2 T$ . This should be compared with Hubble rate  $H(T) \sim 1.66\sqrt{g_*}T^2/M_{\text{Pl}}$ . This condition leads to a stringent constraint on  $y_u < 2.63 \times 10^{-10}$ . Converting the quark-scalar coupling to nucleon level coupling using Eq. (4.61), we get  $y_N < 2.49 \times 10^{-9}$ .

#### 4.4.2 Experimental Constraints on $y_\nu$

**Dirac  $\nu - \phi$  coupling:** The analysis in this case is similar as for the  $\phi - N$  coupling. If the scalar  $\phi$  thermalizes (even partially) in the early Universe, it introduces additional degrees of freedom that contribute to the total entropy [175]. We require that the scalar  $\phi$ , as well as the right-handed neutrinos, should decouple from the thermal plasma at a temperature above the QCD phase transition temperature which will dilute the  $\Delta N_{\text{eff}} = 3 + \frac{4}{7} \sim 3.57$  by the time BBN occurs, in agreement with the currently allowed range from Planck [16]. Thus, requiring that the interaction rate of processes like  $\nu\bar{\nu} \rightarrow \phi$  should be lower than the Hubble rate at  $T = 200$  MeV yields an upper bound of  $y_\nu \sim 2.6 \times 10^{-10}$ . **Majorana  $\nu - \phi$  coupling:** Presence of NSI can lead to re-thermalization of the neutrinos, which otherwise decouple at  $T \sim 1$  MeV in the standard scenario. This can leave a signature in the cosmological observables. The analysis in Ref. [176] constrains the couplings in the secret interaction of neutrinos with a light mediator. Assuming model independence, we use the upper bound on coupling  $y_\nu$  from Ref. [176], which yields a stringent limit of  $y_\nu < 2 \times 10^{-7}$ .

The next-generation CMB experiments, such as CMB-S4 [177] which will have better sensitivity to departures from the  $\Lambda$ CDM paradigm could test such neutrino self-interactions mediated by light scalars, as discussed here.

Additional constraints on  $y_\nu$  exist from neutrino self-interactions within astrophysical sources like core-collapse supernovae [178] with high neutrino number densities of  $n_\nu \sim \mathcal{O}(10^{38}) \text{ cm}^{-3}$ , where they can lose energy via higher-order processes like  $2\nu \rightarrow 4\nu$  and may be unable to transfer enough energy to the stalled supernova shock wave to revive it, halting the explosion altogether [179, 178]. Similarly, elastic scattering of astrophysical

neutrinos off the cosmic neutrino background as they propagate to Earth would distort the energy spectrum of the astrophysical neutrinos by introducing a deficit at high energies and a pileup at low energies, potentially falling below the energy threshold for detection, as well as delaying their arrival time on Earth, compared to their electromagnetic-wave counterpart [180, 178]. However, these astrophysical constraints on  $y_\nu$  turn out to be much weaker than the cosmological constraints discussed above for light scalars with  $m_\phi \lesssim 1$  MeV.

It should also be pointed out that there are other weaker constraints applicable in our scenario but not relevant to the scalar NSI discussion here. For example, coherent elastic neutrino-nucleus scattering data by COHERENT experiment constrains  $y_N$  only at the  $\mathcal{O}(1)$  level for the values of the  $y_\nu$  used in this work [181].

## 4.5 Thermal mass of scalar $\phi$

If the interactions of the scalar  $\phi$  with the medium are significant enough, then it might get thermalized with the medium. Since the scalar field in consideration is ultra-light, medium effects might lead to substantial correction to the vacuum mass of the  $\phi$ . The medium induced mass at one-loop is shown in the Feynman diagram in Fig. 4.2. The relevant contribution to the mass of  $\phi$  at finite density and temperature is given by:

$$\mathcal{M} = 4y_f^2 \int \frac{d^4k}{(2\pi)^4} \left( k^2 - \frac{p^2}{4} + m_f^2 \right) \left[ \frac{\Gamma(k+p/2)}{(k-p/2)^2 - m_f^2} + \frac{\Gamma(k-p/2)}{(k+p/2)^2 - m_f^2} \right]. \quad (4.66)$$

We refer the reader to Appendix B.4 for the evaluation of the scalar mass integral. In the limit  $m_\phi \rightarrow 0$ , the mass correction for scalar is found to be:

$$\Delta m_\phi^2 = \frac{y_f^2}{\pi^2} \int_{m_f}^{\infty} dk_0 n_f(k_0) \sqrt{k_0^2 - m_f^2}. \quad (4.67)$$

Note that the same integral appears in Eq. (4.14). Thus, using the known limiting forms of the integral (cf. Appendix B.1), we obtain:

$$\Delta m_\phi^2 = \begin{cases} \frac{y_f^2}{m_f} (N_f + N_{\bar{f}}) & (\mu, T \ll m_f) & (4.68) \\ \frac{y_f^2}{2} \left(\frac{3}{\pi}\right)^{\frac{2}{3}} (N_f^{2/3} + N_{\bar{f}}^{2/3}) & (\mu > m_f \gg T) & (4.69) \\ \frac{y_f^3}{3} \left(\frac{\pi^2}{12 \zeta(3)}\right)^{\frac{2}{3}} (N_f^{2/3} + N_{\bar{f}}^{2/3}) & (\mu < m_f \ll T) . & (4.70) \end{cases}$$

These expressions are also applicable to Majoron ( $J$ ) propagation in a medium with pseudoscalar interactions of the form  $\bar{\nu}\gamma^5 J\nu$ . For example, in the early Universe, Majoron propagating in a neutrino background will have a mass given by the high-temperature limit, which will be approximately  $m_J \simeq y_\nu T$  [cf. Eqs. (4.70) and (B.14)].

Eq. (4.70) will also be relevant to deriving neutrino self-interaction limits from early Universe cosmology. CMB anisotropies strongly depend on the anisotropy of the neutrino field. Neutrino self-interactions would isotropize the neutrino field, affecting the CMB. It has been found that CMB anisotropy data constrain such interactions to be  $(y_\nu^2/m_\phi^2) \leq (3 \text{ MeV})^{-2}$  (for  $m_\phi > 1 \text{ keV}$ ) [182]. If the scalar field indeed thermalizes with the medium, which occurs for  $y_\nu \geq 10^{-10}$  or so, then one should use the thermal mass of  $\phi$ , Eq. (4.70) in this constraint, which can weaken the constraint significantly. In cosmological simulations involving a light scalar, the thermal mass effects of Eq. (4.70) should be included. Such interactions may be testable in future CMB and large-scale structure observations through the thermally induced mass in such settings.

In the limit when  $m_\phi \rightarrow 0$  but acquires a thermal mass, the scalar NSI expression Eq. (4.14) takes a special form:

$$\Delta m_{\nu,\alpha\beta} = \frac{y_{\alpha\beta}}{y_f} m_f . \quad (4.71)$$

Note that Eq. (4.71) is independent of the scalar mass  $m_\phi$  in this limit. This scenario may

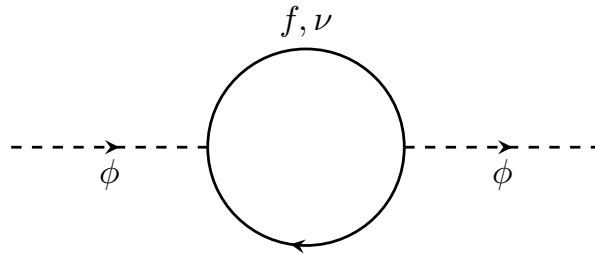


Fig. 4.2: Feynman diagram responsible for the thermal mass of the scalar  $\phi$ .

be realized in supernovae, provided that  $\phi$  has significant interactions with matter. From discussions in Sec. 4.4.1.3, it is clear that for high enough values of  $y_e$  or  $y_N$ , the scalar gets trapped and thermal correction to the mass should be taken into account. Thus, in case of thermalization of the scalar, Eq. (4.71) should be used in lieu of Eqs. (4.15), (4.16) and (4.17).

## 4.6 Quantum-mechanical bound on light scalar mass

Here we show that the uncertainty principle of quantum mechanics sets a lower limit on the minimum  $q^2$  that appears in neutrino forward scattering. This limit applies to a neutrino propagating through Earth, where it interacts either with electrons in atoms, or with nucleons inside the nuclei.

Consider  $\nu_\alpha - e$  elastic scattering. Working in the rest frame of the electron, the initial and final four-momenta of the electron can be written as

$$p^\mu = (m_e, 0, 0, 0), \quad p'^\mu = (\sqrt{p_e^2 + m_e^2}, 0, 0, p_e), \quad (4.72)$$

where  $p_e$  is the recoil momentum of the electron. The  $q^2$  related to coherent forward scattering is then

$$q^2 = (p' - p)^2 = 2m_e(m_e - \sqrt{p_e^2 + m_e^2}) \simeq -p_e^2, \quad (4.73)$$

where in the second step  $q^2 \ll m_e^2$  is assumed.

Now, the recoil momentum of the electron is subject to the uncertainty relation. Its position is not precisely known inside the atom, so we have

$$\Delta p \Delta x \gtrsim \hbar . \quad (4.74)$$

When we set  $q^2 = 0$  in the computation of forward scattering, we only know this up to an uncertainty in  $q^2$  given by (setting  $\hbar = 1$ )

$$q^2 \simeq p_e^2 \sim \frac{1}{(\Delta x)^2} . \quad (4.75)$$

Using  $\Delta x = 140 \times 10^{-8}$  cm, which is the radius of  $^{26}\text{Fe}$  – the most abundant element in Earth’s matter, one obtains for the uncertainty in  $q^2$  to be

$$q_{ye}^2 \approx (14 \text{ eV})^2 . \quad (4.76)$$

Thus, when the mediator mass becomes much smaller than 14 eV, one should use this quantum mechanical cut-off in computing scalar NSI. Similarly for coupling to nucleon, the cut-off would be given by the inverse of the nuclear radius of  $^{26}\text{Fe}$ . Using nuclear diameter  $\Delta x = 9.6$  fm, we obtain

$$q_{yN}^2 \approx (21 \text{ MeV})^2 . \quad (4.77)$$

These rough quantum-mechanical bounds can be better motivated by using atomic/nuclear form factors for coherent forward scattering. In Earth, the expression for scalar NSI will get modified with the inclusion of a form factor.

$$\Delta m_{\nu, \alpha\beta} = \frac{y_f y_{\alpha\beta} N_f}{m_\phi^2 - q^2} F(m_\phi^2) , \quad (4.78)$$

The original result in Eq. (4.15) was obtained by setting  $q^2 = 0$  and  $F(m_\phi^2) = 1$ , but if the

mass of the scalar  $m_\phi \rightarrow 0$  then the denominator is not well-defined. This is remedied by the atomic form factor  $F(m_\phi^2)$  which is of the form [183]:

$$F(m^2) = \frac{m^2}{m^2 + q_0^2}, \quad (4.79)$$

where  $q_0 = 1/4\pi a_0$  and  $a_0$  is the radius of the first orbit for hydrogen-like atoms. Similar qualitative results should apply for the outermost-orbit electrons in  $^{26}\text{Fe}$ . For high values of  $m_\phi^2 \gg q_0^2$ ,  $F(m_\phi^2) \sim 1$  as expected. Thus, the vanishing  $q^2$  limit is well-defined and yields the original result in Eq. (4.15). Difference appears in the regime  $m_\phi^2 \ll q_0^2$ , where  $F(m_\phi^2) \sim m_\phi^2/q_0^2$ . The form of Eq. (4.78) in the low  $m_\phi$  limit and with  $q^2 \rightarrow 0$  is thus given by:

$$\Delta m_{\nu,\alpha\beta} = \frac{y_f y_{\alpha\beta} N_f}{q_0^2}, \quad (4.80)$$

which is independent of  $m_\phi$ . This result agrees with the quantum-mechanical bound discussed above based on the uncertainty principle.

When a scalar mediator couples to the electron, from fifth force constraints either the mass of the mediator should be larger than a keV, or its coupling to the electron should be extremely weak, of order  $10^{-24}$ . For such tiny couplings, to generate scalar NSI in the observable range, one could naively make the mediator mass of order  $10^{-8}$  eV. In this case, the quantum-mechanical intrinsic bound should be applied for computing forward scattering. The result is that scalar NSI arising from coupling to electrons cannot be in the observable range for neutrino propagation in Earth.

These quantum-mechanical limits are not applicable to Sun or supernovae due to the absence of bound states in them. The major baryonic component in Sun and supernovae is ionized hydrogen gas (protons) and neutrons respectively. Thus, the neutrinos scatter off against either free electrons or the protons/neutrons inside these stellar bodies. For the relevant neutrino energies of  $\mathcal{O}(\text{keV} - \text{MeV})$ , the protons/neutrons behave as point particles, and therefore, the finite-size effect discussed above is not applicable to them.

## 4.7 Numerical results

We have discussed the calculation for scalar NSI and the experimental constraints on them in previous sections. Here we put these constraints together and explore possible tests of this scenario in future neutrino experiments. We also provide the numerical models for the density profiles of the earth and supernovae that we adopt to constrain the model parameters.

The results for different cases with scalar coupling to electron/nucleon and in case of either Dirac or Majorana neutrinos have been presented in Figs. 4.3, 4.4, 4.5, 4.6. Here we have fixed the value of  $y_\nu$  at its maximum allowed value in each case, as discussed in Sec. 4.4.2, whereas the other Yukawa coupling (either  $y_e$  or  $y_N$ ) is varied, along with the scalar mass  $m_\phi$ . These results are also summarized in Table 4.2.

### 4.7.1 Earth and Sun

In case of Earth and Sun, the background medium of electrons and nucleons are non-relativistic. Therefore, the expression used for scalar NSI in these media is given by Eq. (4.15) with  $N_{\bar{f}} = 0$ :

$$\Delta m_{\nu,\alpha\beta} = \frac{y_f y_{\alpha\beta}}{m_\phi^2} N_f . \quad (4.81)$$

From the discussion in Sec. 4.6, when the mediator mass becomes lower than the quantum mechanical cut-off of  $m_0 \sim 14$  eV,  $m_0^2$  should be used in the denominator of Eq. (4.81) in lieu of  $m_\phi^2$  for Earth. This leads to the turning of the scalar NSI line in the plots for Earth. We have used  $N_e^{\text{Earth}} = 5.4 N_A \text{ cm}^{-3}$  [51] and  $N_N^{\text{Earth}} = \frac{2.9}{m_N} \text{ g cm}^{-3}$  [184], where the nucleon mass  $m_N = 931.5$  MeV and the Avogadro number  $N_A = 6.022 \times 10^{23}$ . As can be seen from the plots, there are no prospects for observable scalar NSI to be detected on Earth in any of the four cases (Dirac/Majorana and coupling to electrons/nucleons). It can be seen from Table. 4.2 that highest allowed value of scalar NSI in case of Earth is around  $10^{-14}$  eV for the case of  $\phi$  coupling to Majorana neutrinos and electrons.

For the case of Sun, there will also be correction to the scalar NSI from finite size of

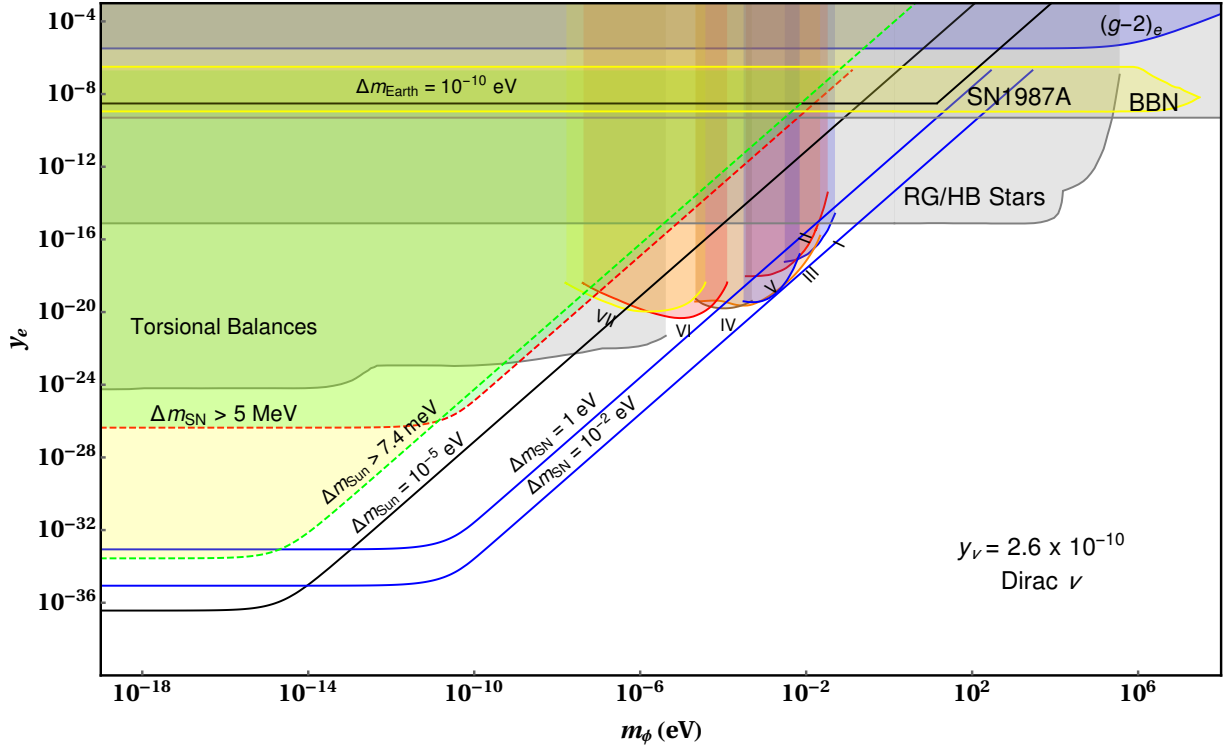


Fig. 4.3: Different experimental constraints on Yukawa coupling of scalar to electron for the case of Dirac neutrinos. The shaded regions are excluded. Some representative values of scalar NSI in Earth, Sun and supernova are also shown.

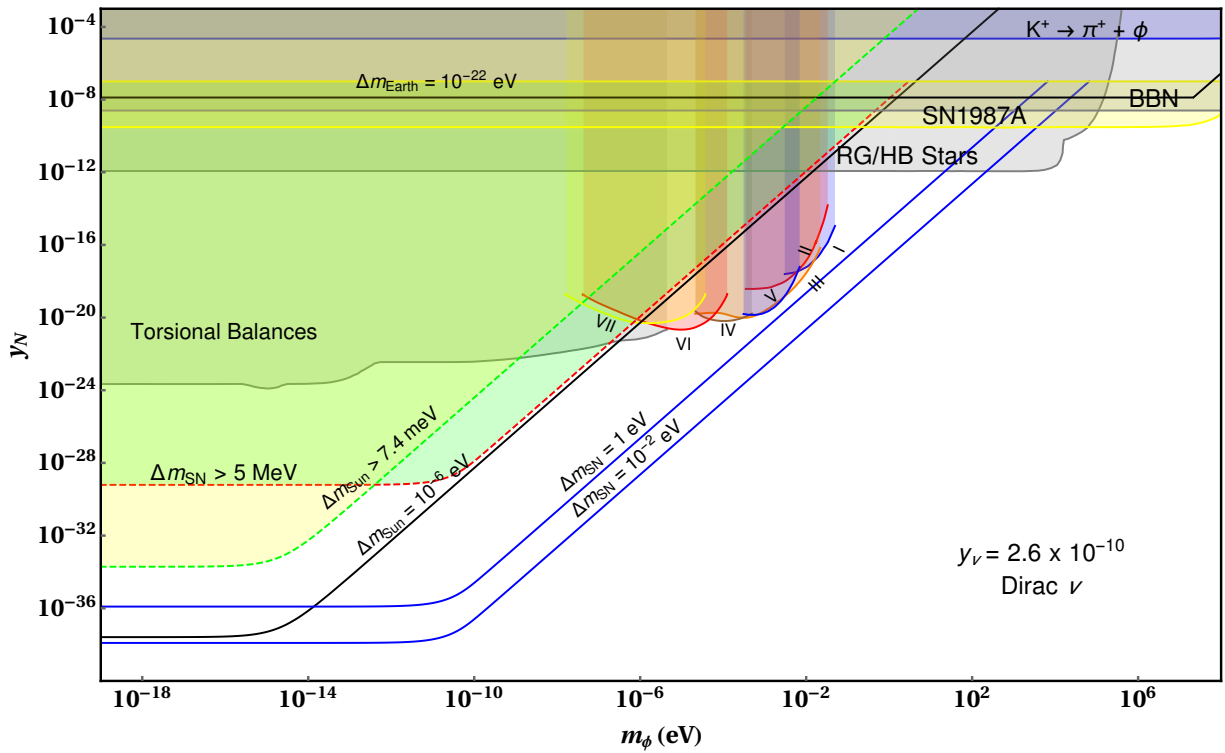


Fig. 4.4: Same as in Fig. 4.3, but for scalar coupling to nucleons.

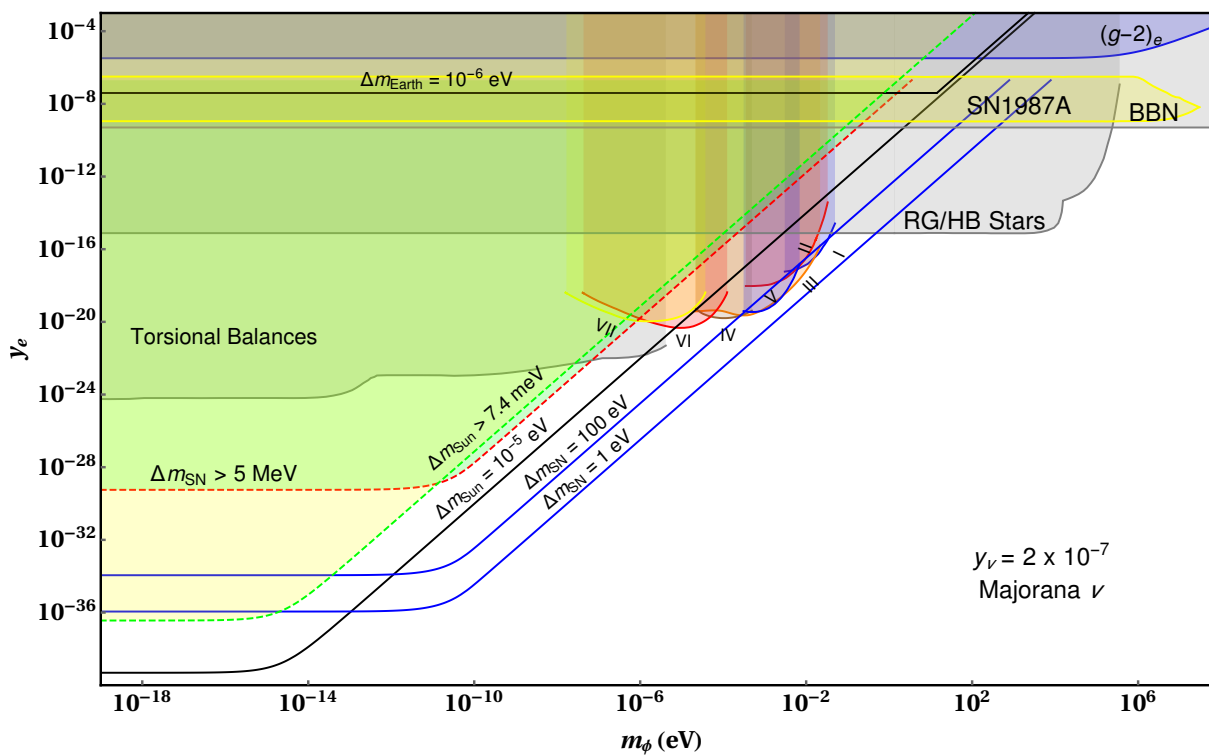


Fig. 4.5: Same as in Fig. 4.3, but for Majorana neutrinos.

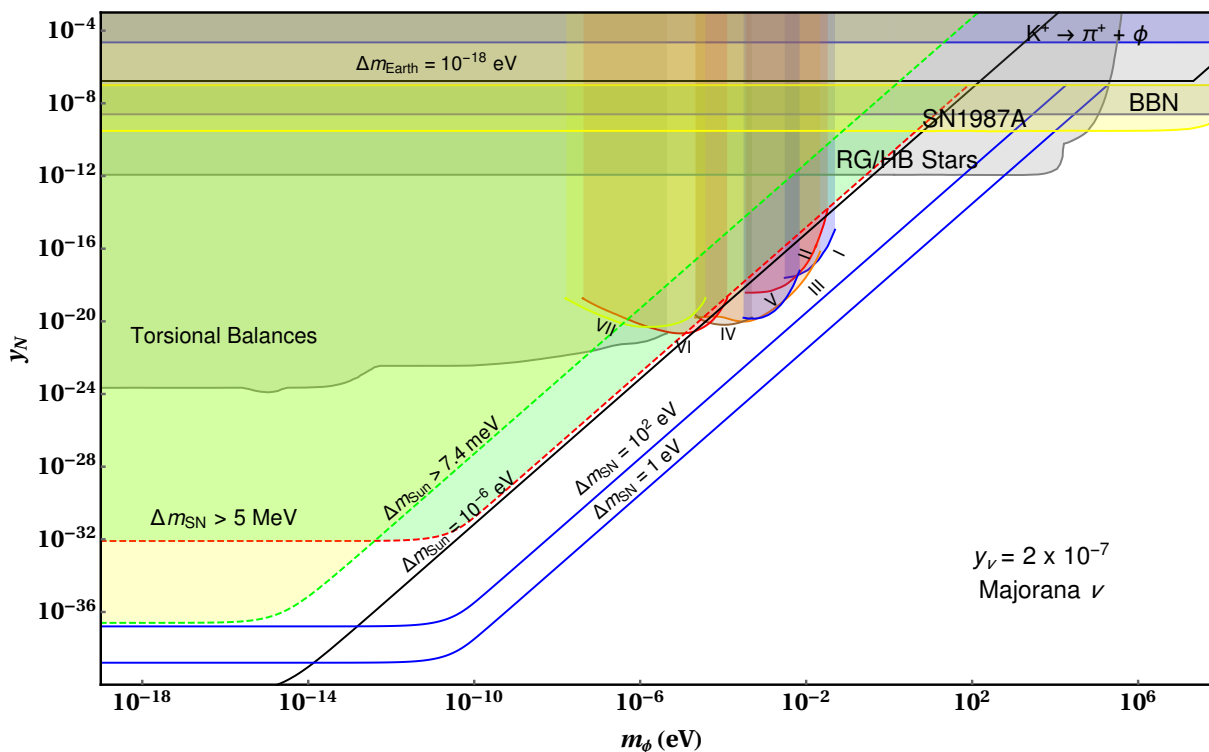


Fig. 4.6: Same as in Fig. 4.4, but for Majorana neutrinos.

the medium in the case of light mediators masses  $m_\phi \simeq R_{\text{Sun}}^{-1}$  as discussed in Sec. 4.3 and Ref. [158]. We calculate the form factor for Sun using Eq. (4.46) and the number density of electrons/nucleons, which is obtained by fitting the known solar density profile given in Refs. [185, 186, 187]. We have used the following best fit to the number density profile for Sun:

$$N(r)_e = 111.61 N_A e^{-(4.81 r + 10.21 r^2)} \text{ cm}^{-3} \quad (\text{for electron}), \quad (4.82)$$

$$N(r)_N = \frac{157.13}{m_N} e^{-(6.1 r + 5.2 r^2)} \text{ g cm}^{-3} \quad (\text{for nucleon}). \quad (4.83)$$

As can be seen from the plots, the existing laboratory and astrophysical constraints do allow for a non-negligible scalar NSI in the Sun, especially for  $m_\phi \lesssim 1\mu\text{eV}$  where the NSI can be as large as  $10^5$  eV for the case of  $\phi$  coupling to Dirac/Majorana neutrinos and electrons. However, this will lead to a large correction term to the solar neutrino mass, which is severely constrained by solar neutrino data. Using the  $\chi^2$ -analysis of the Borexino data from Ref. [152], we find a  $3\sigma$  upper bound on the scalar NSI in Sun:  $\Delta m_{\text{Sun}} \lesssim 7.4 \times 10^{-3}$  eV, as shown by the yellow shaded region in Figs. 4.3, 4.4, 4.5, and 4.6. This still leaves some room for observable scalar NSI effects in future solar neutrino data, especially for ultra-light scalar mediators. Note that very small coupling values for which  $y_f^2 \lesssim Gm_\nu^2 = (m_\nu/M_{\text{Pl}})^2 \sim 10^{-30}$  are disfavored by the weak gravity conjecture [188] which suggests gravity as the weakest force in nature.

### 4.7.2 Supernovae

In the case of supernovae with a typical core temperature  $T \sim 30$  MeV, the electron background is relativistic while the nucleon background can be essentially treated to be at rest.

Thus, there are two different expressions to be used [cf. Eqs. (4.15) and (4.16)]:

$$\Delta m_{\nu,\alpha\beta} = \begin{cases} \frac{y_f y_{\alpha\beta}}{m_\phi^2} N_N^{\text{SN}} & \text{(for nucleon)} \\ \frac{y_{\alpha\beta} y_f}{m_\phi^2} \frac{m_e}{2} \left( \frac{3N_e^{\text{SN}}}{\pi} \right)^{\frac{2}{3}} & \text{(for electron)} . \end{cases} \quad (4.84)$$

$$\quad (4.85)$$

Similar to the case in Sun, there will be correction to the scalar NSI in supernova from the finite size of the medium. Therefore, we numerically integrate Eq. (4.46) to obtain the form factor for a realistic supernova density profile. We use the fiducial model parameters from Ref. [189] given below:

$$\rho(r) = \rho_c \times \begin{cases} 1 + k_\rho(1 - r/R_c) & (r < R_c) \\ (r/R_c)^{-\eta} & (r \geq R_c) \end{cases} \quad (4.86)$$

$$\quad (4.87)$$

where  $\rho_c = 3 \times 10^{14} \text{ g cm}^{-3}$  is the density at core radius  $R_c = 10 \text{ km}$ ,  $k_\rho = 0.2$  and  $\eta = 5$ . Assuming the medium to be electrically neutral and using a proton fraction  $Y_p = 0.3$ , we can obtain the number density for electrons from  $\rho(r)$ .

An interesting feature emerges for scalar NSI in a supernova. Due to the high temperature, a light scalar might develop a considerable thermal mass if it has strong enough coupling to the background as discussed in Sec. 4.5. This leads to Eq. (4.71) which is independent of  $m_\phi$ . Trapping leads to the thermalization of the scalar in the medium. Thus, we have only plotted the scalar NSI expression for the supernova as long as it is not trapped inside.

Scalar NSI produced in a supernova cannot be arbitrarily high. If it becomes too large, then neutrino production would be affected in direct conflict with observations from SN1987A. For typical supernova core temperature around  $T \simeq 30 \text{ MeV}$ , we constrain the scalar NSI to be less than 5 MeV [158], so that neutrinos around 10 MeV could be detected on Earth from SN1987A. In the plots, this bound is shown as a dashed line marked  $\Delta m_{\text{SN}} > 5 \text{ MeV}$ . In any case, we find that sizable scalar NSI can still be observed in supernovae, while being consistent with all other constraints.

Case	Max. NSI (eV)	Scalar Mass Range (eV)	Range for $y_f$
<b>Dirac</b> $\nu, \phi - e$			
Earth	$3.0 \times 10^{-17}$	0.04 -14	$\sim 7.0 \times 10^{-16}$
Sun	$7.4 \times 10^{-3}$	$< 10^{-11}$	$3.3 \times 10^{-34} - 10^{-26}$
Supernova	$5.0 \times 10^6$	$10^{-11} - 10^{-9}$	$10^{-26} - 1.8 \times 10^{-23}$
<b>Dirac</b> $\nu, \phi - N$			
Earth	$10^{-24}$	$5.3 \times 10^3 - 2.1 \times 10^7$	$\sim 2.4 \times 10^{-10}$
Sun	$7.4 \times 10^{-3}$	$< 3.3 \times 10^{-13}$	$2.4 \times 10^{-34} - 7.5 \times 10^{-30}$
Supernova	$5.0 \times 10^6$	$3.3 \times 10^{-13} - 1.8 \times 10^{-7}$	$7.5 \times 10^{-30} - 4.9 \times 10^{-22}$
<b>Majorana</b> $\nu, \phi - e$			
Earth	$10^{-14}$	0.04 -14	$\sim 6.0 \times 10^{-16}$
Sun	$7.4 \times 10^{-3}$	$< 10^{-11}$	$4.4 \times 10^{-37} - 8.7 \times 10^{-30}$
Supernova	$5.0 \times 10^6$	$10^{-11} - 7 \times 10^{-8}$	$8.7 \times 10^{-30} - 9.3 \times 10^{-23}$
<b>Majorana</b> $\nu, \phi - N$			
Earth	$10^{-21}$	$5.3 \times 10^3 - 2.1 \times 10^7$	$\sim 2.1 \times 10^{-10}$
Sun	$7.4 \times 10^{-3}$	$< 3.5 \times 10^{-13}$	$3.1 \times 10^{-37} - 8.4 \times 10^{-33}$
Supernova	$5.0 \times 10^6$	$3.5 \times 10^{-13} - 1.3 \times 10^{-5}$	$8.4 \times 10^{-33} - 2.0 \times 10^{-21}$

Tab. 4.2: The maximum allowed value of scalar NSI in different cases and domains with corresponding ranges for the scalar mass  $\phi$  and the coupling strength  $y_f$ , for a fixed  $y_\nu$  as shown in Figures 4.3-4.6.

## 4.8 UV-complete model for scalar NSI

In this section, we sketch possible ultraviolet completions that would induce interactions of neutrinos with a light scalar. This discussion is intended only as a proof of principle. We focus on the case of Dirac neutrinos, with a light scalar  $\phi$  coupling to the neutrinos and the electron.

First we construct two effective operators that are invariant under the SM gauge symmetry. One induces couplings of the scalar  $\phi$  to neutrinos and the other to the electron. These operators are

$$(i) \quad \bar{\psi}_L \widetilde{H} \nu_R \frac{\phi}{\Lambda_\nu}, \quad (ii) \quad \bar{\psi}_L H e_R \frac{\phi^2}{\Lambda_e^2}. \quad (4.88)$$

Here  $\phi$  is a real scalar field, which is a singlet under SM symmetry,  $H = \begin{pmatrix} H^+ \\ H^0 \end{pmatrix}$  is the SM Higgs doublet and  $\psi_L = \begin{pmatrix} \nu \\ e \end{pmatrix}_L$  is the left-handed lepton doublet. These effective operators exhibit a  $Z_2$  symmetry (apart from lepton number) under which  $\nu_R$  and  $\phi$  are odd, with other

fields being even.  $\phi$  develops a vacuum expectation value,  $\langle\phi\rangle = v_\phi \sim 10$  eV, which breaks the  $Z_2$  symmetry. The neutrino Yukawa coupling  $y_\nu$  and the electron Yukawa coupling  $y_e$  with the  $\phi$  field are respectively given by

$$y_\nu = \frac{v}{\Lambda_\nu}, \quad y_e = \frac{2vv_\phi}{\Lambda_e^2} \quad (4.89)$$

where  $v = 174$  GeV is the VEV of the SM Higgs doublet. Once  $\phi$  acquires a VEV, the operator (i) generates a mass term for the neutrino given by

$$m_\nu = \frac{v_\phi v}{\Lambda_\nu}. \quad (4.90)$$

While this may be the leading contribution, it is not required to be so, as there could be other contributions as well. In any case, this would imply an upper limit on  $y_\nu$  given by

$$y_\nu < \frac{m_\nu}{v_\phi}. \quad (4.91)$$

The cut-off scale  $\Lambda_e$  is expected to be at least a hundred GeV, while  $\Lambda_\nu$  may be lower. Choosing  $\Lambda_e \sim v$ , we would have  $y_e \sim v_\phi/v$ . For  $y_e \sim 10^{-10}$ , as our analysis requires for observable scalar NSI,  $v_\phi \sim 10$  eV is preferable. This in turn implies from Eq. (4.91) that  $y_\nu < 5 \times 10^{-3}$ , using  $m_\nu \equiv \sqrt{\Delta m_{\text{atm}}^2} \sim 0.05$  eV.  $y_\nu$  of course can be smaller than this value, which would be in the interesting range for observable scalar NSI.

The operators in Eq. (4.88) can be generated by adding new vector-like fermions to the SM. For example, operator (i) can arise by the addition of SM singlet fermions  $N_{L,R}$  with a lepton number preserving Dirac mass. The relevant Lagrangian is given by

$$\mathcal{L} \supset y_N \bar{\psi}_L \widetilde{H} N_R + M_N \bar{N}_R N_L + y_\phi^\nu \bar{N}_L \nu_R \phi + \text{H.c.} \quad (4.92)$$

These interactions also preserve the  $Z_2$  symmetry with  $N_{L,R}$  being even under it. The

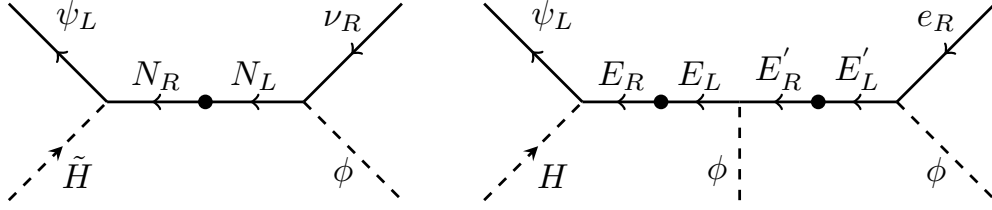


Fig. 4.7: Explicit models generating operators of Eq. (4.88).

diagram generating operator (i) is shown in Fig. 4.7, left panel.

Operator (ii) is induced by integrating out a pair of vector-like leptons,  $E$ ,  $E'$ , both being singlets of  $SU(2)_L$  and carrying hypercharge  $Y = -2$ . Their interaction Lagrangian is given by

$$\mathcal{L} \supset y_E \bar{\psi}_L H E_R + \mu_E \bar{E}_R E_L + y_\phi^E \bar{E}_L E'_R \phi + M_{E'} \bar{E}'_R E_L + y_\phi^e \bar{E}'_L e_R \phi + \text{H.c.} \quad (4.93)$$

Here  $E_{L,R}$  are even and  $E'_{L,R}$  are odd under  $Z_2$ . The effective operator involving electron and  $\phi$  is generated by Fig. 4.7, right panel.

Integrating out the heavy degrees of freedom we obtain the following effective Lagrangian terms:

$$(i) \quad \frac{y_N y_\phi^\nu}{M_N} \bar{\psi}_L \tilde{H} \nu_R \phi, \quad (ii) \quad \frac{y_E y_\phi^E y_\phi^e}{M_E M_{E'}} \bar{\psi}_L H e_R \phi^2. \quad (4.94)$$

These expressions can be mapped to Eq. (4.88) to identify the cut-off scales  $\Lambda_\nu$  and  $\Lambda_e$ , and the constraints discussed in terms of the cut-off scales will apply to them. We thus see broad consistency of the model. In particular, the induced neutrino mass from these interactions is not excessive and the vector-like leptons having mass of order few hundred GeV is consistent with collider data. Note that breaking the  $Z_2$  at a scale of order 10 eV does not cause cosmological domain wall problem, since the energy density carried by the walls is quite small. We have ignored here possible mixing between the  $\phi$  and  $H$  fields since such mixing is small, of order  $v_\phi/v$  and is controlled by a new quartic coupling which may also be small.

## 4.9 Conclusion

We have performed a systematic study of scalar NSI of neutrinos with matter due to a light scalar mediator. First, a general field-theoretic derivation of the scalar NSI formula is given, which is valid at arbitrary temperature and density, and hence, applicable in widely different environments, such as Earth, Sun, supernovae and early Universe. We have also extended the analysis of long-range force effects for all background media, including both relativistic and non-relativistic limits. Using these results and applying various experimental and astrophysical constraints, we find that observable scalar NSI has been precluded in terrestrial experiments, primarily due to atomic form factor effects, which can also be understood from simple quantum-mechanical uncertainty principle. Nevertheless, sizable scalar NSI effects are still possible in the Sun, supernovae and early Universe environments, which could be detected in future solar and supernova neutrino data, as well as in the form of extra relativistic species ( $\Delta N_{\text{eff}}$ ) and neutrino self-interactions in cosmological observations. We have also presented examples of UV-complete models that could give rise to such scalar NSI effects.

## Chapter 5

# Interactions of $\nu_R$ -philic dark photon<sup>24</sup>

*"All Men Have Limits. They Learn What They Are And Learn  
Not To Exceed Them. I Ignore Mine."*

- Batman, (Knightfall)

## 5.1 Introduction

Right-handed neutrinos ( $\nu_R$ ), albeit not included in the Standard Model (SM), are a highly motivated dark sector extension to accommodate neutrino masses [30, 31, 32, 33, 34], dark matter [190, 191, 192], and baryon asymmetry of the universe [193]. Being intrinsically dark,  $\nu_R$  might have abundant new interactions well hidden from experimental searches. In particular, it is tempting to consider the possibility that there might be a hidden gauge symmetry in the  $\nu_R$  sector [194, 195, 196, 197, 198, 199, 200, 201]. The new gauge boson arising from this symmetry does not directly couple to other fermions except for  $\nu_R$  and naturally becomes a dark photon, which we referred to as the  $\nu_R$ -philic dark photon.

The  $\nu_R$ -philic dark photon is not completely dark. It may interact with normal matter via kinetic mixing [36], provided that the new gauge symmetry is Abelian; or, in the presence of mass terms connecting  $\nu_R$  and left-handed neutrinos  $\nu_L$ , via one-loop diagrams containing  $W^\pm/Z$  and neutrinos [202]. In the former case, the strength of dark photon interactions with quarks or charged leptons depends on the kinetic mixing parameter  $\epsilon$  in  $\mathcal{L} \supset \frac{\epsilon}{2} F^{\mu\nu} F'_{\mu\nu}$

---

<sup>24</sup> This chapter is based on [13]

where  $F^{\mu\nu}$  and  $F'_{\mu\nu}$  are the gauge field tensors of the SM hypercharge  $U(1)_Y$  and the new  $U(1)$ , respectively. This case, being essentially independent of the neutrino sector, has been widely considered in a plethora of dark photon studies—for a review, see [203, 204, 205, 206]. In the latter case, the loop-induced couplings depends on neutrino masses and mixing, and will be investigated in this work.

The aim of this work is to address the question of how dark the  $\nu_R$ -philic dark photon could be in the regime that dark-photon-matter interactions dominantly arise from  $\nu_L$ - $\nu_R$  mixing instead of kinetic mixing. We note here that the dominance might be merely due to accidentally small  $\epsilon$ , or due to fundamental reasons such as the SM  $U(1)_Y$  being part of a unified gauge symmetry [e.g.  $SU(5)$ ] in grand unified theories. We opt for a maximally model-independent framework in which generic Dirac and Majorana mass terms are assumed. The loop-induced couplings are UV finite as a consequence of the orthogonality between SM gauge-neutrino couplings and the new ones. Compared to our previous study on loop-induced  $\nu_R$ -philic scalar interactions [207], we find that the couplings in the vector case are not suppressed by light neutrino masses, and might be of potential importance to ongoing/upcoming collider and beam dump searches for dark photons.

The chapter is organized as follows: In Sec. 5.2, we describe the relevant Lagrangian used in this work, reformulate neutrino interactions in the mass basis, and discuss generalized matrix identities for UV divergence cancellation for later use. In Sec. 5.3, we first derive model-independent expression for effective coupling of  $Z'$  to charged leptons/quarks through one-loop diagram involving  $Z$  and  $W$  bosons, respectively. We then evaluate the coupling strength in three different examples. In Sec. 5.4, we present a qualitative discussion about possible connections between the  $U(1)_R$  gauge coupling and the mass of  $Z'$ . In Sec. 5.5, we present constraints from a vast array of current and future experiments spanning from collider searches to astrophysical phenomena. We finally conclude in Sec. 6.8 with details of one-loop diagram calculations relegated to Appendix C.1.

## 5.2 Framework

We consider a hidden  $U(1)$  gauge symmetry, denoted by  $U(1)_R$ , imposed on  $n$  right-handed neutrinos. The gauge boson of  $U(1)_R$  in this work is denoted by  $Z'$ . The relevant part of the Lagrangian for the  $U(1)_R$  extension reads<sup>25</sup>:

$$\begin{aligned} \mathcal{L} \supset & \nu_{R,j}^\dagger i\bar{\sigma}_\mu D_j^\mu \nu_{R,j} + \left[ \frac{(M_R)_{ij}}{2} \nu_{Ri} \nu_{R,j} + (m_D)_{\alpha j} \nu_{L,\alpha} \nu_{R,j} + \text{h.c.} \right] \\ & - \frac{1}{4} F'_{\mu\nu} F'^{\mu\nu} + \frac{1}{2} m_{Z'}^2 Z'_\mu Z'^\mu, \end{aligned} \quad (5.1)$$

where  $\bar{\sigma} \equiv (1, -\vec{\sigma})$  with  $\vec{\sigma}$  being three Pauli matrices;  $\alpha$  denotes flavor indices;  $(i, j) = 1, 2, 3, \dots, n$ ; and

$$D_j^\mu = \partial^\mu - i g_R Q_{R,j} Z'^\mu. \quad (5.2)$$

Here  $g_R$  is the gauge coupling constant of  $U(1)_R$  and  $Q_{R,j}$  is the charge of  $\nu_{R,j}$  under  $U(1)_R$ . Note that for most general forms of  $M_R$  and  $m_D$ , both the Majorana and Dirac mass terms in Eq. (5.1) break the  $U(1)_R$  symmetry. In addition, for arbitrary charge assignments of  $\nu_{R,j}$  under  $U(1)_R$ , the model would not be anomaly free. Nevertheless, one can construct complete models in which  $M_R$  and  $m_D$  arise from spontaneous symmetry breaking and the cancellation of anomalies can be obtained when several  $\nu_{R,j}$ 's have different charges with  $\sum_j Q_{R,j}^3 = 0$ —see the example in Sec. 5.3.2. In this section we neglect these model-dependent details and focus on the general framework proposed in Eq. (5.1).

The Dirac and Majorana neutrino mass terms in Eq. (5.1) can be framed as

$$\mathcal{L}_{\nu \text{ mass}} = \frac{1}{2} (\nu_L^T, \nu_R^T) \begin{pmatrix} 0_{3 \times 3} & m_D \\ m_D^T & M_R \end{pmatrix} \begin{pmatrix} \nu_L \\ \nu_R \end{pmatrix}, \quad (5.3)$$

where  $\nu_L = (\nu_{L,e}, \nu_{L,\mu}, \nu_{L,\tau})^T$  and  $\nu_R = (\nu_{R,1}, \nu_{R,2}, \dots)^T$  are column vectors. The entire mass

---

<sup>25</sup> Throughout the main text we exclusively use Weyl spinors for conceptual simplicity, while in the Appendix we use Dirac/Majorana spinors for loop calculations.

matrix of  $\nu_L$  and  $\nu_R$  can be diagonalized by a unitary matrix  $U$ :

$$\begin{pmatrix} \nu_L \\ \nu_R \end{pmatrix} = U \begin{pmatrix} \nu_{1,2,3} \\ \nu_{4,5,\dots} \end{pmatrix}, \quad U^T \begin{pmatrix} 0_{3 \times 3} & m_D \\ m_D^T & M_R \end{pmatrix} U = \begin{pmatrix} m_{1,2,3} & \\ & m_{4,5,\dots} \end{pmatrix}. \quad (5.4)$$

Here  $\nu_i$  ( $i = 1, 2, \dots, n+3$ ) denote neutrino mass eigenstates, with  $m_i$  being the corresponding masses. We refer to the basis after the  $U$  transformation as the *chiral basis*, and the one before the transformation as the *mass basis*.

In order to facilitate loop calculations, we need to transform neutrino interaction terms from the chiral basis to the mass basis. In the chiral basis, we have the following neutrino interaction terms:

$$\mathcal{L} \supset \left[ \frac{g}{\sqrt{2}} W_\mu^- \ell_{L,\alpha}^\dagger \bar{\sigma}^\mu \nu_{L,\alpha} + \text{h.c.} \right] + \frac{g}{2c_W} Z_\mu \nu_{L,\alpha}^\dagger \bar{\sigma}^\mu \nu_{L,\alpha} + g_R Q_{R,j} Z'_\mu \nu_{R,j}^\dagger \bar{\sigma}^\mu \nu_{R,j}, \quad (5.5)$$

where the first three terms are the SM charged and neutral current interactions, and  $\ell_L$  denotes left-handed charged leptons. Therefore, in the mass basis, after performing the basis transformation, we obtain:

$$\mathcal{L} \supset \left[ (G_W)^{\alpha j} W_\mu^- \ell_{L,\alpha}^\dagger \bar{\sigma}^\mu \nu_j + \text{h.c.} \right] + (G_Z)^{ij} Z_\mu \nu_i^\dagger \bar{\sigma}^\mu \nu_j + (G_R)^{ij} Z'_\mu \nu_i^\dagger \bar{\sigma}^\mu \nu_j, \quad (5.6)$$

where

$$G_Z = \frac{g}{2c_W} U^\dagger \begin{pmatrix} I_{3 \times 3} & \\ & 0_{n \times n} \end{pmatrix} U, \quad G_R = g_R U^\dagger \begin{pmatrix} 0_{3 \times 3} & \\ & Q_R \end{pmatrix} U, \quad (5.7)$$

$$G_W = \frac{g}{\sqrt{2}} \begin{pmatrix} I_{3 \times 3} & 0_{3 \times n} \end{pmatrix} U. \quad (5.8)$$

Here  $Q_R = \text{diag}(Q_{R,1}, Q_{R,2}, \dots)$ ,  $I_{3 \times 3}$  is an identity matrix, and  $0_{x \times y}$  is a zero matrix.

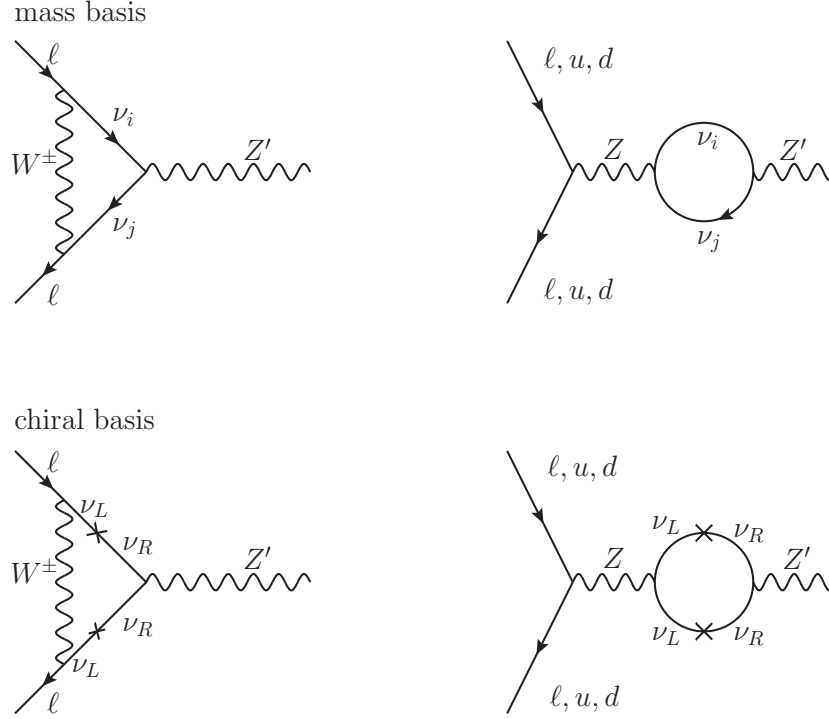


Fig. 5.1: Loop-induced  $Z'$  couplings to charged fermions in the mass basis (upper panels) and in the chiral basis (lower panels).

Notice that some products of the above matrices are zero:

$$G_Z G_R = G_R G_Z = 0, \quad (5.9)$$

$$G_W G_R = G_R G_W^\dagger = 0. \quad (5.10)$$

The above results, which will be used in our loop calculations to cancel UV divergences, have been previously derived in Ref. [202].

### 5.3 Loop-induced couplings of $Z'$

At tree level, the  $\nu_R$ -philic  $Z'$  does not directly couple to charged leptons or quarks. At the one-loop level, there are loop-induced couplings of  $Z'$  generated by the diagrams shown in Fig. 5.1.

In the upper and lower panels, we present diagrams in the mass and chiral bases, respectively. The two descriptions are physically equivalent. The diagrams in the chiral basis imply that the loop-induced couplings are proportional to  $m_D^2$ , due to the two necessary mass insertions on the neutrino lines. Although in the mass basis this conclusion is not evident, technically our calculations are performed using the diagrams in the upper panel because of properly defined propagators.

Throughout this work, we work in the unitarity gauge so that diagrams involving Goldstone bosons can be disregarded. The detailed calculations are presented in Appendix C.1. The result for a single  $W^\pm$  diagram with neutrino mass eigenstates  $\nu_i$  and  $\nu_j$  running in the loop reads:

$$i\mathcal{M}_W^{ij} = i \frac{G_W^{\beta j} (G_R^{ij} G_W^{\alpha i})^*}{16\pi^2} \mathcal{F}(m_i, m_j) \overline{u(p_1)} \gamma^\mu P_L u(p_2) \epsilon_\mu(q), \quad (5.11)$$

where  $\overline{u(p_1)}$  and  $u(p_2)$  denote the two external fermion states,  $\epsilon_\mu(q)$  is the polarization vector of  $Z'_\mu$ , and

$$\begin{aligned} \mathcal{F}(m_i, m_j) &\approx \frac{3}{2} + \frac{m_j^4 \log(m_j^2/m_W^2) - m_i^4 \log(m_i^2/m_W^2)}{(m_i^2 - m_j^2) m_W^2} \\ &+ \frac{(m_i^2 + m_j^2)}{m_W^2} \left[ \frac{1}{\epsilon} + 1 + \log\left(\frac{\mu^2}{m_W^2}\right) \right]. \end{aligned} \quad (5.12)$$

We have adopted dimensional regularization in the loop calculation so the loop integral takes the generalized measure  $\frac{d^4k}{(2\pi)^4} \rightarrow \mu^{2\epsilon} \frac{d^d k}{(2\pi)^d}$  with  $d = 4 - 2\epsilon$ , which defines  $\mu$  and  $\epsilon$  in Eq. (5.12).

Note that for each single diagram in the mass basis, the result is UV divergent. However, when we sum over  $i$  and  $j$ , the UV divergence cancels out. This can be seen as follows:

$$\sum_{ij} \frac{1}{\epsilon} (m_i^2 + m_j^2) G_W^{\beta j} (G_R^{ij} G_W^{\alpha i})^* = \frac{1}{\epsilon} G_W M_d^2 G_R^\dagger G_W^\dagger + \frac{1}{\epsilon} G_W G_R^\dagger M_d^2 G_W^\dagger = 0, \quad (5.13)$$

where  $M_d^2 \equiv \text{diag}(m_1^2, m_2^2, m_3^2, \dots)$  and in the second step we have used Eq. (5.10). Eq. (5.13) implies that we can safely ignore the second line in Eq. (5.12), as long as Eq. (5.10) holds. For a similar reason ( $G_W G_R^\dagger G_W^\dagger = 0$ ), the constant term  $\frac{3}{2}$  can also be ignored.

$f$	$\nu_L$	$e_L$	$u_L$	$d_L$	$e_R$	$u_R$	$d_R$
$Q_Z^{(f)}$	$\frac{1}{2}$	$-\frac{1}{2} + s_W^2$	$\frac{1}{2} - \frac{2}{3}s_W^2$	$-\frac{1}{2} + \frac{1}{3}s_W^2$	$s_W^2$	$-\frac{2}{3}s_W^2$	$\frac{1}{3}s_W^2$

 Tab. 5.1: The values of  $Q_Z^{(f)}$  used in this work.

For the  $Z$  diagram, we have a similar amplitude for each single diagram. In the soft-scattering limit ( $q \rightarrow 0$ ), we find

$$i\mathcal{M}_Z^{ij} = -\frac{igQ_Z^{(f)}G_Z^{ij}(G_R^{ij})^*}{16\pi^2c_Wm_Z^2}\mathcal{F}_2(m_i, m_j)\overline{u(p_1)}\gamma^\mu P_{L/R}u(p_2)\epsilon_\mu(q), \quad (5.14)$$

where  $f = \ell_{L/R}$ ,  $u_{L/R}$ , or  $d_{L/R}$ ; and  $Q_Z^{(f)}$  is the  $Z$  charge of  $f$ , defined in the way that the  $Z$ - $f$ - $f$  coupling can be written as  $gQ_Z^{(f)}/c_W$ . The specific values of  $Q_Z^{(f)}$  used in this work are listed in Tab. 5.1. The  $\mathcal{F}_2$  function reads:

$$\mathcal{F}_2(m_i, m_j) \approx \frac{m_j^4 \log(m_j^2) - m_i^4 \log(m_i^2)}{(m_i^2 - m_j^2)} + (m_i^2 + m_j^2) \left[ \frac{1}{\epsilon} + \frac{1}{2} + \log \mu^2 \right]. \quad (5.15)$$

Once again, we can see that the UV part cancels out during the summation of  $i$  and  $j$  because

$$\sum_{ij} \frac{1}{\epsilon} (m_i^2 + m_j^2) G_Z^{ij} (G_R^{ij})^* = \frac{1}{\epsilon} \text{Tr} [M_d^2 G_Z G_R^\dagger + G_Z M_d^2 G_R^\dagger] = 0. \quad (5.16)$$

Hence only the first term in Eq. (5.15) needs to be taken into account.

Summing over  $i$  and  $j$  in Eq. (5.11), we obtain the following effective coupling generated by the loop diagrams:

$$\mathcal{L}_{\text{eff}} = \left[ g_{\text{eff},W} \ell_{L,\beta}^\dagger \bar{\sigma}^\mu \ell_{L,\alpha} + g_{\text{eff},Z} f^\dagger \bar{\sigma}^\mu f \right] Z'_\mu, \quad (5.17)$$

where

$$g_{\text{eff},W} = \sum_{ij} \frac{G_W^{\beta j} (G_R^{ij} G_W^{\alpha i})^* m_j^4 \log(m_j^2/m_W^2) - m_i^4 \log(m_i^2/m_W^2)}{16\pi^2 (m_i^2 - m_j^2) m_W^2}, \quad (5.18)$$

$$g_{\text{eff},Z} = \sum_{ij} \frac{g Q_Z^{(f)} G_Z^{ij} (G_R^{ij})^* m_i^4 \log(m_i^2) - m_j^4 \log(m_j^2)}{16\pi^2 c_W (m_i^2 - m_j^2) m_Z^2}. \quad (5.19)$$

### 5.3.1 Example A: 1 $\nu_L$ + 1 $\nu_R$

First, let us consider the simplest case that there are only one  $\nu_L$  and one  $\nu_R$ . The neutrino mass matrix  $M_\nu$  for the case can be diagonalized by a  $2 \times 2$  unitary matrix

$$U^T \begin{pmatrix} 0 & m_D \\ m_D & M_R \end{pmatrix} U = \begin{pmatrix} m_1 & 0 \\ 0 & m_4 \end{pmatrix}. \quad (5.20)$$

This unitary matrix can be parametrized as follows

$$U = \begin{pmatrix} -ic_\theta & s_\theta \\ is_\theta & c_\theta \end{pmatrix}, \quad \theta = \arctan\left(\sqrt{\frac{m_1}{m_4}}\right), \quad (5.21)$$

where  $c_\theta = \cos \theta$  and  $s_\theta = \sin \theta$ . Substituting the explicit form of  $U$  in Eqs. (5.7) and (5.8), we obtain

$$G_Z = \frac{g}{2c_W} \begin{pmatrix} c_\theta^2 & ic_\theta s_\theta \\ -ic_\theta s_\theta & s_\theta^2 \end{pmatrix}, \quad G_R = g_R \begin{pmatrix} s_\theta^2 & -ic_\theta s_\theta \\ ic_\theta s_\theta & c_\theta^2 \end{pmatrix}, \quad (5.22)$$

$$G_W = \frac{g}{\sqrt{2}} \begin{pmatrix} -ic_\theta & s_\theta \end{pmatrix}. \quad (5.23)$$

We can now perform the summation in Eqs. (5.18)-(5.19). Expanding the result as a Taylor series in  $s_\theta$  (assuming  $s_\theta \ll 1$ ) and only retaining the dominant contribution, we obtain

$$g_{\text{eff},W} = -\frac{g^2 m^2 s_\theta^2}{32\pi^2 m_W^2} g_R, \quad (5.24)$$

$$g_{\text{eff},Z} = Q_Z^{(f)} \frac{g^2 m^2 s_\theta^2}{32\pi^2 m_Z^2 c_W^2} g_R, \quad (5.25)$$

where

$$m_1 = m s_\theta^2, \quad m_4 = m c_\theta^2. \quad (5.26)$$

Note that for  $m_1 \ll m_4$ ,

$$m^2 s_\theta^2 \simeq m_1 m_4 = m_D^2. \quad (5.27)$$

Using  $G_F = \frac{\sqrt{2}g^2}{8m_W^2}$ , we can rewrite Eqs. (5.24)-(5.25) as

$$g_{\text{eff},W} = -\frac{\sqrt{2} G_F m_D^2}{8\pi^2} g_R, \quad (5.28)$$

$$g_{\text{eff},Z} = Q_Z^{(f)} \frac{\sqrt{2} G_F m_D^2}{8\pi^2} g_R. \quad (5.29)$$

### 5.3.2 Example B: 1 $\nu_L$ + 2 $\nu_R$ with opposite charges

In this example, we construct a UV-complete model with one  $\nu_L$  and two  $\nu_R$  which have opposite  $U(1)_R$  charges so that the model is anomaly free. The off-diagonal Majorana mass term does not violate the  $U(1)_R$  symmetry and the Dirac mass term is generated by a new Higgs doublet  $H'$  that is charged under  $U(1)_R$ . The  $U(1)_R$  charges are assigned as follows:

$$Q_R(\nu_{R,1}) = +1, \quad Q_R(\nu_{R,2}) = -1, \quad Q_R(H') = -1, \quad (5.30)$$

which leads to the following terms that fully respect the  $U(1)_R$  symmetry:

$$\mathcal{L} \supset y_\nu \widetilde{H}'^\dagger L \nu_{R_1} + \frac{M_R}{2} \nu_{R_1} \nu_{R_2} + \text{h.c.}, \quad (5.31)$$

where  $\widetilde{H}' \equiv i\sigma_2(H')^*$ . After spontaneous symmetry breaking,  $H'$  acquires a vacuum expectation value :  $\langle H' \rangle = (0, v')^T / \sqrt{2}$ , leading to

$$\mathcal{L} \supset m_D \nu_L \nu_{R_1} + \frac{M_R}{2} \nu_{R_1} \nu_{R_2} + \text{h.c.} \quad (5.32)$$

Here  $m_D = y_\nu v'/\sqrt{2}$ . The neutrino mass matrix for this case can be diagonalized by a  $3 \times 3$  unitary matrix:

$$U^T \begin{pmatrix} 0 & m_D & 0 \\ m_D & 0 & M_R \\ 0 & M_R & 0 \end{pmatrix} U = \begin{pmatrix} m_1 & 0 & 0 \\ 0 & m_4 & 0 \\ 0 & 0 & m_5 \end{pmatrix}. \quad (5.33)$$

The texture of the mass matrix on the left-hand side of Eq. (5.33) leads to  $m_1 = 0$  and  $m_4 = m_5$ , which is evident from its vanishing trace and determinant. This feature has been often considered in the literature on  $\nu_R$  signals at the LHC—see e.g. [208, 97] and references therein. The  $3 \times 3$  unitary matrix can be parametrized as follows

$$U = \begin{pmatrix} -c_\theta & \frac{is_\theta}{\sqrt{2}} & \frac{s_\theta}{\sqrt{2}} \\ 0 & \frac{-i}{\sqrt{2}} & \frac{1}{\sqrt{2}} \\ s_\theta & \frac{ic_\theta}{\sqrt{2}} & \frac{c_\theta}{\sqrt{2}} \end{pmatrix}, \quad \theta = \arctan\left(\frac{m_D}{M_R}\right). \quad (5.34)$$

Using this form of  $U$  in Eqs. (5.7) and (5.8), we obtain

$$G_Z = \frac{g}{2c_W} \begin{pmatrix} c_\theta^2 & \frac{-ic_\theta s_\theta}{\sqrt{2}} & \frac{-c_\theta s_\theta}{\sqrt{2}} \\ \frac{ic_\theta s_\theta}{\sqrt{2}} & \frac{s_\theta^2}{2} & \frac{-is_\theta^2}{2} \\ \frac{-c_\theta s_\theta}{\sqrt{2}} & \frac{is_\theta^2}{2} & \frac{s_\theta^2}{2} \end{pmatrix}, \quad G_R = g_R \begin{pmatrix} -s_\theta^2 & \frac{-ic_\theta s_\theta}{\sqrt{2}} & \frac{-c_\theta s_\theta}{\sqrt{2}} \\ \frac{ic_\theta s_\theta}{\sqrt{2}} & \frac{s_\theta^2}{2} & \frac{i(1+c_\theta^2)}{2} \\ \frac{-c_\theta s_\theta}{\sqrt{2}} & \frac{-i(1+c_\theta^2)}{2} & \frac{s_\theta^2}{2} \end{pmatrix}, \quad (5.35)$$

$$G_W = \frac{g}{\sqrt{2}} \begin{pmatrix} -c_\theta & \frac{is_\theta}{\sqrt{2}} & \frac{s_\theta}{\sqrt{2}} \end{pmatrix}. \quad (5.36)$$

We can now perform the summation in Eqs. (5.18)-(5.19). Expanding the result as a Taylor series in  $s_\theta$  (assuming  $s_\theta \ll 1$ ) and only retaining the dominant contribution, we obtain

$$g_{\text{eff},W} = \frac{g^2 c_\theta^2 m^2 s_\theta^2}{32\pi^2 m_W^2} g_R, \quad (5.37)$$

$$g_{\text{eff},Z} = -Q_Z^{(f)} \frac{g^2 c_\theta^2 m^2 s_\theta^2}{32\pi^2 m_Z^2 c_W^2} g_R, \quad (5.38)$$

where  $m \equiv \sqrt{m_D^2 + M_R^2}$  and

$$m_D = m s_\theta, \quad M_R = m c_\theta. \quad (5.39)$$

Expressing the results in terms of  $G_F$  and assuming  $s_\theta \ll 1$ , we obtain

$$g_{\text{eff},W} = \frac{\sqrt{2} G_F m_D^2}{8\pi^2} g_R, \quad (5.40)$$

$$g_{\text{eff},Z} = -Q_Z^{(f)} \frac{\sqrt{2} G_F m_D^2}{8\pi^2} g_R. \quad (5.41)$$

We comment here that the above UV-complete and anomaly-free model built on  $1 \nu_L + 2 \nu_R$  can be straightforwardly generalized to  $3 \nu_L + 2n \nu_R$  where half of the right-handed neutrinos have opposite  $U(1)_R$  charges to the other half. Such a generalization can accommodate the realistic three-neutrino mixing measured in neutrino oscillation experiments.

### 5.3.3 Example C: $3 \nu_L + 3 \nu_R$ with diagonal $M_R$

The most general case with three  $\nu_L$  and an arbitrary number of  $\nu_R$  is complicated and often impossible to be computed analytically. Here we consider an analytically calculable example with  $3 \nu_L + 3 \nu_R$  and the following form of the neutrino mass matrix:

$$\begin{pmatrix} 0_{3 \times 3} & m_D \\ m_D^T & M_R \end{pmatrix} = \begin{pmatrix} U_L^* & 0 \\ & I_{3 \times 3} \end{pmatrix} \begin{pmatrix} 0_{3 \times 3} & m_D^{(d)} \\ m_D^{(d)} & M_R^{(d)} \end{pmatrix} \begin{pmatrix} U_L^\dagger & 0 \\ & I_{3 \times 3} \end{pmatrix}, \quad (5.42)$$

$$m_D^{(d)} = \text{diag}(m_{D1}, m_{D2}, m_{D3}), \quad M_R^{(d)} = \text{diag}(M_{R1}, M_{R2}, M_{R3}),$$

where  $U_L$  is a  $3 \times 3$  unitary matrix. Eq. (5.42) is not the most general form, but at least it can accommodate the realistic low-energy neutrino mixing responsible for neutrino oscillation.

The mass matrix in this case can be diagonalized by a  $6 \times 6$  unitary matrix:

$$U'^T \begin{pmatrix} 0_{3 \times 3} & m_D^{(d)} \\ m_D^{(d)} & M_R^{(d)} \end{pmatrix} U' = \text{diag}(m_1 s_{\theta_1}^2, m_2 s_{\theta_2}^2, m_3 s_{\theta_3}^2, m_1 c_{\theta_1}^2, m_2 c_{\theta_2}^2, m_3 c_{\theta_3}^2), \quad (5.43)$$

where  $(s_{\theta_i}, c_{\theta_i}) \equiv (\sin \theta_i, \cos \theta_i)$  and

$$m_i = \sqrt{4m_{Di}^2 + M_{Ri}^2}, \quad \theta_i = \frac{1}{2} \arctan \left( \frac{2m_{Di}}{M_{Ri}} \right). \quad (5.44)$$

The unitary matrix  $U'$  can be parametrized as follows

$$U' = \begin{pmatrix} -iC_\theta & S_\theta \\ iS_\theta & C_\theta \end{pmatrix}, \quad (5.45)$$

where

$$C_\theta = \text{diag}(c_{\theta_1}, c_{\theta_2}, c_{\theta_3}), \quad S_\theta = \text{diag}(s_{\theta_1}, s_{\theta_2}, s_{\theta_3}). \quad (5.46)$$

Thus, the final unitary matrix  $U$  that diagonalizes the original mass matrix is given by

$$U = \begin{pmatrix} U_L & 0 \\ & I_{3 \times 3} \end{pmatrix} \begin{pmatrix} -iC_\theta & S_\theta \\ iS_\theta & C_\theta \end{pmatrix} = \begin{pmatrix} -iU_L C_\theta & U_L S_\theta \\ iS_\theta & C_\theta \end{pmatrix}. \quad (5.47)$$

Substituting it in Eqs. (5.7) and (5.8), we obtain

$$G_Z = \frac{g}{2c_W} \begin{pmatrix} C_\theta^2 & iC_\theta S_\theta \\ -iC_\theta S_\theta & S_\theta^2 \end{pmatrix}, \quad G_R = g_R Q_R \begin{pmatrix} S_\theta^2 & -iC_\theta S_\theta \\ iC_\theta S_\theta & C_\theta^2 \end{pmatrix}, \quad (5.48)$$

$$G_W = \frac{g}{\sqrt{2}} U_L \begin{pmatrix} -iC_\theta & S_\theta \end{pmatrix}, \quad Q_R = \text{diag}(Q_{R1}, Q_{R2}, Q_{R3}). \quad (5.49)$$

Next, we perform the summation in Eqs. (5.18)-(5.19), expand the result in  $s_{\theta_i}$ , and retain the dominant contribution. The final result reads

$$g_{\text{eff},W}^{\alpha\beta} = \sum_i -U_L^{\beta i} (U_L^{\alpha i})^* Q_{Ri} \frac{\sqrt{2} G_F m_{Di}^2}{8\pi^2} g_R, \quad (5.50)$$

$$g_{\text{eff},Z} = \sum_i Q_Z^{(f)} Q_{Ri} \frac{\sqrt{2} G_F m_{Di}^2}{8\pi^2} g_R. \quad (5.51)$$

In the approximation that the  $\nu_L$ - $\nu_R$  mixing is small, the  $3 \times 3$  unitary matrix  $U_L$  is almost

identical to the PMNS matrix. Due to the presence of off-diagonal entries in  $U_L$ ,  $g_{\text{eff},W}^{\alpha\beta}$  is generally not flavor diagonal and might lead to observable lepton flavor violation, which will be discussed in Sec. 5.5.

## 5.4 Dark photon masses and technical naturalness

In this section, we argue that despite being a free parameter, the mass of the  $\nu_R$ -philic dark photon  $m_{Z'}$  is potentially related to the gauge coupling according to 't Hooft's technical naturalness [209]. Generally speaking, from the consideration of model building and the stability of  $m_{Z'}$  under loop corrections, we expect that  $m_{Z'}$  is related to  $g_R$  by

$$m_{Z'} \gtrsim g_R \Lambda_{\text{breaking}}, \quad (5.52)$$

where  $\Lambda_{\text{breaking}}$  stands for the symmetry breaking scale of  $U(1)_R$ . Although without UV completeness we cannot have a more specific interpretation of Eq. (5.52), we would like to discuss a few examples to show how  $m_{Z'}$  is related to  $g_R$ .

First, let us consider that both  $m_{Z'}$  and  $M_R$  arise from a scalar singlet  $\phi$  charged under  $U(1)_R$  with  $\langle\phi\rangle = v_R \neq 0$ . This leads to  $m_{Z'} \sim g_R v_R$  and  $M_R \sim y_R v_R$  where  $y_R$  is the Yukawa coupling of  $\phi$  to  $\nu_R$ . In this case, we consider  $v_R$  as the symmetry breaking scale  $\Lambda_{\text{breaking}}$  so the tree-level relation  $m_{Z'} \sim g_R v_R$  is compatible with Eq. (5.52). The Yukawa coupling has an upper bound from perturbativity,  $y_R \lesssim 4\pi$ , which implies that  $m_{Z'}/M_R \sim g_R/y_R \gtrsim 4\pi g_R$ , or

$$m_{Z'}^2 \gtrsim \frac{g_R^2}{16\pi^2} M_R^2. \quad (5.53)$$

In the absence of a specific symmetry breaking mechanism, we can also obtain Eq. (5.53) purely from loop corrections to  $m_{Z'}$ . If  $M_R$  breaks the  $U(1)_R$  symmetry, the  $Z'$ - $Z'$  vacuum polarization amplitude generated by a  $\nu_R$  loop is  $\Pi^{\mu\nu}(q^2) \sim \frac{g_R^2}{16\pi^2} [\mathcal{O}(M_R^2)g^{\mu\nu} + \mathcal{O}(1)q^\mu q^\nu]$ , which implies that the loop correction to  $m_{Z'}^2$  is of the order of  $\frac{g_R^2}{16\pi^2} M_R^2$ . Therefore, to

make the theory technically natural, the physical mass should not be lower than the loop correction.

Note, however, that Eq. (5.53) is based on the assumption that  $M_R$  breaks the  $U(1)_R$  symmetry. If all the Majorana mass terms fully respect  $U(1)_R$ , such as Example B in Sec. 5.3, then the symmetry breaking scale can be lower, e.g., determined by  $m_D$ . Indeed, for the UV complete model in Example B, the symmetry breaking scale is determined by the VEV of the new Higgs doublet  $H'$  so at tree level we have  $m_{Z'} \sim g_R \langle H' \rangle$  and  $m_D \sim y_D \langle H' \rangle$ . Then using the perturbativity bound on  $y_D$ , we obtain

$$m_{Z'}^2 \gtrsim \frac{g_R^2}{16\pi^2} m_D^2. \quad (5.54)$$

Finally, we comment on the possible mass correction from  $Z$ - $Z'$  mixing. According to the calculation in Appendix C.1, the vacuum polarization diagram leads to mass mixing between  $Z$  and  $Z'$ :

$$\mathcal{L}_{ZZ' \text{ mass}} = \frac{1}{2} (Z, Z')^\mu \begin{pmatrix} m_{Z_0}^2 & m_X^2 \\ m_X^2 & m_{Z'_0}^2 \end{pmatrix} \begin{pmatrix} Z \\ Z' \end{pmatrix}_\mu, \quad (5.55)$$

where  $m_{Z_0}$  and  $m_{Z'_0}$  denote tree-level masses and

$$m_X^2 = \frac{g_R Q_R g}{64\pi^2 \cos \theta_W} m_D^2. \quad (5.56)$$

Here  $m_X^2$  causes  $Z - Z'$  mixing and the mixing angle is roughly  $\frac{m_X^2}{|m_{Z_0}^2 - m_{Z'_0}^2|}$ , which must be small. Otherwise, the SM neutral current would be significantly modified and become inconsistent with electroweak precision data. Taking the approximation  $m_X^2 \ll |m_{Z_0}^2 - m_{Z'_0}^2|$ , we obtain

$$m_Z^2 \simeq m_{Z_0}^2 + \frac{m_X^4}{(m_{Z_0}^2 - m_{Z'_0}^2)}, \quad m_{Z'}^2 \simeq m_{Z'_0}^2 - \frac{m_X^4}{(m_{Z_0}^2 - m_{Z'_0}^2)}. \quad (5.57)$$

Hence we conclude that the mass correction from  $Z$ - $Z'$  mixing is

$$\delta m_{Z'}^2 \sim \frac{g_R^2}{(64\pi^2)^2} \frac{m_D^4}{|m_{Z_0}^2 - m_{Z'_0}^2|}, \quad (5.58)$$

where we have neglected some  $\mathcal{O}(1)$  quantities. This mass correction is generally smaller than the right-hand side of Eq. (5.54) because  $m_D$  cannot be much above the electroweak scale.

To summarize, here we draw a less model-dependent conclusion that without fine-tuning, the  $\nu_R$ -philic dark photon mass is expected to be above the lower bound in Eq. (5.53) or Eq. (5.54), depending on whether  $M_R$  breaks the  $U(1)_R$  symmetry or not, respectively.

## 5.5 Phenomenology

In the previous two sections, we have derived the loop-induced couplings and also argued that from technical naturalness there is a lower bound on the dark photon mass. The results indicate the theoretically favored regime of the mass and the couplings. Therefore, to address the question of how dark the  $\nu_R$ -philic dark photon would be, we shall inspect whether and to what extent the theoretically favored regime could be probed by current and future experiments.

In our model, there are effective couplings to both leptons and quarks with comparable strengths. So the experimental constraints on this model are very similar to those on the  $B - L$  model<sup>26</sup>. Below we discuss a variety of known bounds that could be important for the  $\nu_R$ -philic dark photon. An overview of existing bounds is presented in Fig. 5.2, and the prospect of upcoming experiments in Fig. 5.3.

---

<sup>26</sup> See e.g. Fig. 8 in [210], Fig. 3 in [211], and Fig. 13 in [205]

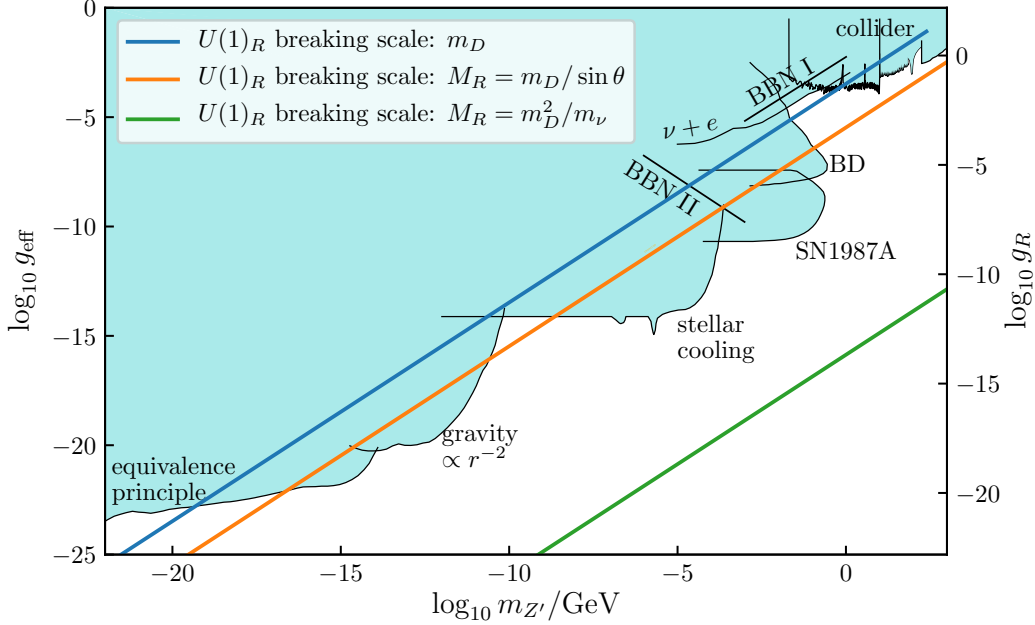


Fig. 5.2: The  $\nu_R$ -philic dark photon confronted with known experimental constraints. Here  $g_{\text{eff}}$  is the loop-induced coupling of  $Z'$  to electrons. The quark couplings are of the same order of magnitude as  $g_{\text{eff}}$  and we have ignored the difference between them when recasting constraints on quark couplings. The theoretically favored values of  $g_{\text{eff}}$  are below the solid blue, orange, or green lines, assuming  $U(1)_R$  breaks at the scale of  $m_D = 246$  GeV,  $M_R = 24.6$  TeV, or  $M_R \sim 10^{14}$  GeV (Type I seesaw), respectively. The collider bound consists of BaBar, LHCb, LEP, and LHC 8 TeV limits—see the text or Fig. 5.3 for more details.

## 5.5.1 Experimental limits

### 5.5.1.1 Collider searches

With effective couplings to electrons and quarks, dark photons could be produced directly in  $e^+e^-$  (BaBar, LEP) and hadron colliders (LHC), typically manifesting themselves as resonances in collider signals. For  $m_{Z'} \gtrsim 175$  GeV ( $t$  quark resonance), LHC data put the strongest bound via Drell-Yan production and detection of leptonic final states ( $pp \rightarrow Z' \rightarrow \ell^+\ell^-$ ). At lower masses when  $m_{Z'}$  is close to the  $Z$  pole, electroweak precision tests (EWPT, including LEP measurement and other electroweak precision observables) become more important. A dedicated analysis on LHC and EWPT bounds and future prospects can be found in Ref. [212]. For  $m_{Z'}$  below the  $Z$  pole but above 10 GeV, according to the analyses in [205], the most stringent constraint comes from LHCb di-muon ( $Z' \rightarrow \mu^+\mu^-$ )

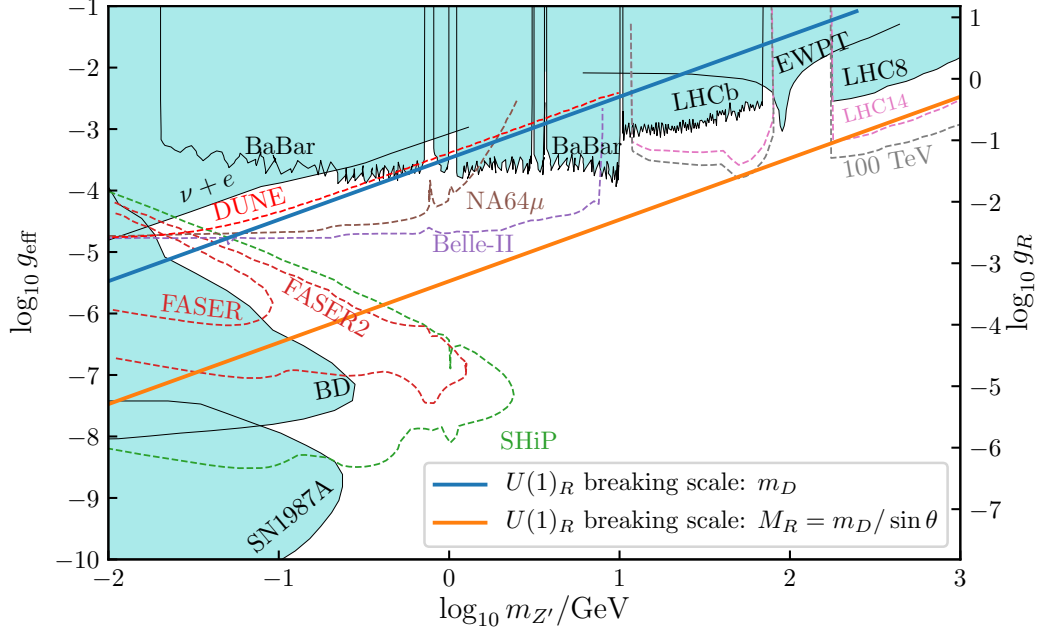


Fig. 5.3: Sensitivity of future experiments (SHiP, FASER, Belle-II) on the  $\nu_R$ -phillic dark photon. Here  $g_{\text{eff}}$  is the loop-induced coupling of  $Z'$  to electrons. The quark couplings are of the same order of magnitude as  $g_{\text{eff}}$  and we have ignored the difference between them when recasting constraints on quark couplings. The theoretically favored values of  $g_{\text{eff}}$  is below the solid blue or orange lines, assuming  $U(1)_R$  breaks at the scale of  $m_D = 246$  GeV or  $M_R = 24.6$  TeV, respectively.

measurements [213]. Below 10 GeV, the BaBar experiment [214] provides more stringent constraints via  $e^+e^- \rightarrow \gamma Z'$  where  $Z'$  may or may not decay to visible final states. In Figs. 5.2 and 5.3, we present all aforementioned constraints (for compactness in Fig. 5.2 they are labeled together as the collider bound). Besides, there is also an indirect LEP bound on four-fermion effective interactions—see Sec. 3.5.2 in Ref. [215]. We find that this bound approximately corresponds to  $g_{\text{eff}}/m_{Z'} \lesssim (4.4 \text{ TeV})^{-1}$ , which is weaker than the aforementioned collider bounds and hence not shown in Figs. 5.2 and 5.3.

### 5.5.1.2 Beam dump and neutrino scattering bounds

For  $1 \text{ MeV} \lesssim m_{Z'} \lesssim 100 \text{ MeV}$ , beam dump (BD) and neutrino scattering experiments become important. BD experiments search for dark photons by scattering an electron/proton beam on fixed targets and looking for dark particles that might be produced and subsequently

decay after the shield to visible particles such as electrons. A compilation of existing BD bounds from SLAC E141, SLAC E137, Fermilab E774, Orsay, and KEK experiments can be found in [216]. Note that these BD bounds relies on  $Z' \rightarrow e^+e^-$  decay, which implies that such bounds do not apply for  $m_{Z'} \lesssim 2m_e$ . Nonetheless, below 1 MeV there are much stronger bounds from cosmological and astrophysical observations hence for simplicity we do not show the invalidity of BD bounds below 1 MeV. The combined BD bound adopted in this work is taken from [211].

The dark photon in our model could contribute to elastic neutrino scattering by a new neutral-current-like process. Current data from elastic neutrino-electron (CHARM-II [217, 218], TEXONO [219], GEMMA [220], Borexino [221], etc.) and neutrino-nucleus (COHERENT [222]) scattering are all well consistent with the SM predictions. By comparing the results in Refs. [223, 181, 224], we find that the COHERENT bound is weaker than  $\nu + e$  scattering bounds, among which the most stringent ones come from CHARM-II, TEXONO, and GEMMA. So the combined result from these experiments is taken from Ref. [224] and presented in Figs. 5.2 and 5.3. The future DUNE experiment will be able to further improve the measurement of elastic neutrino scattering [225]. We adopt the DUNE sensitivity from Ref. [226] and present it in Fig. 5.3.

### 5.5.1.3 Astrophysical and cosmological bounds

Astrophysical bounds on dark photons are usually derived from energy loss in celestial bodies such as the sun, red giants, horizontal branch stars, and supernovae. Dark photons may contribute to stellar energy loss directly via dark photon free streaming or indirectly via neutrino production. The enhanced energy loss rate could alter stellar evolution on the horizontal branch in the Hertzsprung-Russell diagram. This sets the strongest limit for sub-MeV dark photons [227]. For smaller  $m_{Z'}$ , there are also similar bounds from the sun and red giants [227]. We adopt a combined bound from Ref. [210] with energy loss via neutrinos taken into account, and refer to it as the stellar cooling bound in Fig. 5.2.

The observation of SN1987A can be used to set strong limits on the effective coupling when  $m_{Z'} \lesssim \mathcal{O}(100)$  MeV [228]. The resulting bound further excludes the space below BD constraints by about three orders of magnitude.

In Fig. 5.2 we also show two bounds derived from the effect of  $Z'$  on big bang nucleosynthesis (BBN). The effect of  $Z'$  on BBN is two-fold: if  $Z'$  is light and dominantly decays to invisible states, it would increase the effective number of relativistic dark species  $N_{\text{eff}}$ . We refer to the bound derived from this effect as the BBN II bound. If  $Z'$  is heavy, it decays before neutrino decoupling and does not contribute to  $N_{\text{eff}}$  directly but the neutrino decoupling temperature could be modified if  $g_{\text{eff}}^2/m_{Z'}^2$  is comparable to  $G_F$  (referred to as BBN I). Among various studies on this subject (see e.g. [169, 229, 230, 231, 232]), we adopt the bounds from [169] for the  $B - L$  model and label them as BBN I and BBN II in Fig. 5.2.

#### 5.5.1.4 Charged lepton flavor violation

The loop-induced couplings do not necessarily conserve lepton flavors, as indicated by Eq. (5.50). Note, however, that neither the  $W$ -diagram nor the  $Z$ -diagram causes flavor violation in the quark sector. In the presence of flavor-changing couplings of  $Z'$  to charged leptons, there are strong constraints from charged lepton flavor violating (CLFV) decay such as  $\ell_\alpha \rightarrow \ell_\beta \nu \bar{\nu}$ ,  $\mu \rightarrow 3e$  [233],  $\pi^0 \rightarrow e\mu$ ; from  $\mu \rightarrow e$  conversion in muonic atoms [234], and from the non-observation of muonium-antimuonium transitions [235]. Constraints from  $\ell_\alpha \rightarrow \ell_\beta \gamma$  are weaker since they arise only from two-loop contributions. We do not include CLFV bounds in Figs. 5.2 and 5.3 because such bounds depend on the flavor structure of  $m_D$  which in the Casas-Ibarra parametrization [236]:  $m_D = iU_L^* \sqrt{m_\nu} R^T \sqrt{M_R}$  where  $R$  is a complex orthogonal matrix, depends not only on the PMNS matrix  $U_L$  but also on the  $R$  matrix. The effective flavor-changing couplings in the presence of non-trivial  $R$  are more complicated and we leave them for future work.

### 5.5.1.5 Long-range force searches

Below 0.1 eV, laboratory tests of gravity and gravity-like forces provide highly restrictive constraints, including high precision tests of the inverse-square law (gravity  $\propto r^{-2}$ ) [237, 238] and of the equivalence principle via torsion-balance experiments [239] and lunar laser-ranging (LLR) measurements [239, 240]. Besides, measurements of the Casimir effect [241] could set a limit that is slightly stronger than that from the inverse-square law when  $0.05 \lesssim m_{Z'}/\text{eV} \lesssim 0.1$ , which is not presented in Fig. 5.2. Also not presented here is the bound from black hole superradiance [242], which would only enter the lower left corner in Fig. 5.2. We refer to our previous work [207] for more detailed discussions on the long-range force searches and present only the dominant constraints from torsion-balance tests of the inverse-square law and the equivalence principle. We comment here that neutrino oscillation could also be used to probe long-range forces [157, 243, 244, 12] but similar to the aforementioned CLFV bounds, the flavor structure cannot be simply taken into account by the PMNS matrix. Hence we leave this possibility to future studies.

### 5.5.1.6 Prospect of upcoming experiments

Future hadron collider searches could significantly improve the experimental limits on heavy dark photons by almost one order of magnitude, as illustrated in Fig. 5.3 by the LHC 14 TeV and future 100 TeV collider sensitivity [212]. Moreover, several LHC-based experiments searching for displaced dark photon decays such as FASER [245], MATHUSLA [246, 247], and CodexB [248] will improve the BD bound in the low-mass regime. And the future SHiP experiment [249, 250] will substantially broaden the BD bound regarding both the dark photon mass and coupling. The current BaBar bound may be superseded by future bounds from Belle-II [251] and a muon run of NA64 [252, 253]. Hence a large part of the space that is often considered for dark photons ( $20\text{MeV} \lesssim m_{Z'} \lesssim 10 \text{ GeV}$  and  $10^{-8} \lesssim g_{\text{eff}} \lesssim 10^{-3}$ ) will be probed by future experiments. Here we selectively present the sensitivity curves of SHiP, FASER, NA64 $\mu$ , and Belle-II. Most of them are taken from Ref. [205], except for the

FASER/FASER2 sensitivity which is taken from Ref. [254].

### 5.5.2 How dark is the $\nu_R$ -philic dark photon?

Since the effective coupling  $g_{\text{eff}}$  is proportional to  $g_R$ , by tuning down  $g_R$  one can obtain arbitrarily small  $g_{\text{eff}}$  to circumvent all constraints presented in Figs. 5.2 and 5.3. On the other hand, if  $g_R$  is very small, then the lower bounds of  $m_{Z'}$  discussed in Sec. 5.4 will also be alleviated, implying that the dark photon could be very light. Taking Eqs. (5.40), (5.41) and (5.54), we plot the blue lines in Figs. 5.2 and 5.3 with  $m_D = v = 246$  GeV and  $g_R$  varying from 0 to  $4\pi$ . The space below the blues lines is the theoretically favored region if only the Dirac mass term breaks the  $U(1)_R$  symmetry. This applies to the UV complete model in Sec. 5.3.2.

If the Majorana mass term also breaks the  $U(1)_R$  symmetry, then the lower bound of  $m_{Z'}$  is set by Eq. (5.53) instead of Eq. (5.54). In the standard type I seesaw, we have  $M_R \sim m_D^2/m_\nu$  which implies that for  $m_\nu = 0.1$  eV and  $m_D = 246$  GeV, the  $U(1)_R$  symmetry breaks at a high energy scale around  $10^{14}$  GeV. For this case, we plot the green curve in Fig. 5.2. As shown in Fig. 5.2, even though with  $g_R \lesssim 10^{-11}$  the mass of  $m_{Z'}$  could be below the electroweak scale or lower, the effective coupling is many orders of magnitude below any of known experimental limits.

The inaccessibly large  $m_{Z'}$  of the green curve is due to the underlying connection between  $m_\nu$  and  $M_R$  in the standard type I seesaw. In some alternative neutrino mass models such as inverse seesaw [255], the scale of  $M_R$  is decoupled from  $m_\nu$ , which allows for a sizable  $\nu_L$ - $\nu_R$  mixing even when  $M_R$  is reduced to the TeV scale, and has motivated many studies on collider searches for right-handed neutrinos—see Ref. [97] for a review. Here for illustration we simply set  $M_R = m_D/\sin\theta$  with  $m_D = 246$  GeV and  $\sin\theta = 10^{-2}$ , which ensures that  $\nu_R$  is sufficiently heavy to avoid all current collider bounds. The possibility of collider-accessible  $\nu_R$  involves more complicated phenomenology which is beyond the scope of this work. The strength of  $g_{\text{eff}}$  and the lower bound of  $m_{Z'}$  in this case is presented by the orange lines in

Figs. 5.2 and 5.3.

Now confronting the theoretically favored  $g_{\text{eff}}$  and  $m_{Z'}$  of the aforementioned three scenarios with the experimental limits, we can see that only when the  $U(1)_R$  breaking scale is determined by  $m_D$  or  $M_R = m_D/\sin\theta$  with sizable  $\sin\theta$ , the  $\nu_R$ -phillic dark photon could be of phenomenological interest. The former could potentially give rise to observable effects in long-range force searches, astrophysical observations, beam dump and collider experiments. The latter, albeit beyond the current collider bounds, might be of importance to future collider searches. In addition, the SHiP experiment will be able to considerably dig into the parameter space of the latter.

## 5.6 Conclusion

The  $\nu_R$ -phillic dark photon  $Z'$  which arises from a hidden  $U(1)_R$  gauge symmetry and at the tree-level couples only to the right-handed neutrinos, interacts weakly with SM particles via loop-level processes—see Fig. 5.1. Assuming the most general Dirac and Majorana mass matrices, we have derived loop-induced couplings of  $Z'$  to charged leptons and quarks. The results are given in Eqs. (5.18) and (5.19), which are applied to a few examples including a UV complete model. For a special case with three  $\nu_L$  and three  $\nu_R$ , the loop-induced couplings are given by Eqs.(5.50) and (5.51). We have also discussed potential connections between the mass  $m'_Z$  and the gauge coupling  $g_R$  from the point of view of technical naturalness, which implies that  $m'_Z$  should be generally above the lower bound in Eq. (5.53) if  $M_R$  breaks  $U(1)_R$ , or the bound in Eq. (5.54) if only  $m_D$  breaks the symmetry.

The theoretically favored values of the loop-induced couplings are confronted with experimental constraints and prospects in Figs. 5.2 and 5.3. We find that the magnitude of loop-induced couplings allows current experiments to put noteworthy constraints on it. Future beam dump experiments like SHiP and FASER together with upgraded collider searches will have substantially improved sensitivity on such a dark photon.

Thus, we conclude that the  $\nu_R$ -philic dark photon might not be inaccessibly dark and could be of importance to a variety of experiments!

## Chapter 6

# Resonant Leptogenesis in a Model of Discrete Flavor and CP Symmetries<sup>27</sup>

*"Science progresses best when observations force us to alter our preconceptions."*

- Vera Rubin

## 6.1 Introduction

Most recent precise measurement done by Planck Collaboration (2018) [16] sets the matter-antimatter asymmetry parameter  $\eta_B$

$$\eta_B = \frac{n_b - n_{\bar{b}}}{n_\gamma} = (6.12 \pm 0.08) \times 10^{-10} \quad (6.1)$$

This can be explained through the dynamical generation of baryon asymmetry for which required basic ingredients includes the 3 Sakharov conditions. All these conditions are met by resonant leptogenesis, which not only lowers the scale of  $\eta_B$  production and predicts TeV-scale accessible particles but also can be embedded minimally into an extension of SM through type-I seesaw mechanism for neutrino masses. The central idea of leptogenesis is the production of leptonic asymmetry in early Universe which is then converted to baryonic

---

<sup>27</sup> This chapter is based on upcoming work : **Garv Chauhan** and P. S. Bhupal Dev, "Resonant Leptogenesis, Neutrinoless Double Beta Decay and Collider Signals in a Model of Discrete Flavor and CP Symmetries", (to be submitted).

asymmetry of the Universe (BAU) through B-L conserving electroweak sphaleron interactions. This mechanism satisfies all 3 Sakharov conditions : presence of CP violation in the leptonic sector through complex neutrino Yukawa matrix  $Y_D$  and/or lepton mixing matrix  $U_{PMNS}$  phases, lepton number violation (LNV) occurs due to the Majorana nature of the heavy right-handed (RH) neutrinos and condition for departure from thermal equilibrium is met, when RH neutrino decay rate falls below the Hubble expansion rate i.e.  $\Gamma_N \leq H$ . Thus, leptogenesis can connect neutrino mass mechanism and production of matter-antimatter asymmetry.

Leptogenesis depends on both low-and high- scale neutrino data while current experiments have access only to the low-energy neutrino data. Since, there is no relation between low-and high- scale neutrino data, this implies high energy neutrino parameters are free parameters in the leptogenesis mechanism. One way forward can be paved by patterns in the neutrino mixing matrix, if generated due to the presence of flavor symmetries. If true, this can lead to connections between high and low energy phenomenology, which can provide complementary probes for the leptogenesis scenario through low-energy signatures. In this chapter, we will look at the idea of residual flavor and CP symmetries that determine lepton mixing angles, low- and high energy CP phases with only one free parameter. This helps us not only connect the high- and low- energy phenomena but also explains the leptonic mixing angles along with CP phases. This has a major impact on predictions in low-energy experiments such as long-lived particle (LLP) searches ,  $0\nu\beta\beta$  experiments and colliders.

We consider a type-I seesaw scenario with a flavor  $G_f$  and a CP symmetry that strongly constrain lepton mixing angles, and both low- and high-energy CP phases [256]. The three right-handed (RH) neutrinos  $N_i$  have (almost) degenerate masses. Their decays are responsible for the generation of the baryon asymmetry  $\eta_B$  of the Universe via resonant leptogenesis [257, 258]. At points of *enhanced residual symmetry* (ERS), the RH neutrino  $N_3$  can be long-lived enough in order to be detected with the MATHUSLA detector [246], while  $N_{1,2}$  can be searched for via either prompt or displaced vertex signals at the LHC [259, 260].

This chapter is organised as follows : In Sec. 6.2, we discuss the embedding of lepton sector and light neutrinos (with masses arising from the type-I seesaw mechanism) with three right-handed (RH) neutrino, in a given flavor group  $G_f$  and CP symmetry group. In Sec. 6.3, we discuss the residual symmetries and the form of the corresponding representation matrices for the different cases, along with additional constraints imposed from light neutrino masses. In Sec. 6.4, we discuss the CP asymmetries produced in our scenario through out-of-equilibrium decays of the RH neutrinos. In Sec. 6.5, we study the decay lengths and branching ratios of the heavy right-handed neutrinos in different cases of lepton mixing. We also discuss the effects of Enhanced Residual Symmetry (ERS) points. In the next Sec. 6.6, we discuss the collider signatures in our scenario and probe further to understand their complementary nature to the prospects of leptogenesis. We probe the collider signatures at the LHC for the production of RH neutrinos through the low background lepton number violating (LNV) processes. In Sec. 6.7, we study the correlation of low energy and high energy CP phases through effective Majorana mass and  $\eta_B$ . Finally we conclude in Sec. 6.8.

## 6.2 Framework

We focus on the lepton sector and assume that light neutrino masses arise from the type-I seesaw mechanism [30, 125, 32, 33] with three right-handed neutrinos. The latter have nearly degenerate masses of the order of 1 TeV. We consider a scenario in which a flavor and a CP symmetry and their residual groups  $G_l$  and  $G_\nu$  determine the form of the mass matrices of charged leptons and neutrinos, respectively.

For flavor symmetry  $G_f$ , we use a group of the form  $\Delta(6n^2)$  with  $n$  even and  $3 \nmid n$  [261, 9] which can be generated by the generators  $a$ ,  $b$ ,  $c$  and  $d$ .<sup>28</sup> These are given for the relevant representations in appendix D.1. The groups  $\Delta(6n^2)$  for  $n \geq 2$  are interesting, as they possess at least one irreducible, faithful, complex three-dimensional representation  $\mathbf{3}$ .<sup>29</sup> In

---

<sup>28</sup> We could also consider a group of the form  $\Delta(3n^2)$ . This is, however, contained in the corresponding group  $\Delta(6n^2)$  so that we can stick, without loss of generality, to the latter only.

<sup>29</sup> For  $n = 2$  the irreducible three-dimensional representations are real.

the following, we assign the three generations of LH leptons  $l_\alpha$ ,  $\alpha = e, \mu, \tau$ , to  $\mathbf{3}$ . RH charged leptons are assigned to the representation  $\mathbf{1}$ , the trivial singlet, of  $G_f$ , while three generations of RH neutrinos  $N_i$ ,  $i = 1, 2, 3$ , are unified in an irreducible, in general unfaithful, real representation  $\mathbf{3}'$  of  $G_f$  which requires the index  $n$  of the group  $\Delta(6n^2)$  to be even, see appendix D.1 for details.<sup>30</sup> Assigning LH leptons and RH neutrinos to these in general different three-dimensional representations of  $G_f$  is crucial, as the assignment  $l_\alpha \sim \mathbf{3}$  allows to fully explore the predictive power of  $G_f$  (and not only of one of its subgroups), while  $N_i \sim \mathbf{3}'$  permits the RH neutrinos to have a flavor-universal mass term without breaking  $G_f$  and the CP symmetry. In addition, we assume the existence of a  $Z_3$  symmetry, called  $Z_3^{(\text{aux})}$ , which is employed in order to distinguish the three right-handed charged leptons  $e_R$ ,  $\mu_R$  and  $\tau_R$  which are assigned to 1,  $\omega$  and  $\omega^2$  with  $\omega = e^{2\pi i/3}$ , whereas left-handed leptons and right-handed neutrinos are invariant under  $Z_3^{(\text{aux})}$ .

The CP symmetry imposed on the theory corresponds to an automorphism of  $G_f$  [262, 263]. They are represented by the CP transformation  $X(\mathbf{r})$  in the different (irreducible) representations  $\mathbf{r}$  of  $G_f$  and depend on the parameters determining the automorphism. For completeness, we show the form of the automorphisms and of  $X(\mathbf{r})$  for the relevant representations in appendix D.3.

The residual symmetries  $G_l$  and  $G_\nu$  are chosen as  $Z_3^{(\text{D})}$ , which is the diagonal subgroup of the group, generated by  $a$  of  $G_f$ , see appendix D.1, and the auxiliary symmetry  $Z_3^{(\text{aux})}$ , and  $Z_2 \times CP$ , where the  $Z_2$  symmetry is a subgroup of  $G_f$  and the CP symmetry the one of the underlying theory. In the following, the generator  $Z$  of the residual  $Z_2$  symmetry in the different representations  $\mathbf{r}$  is denoted as  $Z(\mathbf{r})$ . The  $Z_2$  symmetry and CP commute, i.e. they fulfil

$$X(\mathbf{r}) Z(\mathbf{r}) - Z(\mathbf{r})^* X(\mathbf{r}) = 0 \tag{6.2}$$

for all representations  $\mathbf{r}$  of  $G_f$ . The mismatch of the residual symmetries  $G_l$  and  $G_\nu$  determines the form of lepton mixing, has been discussed in particular for the groups  $\Delta(3n^2)$

---

<sup>30</sup> Only for  $n = 2$  this representation is faithful. This, however, does not affect our discussion.

and  $\Delta(6n^2)$ , in [9] as well as in [264]. It has been found that lepton mixing patterns can be classified according to four types, called Case 1, Case 2, Case 3a and Case 3b.1 in [264], which have different features. The form of the lepton mixing matrices for the four different types are shown in section 6.3.

The form of the charged lepton mass matrix  $m_l$ , the neutrino Yukawa coupling matrix  $Y_D$  and RH neutrino Majorana mass matrix  $M_R$  are determined by  $G_l$  and  $G_\nu$ . In the chosen basis, see appendix D.1, the mass matrix  $m_l$  is diagonal and contains three independent parameters that correspond to the three different charged lepton masses. As  $m_l$  is diagonal, there is no contribution to lepton mixing from the charged lepton sector. As regards the neutrino sector, we take the neutrino Yukawa coupling matrix  $Y_D$  to be invariant under  $G_\nu$ , whereas the matrix  $M_R$  does neither break  $G_f$  nor CP. Being invariant under  $Z_2 \times CP$ , the matrix  $Y_D$ , in the basis in which left-handed fields are on the left and right-handed ones on the right, fulfils the following relations

$$Z^\dagger(\mathbf{3}) Y_D Z(\mathbf{3}') = Y_D \quad \text{and} \quad X^*(\mathbf{3}) Y_D X(\mathbf{3}') = Y_D^*. \quad (6.3)$$

The form of  $Y_D$  is thus<sup>31</sup>

$$Y_D = \Omega(\mathbf{3}) R_{ij}(\theta_L) \begin{pmatrix} y_1 & 0 & 0 \\ 0 & y_2 & 0 \\ 0 & 0 & y_3 \end{pmatrix} R_{kl}(-\theta_R) \Omega(\mathbf{3}')^\dagger. \quad (6.4)$$

The matrices  $\Omega(\mathbf{3})$  and  $\Omega(\mathbf{3}')$  are unitary and are determined by the form of the CP trans-

---

<sup>31</sup> We can re-write the conditions in Eq. (6.3) using the matrices  $\Omega(s)(\mathbf{3})$  and  $\Omega(s)(\mathbf{3}')$ , see Eq. (??), and find

$$\Omega(s)(\mathbf{3})^\dagger Y_D \Omega(s)(\mathbf{3}')$$

is real and can be diagonalized by two rotation matrices from the left and right, respectively,

$$\Omega(s)(\mathbf{3})^\dagger Y_D \Omega(s)(\mathbf{3}') = R_{ij}(\theta_L) \begin{pmatrix} y_1 & 0 & 0 \\ 0 & y_2 & 0 \\ 0 & 0 & y_3 \end{pmatrix} R_{kl}(-\theta_R).$$

formations  $X(\mathbf{3})$  and  $X(\mathbf{3}')$  in the representations of left-handed leptons and right-handed neutrinos, i.e. they fulfil

$$X(\mathbf{3}) = \Omega(\mathbf{3})\Omega(\mathbf{3})^T \quad \text{and} \quad X(\mathbf{3}') = \Omega(\mathbf{3}')\Omega(\mathbf{3}')^T. \quad (6.5)$$

As the choice of CP symmetry and thus the corresponding CP transformations  $X(\mathbf{3})$  is in general indicated by natural numbers, see e.g. the parameter  $s$  in Eq. (6.19), also the matrices  $\Omega(\mathbf{3})$  and  $\Omega(\mathbf{3}')$  (potentially) depend on these parameters. The matrices  $R_{ij}(\theta_L)$  and  $R_{kl}(\theta_R)$  denote rotations in the  $(ij)$  and  $(kl)$  plane,  $i, j, k, l = 1, 2, 3$  with  $i < j$  and  $k < l$ , through the angles  $\theta_L$  and  $\theta_R$ , respectively.<sup>32</sup> These angles are free parameters, i.e. not fixed by the residual symmetry  $G_\nu$ , and can take values in the range  $[0, \pi)$ . The planes, in which the rotations  $R_{ij}(\theta_L)$  and  $R_{kl}(\theta_R)$  act, are determined by the  $(ij)$ - and  $(kl)$ -subspaces of degenerate eigenvalues of the generator  $Z$  in the representation  $\mathbf{3}$  and  $\mathbf{3}'$ , when transformed with the matrix  $\Omega(\mathbf{3})$  and  $\Omega(\mathbf{3}')$ , respectively (examples can be found in the discussion of the different cases). In addition to these two angles,  $Y_D$  contains further three real parameters, namely the Yukawa couplings  $y_f$ ,  $f = 1, 2, 3$ . This has also been pointed out in [264]. The Dirac neutrino mass matrix  $m_D$  is in turn given by

$$m_D = Y_D \langle h \rangle \quad (6.6)$$

where  $\langle h \rangle \approx 174 \text{ GeV}$  is the VEV of the SM Higgs field. As  $M_R$  leaves  $G_f$  and CP invariant, its form is simply

$$M_R = M_N \begin{pmatrix} 1 & 0 & 0 \\ 0 & 0 & 1 \\ 0 & 1 & 0 \end{pmatrix} \quad (6.7)$$

---

<sup>32</sup> We define the rotations  $R_{ij}$ ,  $i < j$ , through the angle  $\theta$  in the  $(ij)$ -plane as follows

$$R_{12}(\theta) = \begin{pmatrix} \cos \theta & \sin \theta & 0 \\ -\sin \theta & \cos \theta & 0 \\ 0 & 0 & 1 \end{pmatrix}, \quad R_{13}(\theta) = \begin{pmatrix} \cos \theta & 0 & \sin \theta \\ 0 & 1 & 0 \\ -\sin \theta & 0 & \cos \theta \end{pmatrix}, \quad R_{23}(\theta) = \begin{pmatrix} 1 & 0 & 0 \\ 0 & \cos \theta & \sin \theta \\ 0 & -\sin \theta & \cos \theta \end{pmatrix}.$$

with  $M_N > 0$ , setting the mass scale of the RH neutrinos. The light neutrino mass matrix  $m_\nu$  follows from the type-I seesaw mechanism

$$m_\nu = m_D M_R^{-1} m_D^T. \quad (6.8)$$

As the charged lepton mass matrix  $m_l$  is diagonal, lepton mixing arises from the diagonalization of  $m_\nu$  only. In general, the resulting lepton mixing angles involve a combination of all parameters, appearing in  $Y_D$ . However, if

$$[\Omega(\mathbf{3}')^T M_R^{-1} \Omega(\mathbf{3}')^*, R_{kl}(\theta_R)] = 0, \quad (6.9)$$

see section 6.3 for such cases, the lepton mixing angles only depend on the free parameter  $\theta_L$  and the parameters, describing the flavor and CP symmetry as well as the residual symmetry  $G_\nu$ , i.e. we find then

$$U_{\text{PMNS}} = \Omega(\mathbf{3}) R_{ij}(\theta_L) K_\nu, \quad (6.10)$$

where  $K_\nu$  is a diagonal matrix with entries equal to  $\pm 1$  and  $\pm i$  and is necessary to make neutrino masses positive. This matrix is generally parametrized in the following form :

$$K_\nu = \begin{pmatrix} 1 & 0 & 0 \\ 0 & i^{k_1} & 0 \\ 0 & 0 & i^{k_2} \end{pmatrix}. \quad (6.11)$$

with  $k_{1,2} = 0, 1, 2, 3$ . We can verify that  $U_{\text{PMNS}}$  fulfils

$$U_{\text{PMNS}}^\dagger m_\nu U_{\text{PMNS}}^* = \text{diag}(m_1, m_2, m_3) \quad (6.12)$$

with the mass spectrum of the light neutrinos being determined by the Yukawa couplings

$y_f$ ,

$$m_f = \frac{y_f^2 \langle h \rangle^2}{M_N} \quad \text{for } f = 1, 2, 3. \quad (6.13)$$

As the Yukawa couplings are not constrained other than being real, the scenario can accommodate both neutrino mass orderings as well as a QD neutrino mass spectrum. The resulting PMNS mixing matrix in Eq. (6.10) coincides with the lepton mixing matrix, obtained in a scenario with three RH neutrinos [264], in which the mass matrix  $m_D$  is invariant under the entire flavor and CP symmetry, while the RH neutrino Majorana mass matrix  $M_R$  possesses the residual symmetry  $G_\nu$ . The requirement to accommodate the measured lepton mixing angles well further constrains the index  $n$  of  $G_f$  as well as the combination of residual symmetries  $G_e$  and  $G_\nu$ , as discussed in detail in [264].

In order to successfully generate the baryon asymmetry of the Universe via the mechanism of resonant leptogenesis, the masses of the RH neutrinos have to be, at least partly, (slightly) different. This can be achieved by corrections  $\delta M_R$  to the RH neutrino Majorana mass matrix. These corrections are expected to arise by (higher order) residual symmetry breaking effects which are generically present in model realizations. In the following, we consider corrections to  $M_R$  which are invariant under the residual symmetry  $G_e$ . The generator of  $G_e$  is represented in the representation of the RH neutrinos  $N_i$  as

$$a(\mathbf{3}') = \begin{pmatrix} 1 & 0 & 0 \\ 0 & \omega & 0 \\ 0 & 0 & \omega^2 \end{pmatrix}, \quad (6.14)$$

since  $N_i$  are not charged under the auxiliary symmetry  $Z_3^{(\text{aux})}$ . The correction  $\delta M_R$  must thus fulfil

$$a(\mathbf{3}')^T \delta M_R a(\mathbf{3}') = \delta M_R, \quad (6.15)$$

meaning it is of the form

$$\delta M_R = \kappa M_N \begin{pmatrix} 2 & 0 & 0 \\ 0 & 0 & -1 \\ 0 & -1 & 0 \end{pmatrix} \quad (6.16)$$

with  $\kappa$  being a small symmetry breaking parameter,  $\kappa \ll 1$ . The RH neutrino masses  $M_i$ ,  $i = 1, 2, 3$  acquire then a small correction

$$M_1 = M_N (1 + 2\kappa) \quad \text{and} \quad M_2 = M_3 = M_N (1 - \kappa). \quad (6.17)$$

## 6.3 Different Cases

In the following, we discuss the residual symmetries and the form of the corresponding representation matrices for the different cases Case 1, Case 2, Case 3a and Case 3b.1. We discuss additional constraints imposed from light neutrino masses and the constraints on the neutrino mass spectrum arising from imposing the condition in Eq. (6.3). Furthermore, we briefly repeat the results for lepton mixing and give numerical examples, as found in [264]. For Case 1, we also comment on special points corresponding to specific choices of the parameters  $\theta_L$  and  $\theta_R$ , that lead to enhanced residual symmetries of the Dirac neutrino Yukawa couplings.

### 6.3.1 Case 1

#### 6.3.1.1 Residual Symmetries

The residual  $Z_2$  symmetry in the neutrino sector is generated by

$$Z = c^{n/2} \quad (6.18)$$

which requires the index  $n$  of the flavor group  $\Delta(6n^2)$  to be even. The explicit form of  $Z$  in the irreducible, faithful, complex three-dimensional representation  $\mathbf{3}$  and in the irreducible, unfaithful, in general real three-dimensional representation  $\mathbf{3}'$  can be found in appendix D.1. As we see in section 6.3.1.2, due to the form of the generator  $Z$  in  $\mathbf{3}'$  for  $n$  divisible by four the Dirac neutrino Yukawa coupling matrix  $Y_D$  becomes singular so that the light neutrino mass is not viable. For this reason, we focus in the following on  $n$  not divisible by four.

The CP symmetry corresponds to the automorphism, given in Eq. (D.14) in appendix D.3, conjugated with the inner automorphism associated with the group transformation  $a b c^s d^{2s}$  with  $s = 0, 1, \dots, n - 1$ . The corresponding CP transformation  $X(s)$  reads in  $\mathbf{3}$

$$X(s)(\mathbf{3}) = a(\mathbf{3}) b(\mathbf{3}) c(\mathbf{3})^s d(\mathbf{3})^{2s} X_0(\mathbf{3}) \quad (6.19)$$

and in  $\mathbf{3}'$

$$X(s)(\mathbf{3}') = a(\mathbf{3}') b(\mathbf{3}') c(\mathbf{3}')^s d(\mathbf{3}')^{2s} X_0(\mathbf{3}') \quad (6.20)$$

and the explicit form of  $X(s)(\mathbf{3})$  and  $X(s)(\mathbf{3}')$  can be found in appendix D.3.

The matrix  $\Omega(s)(\mathbf{3})$ , derived from  $X(\mathbf{3})(s)$ , given in Eq. (??) in appendix D.3, can be chosen as

$$\Omega(s)(\mathbf{3}) = e^{i\phi_s} U_{\text{TB}} \begin{pmatrix} 1 & 0 & 0 \\ 0 & e^{-3i\phi_s} & 0 \\ 0 & 0 & -1 \end{pmatrix} \quad (6.21)$$

with

$$U_{\text{TB}} = \begin{pmatrix} \sqrt{2/3} & \sqrt{1/3} & 0 \\ -\sqrt{1/6} & \sqrt{1/3} & \sqrt{1/2} \\ -\sqrt{1/6} & \sqrt{1/3} & -\sqrt{1/2} \end{pmatrix} \quad (6.22)$$

and  $\phi_s = \frac{\pi s}{n}$ . Based only on theoretical requirements, the form of the matrix  $\Omega(s)(\mathbf{3}')$

depends on whether  $s$  is even or odd, i. e.

$$\Omega(s \text{ even})(\mathbf{3}') = U_{\text{TB}} , \quad (6.23)$$

and

$$\Omega(s \text{ odd})(\mathbf{3}') = U_{\text{TB}} \begin{pmatrix} i & 0 & 0 \\ 0 & 1 & 0 \\ 0 & 0 & i \end{pmatrix} . \quad (6.24)$$

Comparing these forms to the form of  $\Omega(s)(\mathbf{3})$ , we observe that they have the same structure and the crucial difference lies in the phase matrix multiplied from the right (overall phases are clearly irrelevant).

In order to determine the plane in which the rotation  $R_{ij}(\theta_L)$  acts, we look at

$$\Omega(s)(\mathbf{3})^\dagger Z(\mathbf{3}) \Omega(s)(\mathbf{3}) = \begin{pmatrix} -1 & 0 & 0 \\ 0 & 1 & 0 \\ 0 & 0 & -1 \end{pmatrix} , \quad (6.25)$$

implying that the rotation through  $\theta_L$  will be in the (13)-plane [9]. Similarly, we can find the plane in which the rotation  $R_{kl}(\theta_R)$  acts. The representation matrix  $Z(\mathbf{3}')$  for  $n$  not divisible by four reads after the transformation with  $\Omega(s)(\mathbf{3}')$  for both,  $s$  even as well as  $s$  odd,

$$\Omega(s)(\mathbf{3}')^\dagger Z(\mathbf{3}') \Omega(s)(\mathbf{3}') = \begin{pmatrix} -1 & 0 & 0 \\ 0 & 1 & 0 \\ 0 & 0 & -1 \end{pmatrix} , \quad (6.26)$$

meaning that also  $R_{kl}(\theta_R)$  acts in the (13)-plane.

### 6.3.1.2 Constraints from and on light neutrino mass spectrum

First, we discuss constraints on the possible choices of the residual symmetry  $G_\nu$  arising from the light neutrino mass spectrum. In order to find these we consider the form of the Dirac neutrino Yukawa coupling matrix  $Y_D$  fulfilling the conditions in Eq. (6.3). For  $n$  divisible by four  $Z(\mathbf{3}')$  is given by Eq. (D.7) and we find that the form of  $Y_D$  needs to be

$$Y_D = \begin{pmatrix} y_{11} & y_{12} & y_{13} \\ y_{11} & y_{12} & y_{13} \\ y_{11} & y_{12} & y_{13} \end{pmatrix} \quad (6.27)$$

with  $y_{1i}$  complex,  $i = 1, 2, 3$ , showing that the determinant of  $Y_D$  vanishes and that  $Y_D$  has two zero eigenvalues. As a consequence also the light neutrino mass matrix arising from the type-I seesaw mechanism, see Eq. (6.8), has two zero eigenvalues.<sup>33</sup> Furthermore, we can check that the non-zero eigenvalue has to correspond to the second light neutrino mass, since it is always associated with the eigenvector proportional to  $(1, 1, 1)^T$  which can only be identified with the second column of the PMNS mixing matrix. It is, however, experimentally highly disfavored that such a form can be the dominant contribution to light neutrino masses. We thus do not discuss this case further.

For  $n$  not divisible by four the form of the matrix  $Z(\mathbf{3}')$  is shown in Eq. (D.8). Again, we can compute the constraints on  $Y_D$ , arising from imposing the conditions in Eq. (6.3). In

---

<sup>33</sup> Indeed, we can show that, if  $Z(\mathbf{3}')$  is the identity matrix and  $Z(\mathbf{3})$  is any generator of a  $Z_2$  symmetry, i.e. it can be represented by a matrix  $Z(\mathbf{3})$  that fulfils  $V^\dagger Z(\mathbf{3}) V = \text{diag}(1, -1, -1)$  with  $V$  being a unitary matrix, we find

$$Z(\mathbf{3})^\dagger Y_D = V \text{diag}(1, -1, -1) V^\dagger Y_D = Y_D, \quad (6.28)$$

meaning we can re-write this condition as

$$\text{diag}(1, -1, -1) [V^\dagger Y_D] = [V^\dagger Y_D]. \quad (6.29)$$

Consequently, the combination  $V^\dagger Y_D$  must have two vanishing rows, namely the second and the third one. In particular, the determinant of  $V^\dagger Y_D$  vanishes. From the latter we can conclude for  $Y_D$  itself that its determinant must vanish, since the determinant of  $V$  cannot be zero. In addition, we can also know that  $Y_D$  must have two vanishing eigenvalues. So, in general knowing that  $Z(\mathbf{3}')$  is given by the identity matrix is sufficient in order to discard this case as realistic without corrections which can induce, at least, one further non-vanishing neutrino mass.

particular, we see that the first condition in the latter equation reduces the number of free (complex) parameters in  $Y_D$  to five, meaning the other four ones can be expressed in these, e. g.

$$y_{23} = y_{11} + y_{12} + y_{13} - y_{21} - y_{22} \quad , \quad y_{31} = y_{12} + y_{13} - y_{21} \quad , \quad (6.30)$$

$$y_{32} = y_{11} + y_{13} - y_{22} \quad \text{and} \quad y_{33} = -y_{13} + y_{21} + y_{22} \quad . \quad (6.31)$$

The five free complex parameters in  $Y_D$  are further constrained by requiring that also the second condition in Eq. (6.3) is fulfilled. As a consequence, these parameters have to be real. This is consistent with the findings in the general case where  $Y_D$  contains three real Yukawa couplings  $y_f$ ,  $f = 1, 2, 3$  and two angles  $\theta_L$  and  $\theta_R$ . In general, such a matrix  $Y_D$  has a non-vanishing determinant and three different eigenvalues, namely (proportional to)  $y_f$ .

We know in type 1 seesaw mechanism for eventually relating the parameters of  $Y_D$  to the light neutrino masses, we have to look at the following expression

$$\Omega(s)(\mathbf{3}')^\dagger M_R^{-1} \Omega(s)(\mathbf{3}')^* \quad (6.32)$$

with  $M_R$  as in Eq. (6.7). For  $\Omega(s)(\mathbf{3}')$  as in (6.23) we find

$$\Omega(s \text{ even})(\mathbf{3}')^\dagger M_R^{-1} \Omega(s \text{ even})(\mathbf{3}')^* = \frac{1}{M_0} \begin{pmatrix} 1 & 0 & 0 \\ 0 & 1 & 0 \\ 0 & 0 & -1 \end{pmatrix} \quad (6.33)$$

and for  $\Omega(s)(\mathbf{3}')$  as in (6.24) we get

$$\Omega(s \text{ odd})(\mathbf{3}')^\dagger M_R^{-1} \Omega(s \text{ odd})(\mathbf{3}')^* = \frac{1}{M_0} \begin{pmatrix} -1 & 0 & 0 \\ 0 & 1 & 0 \\ 0 & 0 & 1 \end{pmatrix} . \quad (6.34)$$

Note that in both cases the resulting structure is simple but does not commute with the arbitrary rotations  $R_{13}(\theta_{L,R})$ . Hence, this has to be taken into account when computing the light neutrino masses from the type-1 seesaw formula. Indeed only the light neutrino mass  $m_2$  is related to  $y_2$  and  $M_0$  in the following simple way

$$m_2 = \frac{y_2^2 v^2}{M_0}, \quad (6.35)$$

while for the full matrix part, we calculate

$$\begin{pmatrix} y_1 & 0 & 0 \\ 0 & y_2 & 0 \\ 0 & 0 & y_3 \end{pmatrix} R_{13}(-\theta_R) \Omega(s)(\mathbf{3}')^\dagger M_R^{-1} \Omega(s)(\mathbf{3}')^* R_{13}(\theta_R) \begin{pmatrix} y_1 & 0 & 0 \\ 0 & y_2 & 0 \\ 0 & 0 & y_3 \end{pmatrix} \quad (6.36)$$

with  $\Omega(s \text{ even})(\mathbf{3}')$  as in (6.23) we obtain

$$\frac{1}{M_0} \begin{pmatrix} y_1^2 \cos 2\theta_R & 0 & y_1 y_3 \sin 2\theta_R \\ 0 & y_2^2 & 0 \\ y_1 y_3 \sin 2\theta_R & 0 & -y_3^2 \cos 2\theta_R \end{pmatrix} \quad (6.37)$$

and for  $\Omega(s \text{ odd})(\mathbf{3}')$  as in (6.24)

$$\frac{1}{M_0} \begin{pmatrix} -y_1^2 \cos 2\theta_R & 0 & -y_1 y_3 \sin 2\theta_R \\ 0 & y_2^2 & 0 \\ -y_1 y_3 \sin 2\theta_R & 0 & y_3^2 \cos 2\theta_R \end{pmatrix}. \quad (6.38)$$

The difference is just the overall sign so we can nicely treat both cases at once.

We note a few things regarding the matrices in Eqs. (6.37) and (6.38) : if we set  $y_1 = 0$ ,  $m_1$  vanishes, we obtain NO with the matrix being automatically diagonal and does not need a further rotation; if we set  $y_3 = 0$ ,  $m_3 = 0$  follows, we obtain IO and again the matrix is automatically diagonal with no further rotation required. We can also set  $\sin 2\theta_R = 0$  leading

to no further rotation needed as well, but in this case there are also no constraints on the neutrino masses. Some values of  $\theta_R$  are not admitted, for e.g.  $\cos 2\theta_R = 0$  and consequently,  $\sin 2\theta_R = \pm 1$  (meaning  $\theta_R = \pi/4$ ,  $\theta_R = 3\pi/4$ , etc.), since then two of the neutrino masses are degenerate (for the matrices in Eqs. (6.37) and (6.38), these two are the first and the third neutrino mass and thus the spectrum is completely unrealistic). Similar statements hold in the other cases that have matrices like in Eqs. (6.37) and (6.38) as part of the light neutrino mass matrix, because the combination in (6.32) is not trivial in flavor space. We present general solution for both cases below :

***s* even** The PMNS lepton mixing matrix is

$$U = \Omega(s)(\mathbf{3}) R_{13}(\theta_L - \psi) \text{diag}(1, 1, \pm i), \quad (6.39)$$

with

$$\tan^2 \psi \equiv \frac{m_1 + m_3 - \sqrt{m_1^2 + m_3^2 + 2m_1 m_3 \cos(4\theta_R)}}{m_1 + m_3 + \sqrt{m_1^2 + m_3^2 + 2m_1 m_3 \cos(4\theta_R)}}. \quad (6.40)$$

The Yukawa matrix  $Y_D$  ( $\hat{Y}_D$ ) is constructed from Eq. (6.4), using the expressions of  $\Omega(s)(\mathbf{3})$  and  $\Omega(s)(\mathbf{3}')$  corresponding to *s*-even. The parameters  $y_k$  are in this case

$$\begin{aligned} y_1^2 &= \frac{M_0}{2v^2} \left( m_1 - m_3 + \sqrt{m_1^2 + m_3^2 + 2m_1 m_3 \cos(4\theta_R)} \right) \sec(2\theta_R), \\ y_2^2 &= \frac{M_0 m_2}{v^2}, \\ y_3^2 &= \frac{M_0}{2v^2} \left( -m_1 + m_3 + \sqrt{m_1^2 + m_3^2 + 2m_1 m_3 \cos(4\theta_R)} \right) \sec(2\theta_R), \end{aligned} \quad (6.41)$$

where  $v \approx 174$  GeV. Notice that  $y_k$  are real quantities, provided  $-\pi/4 < \theta_R < \pi/4$ .

***s* odd** The PMNS lepton mixing matrix is

$$U = \Omega(s)(\mathbf{3}) R_{13}(\theta_L - \psi) \text{diag}(\pm i, 1, 1), \quad (6.42)$$

with  $\psi$  introduced in (6.95). The Yukawa matrix  $Y_D$  ( $\hat{Y}_D$ ) is constructed using the expressions of  $\Omega(s)(\mathbf{3})$  and  $\Omega(s)(\mathbf{3}')$  corresponding to  $s$ -odd. The parameters  $y_k$  are defined as in (6.41).

The smallest group  $\Delta(6n^2)$  which fulfills all constraints on  $n$  :  $n$  even and not divisible by 3 and 4 is  $n = 10$ . For concreteness, we choose two explicit examples for this choice of  $n$ , namely  $s = 1$  and  $s = 2$ . The form of  $Y_D$  is easiest computed from Eq. (6.4), but we can also explicitly check by applying the conditions in (6.3) to a general complex 3-by-3 matrix  $Y_D$  that this is the correct form of the Dirac mass matrix of the neutrinos. The expressions are quite lengthy and thus we do not display them explicitly, but can be easily derived with the information given above.

We notice that only five real parameters  $y_i$ ,  $\theta_L$  and  $\theta_R$  appear in  $Y_D$  and that lepton mixing depends effectively only on one free parameter  $\theta$ , adjusted to  $\theta_{\text{bf}}$  in order to obtain best-fit with the measured mixing angles. If the expression in Eq. (6.32) is proportional to the identity matrix,  $\theta$  is given by  $\theta_L$  and  $y_i$  can be directly matched to the light neutrino masses  $m_i$ . If this is not true and we find a situation like in (6.33), there is only one coupling  $y_{i'}$  directly proportional to one light neutrino mass  $m_{i'}$ , whereas the other two together with  $\theta_R$  determine the other two light neutrino masses. In addition, these three parameters determine a further mixing angle, called  $\psi$  in earlier notes, that together with  $\theta_L$  gives  $\theta_{\text{bf}}$ . Hence, in both cases there are four experimentally constrained quantities (three neutrino masses and  $\theta_{\text{bf}}$ ) which determine five free parameters,  $y_i$ ,  $\theta_L$  and  $\theta_R$ . Thus, only one of them (usually  $\theta_R$ ) can be chosen freely.

### 6.3.1.3 Numerical Example

We give here an example which leads to the mixing pattern of case 1, see [9]. The characteristics of this mixing pattern are the following: the mixing angles can always be fitted well (independent of the choice of the group  $\Delta(6n^2)$  as well as the CP symmetry  $X(s)$ ), if we choose the free parameter  $\theta$  correctly, i.e. we quote as best-fitting values for the mixing

angles [9]

$$\sin^2 \theta_{13} \approx 0.0219 \quad , \quad \sin^2 \theta_{12} \approx 0.341 \quad , \quad \sin^2 \theta_{23} \approx \begin{cases} 0.605 \\ 0.395 \end{cases} \quad (6.43)$$

where the reactor mixing angle has been fitted to its central value. The free parameter  $\theta$  is thereby chosen as  $\theta \approx 0.18$  or  $\theta \approx 2.96$ . The difference results only in the change of the octant of the atmospheric mixing angle, for details see [9]. The results of the CP phases are simple: the Dirac phase as well as the Majorana phase  $\beta$  are trivial,

$$\sin \delta = 0 \quad \text{and} \quad \sin \beta = 0 \quad , \quad (6.44)$$

while the Majorana phase  $\alpha$  depends on the chosen CP symmetry  $X(s)$

$$\sin \alpha = (-1)^{k_1+1} \sin \left( \frac{6 \pi s}{n} \right) \quad . \quad (6.45)$$

The parameter  $k_1$  takes values  $k_1 = 0, 1, 2, 3$  and is related to the CP parity of the neutrinos, see for details [9]. For convenience, we show a numerical example in table 6.1 where  $n = 26$  fulfills all constraints (see below) and we only display values of  $\sin \alpha$  that are different in magnitude. We always take  $k_1 = 0$  for concreteness.

$s$	$s = 1$	$s = 2$	$s = 3$	$s = 4$	$s = 5$	$s = 6$
$\sin \alpha$	-0.663	-0.993	-0.823	-0.239	0.465	0.935

Tab. 6.1: Numerical example for mixing pattern of case 1). We choose  $n = 26$  and only display values of  $s$  for which  $\sin \alpha$  is different in magnitude and different from zero. The parameter  $k_1$  is always set as  $k_1 = 0$ . The sign of  $\sin \alpha$  can be changed by taking  $k_1 = 1$  or by choosing a different value of  $s$  than the displayed one. Remember  $s$  is constrained to be  $0 \leq s \leq n - 1 = 25$ . The given values for  $\sin \alpha$  are approximated. We use the formula in (6.46) for computing  $\sin \alpha$ .

In the limit of residual symmetries  $G_\nu$  and  $G_e$ , we obtain that the lepton mixing angles can be accommodated well for  $\vartheta_L \approx 0.18 (2.96)$  [9], i.e.  $\sin^2 \theta_{13} \approx 0.0219$ ,  $\sin^2 \theta_{12} \approx 0.341$  and  $\sin^2 \theta_{23} \approx 0.605 (0.395)$ . Regarding the two physical CP phases in the cases of strong NO

and IO, we find that the Dirac phase  $\delta$  is trivial, whereas the Majorana phase  $\alpha_2$  depends on the chosen CP transformation  $X(s)$

$$\sin \alpha_2 = (-1)^{k+r+s} \sin 6 \phi_s \quad \text{and} \quad \cos \alpha_2 = (-1)^{k+r+s+1} \cos 6 \phi_s, \quad \text{with } \phi_s = \frac{\pi s}{n}, \quad (6.46)$$

where  $k = 0$  ( $k = 1$ ) for  $\cos 2 \vartheta_R > 0$  ( $\cos 2 \vartheta_R < 0$ ) and  $r = 0$  ( $r = 1$ ) for strong NO (IO).

### 6.3.1.4 Special Points

For particular values of  $\vartheta_L$  and  $\vartheta_R$ , the residual symmetry  $G_\nu = Z_2 \times CP$  can be enhanced. If  $\vartheta_L = 0, \pi$ , the combination  $m_D m_D^\dagger$  becomes invariant under a further  $Z_2$  subgroup of  $G_f$ . Similarly, for the choices  $\vartheta_R = 0, \pi/2, \pi, 3\pi/2$  the combination  $m_D^\dagger m_D$  preserves a symmetry larger than  $G_\nu$ . This symmetry is also larger than the one of  $m_D m_D^\dagger$  for  $\vartheta_L = 0, \pi$ , since RH neutrinos transform as the real representation  $\mathbf{3}'$  of  $G_f$  that is unfaithful for  $n > 2$ .

These points of ERS are of particular relevance for phenomenology, since  $\vartheta_L$  deviating from  $\vartheta_{L,0} = 0$  or  $\pi$  leads to a non-zero value of the reactor mixing angle  $\theta_{13}$ .  $\vartheta_R$  close to  $\vartheta_{R,0} = 0, \pi/2, \pi$  or  $3\pi/2$  makes it possible for the RH neutrino  $N_3$  to be long-lived enough for being detected with the LLP searches (see Eq. (6.106) and Fig. 6.1), while simultaneously maximizing the CP asymmetries  $\epsilon_{i\alpha}$  relevant for leptogenesis (see Eqs. (6.102) and (6.103)). One can argue that the larger the ERS is, the smaller the deviation from points of ERS will be, i.e.  $\vartheta_R$  is expected to deviate from  $\vartheta_{R,0}$  by  $\delta\vartheta_R = |\vartheta_R - \vartheta_{R,0}| \lesssim 0.01$ , while  $\vartheta_L$  can deviate from  $\vartheta_{L,0}$  up to  $\delta\vartheta_L = |\vartheta_L - \vartheta_{L,0}| \sim 0.2$ .

In one type of explicit models [265], the flavour and CP symmetry are spontaneously broken to the residual symmetries  $G_\nu$  and  $G_e$  with the help of flavour symmetry breaking fields and a peculiar alignment of their VEVs, achieved with a potential with a particular form. Depending on the fields and the form of the potential, an ERS larger than  $G_\nu$  and  $G_e$  can be preserved at leading order. Higher-dimensional operators then induce small deviations from these points of ERS, thus explaining the particular sizes of  $\vartheta_L$  and  $\vartheta_R$ . An example

can be found in Ref. [266], where the correct size of  $\vartheta_L$  and thus the reactor mixing angle  $\theta_{13}$  is generated in this way.

Higher-dimensional operators connecting different sectors of the theory are responsible for the eventual breaking of the residual symmetries  $G_\nu$  and  $G_e$  and thus affect the given form of  $m_D$ ,  $m_l$  and  $M_M$ . In particular, they are also the source of corrections leading to a small splitting in the RH neutrino masses. This splitting is crucial for resonant leptogenesis. In the following, we focus on contributions to  $M_M$  that possess the residual symmetry  $G_e$ . These are proportional to  $\kappa$ , a positive power of the symmetry breaking parameter, measured in units of  $M$ . A small splitting of the RH neutrino masses therefore arises:

$$M_1 = M(1 + 2\kappa) \quad \text{and} \quad M_2 = M_3 = M(1 - \kappa). \quad (6.47)$$

## 6.3.2 Case 2

### 6.3.2.1 Residual Symmetries

The residual  $Z_2$  symmetry in the neutrino sector is generated by the same element

$$Z = c^{n/2}, \quad (6.48)$$

as in Case 1. Thus, all comments made, in particular, the forms of  $Z(\mathbf{3})$  and  $Z(\mathbf{3}')$  in (D.6) and (D.7), (D.8), apply respectively.

The CP symmetry is given by the automorphism in (D.14) and the inner automorphism  $h = c^s d^t$  with  $0 \leq s, t \leq n - 1$  and thus depends on two parameters:  $X(s, t)$ . In the three-dimensional representations  $\mathbf{3}$  and  $\mathbf{3}'$   $X(s, t)$  is given by

$$X(s, t)(\mathbf{3}) = c(\mathbf{3})^s d(\mathbf{3})^t X_0(\mathbf{3}) \quad \text{and} \quad X(s, t)(\mathbf{3}') = c(\mathbf{3}')^s d(\mathbf{3}')^t X_0(\mathbf{3}') \quad (6.49)$$

and the explicit forms can be found in appendix D.3.

Here we always use  $s$  and  $t$  as parameters unlike in the analysis of lepton mixing patterns in [9], where it turned out to be more convenient to use the parameters  $u$  and  $v$  that are linearly related to  $s$  and  $t$  as follows

$$u = 2s - t \quad \text{and} \quad v = 3t. \quad (6.50)$$

According to the findings in [9], a suitable choice of the matrix  $\Omega(s, t)(\mathbf{3})$  is given by

$$\Omega(s, t)(\mathbf{3}) = \Omega(u, v)(\mathbf{3}) = e^{i\phi_v/6} U_{\text{TB}} R_{13} \left( -\frac{\phi_u}{2} \right) \begin{pmatrix} 1 & 0 & 0 \\ 0 & e^{-i\phi_v/2} & 0 \\ 0 & 0 & -i \end{pmatrix} \quad (6.51)$$

with  $\phi_u = \frac{\pi u}{n}$  and  $\phi_v = \frac{\pi v}{n}$ . The form of the matrix  $\Omega(s, t)(\mathbf{3}')$ , derived from  $X(\mathbf{3})(s, t)$ , depends like the latter on whether  $s$  and  $t$  are even or odd. The explicit form of  $\Omega(s, t)(\mathbf{3}')$ , however, does neither contain  $s$  nor  $t$  are parameters. For  $s$  and  $t$  even, we can use

$$\Omega(s \text{ even}, t \text{ even})(\mathbf{3}') = U_{\text{TB}} \begin{pmatrix} 1 & 0 & 0 \\ 0 & 1 & 0 \\ 0 & 0 & i \end{pmatrix}, \quad (6.52)$$

for  $s$  even and  $t$  odd, a possible choice is

$$\Omega(s \text{ even}, t \text{ odd})(\mathbf{3}') = e^{-i\pi/4} U_{\text{TB}} R_{13} \left( \frac{\pi}{4} \right) \begin{pmatrix} e^{-i\pi/2} & 0 & 0 \\ 0 & e^{-i\pi/4} & 0 \\ 0 & 0 & 1 \end{pmatrix}, \quad (6.53)$$

for  $s$  odd and  $t$  even, we can choose

$$\Omega(s \text{ odd}, t \text{ even})(\mathbf{3}') = U_{\text{TB}} \begin{pmatrix} i & 0 & 0 \\ 0 & 1 & 0 \\ 0 & 0 & 1 \end{pmatrix}, \quad (6.54)$$

and for  $s$  and  $t$  odd, we use

$$\Omega(s \text{ odd}, t \text{ odd})(\mathbf{3}') = e^{-3i\pi/4} U_{\text{TB}} R_{13} \left( \frac{\pi}{4} \right) \begin{pmatrix} e^{-i\pi/2} & 0 & 0 \\ 0 & e^{i\pi/4} & 0 \\ 0 & 0 & 1 \end{pmatrix}. \quad (6.55)$$

Similar as in Case 1, the rotation associated with the representation  $\mathbf{3}$  and thus with LH leptons is always  $R_{13}(\theta_L)$ . In all these cases,  $\Omega(s, t)(\mathbf{3}')$  fulfills the two equations ( $Z(\mathbf{3}')$  always like in (D.8))

$$\Omega(s, t)(\mathbf{3}')^\dagger Z(\mathbf{3}') \Omega(s, t)(\mathbf{3}') = \begin{pmatrix} -1 & 0 & 0 \\ 0 & 1 & 0 \\ 0 & 0 & -1 \end{pmatrix} \quad (6.56)$$

and, hence also for the representation  $\mathbf{3}'$ , i.e. RH neutrinos, the relevant rotation is in the (13)-plane, namely  $R_{13}(\theta_R)$ . We observe that for none of the above combinations of  $X$  and  $Z$  in  $\mathbf{3}$  and  $\mathbf{3}'$ , we find zero eigenvalues for  $Y_D$  as long as we only consider cases in which  $n$  is not divisible by four so that  $Z(\mathbf{3}')$  is not the identity matrix, compare (D.7) and (6.27).

### 6.3.2.2 Constraints from and on light neutrino mass spectrum

As a further step, we present the form of the relevant matrix combination appearing in the type 1 seesaw formula, involving  $\Omega(s, t)(\mathbf{3}')$  and  $M_R$ , see (6.32). We find that

for  $s$  even and  $t$  even

$$\Omega(s, t)(\mathbf{3}')^\dagger M_R^{-1} \Omega(s, t)(\mathbf{3}')^\star = \frac{1}{M_0} \mathbb{1}, \quad (6.57)$$

for  $s$  even and  $t$  odd

$$\Omega(s, t)(\mathbf{3}')^\dagger M_R^{-1} \Omega(s, t)(\mathbf{3}')^\star = -\frac{1}{M_0} \begin{pmatrix} 0 & 0 & 1 \\ 0 & 1 & 0 \\ 1 & 0 & 0 \end{pmatrix}, \quad (6.58)$$

for  $s$  odd and  $t$  even

$$\Omega(s, t)(\mathbf{3}')^\dagger M_R^{-1} \Omega(s, t)(\mathbf{3}')^\star = \frac{1}{M_0} \begin{pmatrix} -1 & 0 & 0 \\ 0 & 1 & 0 \\ 0 & 0 & -1 \end{pmatrix}, \quad (6.59)$$

for  $s$  odd and  $t$  odd

$$\Omega(s, t)(\mathbf{3}')^\dagger M_R^{-1} \Omega(s, t)(\mathbf{3}')^\star = \frac{1}{M_0} \begin{pmatrix} 0 & 0 & 1 \\ 0 & -1 & 0 \\ 1 & 0 & 0 \end{pmatrix}. \quad (6.60)$$

We continue with computing the form of the matrix in (6.36) for the different choices of  $s$  and  $t$  being even and odd:

for  $s$  even and  $t$  even

$$\frac{1}{M_0} \begin{pmatrix} y_1^2 & 0 & 0 \\ 0 & y_2^2 & 0 \\ 0 & 0 & y_3^2 \end{pmatrix}, \quad (6.61)$$

for  $s$  even and  $t$  odd

$$\frac{1}{M_0} \begin{pmatrix} y_1^2 \sin 2\theta_R & 0 & -y_1 y_3 \cos 2\theta_R \\ 0 & -y_2^2 & 0 \\ -y_1 y_3 \cos 2\theta_R & 0 & -y_3^2 \sin 2\theta_R \end{pmatrix}, \quad (6.62)$$

for  $s$  odd and  $t$  even

$$\frac{1}{M_0} \begin{pmatrix} -y_1^2 & 0 & 0 \\ 0 & y_2^2 & 0 \\ 0 & 0 & -y_3^2 \end{pmatrix}, \quad (6.63)$$

for  $s$  odd and  $t$  odd

$$\frac{1}{M_0} \begin{pmatrix} -y_1^2 \sin 2\theta_R & 0 & y_1 y_3 \cos 2\theta_R \\ 0 & -y_2^2 & 0 \\ y_1 y_3 \cos 2\theta_R & 0 & y_3^2 \sin 2\theta_R \end{pmatrix}. \quad (6.64)$$

These forms are very similar to those encountered before in Case 1 and thus can be treated in the same way to obtain PMNS lepton mixing matrix. As an example, we present the general solution for one of the cases.

**$s$  even and  $t$  odd** The PMNS lepton mixing matrix is in this case

$$U = \Omega(u, v)(\mathbf{3}) R_{13}(\theta_L - \eta) \text{diag}(\pm i, \pm i, 1), \quad (6.65)$$

with

$$\tan^2 \eta \equiv \frac{m_1 + m_3 + \sqrt{m_1^2 + m_3^2 - 2m_1 m_3 \cos(4\theta_R)}}{m_1 + m_3 - \sqrt{m_1^2 + m_3^2 - 2m_1 m_3 \cos(4\theta_R)}}. \quad (6.66)$$

The Yukawa matrix  $Y_D$  ( $\hat{Y}_D$ ) is constructed from Eq. (6.4), using the expressions of  $\Omega(u, v)$ (**3**) and  $\Omega(u, v)$ (**3'**) corresponding to  $s$ -even and  $t$ -even. The parameters  $y_k$  are defined as

$$\begin{aligned} y_1^2 &= \frac{M_0}{2v^2} \left( -m_1 + m_3 + \sqrt{m_1^2 + m_3^2 - 2m_1 m_3 \cos(4\theta_R)} \right) \csc(2\theta_R) , \\ y_2^2 &= \frac{M_0 m_2}{v^2} , \\ y_3^2 &= \frac{M_0}{2v^2} \left( m_1 - m_3 + \sqrt{m_1^2 + m_3^2 - 2m_1 m_3 \cos(4\theta_R)} \right) \csc(2\theta_R) , \end{aligned} \quad (6.67)$$

which are real for  $0 < \theta_R < \pi/2$ .

### 6.3.2.3 Numerical Examples

The results for lepton mixing are much richer and indeed in general all CP phases are non-trivial. We can observe the following approximate dependence of the different CP phases on the parameters  $u$  and  $v$  of case 2) (for  $k_{1,2} = 0$  and no shift in  $u$ )

$$\sin \delta \approx \pm 1 \mp 3.3 \left( \frac{\pi u}{n} \right)^2 , \quad \sin \beta \approx \mp 5.6 \left( \frac{\pi u}{n} \right) \pm 23 \left( \frac{\pi u}{n} \right)^3 \quad (6.68)$$

and most importantly

$$\sin \alpha \approx - \sin \left( \frac{\pi v}{n} \right) . \quad (6.69)$$

Detailed numerical results, i.e. tables with examples of  $n$  and  $u$  as well as  $v$  and  $\theta$  along with explanations can be found in [9].

In order finish up the discussion of case 2, we present a choice for  $n$  and  $u$  (a combination of  $s$  and  $t$ , see (6.50)) (as well as examples for  $v$ ) that permit agreement of the three lepton mixing angles with experimental observations at the  $3\sigma$  level or better. We take all examples from the analysis performed in [9]. We consider the two interesting cases with  $n$  even,  $n$  not divisible by three and  $n$  not divisible by four, that have been analyzed in [9]. For simplicity, we only take into account "unshifted" cases. So, there are two possible values of  $n$  that we

can use:

$$n = 10 \quad \text{and} \quad n = 14 . \quad (6.70)$$

For both of these values of  $n$  three possible values of the parameter  $u = 2s - t$  allow to adjust the experimental data of the lepton mixing angles well

$$u = -1 , \quad u = 0 , \quad u = 1 . \quad (6.71)$$

In table 6.2, we list the best fitting value of  $\theta_{\text{bf}}$  (there is another value of  $\theta$  that also fits the experimental data well, but we focus one value only for the moment, see [9] for details), the results for the lepton mixing angles as well as for the two CP invariants  $J_{CP}$  and  $I_2$  (for definition of these two see also [9]) and CP phases  $\delta$  and  $\beta$ . We display the different

$n$	$n = 10$			$n = 14$		
	$u = -1$	$u = 0$	$u = +1$	$u = -1$	$u = 0$	$u = +1$
$\theta_{\text{bf}}$	0.0932	2.96	0.0932	0.144	2.96	0.144
$\sin^2 \theta_{12}$	0.341	0.341	0.341	0.341	0.341	0.341
$\sin^2 \theta_{13}$	0.0218	0.0218	0.0218	0.0218	0.0218	0.0218
$\sin^2 \theta_{23}$	0.410	1/2	0.590	0.437	1/2	0.563
$J_{CP}$	-0.0178	0.0342	-0.0178	-0.0274	0.0342	-0.0274
$\sin \delta$	-0.529	1	-0.529	-0.807	1	-0.807
$I_2$	-0.0121	0	0.0121	-0.0137	0	0.0137
$\sin \beta$	-0.861	0	0.861	-0.976	0	0.976

Tab. 6.2: Two examples for case 2) that fulfill all constraints on the index  $n$  and that can accommodate the lepton mixing angles well for some value of  $\theta$ , if  $u = 2s - t$  is properly chosen. Since the CP invariant  $I_1$  or better to say the Majorana phase  $\alpha$  depends on  $v = 3t$  only that can take a variety of values we discuss this Majorana phase and its different admitted values for  $n$  and  $u$  in the main text. As always we take  $k_1 = 0$  and  $k_2 = 0$ .

combinations  $s$  and  $t$  that lead to the values of  $u$  in (6.71): for  $n = 10$  and  $n = 14$  the value  $u = -1$  can be produced for

$$(s, t) = (0, 1), (1, 3), (2, 5), (3, 7), (4, 9) \quad (6.72)$$

and for  $n = 14$  we additionally have

$$(s, t) = (5, 11), (6, 13); \quad (6.73)$$

similarly for  $n = 10$  and  $n = 14$  the value  $u = 0$  can be produced for

$$(s, t) = (0, 0), (1, 2), (2, 4), (3, 6), (4, 8) \quad (6.74)$$

and for  $n = 14$  we additionally have

$$(s, t) = (5, 10), (6, 12); \quad (6.75)$$

and for  $n = 10$  and  $n = 14$  the value  $u = 1$  can be produced for

$$(s, t) = (1, 1), (2, 3), (3, 5), (4, 7), (5, 9) \quad (6.76)$$

and for  $n = 14$  we additionally have

$$(s, t) = (6, 11), (7, 13). \quad (6.77)$$

For  $n = 10$  and  $u = 1$  as well as  $u = -1$  we obtain using these combinations of  $(s, t)$  the following values of  $v$  and approximate values of  $\sin \alpha$ , using the formula in (6.69) with  $k_1 = 0$

$v$	$v = 3$	$v = 9$	$v = 15$	$v = 21$	$v = 27$
$\sin \alpha$	-0.809	-0.309	1	-0.309	-0.809

For  $n = 10$  and  $u = 0$  we obtain using these combinations of  $(s, t)$  the following values of  $v$  and approximate values of  $\sin \alpha$ , using the formula in (6.69) with  $k_1 = 0$

$v$	$v = 0$	$v = 6$	$v = 12$	$v = 18$	$v = 24$
$\sin \alpha$	0	-0.951	0.588	0.588	-0.951

For  $n = 14$  and  $u = 1$  as well as  $u = -1$  we obtain using these combinations of  $(s, t)$  the following values of  $v$  and approximate values of  $\sin \alpha$ , using the formula in (6.69) with  $k_1 = 0$

$v$	$v = 3$	$v = 9$	$v = 15$	$v = 21$	$v = 27$	$v = 33$	$v = 39$
$\sin \alpha$	-0.623	-0.901	0.223	1	0.223	-0.901	-0.623

For  $n = 14$  and  $u = 0$  we obtain using these combinations of  $(s, t)$  the following values of  $v$  and approximate values of  $\sin \alpha$ , using the formula in (6.69) with  $k_1 = 0$

$v$	$v = 0$	$v = 6$	$v = 12$	$v = 18$	$v = 24$	$v = 30$	$v = 36$
$\sin \alpha$	0	-0.975	-0.434	0.782	0.782	-0.434	-0.975

### 6.3.3 Case 3a and Case 3b.1

#### 6.3.3.1 Residual Symmetries

The residual symmetries in Case 3a and Case 3b.1 are chosen as follows: the  $Z_2$  symmetry in the neutrino sector is generated by

$$Z = bc^m d^m \quad \text{with } m = 0, \dots, n - 1. \quad (6.78)$$

Since  $Z$  involves the generator  $b$  Case 3a and Case 3b.1 can only be achieved with the help of the flavor groups  $\Delta(6n^2)$ . We have in general  $n$  different choices for the generator  $Z$ . However, as discussed in [9], preferred values of  $m$  are either around  $m \approx 0$  and  $m \approx n$  for Case 3 a) or  $m \approx n/2$  for Case 3 b.1), as long as the charged lepton masses are ordered canonically. The form of  $Z$  in the representations  $\mathbf{3}$  and  $\mathbf{3}'$ ,  $Z(\mathbf{3})$  and  $Z(\mathbf{3}')$ , can be found in appendix D.1.

The CP symmetry, used in Case 3a and Case 3b.1 is induced by the automorphism, shown in Eq. (D.14) in appendix D.3, conjugated with the inner one, represented by the group transformation  $h = b c^s d^{n-s}$ ,  $s = 0, \dots, n - 1$ . The corresponding CP transformation  $X(s)$  in  $\mathbf{3}$  and  $\mathbf{3}'$  is given by

$$X(s)(\mathbf{3}) = b(\mathbf{3})^s c(\mathbf{3})^s d(\mathbf{3})^{n-s} X_0(\mathbf{3}) \quad (6.79)$$

and

$$X(s)(\mathbf{3}') = b(\mathbf{3}')^s c(\mathbf{3}')^s d(\mathbf{3}')^{n-s} X_0(\mathbf{3}'). \quad (6.80)$$

The explicit forms of  $X(s)(\mathbf{3})$  and  $X(s)(\mathbf{3}')$  can be found in appendix D.3.

The form of the matrix  $\Omega(s, m)(\mathbf{3})$ , derived from  $X(s, m)(\mathbf{3})$  in Eq. (6.19) in appendix D.3, can be chosen as [9]

$$\Omega(s, m)(\mathbf{3}) = e^{i\phi_s} \begin{pmatrix} 1 & 0 & 0 \\ 0 & \omega & 0 \\ 0 & 0 & \omega^2 \end{pmatrix} U_{\text{TB}} \begin{pmatrix} 1 & 0 & 0 \\ 0 & e^{-3i\phi_s} & 0 \\ 0 & 0 & -1 \end{pmatrix} R_{13}(\phi_m) \quad (6.81)$$

with  $\phi_s = \frac{\pi s}{n}$ ,  $\phi_m = \frac{\pi m}{s}$  and  $\omega = e^{\frac{2\pi i}{3}}$ . The form of the matrix  $\Omega(s)(\mathbf{3}')$  only depends on whether  $s$  is even or odd and is also independent of the choice of the parameter  $m$ . In particular, we can use for  $s$  even

$$\Omega(s \text{ even})(\mathbf{3}') = \begin{pmatrix} 1 & 0 & 0 \\ 0 & \omega & 0 \\ 0 & 0 & \omega^2 \end{pmatrix} U_{\text{TB}} \begin{pmatrix} 1 & 0 & 0 \\ 0 & 1 & 0 \\ 0 & 0 & -1 \end{pmatrix}. \quad (6.82)$$

and for  $s$  odd

$$\Omega(s \text{ odd})(\mathbf{3}') = \begin{pmatrix} 1 & 0 & 0 \\ 0 & \omega & 0 \\ 0 & 0 & \omega^2 \end{pmatrix} U_{\text{TB}} \begin{pmatrix} i & 0 & 0 \\ 0 & -1 & 0 \\ 0 & 0 & -i \end{pmatrix}. \quad (6.83)$$

We note that the form of  $\Omega(s \text{ even})(\mathbf{3}')$  coincides with  $\Omega(s, m)(\mathbf{3})$  for the special choices  $s = 0$  and  $m = 0$  as well as that  $\Omega(s \text{ odd})(\mathbf{3}')$  coincides with a special form of  $\Omega(s, m)(\mathbf{3})$ , namely for  $s = n/2$  and  $m = 0$ .

We have to compute the form of the matrix  $Z(m)(\mathbf{3})$  in the basis rotated via  $\Omega(s, m)(\mathbf{3})$  for the representation  $\mathbf{3}$  which means

$$\Omega(s, m)(\mathbf{3})^\dagger Z(m)(\mathbf{3}) \Omega(s, m)(\mathbf{3}) = \begin{pmatrix} 1 & 0 & 0 \\ 0 & 1 & 0 \\ 0 & 0 & -1 \end{pmatrix}. \quad (6.84)$$

Note that this holds for all choices of  $s$ ,  $m$  and  $n$ . So, we know that LH leptons, being in the representation  $\mathbf{3}$ , are always accompanied with a rotation  $R_{12}(\theta_L)$  with  $\theta_L$  being an arbitrary rotation angle, related to the fitting of the lepton mixing angles.

In a next step we consider the form of  $Z(\mathbf{3}')$ , see (D.12) and (D.13), in the basis rotated by  $\Omega(s \text{ even})(\mathbf{3}')$  and  $\Omega(s \text{ odd})(\mathbf{3}')$ , respectively. The matrix  $Z(m \text{ even})(\mathbf{3}')$  reads as follows in the basis rotated by  $\Omega(s \text{ even})(\mathbf{3}')$

$$\Omega(s \text{ even})(\mathbf{3}')^\dagger Z(m \text{ even})(\mathbf{3}') \Omega(s \text{ even})(\mathbf{3}') = \begin{pmatrix} 1 & 0 & 0 \\ 0 & 1 & 0 \\ 0 & 0 & -1 \end{pmatrix} \quad (6.85)$$

and in the basis rotated with  $\Omega(s \text{ odd})(\mathbf{3}')$  it reads

$$\Omega(s \text{ odd})(\mathbf{3}')^\dagger Z(m \text{ even})(\mathbf{3}') \Omega(s \text{ odd})(\mathbf{3}') = \begin{pmatrix} 1 & 0 & 0 \\ 0 & 1 & 0 \\ 0 & 0 & -1 \end{pmatrix}. \quad (6.86)$$

Hence, in both cases we need a rotation  $R_{12}(\theta_R)$  for fields in the representation  $\mathbf{3}'$ , i.e. RH neu-

trinos. Doing the same for the matrix  $Z(m \text{ odd})(\mathbf{3}')$  in the basis rotated with  $\Omega(s \text{ even})(\mathbf{3}')$

$$\Omega(s \text{ even})(\mathbf{3}')^\dagger Z(m \text{ odd})(\mathbf{3}') \Omega(s \text{ even})(\mathbf{3}') = \begin{pmatrix} -1 & 0 & 0 \\ 0 & 1 & 0 \\ 0 & 0 & 1 \end{pmatrix} \quad (6.87)$$

and in the basis rotated with  $\Omega(s \text{ odd})(\mathbf{3}')$ , we find as well

$$\Omega(s \text{ odd})(\mathbf{3}')^\dagger Z(m \text{ odd})(\mathbf{3}') \Omega(s \text{ odd})(\mathbf{3}') = \begin{pmatrix} -1 & 0 & 0 \\ 0 & 1 & 0 \\ 0 & 0 & 1 \end{pmatrix}. \quad (6.88)$$

Thus, in both bases the free rotation due to  $Z(m \text{ odd})(\mathbf{3}')$  is given by  $R_{23}(\theta_R)$  among the RH neutrinos.

### 6.3.3.2 Constraints from and on light neutrino mass spectrum

A further step is to check the relevant combination in (6.32) for  $\Omega(s \text{ even})(\mathbf{3}')$  for which we find

$$\Omega(s \text{ even})(\mathbf{3}')^\dagger M_R^{-1} \Omega(s \text{ even})(\mathbf{3}')^* = \frac{1}{M_0} \begin{pmatrix} 1 & 0 & 0 \\ 0 & 1 & 0 \\ 0 & 0 & -1 \end{pmatrix} \quad (6.89)$$

as well as for  $\Omega(s \text{ odd})(\mathbf{3}')$  which leads to

$$\Omega(s \text{ odd})(\mathbf{3}')^\dagger M_R^{-1} \Omega(s \text{ odd})(\mathbf{3}')^* = \frac{1}{M_0} \begin{pmatrix} -1 & 0 & 0 \\ 0 & 1 & 0 \\ 0 & 0 & 1 \end{pmatrix}. \quad (6.90)$$

Using these results we see that for the combination analogous to the one shown in (6.36) (you have to change the rotation plane for  $R_{ij}(\theta_R)$ ) the following holds

for  $m$  even and  $s$  even: the structure of the matrix is trivial, i.e. diagonal.

for  $m$  even and  $s$  odd:

$$\begin{aligned} \begin{pmatrix} y_1 & 0 & 0 \\ 0 & y_2 & 0 \\ 0 & 0 & y_3 \end{pmatrix} R_{12}(-\theta_R) \Omega(s \text{ odd})(\mathbf{3}')^\dagger M_R^{-1} \Omega(s \text{ odd})(\mathbf{3}')^* R_{12}(\theta_R) \begin{pmatrix} y_1 & 0 & 0 \\ 0 & y_2 & 0 \\ 0 & 0 & y_3 \end{pmatrix} \\ = \frac{1}{M_0} \begin{pmatrix} -y_1^2 \cos 2\theta_R & -y_1 y_2 \sin 2\theta_R & 0 \\ -y_1 y_2 \sin 2\theta_R & y_2^2 \cos 2\theta_R & 0 \\ 0 & 0 & y_3^2 \end{pmatrix} \end{aligned} \quad (6.91)$$

for  $m$  odd and  $s$  even:

$$\begin{aligned} \begin{pmatrix} y_1 & 0 & 0 \\ 0 & y_2 & 0 \\ 0 & 0 & y_3 \end{pmatrix} R_{23}(-\theta_R) \Omega(s \text{ even})(\mathbf{3}')^\dagger M_R^{-1} \Omega(s \text{ even})(\mathbf{3}')^* R_{23}(\theta_R) \begin{pmatrix} y_1 & 0 & 0 \\ 0 & y_2 & 0 \\ 0 & 0 & y_3 \end{pmatrix} \\ = \frac{1}{M_0} \begin{pmatrix} y_1^2 & 0 & 0 \\ 0 & y_2^2 \cos 2\theta_R & y_2 y_3 \sin 2\theta_R \\ 0 & y_2 y_3 \sin 2\theta_R & -y_3^2 \cos 2\theta_R \end{pmatrix} \end{aligned} \quad (6.92)$$

for  $m$  odd and  $s$  odd: the structure of the matrix is trivial, i.e. diagonal.

In conclusion, either the structure is trivial and we obtain a direct relation between the Yukawa couplings and the light neutrino masses of the form

$$m_i = \frac{y_i^2 v^2}{M_0} \quad (6.93)$$

or this holds for only one of the three neutrino generations, whereas the other two belong to a sub-sector that requires further diagonalization, in a way discussed already for Case 1. We present one of the cases as an example below  **$m$  even and  $s$  odd** The lepton mixing

matrix is in this case

$$U = \Omega(m, s)(\mathbf{3}) R_{12}(\theta_L - \zeta) \text{diag}(\pm i, 1, 1). \quad (6.94)$$

with

$$\tan^2 \zeta \equiv \frac{m_1 + m_2 - \sqrt{m_1^2 + m_2^2 + 2 m_1 m_2 \cos(4\theta_R)}}{m_1 + m_3 + \sqrt{m_1^2 + m_3^2 + 2 m_1 m_2 \cos(4\theta_R)}}. \quad (6.95)$$

The Yukawa matrix  $Y_D$  ( $\hat{Y}_D$ ) is constructed from (??), using the expressions of  $\Omega(m, s)(\mathbf{3})$  and  $\Omega(m, s)(\mathbf{3}')$  corresponding to  $s$ -even and  $t$ -odd. The parameters  $y_k$  are defined in this case as

$$\begin{aligned} y_1^2 &= \frac{M_0}{2v^2} \left( m_1 - m_2 + \sqrt{m_1^2 + m_2^2 + 2 m_1 m_2 \cos(4\theta_R)} \right) \sec(2\theta_R), \\ y_2^2 &= \frac{M_0}{2v^2} \left( -m_1 + m_2 + \sqrt{m_1^2 + m_2^2 + 2 m_1 m_2 \cos(4\theta_R)} \right) \sin(2\theta_R), \\ y_3^2 &= \frac{M_0 m_3}{v^2}, \end{aligned} \quad (6.96)$$

which are real for  $-\pi/4 < \theta_R < \pi/4$ .

### 6.3.3.3 Numerical Examples

Here we present two numerical examples for the mixing patterns of Case 3a and Case 3b.1. The example for case 3a is taken from [9]. It also appears in [264] in the discussion of neutrinoless double beta decay. The example for Case 3b.1 appears in [9] as well as in [264], where unflavored leptogenesis in a ‘‘classical’’ type 1 seesaw scenario is analyzed.

#### Case 3a

For the mixing pattern of Case 3a, we choose

$$n = 17 \quad \text{and} \quad m = 1. \quad (6.97)$$

$s$	$\theta_{\text{bf}}$	$\sin^2 \theta_{12}$	$J_{CP}$	$\sin \delta$	$I_1$	$\sin \alpha$	$I_2$	$\sin \beta$
$s = 2$	2.31	0.304	0.0319	0.969	0.144	0.712	0.0126	0.820
$s = 2$	3.05	0.304	0.0060	0.184	-0.144	-0.712	0.0018	0.119
$s = 3$	0.134	0.335	-0.0095	-0.280	0	0	-0.0028	-0.190

Tab. 6.3: Example for mixing pattern of Case 3a. The parameters  $n$  and  $m$  are chosen as  $n = 17$  and  $m = 1$ . This entails as values for the reactor and the atmospheric mixing angles:  $\sin^2 \theta_{13} \approx 0.0225$  and  $\sin^2 \theta_{23} \approx 0.607$ . Note there are two different best fitting points for the choice  $s = 2$  that indeed lead to different results for the CP phases  $\delta$  and  $\beta$ . The Majorana phase  $\alpha$  only changes sign. The fact that there is only one value for  $s = 3$  is related to the question whether the solar mixing angle can be fitted to its experimental central value or not. If it cannot, then there is only one value of  $\theta_{\text{bf}}$  and it also entails that  $\sin \alpha$  vanishes exactly. For details see [9]. As in all other cases  $k_1 = k_2 = 0$ .

Note this time there is no additional constraint on the choice of the index  $n$  apart from that the resulting lepton mixing angles should match the experimental data well. The only constraint on the group is the request to use one of the series  $\Delta(6n^2)$ , since the generator  $b$  is needed which is not part of the groups  $\Delta(3n^2)$ . For  $m$  we have chosen the smallest non-trivial value, as already mentioned above. Effectively a small ratio  $m/n$  (or close to one) is needed for achieving small  $\theta_{13}$ . Regarding the choice of the CP transformation  $X(s)$  there are, indeed, in total 16 choices and all of them lead to a reasonable agreement of the lepton mixing angles with experimental data. However, we restrict ourselves to two choices only. Some of them like  $s = 0$  and  $s = 8$  lead to CP conservation (either due to symmetry or rather accidentally) and values  $s > n/2$  usually reproduce results like the corresponding value  $s' = n - s < n/2$ . The two examples for CP transformations are characterized by

$$s = 2 \quad \text{and} \quad s = 3. \tag{6.98}$$

In table 6.3, we show the results for the parameter  $\theta_{\text{bf}}$ , the mixing angles and the CP invariants and CP phases.

$s$	$\theta_{\text{bf}}$	$\sin^2 \theta_{23}$	$\sin^2 \theta_{12}$	$\sin^2 \theta_{13}$	$J_{CP}$	$\sin \delta$	$I_1$	$I_2$	$\sin \alpha = \sin \beta$
$s = 1$	1.31	0.579	0.318	0.0220	0.0312	0.936	-0.147	-0.0104	$-1/\sqrt{2} \approx -0.707$
$s = 1$	1.83	0.421	0.318	0.0220	-0.0312	-0.936	-0.147	-0.0104	$-1/\sqrt{2} \approx -0.707$
$s = 2$	1.83	0.645	0.319	0.0216	-0.0237	-0.739	0.208	0.0144	1
$s = 4$	1.31	1/2	0.318	0.0220	-0.0338	-1	0	0	0
$s = 4$	1.83	1/2	0.318	0.0220	0.0338	1	0	0	0

Tab. 6.4: Example for mixing pattern of case 3 b.1). The parameters  $n$  and  $m$  are chosen as  $n = 8$  and  $m = 4$ . Note there are two different best fitting points for the choice  $s = 1$  and  $s = 4$ . As in all other cases  $k_1 = k_2 = 0$ . Due to that  $\sin \alpha$  and  $\sin \beta$  are not only coinciding in magnitude (coming from the choice  $m = n/2$ ), but also in sign.

### Case 3b.1

For the mixing pattern of Case 3b.1, we choose like in [9] and [264]

$$n = 8 \quad \text{and} \quad m = 4 . \tag{6.99}$$

This combination fulfills the request  $m/n = 1/2$ , see above. And indeed with this choice the sines of the two Majorana phases  $\alpha$  and  $\beta$  have the same magnitude, compare [9]. We select three choices of the CP symmetry

$$s = 1 \quad , \quad s = 2 \quad \text{and} \quad s = 4 \tag{6.100}$$

that all lead to at least one non-trivial CP phase. The particular choice  $s = n/2 = 4$  gives trivial Majorana phases and maximal Dirac phase (as well as maximal atmospheric mixing, see table 6.4). Again, some values of  $s$  like  $s = 0$  lead to no CP violation at all and other values of  $s$  like  $s' = n - s > n/2$  only produce results equivalent to those of  $s < n/2$ . In table 6.4 we display the values for  $\theta_{\text{bf}}$  and the results for the mixing parameters. We note that again we only display the best fitting value of  $\theta$  and that we – for completeness – display two such values for the choices  $s = 1$  and  $s = 4$ . This example is only one of the simplest ones, since  $n$  is small and thus we need to have  $m = n/2$  in order to accommodate the lepton

mixing angles well. For richer structures see tables and figures in [9].

A final comment regarding the numerical examples: since these are all taken from [9], the value of  $\theta$  is always adjusted in such a way that the  $\chi^2$  for fitting to the experimentally measured mixing angles is smallest. However, in principle  $\theta$  can vary a little and the lepton mixing angles are still compatible with experiments at the  $3\sigma$  level or better. This can be easily taken into account, as indeed done in the analysis of leptogenesis and neutrinoless double beta decay in [264]. This can also impact the resulting values for CP phases. Thus, it should be noted that the values given here are only the ones for the best fitting case.

## 6.4 CP Asymmetries

Including the small mass splitting of the RH neutrinos, their out-of-equilibrium decays can generate  $\eta_B$  via resonant leptogenesis [257, 258]. The CP asymmetries  $\epsilon_{i\alpha}$  due to the decay of  $N_i$  and in the lepton flavour  $\alpha$  read

$$\epsilon_{i\alpha} \approx \frac{1}{v^4} \sum_{j \neq i} \text{Im} \left( \hat{m}_{D,\alpha i}^* \hat{m}_{D,\alpha j} \right) \text{Re} \left( \left( \hat{m}_D^\dagger \hat{m}_D \right)_{ij} \right) \mathcal{F}_{ij}, \quad (6.101)$$

with  $\hat{m}_D$  being  $m_D$  in the RH neutrino mass basis and  $\mathcal{F}_{ij}$  related to the regulator that is proportional to the mass splitting of  $N_i$  [267].

We find the real part of  $(\hat{m}_D^\dagger \hat{m}_D)_{ij}$  to be zero, if either  $i = 3$  or  $j = 3$ . Hence,  $\epsilon_{3\alpha} = 0$  for all  $\alpha$  and  $\epsilon_{i\alpha}$  only has one contribution for  $i = 1, 2$ . The imaginary part of  $\hat{m}_{D,\alpha 1}^* \hat{m}_{D,\alpha 2}$  is proportional to  $\sin 3\phi_s$  for even  $s$  and to  $\cos 3\phi_s$  for odd  $s$ , independent of the flavour  $\alpha$ . If  $\alpha$  is summed over,  $\epsilon_1$  and  $\epsilon_2$  both vanish. For strong NO and even  $s$ , the CP asymmetries  $\epsilon_{1\alpha}$  read

$$\epsilon_{1\alpha} \approx \frac{y_2 y_3}{9} (-2 y_2^2 + y_3^2 (1 - \cos 2\vartheta_R)) \sin 3\phi_s \sin \vartheta_R \sin \vartheta_{L,\alpha} \mathcal{F}_{12}, \quad (6.102)$$

and for strong IO, we find

$$\epsilon_{1\alpha} \approx \frac{y_1 y_2}{9} (-2 y_2^2 + y_1^2 (1 + \cos 2 \vartheta_R)) \sin 3 \phi_s \cos \vartheta_R \cos \vartheta_{L,\alpha} \mathcal{F}_{12}, \quad (6.103)$$

with  $\vartheta_{L,\alpha} = \vartheta_L + \rho_\alpha 4\pi/3$  and  $\rho_e = 0, \rho_\mu = 1, \rho_\tau = -1$ . For strong NO (IO)  $\epsilon_{i\alpha}$  becomes very small, if  $\vartheta_R \approx 0, \pi$  ( $\vartheta_R \approx \pi/2, 3\pi/2$ ). In addition,  $\mathcal{F}_{ij}$  vanishes for  $\cos 2 \vartheta_R = 0$ . The CP asymmetries  $\epsilon_{2\alpha}$  are the negative of  $\epsilon_{1\alpha}$  with  $\mathcal{F}_{12}$  being replaced by  $\mathcal{F}_{21}$ . We note that different values of  $s$  can lead to the same value of  $\epsilon_{i\alpha}$ . In particular, we find

$$\epsilon_{i\alpha}(s) = (-1)^s \epsilon_{i\alpha}(n - s) = \epsilon_{i\alpha}(n/2 - s) = (-1)^{s+1} \epsilon_{i\alpha}(n/2 + s) \text{ for } s \leq n/2. \quad (6.104)$$

Eqs. (6.46), (6.102) and (6.103) show the close correlation between CP violation at low and high energies.

## 6.5 Decay of Heavy Neutrinos

In this section, we study the decay lengths and branching ratios of the heavy right-handed neutrinos in different cases of lepton mixing. Firstly, we discuss the decay lengths of the RH neutrinos using their decay widths and identifying the enhanced residual symmetry (ERS) points. The decay lengths near the points of ERS tend to be the longest. We discuss the results in different cases of lepton mixing as well as for different neutrino mass hierarchies. Secondly, we calculate the branching ratios for the decay of RH neutrinos by using the partial decay widths for the relevant processes. We then discuss the results for branching ratios for all RH neutrinos as well as their different decay modes.

### 6.5.1 Decay Length

The decay widths  $\Gamma_i$  of the RH neutrinos  $N_i$  are given at the tree level by

$$\Gamma_i \approx \frac{(\hat{Y}_D^\dagger \hat{Y}_D)_{ii}}{8\pi} M_i = \frac{(\hat{m}_D^\dagger \hat{m}_D)_{ii}}{8\pi v^2} M_i \quad (6.105)$$

where the form of  $\hat{Y}_D$  is determined by the choice for generator  $Z$  of the  $Z_2$  symmetry and the choice of the CP transformation  $X$ . Despite this dependence on the generators of  $Z_2$  symmetry and CP transformation, we will see that  $\Gamma_i$  is independent of value of  $n$  and depends only on odd/even behaviour for parameters  $s, t$  and  $m$ <sup>34</sup>.

For  $M$  in the few hundred GeV range, we expect  $y_i \sim 10^{-7}$  and thus mostly non-prompt decays at the LHC. To enhance the production cross-section at colliders, we can embed our minimal scenario in the SM with extended gauge symmetry. If the RH neutrinos  $N_i$  are charged under the new gauge group, they may be produced through the decays of the new gauge boson(s) (for detailed discussion, see sec. 6.6.1).

#### 6.5.1.1 Case 1

The expressions for decay widths of the 3 heavy RH neutrinos in this case do not depend on the values of  $s$ , and are given below :

$$\begin{aligned} \Gamma_1 &\approx \frac{M}{24\pi} \left( 2y_1^2 \cos^2 \vartheta_R + y_2^2 + 2y_3^2 \sin^2 \vartheta_R \right), \quad \Gamma_2 \approx \frac{M}{24\pi} \left( y_1^2 \cos^2 \vartheta_R + 2y_2^2 + y_3^2 \sin^2 \vartheta_R \right), \\ \Gamma_3 &\approx \frac{M}{8\pi} \left( y_1^2 \sin^2 \vartheta_R + y_3^2 \cos^2 \vartheta_R \right). \end{aligned} \quad (6.106)$$

In Case 1, strong NO and strong IO corresponds to  $y_1 = 0$  and  $y_3 = 0$  respectively, i.e. the lightest neutrino becomes massless. If  $\vartheta_R \approx \pi/2, 3\pi/2$  (for strong NO) or  $\vartheta_R \approx 0, \pi$  (for strong IO), i.e.  $\vartheta_R$  close to points of ERS,  $N_3$  can have a very long lifetime, since  $\Gamma_3$  tends to zero. Thus,  $N_3$  can be searched for with the long-lived particle detectors. The decay lengths  $L$  for  $N_{1,2,3}$  are shown in Fig. 6.1 for different values of  $M$  and mass scale for the lightest

<sup>34</sup> It might also happen that  $\Gamma_i$  is totally independent of values

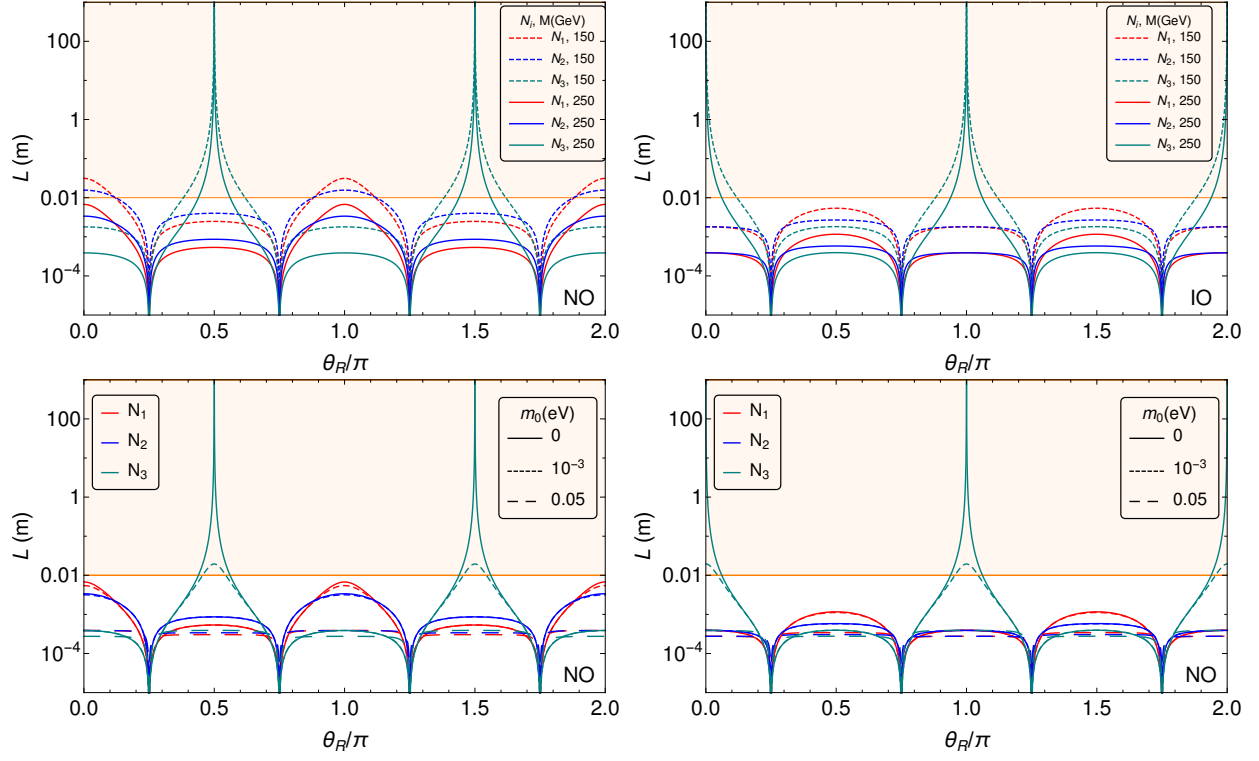


Fig. 6.1: Case 1  $N_{1,2,3}$  decay lengths plotted against  $\theta_R$  for different values of RHN mass scale  $M$  (upper Panels) and light neutrino mass  $m_0$  (lower panels) for  $M_{Z'} = 4$  TeV.

neutrino  $m_0$ . In doing so, we assume that  $N_i$  are produced via a new gauge boson  $Z'$  with mass  $M_{Z'} = 4$  TeV, meaning the Lorentz boost factor is given by  $\gamma = M_{Z'}/(2M)$ . As  $M$  is increased, there is an enhancement in  $L$  for  $N_3$  for  $\vartheta_R$  around the ERS. The decay lengths become more sharply peaked with decreasing  $m_0$ , especially for  $N_3$ .  $N_3$  can be detected with the MATHUSLA detector or can be probed at the LHC via displaced vertex signatures, along with  $N_{1,2}$  decays, the latter giving rise to either prompt or displaced vertex signals at the LHC, depending on the choice of  $\vartheta_R$ .

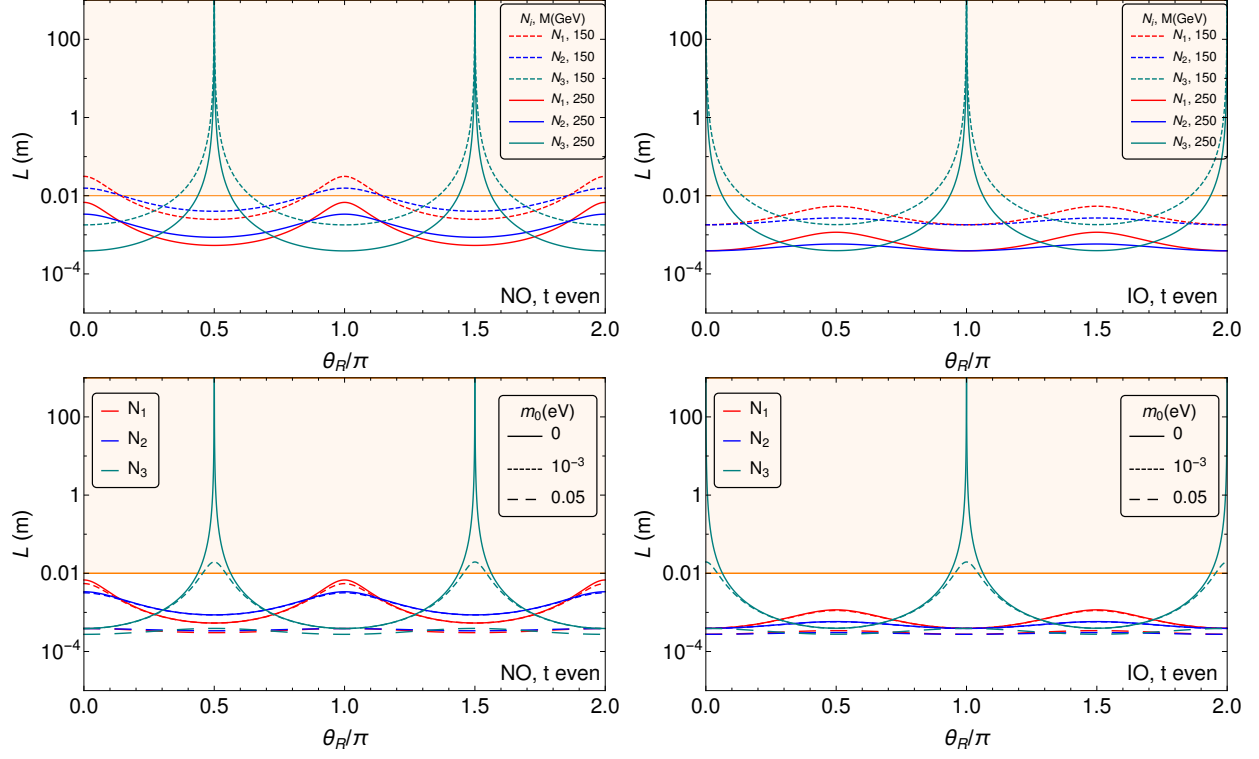


Fig. 6.2: Case 2  $N_{1,2,3}$  decay lengths plotted against  $\theta_R$  for different values of RHN mass scale  $M$  (upper Panels) and light neutrino mass  $m_0$  (lower panels) for  $M_{Z'} = 4$  TeV.

### 6.5.1.2 Case 2

The decay widths of the RH neutrinos in this case depends whether  $t$  is even/odd and independent of  $s$ .

**t even :**

$$\begin{aligned} \Gamma_1 &\approx \frac{M}{24\pi} \left( 2y_1^2 \cos^2 \vartheta_R + y_2^2 + 2y_3^2 \sin^2 \vartheta_R \right), \quad \Gamma_2 \approx \frac{M}{24\pi} \left( y_1^2 \cos^2 \vartheta_R + 2y_2^2 + y_3^2 \sin^2 \vartheta_R \right), \\ \Gamma_3 &\approx \frac{M}{8\pi} \left( y_1^2 \sin^2 \vartheta_R + y_3^2 \cos^2 \vartheta_R \right). \end{aligned} \quad (6.107)$$

**t odd :**

$$\begin{aligned} \Gamma_1 &\approx \frac{M}{24\pi} \left( y_1^2 + y_2^2 + y_3^2 \right), \quad \Gamma_2 \approx \frac{M}{24\pi} \left( y_1^2 + 4y_2^2 + y_3^2 \right), \\ \Gamma_3 &\approx \frac{M}{24\pi} \left( y_1^2 + y_3^2 \right). \end{aligned} \quad (6.108)$$

As can be seen above,  $\Gamma_3$  is independent of  $\vartheta_R$  for odd values of  $t$  and non-zero in all cases

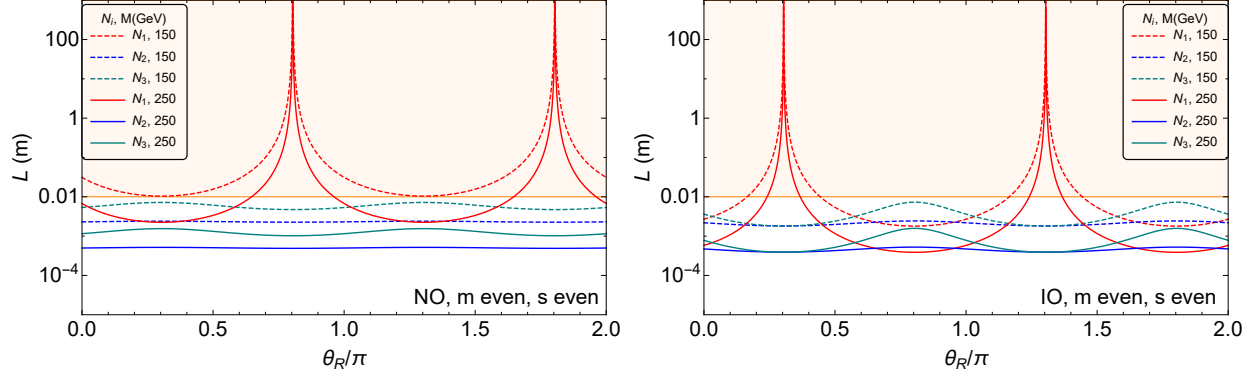


Fig. 6.3:  $N_{1,2,3}$  decay lengths plotted against  $\theta_R$  for different values of RHN mass scale  $M$  for Case 3a (left panel) and for Case 3b.1 (right panel) with  $M_{Z'} = 4$  TeV.

including strong NO and strong IO. Thus in Case 2, the ERS points are present only for even values of  $t$  and lies at the same values of  $\vartheta_R$  as in Case 1 for both mass orderings, irrespective of  $s$  values as shown in Fig. 6.2. Note that similar to Case 1, strong NO and strong IO in this case corresponds to  $y_1 = 0$  and  $y_3 = 0$  respectively.

### 6.5.1.3 Case 3a and 3b.1

The decay widths of the RH neutrinos in Case 3a and 3b.1 depends on the combination of  $(m, s)$  being even/odd as well as allowed mass orderings are restricted. There is an important distinction to be noted that unlike other cases where  $N_3$  becomes long-lived, in Case 3a and

3b.1, it is  $N_1$  for which the decay length is the longest near ERS points.

**m even, s even :**

$$\begin{aligned}\Gamma_1 &\approx \frac{M}{48\pi} \left( 3(y_1^2 + y_2^2) + (y_1^2 - y_2^2)(\cos 2\vartheta_R - 2\sqrt{2} \sin 2\vartheta_R) \right), \\ \Gamma_2 &\approx \frac{M}{192\pi} \left( 3(y_1^2 + y_2^2 + 6y_3^2) - (y_1^2 - y_2^2)(\cos 2\vartheta_R - 2\sqrt{2} \sin 2\vartheta_R) \right), \\ \Gamma_3 &\approx \frac{M}{64\pi} \left( 3(y_1^2 + y_2^2) + 2y_3^2 - (y_1^2 - y_2^2)(\cos 2\vartheta_R - 2\sqrt{2} \sin 2\vartheta_R) \right).\end{aligned}\quad (6.109)$$

**m even, s odd :**

$$\begin{aligned}\Gamma_1 &\approx \frac{M}{48\pi} \left( 3(y_1^2 + y_2^2) + (y_1^2 - y_2^2) \cos 2\vartheta_R \right), \\ \Gamma_2 &\approx \frac{M}{192\pi} \left( 3(y_1^2 + y_2^2 + 6y_3^2) - (y_1^2 - y_2^2) \cos 2\vartheta_R \right), \\ \Gamma_3 &\approx \frac{M}{64\pi} \left( 3(y_1^2 + y_2^2) + 2y_3^2 - (y_1^2 - y_2^2) \cos 2\vartheta_R \right).\end{aligned}\quad (6.110)$$

**m odd, s even :**

$$\begin{aligned}\Gamma_1 &\approx \frac{M}{48\pi} \left( 4y_1^2 + y_2^2 + y_3^2 + (y_2^2 - y_3^2) \cos 2\vartheta_R \right), \\ \Gamma_2 &\approx \frac{M}{192\pi} \left( 2y_1^2 + 11(y_2^2 + y_3^2) - 7(y_2^2 - y_3^2) \cos 2\vartheta_R \right), \\ \Gamma_3 &\approx \frac{M}{64\pi} \left( 2y_1^2 + 3(y_2^2 + y_3^2) + (y_2^2 - y_3^2) \cos 2\vartheta_R \right).\end{aligned}\quad (6.111)$$

**m odd, s odd :**

$$\begin{aligned}\Gamma_1 &\approx \frac{M}{48\pi} \left( 4y_1^2 + y_2^2 + y_3^2 + (y_2^2 - y_3^2) \cos 2\vartheta_R \right), \\ \Gamma_2 &\approx \frac{M}{192\pi} \left( 2y_1^2 + 11(y_2^2 + y_3^2) - (y_2^2 - y_3^2)(7 \cos 2\vartheta_R + 6\sqrt{2} \sin 2\vartheta_R) \right), \\ \Gamma_3 &\approx \frac{M}{64\pi} \left( 2y_1^2 + 3(y_2^2 + y_3^2) + (y_2^2 - y_3^2)(\cos 2\vartheta_R + 2\sqrt{2} \sin 2\vartheta_R) \right).\end{aligned}\quad (6.112)$$

In Case 3a, strong NO and strong IO corresponds to  $y_1 = 0$  and  $y_3 = 0$  respectively. As can be verified, ERS points are exhibited only for even values of  $(m, s)$  with mass ordering restricted to being normal ordered (NO). These points correspond to values of  $\vartheta_R \approx 0.8\pi, 1.8\pi$ , obtained by setting  $\gamma_1 = 0$ . While in Case 3b.1, strong NO and strong IO corresponds to  $y_3 = 0$  and  $y_2 = 0$  respectively. In this case, ERS points are also exhibited only for even

values of  $(m, s)$  but with mass ordering being restricted to IO and these points correspond to values of  $\vartheta_R \approx 0.3\pi, 1.3\pi$ .

### 6.5.2 Branching Ratios and Signals at MATHUSLA

Assuming  $M > \{m_H, m_w, m_z\}$ , a heavy RH neutrino  $N_i$  can decay into  $l_\alpha W$ ,  $\nu_\alpha Z$  and  $\nu_\alpha H$ , through its mixing with SM leptons. The corresponding partial decay widths for these channels are

$$\begin{aligned}\Gamma(N_i \rightarrow l_\alpha W) &= \frac{g^2 v^2 (M_i^2 - m_W^2)^2 (M_i^2 + 2m_W^2)}{64 \pi M_i^5 m_W^2} (\hat{Y}_D^\dagger \hat{Y}_D)_{i\alpha}, \\ \Gamma(N_i \rightarrow \nu_\alpha Z) &= \frac{g^2 v^2 (M_i^2 - m_Z^2)^2 (M_i^2 + 2m_Z^2)}{128 \pi \cos^2 \theta_W M_i^5 m_Z^2} (\hat{Y}_D^\dagger \hat{Y}_D)_{i\alpha}, \\ \Gamma(N_i \rightarrow \nu_\alpha H) &= \frac{g^2 v^2 (M_i^2 - m_H^2)^2}{128 \pi M_i^3 m_W^2} (\hat{Y}_D^\dagger \hat{Y}_D)_{i\alpha}.\end{aligned}\quad (6.113)$$

The branching ratio for  $N_i \rightarrow X$ , where  $X$  refers to any of the three above mentioned final states

$$\text{BR}(N_i \rightarrow X) = \frac{\Gamma(N_i \rightarrow X)}{2 [\Gamma(N_i \rightarrow l_\alpha W) + \Gamma(N_i \rightarrow \nu_\alpha Z) + \Gamma(N_i \rightarrow \nu_\alpha H)]}.\quad (6.114)$$

A production cross section  $\sigma_{\text{prod}} \equiv \sigma(pp \rightarrow Z' \rightarrow N_i N_i) \gtrsim 1 \text{ fb}$  is needed at the  $\sqrt{s} = 14 \text{ TeV}$  LHC with an integrated luminosity of  $3 \text{ ab}^{-1}$  for at least 4 signal events at MATHUSLA [268]. Once the RH neutrinos are produced, the different BRs for  $N_i \rightarrow \ell_\alpha^\pm W^\mp$  are predicted in terms of the underlying Yukawa structure.

Consider  $N_3$  decay at MATHUSLA, for Case 1 we find

$$\text{BR}(N_3 \rightarrow e^\pm W^\mp) : \text{BR}(N_3 \rightarrow \mu^\pm W^\mp) : \text{BR}(N_3 \rightarrow \tau^\pm W^\mp) = \begin{cases} 1 : 27.7 : 18.1 \\ 8.5 : 1 : 3.7 \end{cases}, \quad (6.115)$$

where the ratios in the upper (lower) line are given for strong NO (IO). These are independent

of  $\vartheta_R$  and  $s$ , and almost independent of  $M$ , if  $M \gg M_W$ . This can also be seen in Fig. 6.6, where  $\text{BR}(N_i \rightarrow l_\alpha W)$  remains constant for all values of  $s/n$  with  $M = 250$  GeV,  $m_0 = 0$  eV and  $\vartheta_R$  tuned near the ERS. Measuring them at MATHUSLA for at least two charged lepton flavours  $\alpha$  [268], allows a test of the neutrino mass hierarchy at the high-energy frontier. It could also be tested with prompt or displaced vertex signals from the decays of  $N_{1,2}$  at the LHC. However, their BRs depend on the chosen CP symmetry  $X(s)$  as well as on  $\vartheta_R$ . For instance, for  $M = 500$  GeV,  $s = 2$ ,  $n = 26$  and  $\delta\vartheta_R = 0.01$  (i.e.  $\vartheta_R$  close to a point of ERS), we get

$$\begin{aligned} \text{BR}(N_1 \rightarrow e^\pm W^\mp) : \text{BR}(N_1 \rightarrow \mu^\pm W^\mp) : \text{BR}(N_1 \rightarrow \tau^\pm W^\mp) &= \begin{cases} 1 : 4.9 : 6.6 \\ 17.3 : 1 : 1.6 \end{cases}, \\ \text{BR}(N_2 \rightarrow e^\pm W^\mp) : \text{BR}(N_2 \rightarrow \mu^\pm W^\mp) : \text{BR}(N_2 \rightarrow \tau^\pm W^\mp) &= \begin{cases} 1 : 17.6 : 3.0 \\ 1 : 3.3 : 4.8 \end{cases}. \end{aligned} \quad (6.116)$$

where the ratios in the upper (lower) line are given for strong NO (IO). Note that due to the Majorana nature of the RH neutrinos in the type-I seesaw scenario,  $\text{BR}(N_i \rightarrow \ell_\alpha^+ W^-)$  and  $\text{BR}(N_i \rightarrow \ell_\alpha^- W^+)$  are the same.

For Case 2, the BRs have been plotted for  $N_1$  and  $N_2$  for different  $(s, t)$  cases that showcase points of ERS, shown in Fig. 6.7 and Fig. 6.8 respectively. Similar to Case 1, the BR for  $N_3$  decay to  $\ell_\alpha W$  is independent of  $\vartheta_R$  and  $s$ , and almost independent of  $M$ , if  $M \gg M_W$ . Moreover, the BRs for  $(N_3 \rightarrow \mu W)$  and  $(N_3 \rightarrow \tau W)$  are equal for both NO and IO, as can be seen in in Fig. 6.9.

For Case 3a and 3b, the BRs are shown in Fig. 6.10 and Fig. 6.11 respectively. Unlike previous cases, BR for  $N_3$  decay is not constant and depends on the the chosen CP symmetry  $X(s, m)$  as well as on  $\vartheta_R$ .

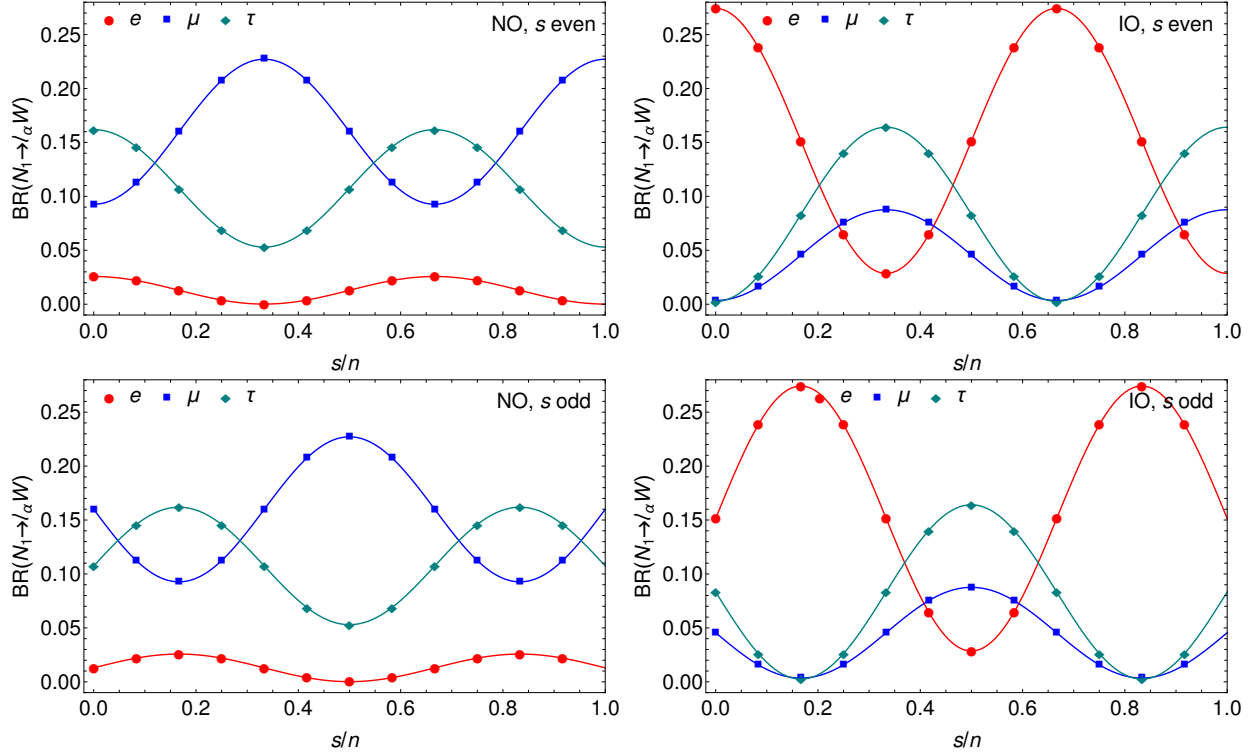


Fig. 6.4: Case 1  $N_1$  decay branching ratios for  $N_1 \rightarrow l_\alpha W$ , ( $\alpha = e, \mu, \tau$ ) as a function of  $s/n$  for strong NO and strong IO with  $M = 250$  GeV.

## 6.6 Collider Signals

In this section, we discuss the collider signatures in our scenario and probe further to understand their complementary nature to the prospects of leptogenesis. Firstly, we discuss the production of heavy RH neutrinos at the colliders and our use of SM extension for enhancing the production cross section. Next, we discuss the collider signatures at LHC for the production of RH neutrinos, specifically the LNV processes with a really low SM background. Finally, we present the relevant parameter space for the prospects of successful leptogenesis and its implications for detection at LHC and future 100 TeV collider.

### 6.6.1 Production of Heavy Neutrinos at Colliders

To observe  $N_i$  decays at colliders, an efficient production mechanism is required. In our scenario, however, Yukawa couplings  $y_i$  are too small,  $y_i \sim 10^{-7}$ , for the production cross

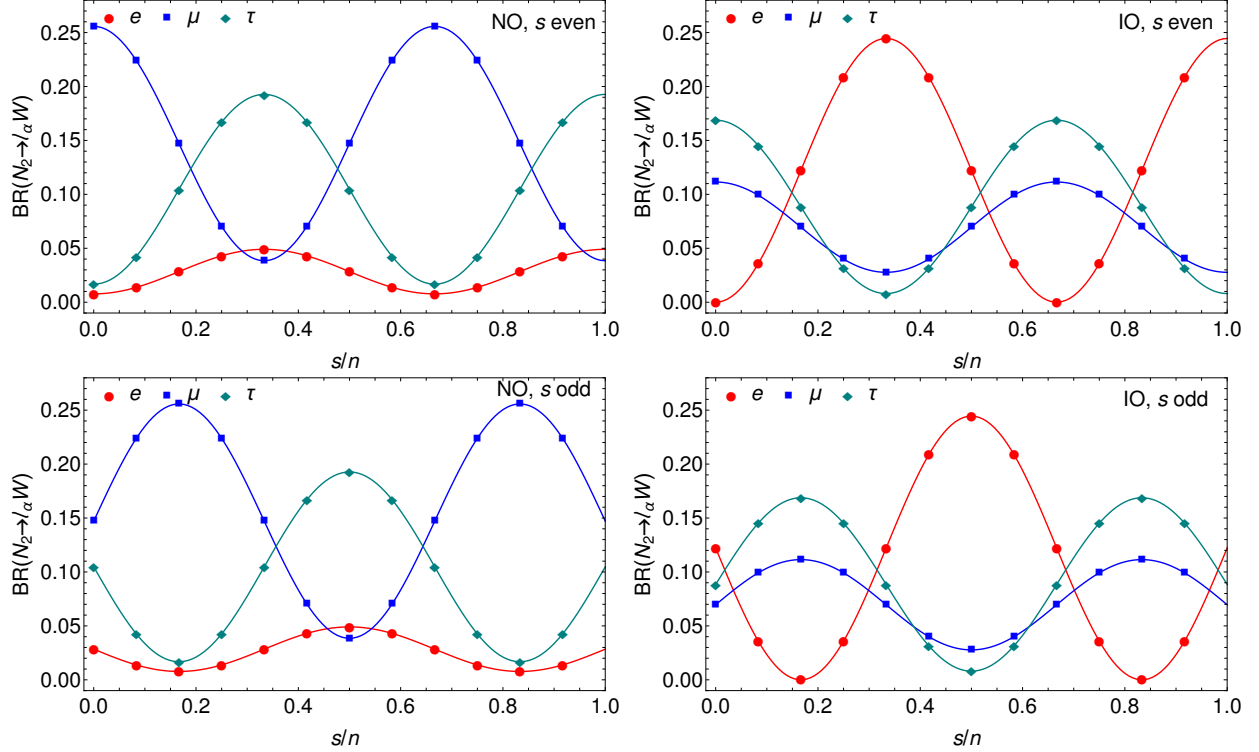


Fig. 6.5: Case 1  $N_2$  decay branching ratios for  $N_2 \rightarrow l_\alpha W$ , ( $\alpha = e, \mu, \tau$ ) as a function of  $s/n$  for strong NO and strong IO with  $M = 250$  GeV.

section via the Drell-Yan process  $pp \rightarrow W^* \rightarrow N_i l_\alpha$  (where  $l_\alpha$  stands for a charged lepton with flavour  $\alpha$ ) to be observable at the LHC [269, 97]. We thus consider a mechanism for RH neutrino production that does not rely on Yukawa interactions. An example is the extension of the SM with a gauge symmetry  $U(1)_X$  that is a linear combination of the symmetries  $U(1)_Y$  and  $U(1)_{B-L}$  [40, 270]. The charges of the SM particles, the RH neutrinos and one new scalar under  $U(1)_X$  are given in terms of two real parameters  $x_H$  and  $x_\Phi$ . The associated gauge coupling is  $g_X$  and the gauge boson  $Z'$ . We assume that the couplings of the latter to all fermions are flavour-diagonal and -universal. RH neutrinos are pair produced via gauge interactions  $pp \rightarrow Z' \rightarrow N_i N_i$ . This production channel is only kinematically suppressed by the mass of the new gauge boson,  $M_{Z'}$ . If  $M_i < M_{Z'}/2$ , the two RH neutrinos are produced on-shell. Very similar production cross sections are expected for all  $N_i$ , since their masses are (almost) degenerate, see Eq. (6.47). For some values  $(x_H, x_\Phi)$ , the branching ratio (BR) of  $Z'$  to two RH neutrinos can be enhanced with respect to the other decay modes by up to

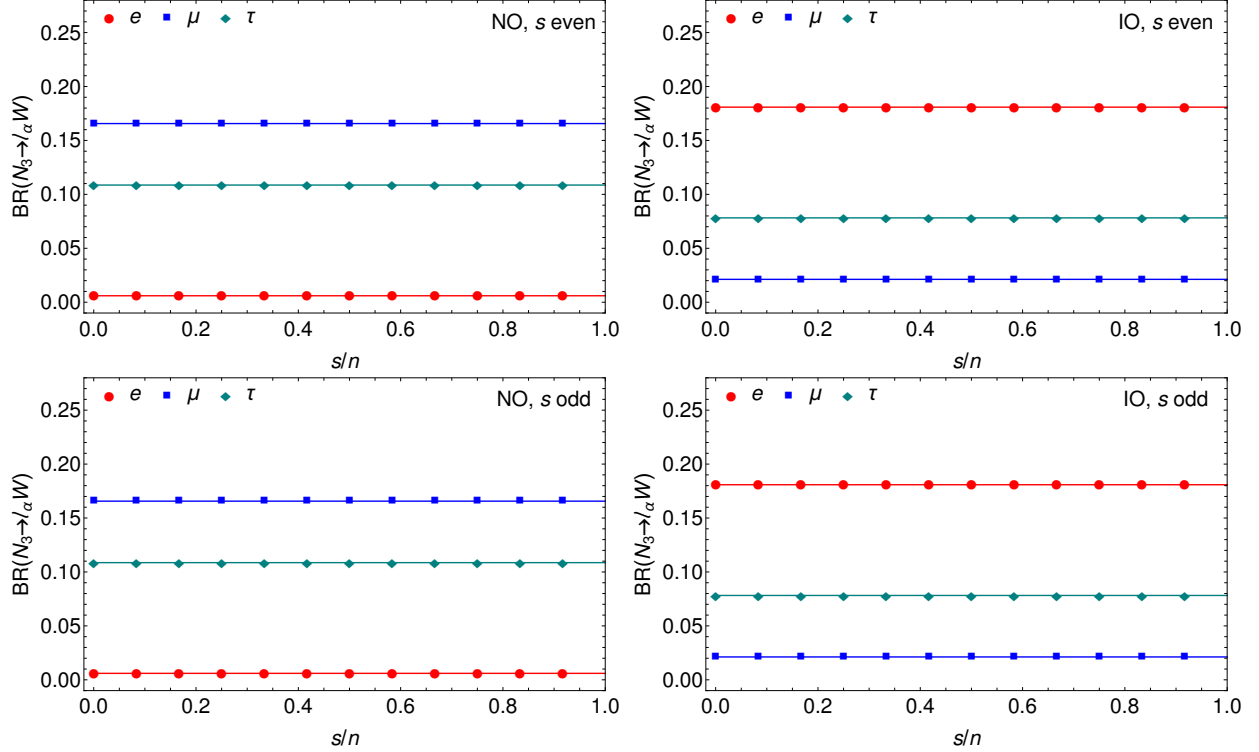


Fig. 6.6: Case 1  $N_3$  decay branching ratios for  $N_3 \rightarrow l_\alpha W$ , ( $\alpha = e, \mu, \tau$ ) as a function of  $s/n$  for strong NO and strong IO with  $M = 250$  GeV.

a factor of 5 [271]. Stringent LHC dilepton limits [1, 2] require  $M_{Z'} \gtrsim 3.7$  TeV for  $g_X$  equal to the  $SU(2)_L$  gauge coupling, as in the so-called sequential SM. They can be relaxed for smaller  $g_X$  and completely avoided, if  $Z'$  is leptophobic. The latter necessitates, however, an extension with new fermions in order to keep  $U(1)_X$  anomaly-free [272, 273, 274, 275]. In this work, we only consider the special case  $(x_H, x_\Phi) = (0, 2)$ , which corresponds to the minimal  $B - L$  model [38, 39].

### 6.6.2 Same-Sign Dilepton Signals at LHC

For decays of  $N_{1,2}$  at the LHC, one can therefore search for the striking lepton number violating (LNV) process  $pp \rightarrow Z' \rightarrow N_i N_i \rightarrow \ell_\alpha^\pm \ell_\beta^\pm + 2W^\mp \rightarrow \ell_\alpha^\pm \ell_\beta^\pm + 4j$  (for  $\alpha \neq \beta$  this process also violates lepton flavour) [259], which has a much smaller SM background than the corresponding lepton number conserving process,  $pp \rightarrow Z' \rightarrow N_i N_i \rightarrow \ell_\alpha^\pm \ell_\beta^\mp + W^+ W^- \rightarrow \ell_\alpha^\pm \ell_\beta^\mp + 4j$ . In the narrow decay width approximation, the cross section for the LNV process

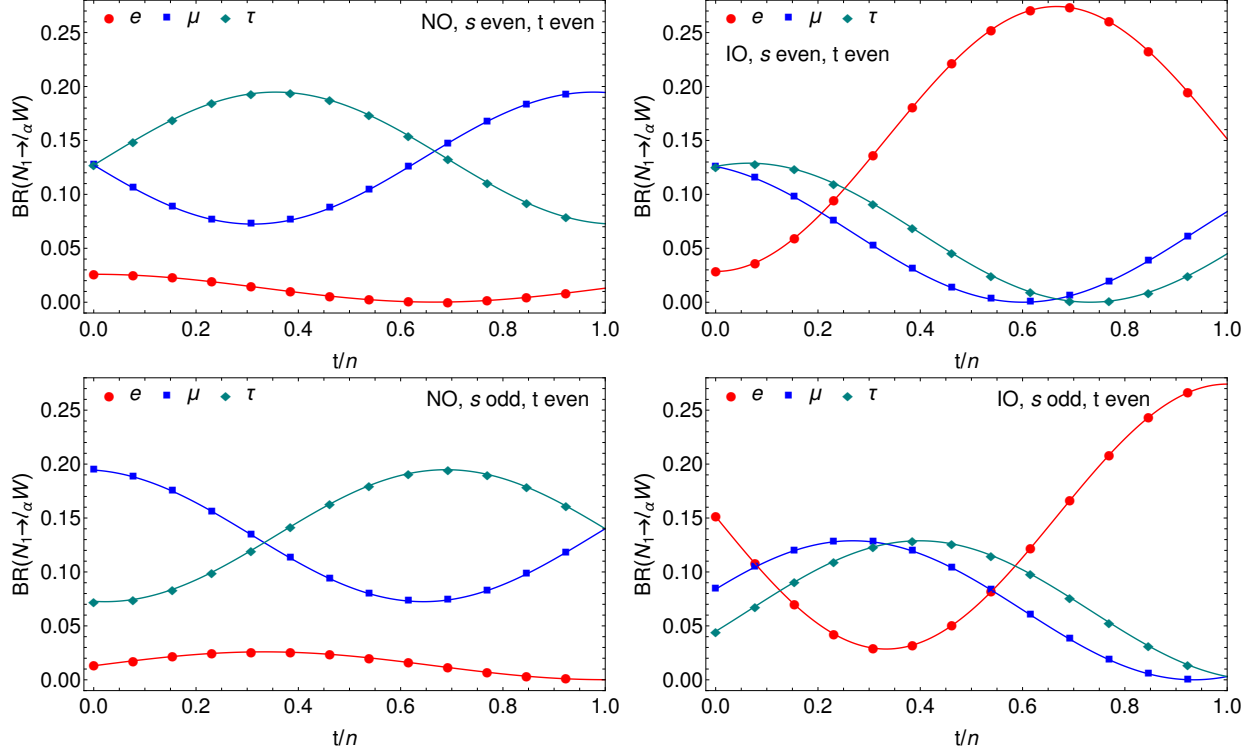


Fig. 6.7: Case 2  $N_1$  decay branching ratios for  $N_1 \rightarrow l_\alpha W$ , ( $\alpha = e, \mu, \tau$ ) as a function of  $t/n$  for strong NO and strong IO with  $M = 250$  GeV.

can written as

$$\sigma_{\text{LNV}} = \sigma(pp \rightarrow Z' \rightarrow N_i N_j) \times \text{BR}(N_i \rightarrow \ell_\alpha^\pm W^\mp) \times \text{BR}(N_j \rightarrow \ell_\beta^\pm W^\mp) \times [\text{BR}(W^\mp \rightarrow jj)]^2. \quad (6.117)$$

The production cross section for  $N_i N_j$  is generated using the universal FeynRules output (UFO) file for B-L-SM model [276, 277, 278] along with the MadGraph\_aMC@NLO-v2.8.3 - Monte Carlo event generator at parton level as shown in Fig. 6.13. The BRs for  $N \rightarrow lW$  have been discussed earlier in Sec. 6.5.2 and BR for  $W^\mp \rightarrow jj$  is already known from the SM. The results for  $\sigma_{\text{LNV}}$  with Yukawa structure from Case 1 as a function of heavy neutrino mass scale  $M_N$  for  $M_{Z'} = 4$  TeV,  $s = 2$ ,  $n = 26$  and normalized to the coupling strength  $g_{B-L} = 1$  is shown in Fig. 6.14. For NO,  $\tau\tau$ -channel has the highest production cross section and lowest the  $ee$ -channel for IO. For IO,  $ee$ -channel has the highest production cross section and lowest for  $\mu\mu$ -channel for IO. These results can be understood from analyzing Eq. (6.117)

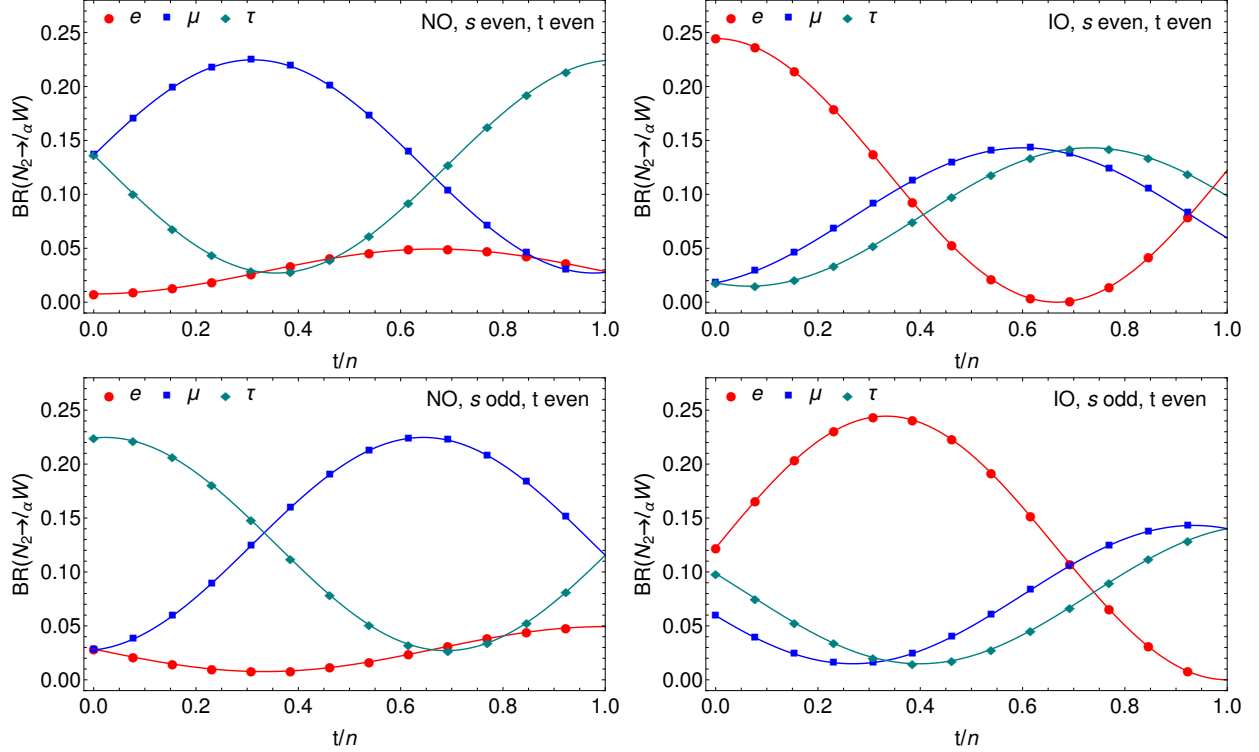


Fig. 6.8: Case 2  $N_2$  decay branching ratios for  $N_2 \rightarrow l_\alpha W$ , ( $\alpha = e, \mu, \tau$ ) as a function of  $t/n$  for strong NO and strong IO with  $M = 250$  GeV.

and Fig. 6.4. For points corresponding to  $s = 2$ ,  $n = 26$  in Fig. 6.4, the BR for  $N \rightarrow lW$  is highest for  $\tau$ -channel and lowest for  $e$ -channel in NO,  $s$  even case while it is highest for  $e$ -channel and lowest for  $\mu$ -channel in IO,  $s$  even case.

### 6.6.3 Correlation with Leptogenesis

Following the formalism developed in Refs. [279, 267], we compute the baryon asymmetry  $\eta_B$  in our scenario. For the SM extended by  $U(1)_{B-L}$ , important washout processes, like  $N_i N_i \rightarrow Z' \rightarrow f \bar{f}$  ( $f$  stands for any SM fermion), are mediated by  $Z'$  [280, 281]. These affect both washout and dilution factors in the Boltzmann equations for the RH neutrino and lepton asymmetry number densities. A *lower* limit on  $M_{Z'}$  follows for a given value of  $g_{B-L}$ , if successful leptogenesis is demanded. This is illustrated in Fig. 6.15 for Case 1 with  $g_{B-L} = 0.1$ ,  $n = 26$  and  $\vartheta_R$  being a point of ERS for strong NO (IO). In addition, we choose  $s = 2$  in order to maximize the Majorana phase (see Eq. (6.46)) and generate higher  $\eta_B$  as

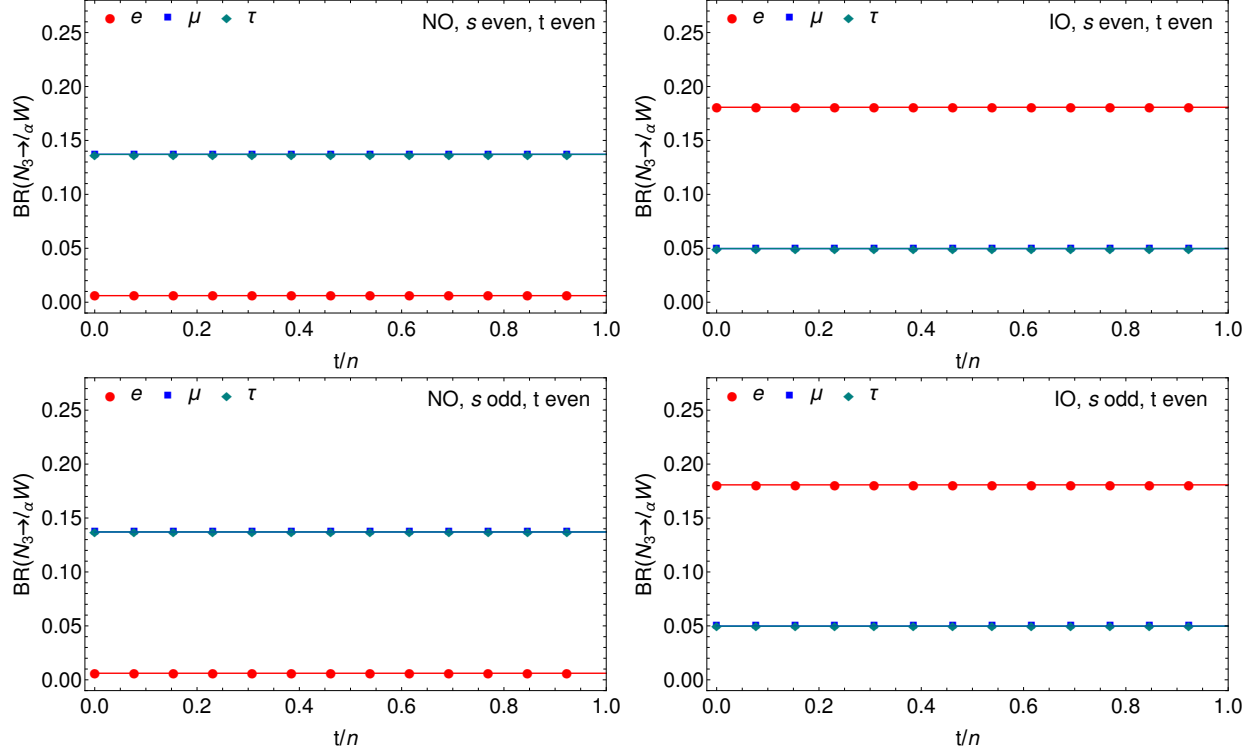


Fig. 6.9: Case 2  $N_3$  decay branching ratios for  $N_3 \rightarrow l_\alpha W$ , ( $\alpha = e, \mu, \tau$ ) as a function of  $t/n$  for strong NO and strong IO with  $M = 250$  GeV.

well as  $m_{\beta\beta}$ , as discussed in next section. The color graded legend indicates the value of  $\eta_B/\eta_B^{\text{obs}}$ , where  $\eta_B$  is the baryon asymmetry produced in the model and  $\eta_B^{\text{obs}}$  is the observed baryon asymmetry of the Universe. We are interested in collider production of  $N$  through the decays of  $Z'$  and hence do not concern ourselves with the mass range  $M_N > M_{Z'}/2$  indicated as the white region. The bounds from dilepton channels data studied by ATLAS collaboration requires  $M_{Z'} \geq 4.12$  TeV for  $g_{B-L} = 0.1$ , shown as grayed out region in the plots. As one can see in Fig. 6.15, successful leptogenesis requires  $M_{Z'} \gtrsim 4.3(5)$  TeV for strong NO (IO) in Case 1. For a  $U(1)_X$  model with leptophobic  $Z'$  instead, these limits can be relaxed to a certain extent.

An important feature to be noted in Fig. 6.15, for a given point in the  $M_N - M_{Z'}$  plane,

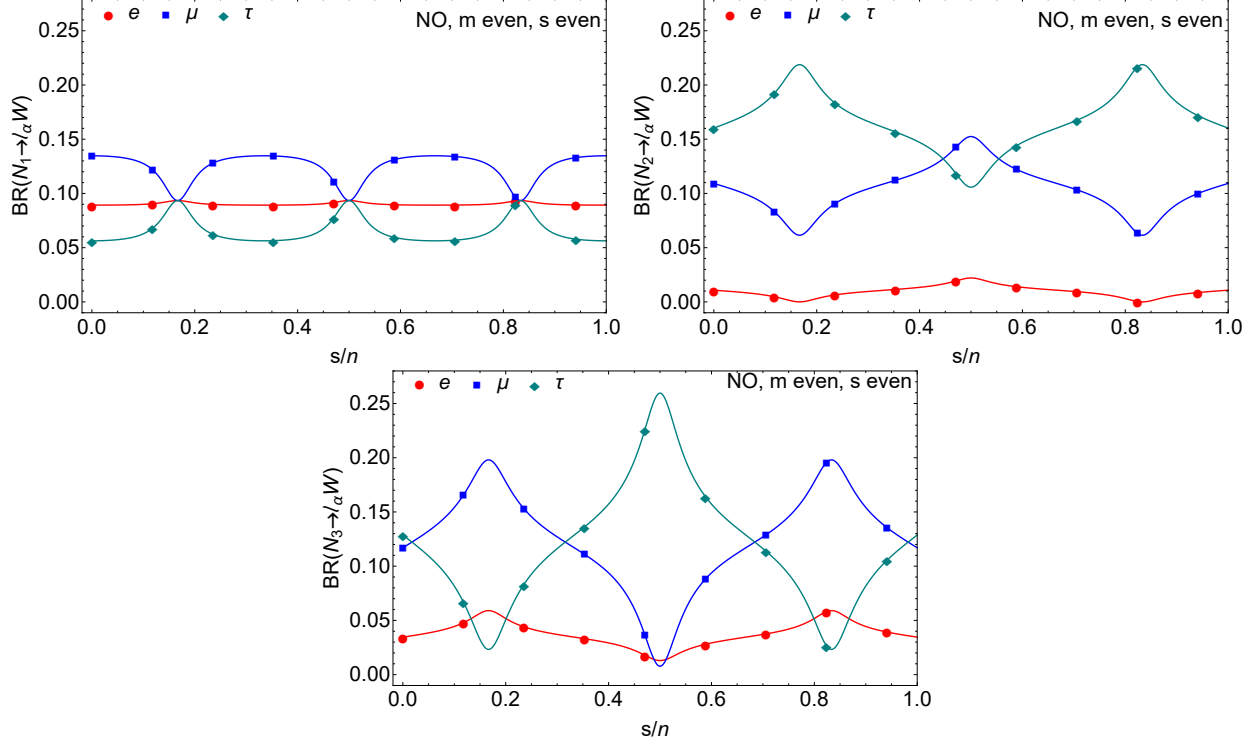


Fig. 6.10: Case 3a  $N_{1,2,3}$  decay branching ratios for  $N_i \rightarrow l_\alpha W$ , ( $\alpha = e, \mu, \tau$ ) as a function of  $s/n$  for strong NO,  $m$  even,  $s$  even with  $M = 250$  GeV.

$\eta_B^{\text{NO}} > \eta_B^{\text{IO}}$ . This can be qualitatively understood using Eqs. (6.102) and (6.103)<sup>35</sup>,

$$\frac{\eta_B^{\text{NO}}}{\eta_B^{\text{IO}}} \sim \frac{\varepsilon_{\text{NO}}}{\varepsilon_{\text{IO}}} \approx \frac{(y_2 y_3 (-y_2^2 + y_3^2) \sin \vartheta_{L,\alpha})_{\text{NO}}}{(y_1 y_2 (-y_2^2 + y_1^2) \cos \vartheta_{L,\alpha})_{\text{IO}}} \approx \frac{2\Delta m_{\text{atm}}^2}{\Delta m_{\text{sol}}^2} \tan \vartheta_{L,\alpha} \gg 1 \quad (6.118)$$

Furthermore, the results for  $\eta_B$  from resonant leptogenesis are compared with the contours of  $\sigma_{\text{prod}}$  in Fig. 6.15. It turns out that the region of parameter space in Case 1 allowing successful leptogenesis yields  $\sigma_{\text{prod}} \lesssim 0.1$  ab for strong NO at the  $\sqrt{s} = 14$  TeV LHC, which is not sufficient for the detection of decays of  $N_3$  at LLP searches. In a future 100 TeV collider,  $\sigma_{\text{prod}}$  is less than 30 ab but for a fairly low background can lead upto  $\sim 900$  events. For strong IO, the cross sections are smaller than strong NO case by at least an order of magnitude. However, these conclusions might change in other models, if, *e.g.*,  $Z'$  is leptophobic. Since the production cross section strongly depends on  $g_{B-L}^4$ , the prospects

<sup>35</sup> For a comprehensive quantitative comparison of  $\eta_B$  in both cases, efficiency factor for asymmetry production needs to be taken into account.

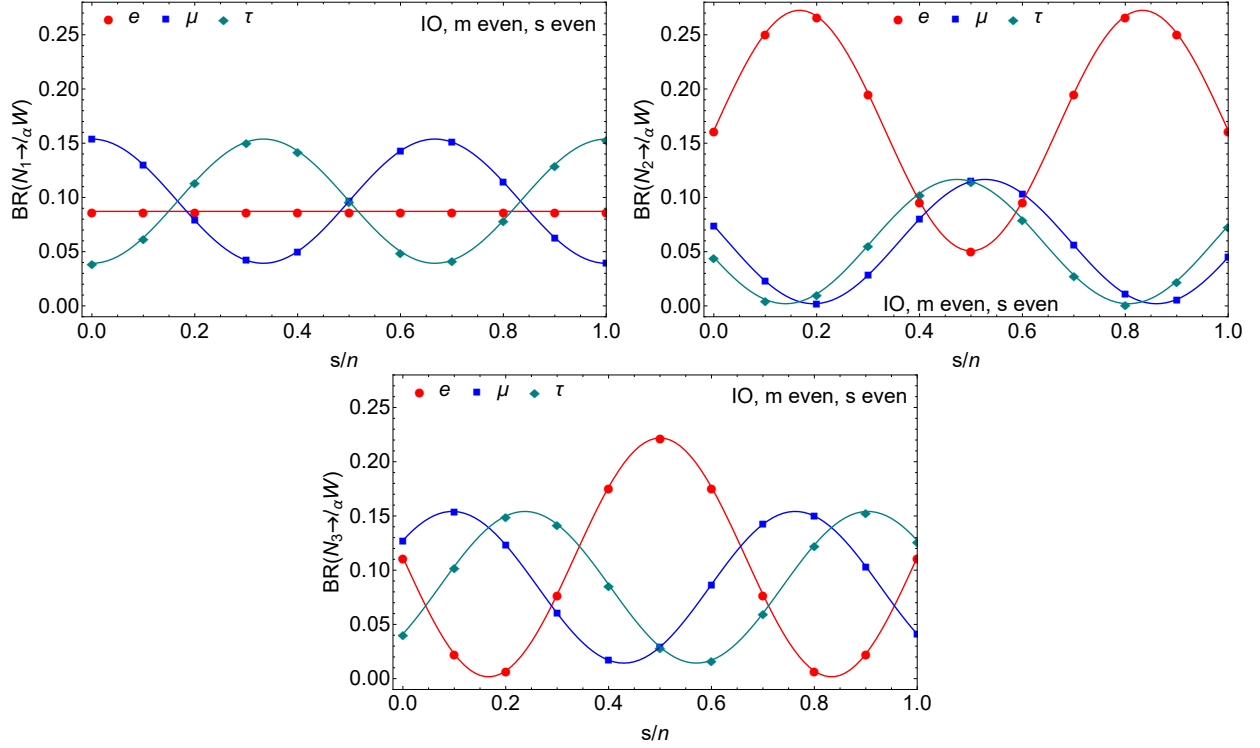


Fig. 6.11: Case 3b.1  $N_{1,2,3}$  decay branching ratios for  $N_i \rightarrow l_\alpha W$ , ( $\alpha = e, \mu, \tau$ ) as a function of  $s/n$  for strong IO,  $m$  even,  $s$  even with  $M = 250$  GeV.

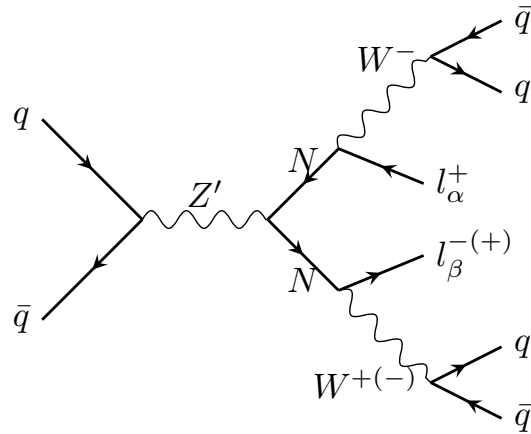


Fig. 6.12: lepton number violating (LNV) process  $pp \rightarrow Z' \rightarrow N_i N_i \rightarrow l_\alpha^\pm l_\beta^\pm + 2W^\mp \rightarrow l_\alpha^\pm l_\beta^\pm + 4j$  (for  $\alpha \neq \beta$  also violates lepton flavour)

might be improved for heavy  $Z'$  due to the relaxed constraints on the maximum allowed value of  $g_{B-L}$ . For instance if  $M_{Z'} \sim 6$  TeV, the production cross section at 100 TeV collider can reach nearly upto 18 fb in Case 1 for strong NO.

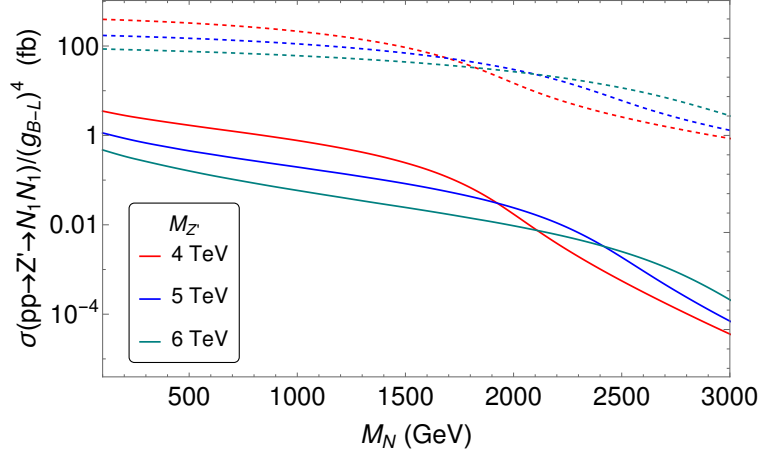


Fig. 6.13:  $pp \rightarrow Z' \rightarrow N_1 N_1$  production cross section as function of RHN mass scale  $M_N$  at  $\sqrt{s} = 14$  TeV LHC (solid lines) and  $\sqrt{s} = 100$  TeV future collider (dotted lines) for  $M_{Z'} = (4, 5, 6)$  TeV.

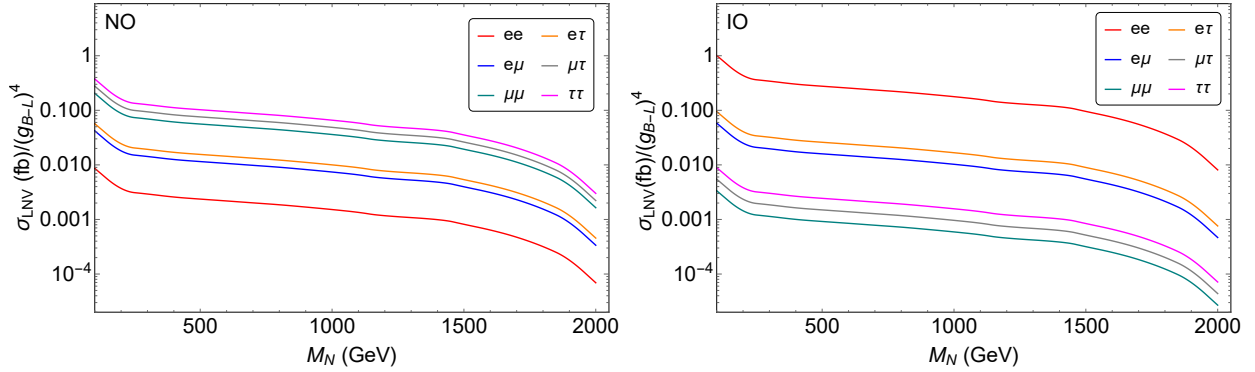


Fig. 6.14: Production cross section for same-sign LNV dilepton signals (see Sec. 6.6.2) as function of RHN mass scale  $M_N$  at  $\sqrt{s} = 14$  TeV LHC for strong NO and strong IO for  $M_{Z'} = 4$  TeV.

For Case 2, successful leptogenesis requires  $M_{Z'} \gtrsim 4.2$  (4.3) TeV for strong NO (IO), with the results for  $\sigma_{\text{prod}}$  remaining same as in Case 1. For the parameter space in  $M_{Z'} - M_N$  plane, successful leptogenesis occurs only for Case 3b.1 and absent in Case 3a, and requires  $M_{Z'} \gtrsim 5.2$  TeV for strong IO as shown in Fig. 6.17. The region of parameter space in Case 3b.1 allowing successful leptogenesis yields  $\sigma_{\text{prod}} \lesssim 0.01$  ab for strong IO at the  $\sqrt{s} = 14$  TeV LHC, which is not sufficient for the detection of decays of  $N_3$  at LLP searches.

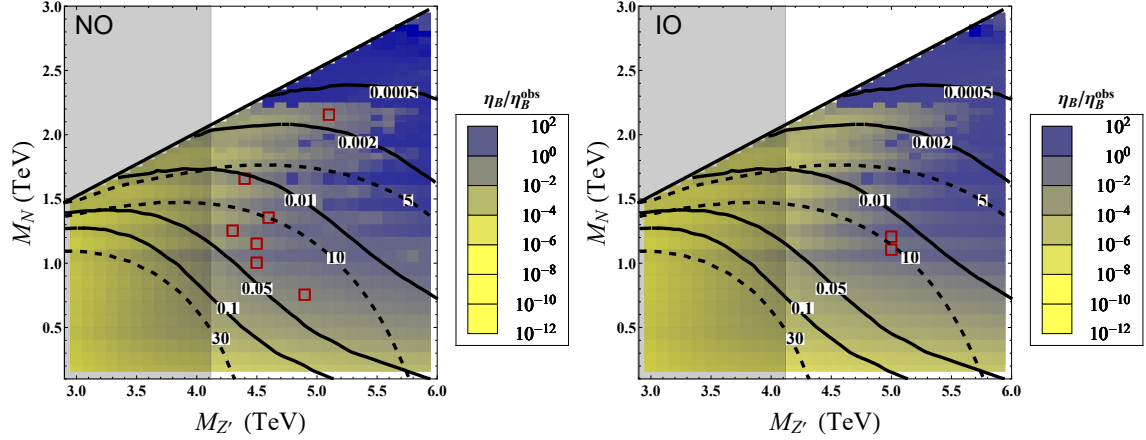


Fig. 6.15: Case 1 : Prediction of the baryon asymmetry  $\eta_B$  relative to the observed value  $\eta_B^{\text{obs}}$  in the plane of the RH neutrino mass  $M$  and the mass  $M_{Z'}$  at  $g_{B-L} = 0.1$ ,  $n = 26$  with  $\vartheta_R$  being a point of ERS and  $s$  set to 2(17) for strong NO (IO) in the left (right) panel. Red points correspond to  $|\eta_B|$  in the  $5\sigma$  interval around  $\eta_B^{\text{obs}}$ . The contours show  $\sigma_{\text{prod}}$  at the  $\sqrt{s} = 14$  TeV LHC (solid) and and  $\sqrt{s} = 100$  TeV future collider (dashed) in ab.

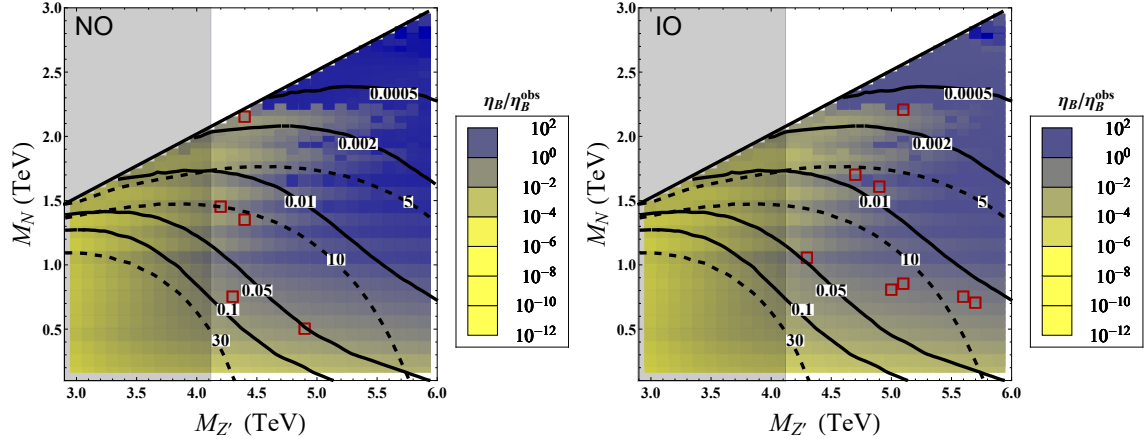


Fig. 6.16: Case 2 : Prediction of the baryon asymmetry  $\eta_B$  relative to the observed value  $\eta_B^{\text{obs}}$  in the plane of the RH neutrino mass  $M$  and the mass  $M_{Z'}$  at  $g_{B-L} = 0.1$ ,  $n = 14$ ,  $s = 1$ ,  $t = 2$  (i.e.  $u = 2s - t = 0$ ) with  $\vartheta_R$  being a point of ERS for strong NO (IO) in the left (right) panel. Red points correspond to  $|\eta_B|$  in the  $5\sigma$  interval around  $\eta_B^{\text{obs}}$ . The contours show  $\sigma_{\text{prod}}$  at the  $\sqrt{s} = 14$  TeV LHC (solid) and and  $\sqrt{s} = 100$  TeV future collider (dashed) in ab.

## 6.7 Correlation of Low Energy and High Energy CP

### Phases

In this section, we discuss about neutrinoless double beta ( $0\nu\beta\beta$ ) decay, which is one of the most important theorised LNV process to discern about the Majorana nature of the neu-

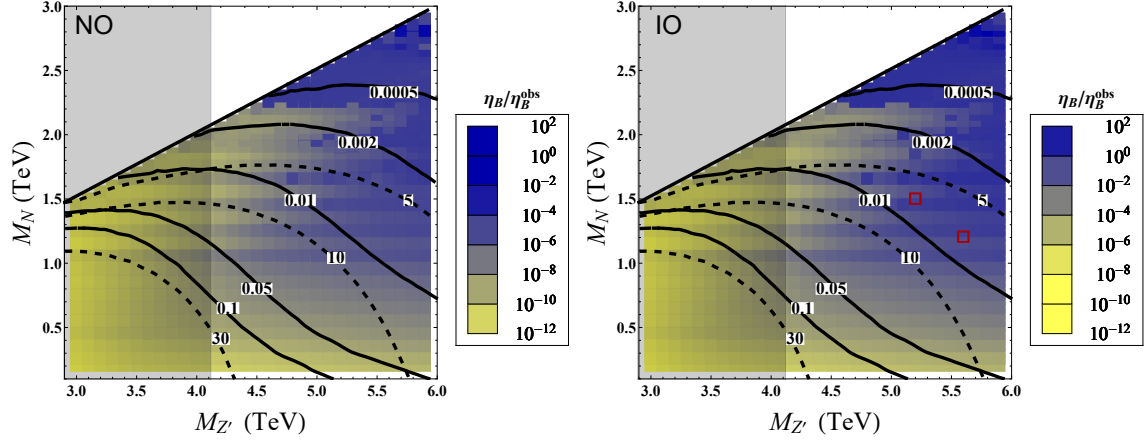


Fig. 6.17: Case 3a (left panel) and Case 3b.1 (right panel) : Prediction of the baryon asymmetry  $\eta_B$  relative to the observed value  $\eta_B^{\text{obs}}$  in the plane of the RH neutrino mass  $M$  and the mass  $M_{Z'}$  at  $g_{B-L} = 0.1$ ,  $n = 17(20)$ ,  $m = 16(10)$  with  $\vartheta_R$  being a point of ERS and  $s$  set to  $10(2)$  for strong NO (IO) in the left (right) panel. Red points correspond to  $|\eta_B|$  in the  $5\sigma$  interval around  $\eta_B^{\text{obs}}$ . The contours show  $\sigma_{\text{prod}}$  at the  $\sqrt{s} = 14$  TeV LHC (solid) and  $\sqrt{s} = 100$  TeV future collider (dashed) in ab.

trinos. The predictions for this yet unobserved process depends explicitly on the Majorana phases  $\alpha$  and  $\beta$ . We focus on various scenarios of lepton mixing for which leptogenesis has been studied earlier. A nuclear isotope decaying through  $0\nu\beta\beta$  decay would exhibit a half-life  $T_{1/2}^{0\nu\beta\beta}$  of

$$\Gamma^{0\nu\beta\beta} = \frac{1}{T_{1/2}^{0\nu\beta\beta}} = G^{0\nu} |M^{0\nu}|^2 \frac{m_{ee}}{m_e} \quad (6.119)$$

where  $G^{0\nu}$  is the phase-space factor,  $|M^{0\nu}|^2$  is the matrix element squared for this LNV transition,  $m_{ee}$  is the effective Majorana neutrino mass and  $m_e$  is the electron mass. The values of  $G^{0\nu}$  and  $|M^{0\nu}|^2$  cannot be measured independently but can be computed based on the nuclear isotope, whereas  $m_{ee}$  is expressed only in terms of neutrino masses and lepton mixing parameters,

$$m_{ee} = \left| U_{\text{PMNS},11}^2 m_1 + U_{\text{PMNS},12}^2 m_2 + U_{\text{PMNS},13}^2 m_3 \right|, \quad (6.120)$$

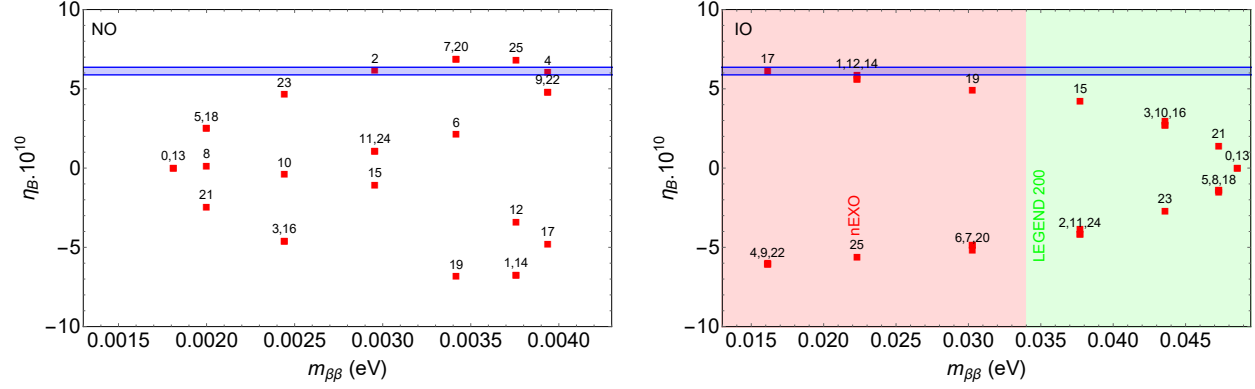


Fig. 6.18: Case 1 : Predictions for  $\eta_B$  as a function of effective neutrino mass  $m_{\beta\beta}$  for all values of  $s$  for  $n = 26$ ,  $M_N = 0.8(1.1)$  TeV with  $M_{Z'} = 4.9(5.0)$  TeV for strong NO(IO) in the left(right) panel. The shaded region indicates the  $m_{\beta\beta}$  range accessible to future  $0\nu\beta\beta$  experiments, LEGEND200 (green) and nEXO (red). The blue shaded bar corresponds to  $3\sigma$  interval around  $\eta_B^{\text{obs}}$ .

that, according to the parametrization of  $U_{\text{PMNS}}$ , given in appendix ??, reads

$$m_{ee} = \left| \cos^2 \theta_{12} \cos^2 \theta_{13} m_1 + \sin^2 \theta_{12} \cos^2 \theta_{13} e^{i\alpha} m_2 + \sin^2 \theta_{13} e^{i\beta} m_3 \right|. \quad (6.121)$$

An upper bound on the effective Majorana neutrino mass has been set by several experiments, using different nuclear isotopes: GERDA ( $^{76}\text{Ge}$ ) [282], KamLAND-Zen ( $^{136}\text{Xe}$ ) [283], EXO-200 ( $^{136}\text{Xe}$ ) [284], CUORE-0 ( $^{130}\text{Te}$ ) [285], and NEMO 3 ( $^{100}\text{Mo}$  among others) [286]. The strongest bound on  $m_{ee}$  is given by the KamLAND-Zen experiment

$$m_{ee} < (61 - 165) \text{ meV} \quad \text{at } 90\% \text{ C.L.} \quad (6.122)$$

with the largest uncertainty arising from the one of the associated nuclear matrix element.

### 6.7.1 Case 1

$$m_{ee}^{\text{NO}} \approx \frac{1}{3} \left| \sqrt{\Delta m_{\text{sol}}^2} + 2(-1)^{k_1+k_2} \sin^2 \theta e^{\delta i\phi_s} \sqrt{\Delta m_{\text{atm}}^2} \right|, \quad (6.123)$$

$$m_{ee}^{\text{IO}} \approx \frac{1}{3} \left| 1 + 2(-1)^{k_1} \cos^2 \theta e^{\delta i\phi_s} \right| \sqrt{\Delta m_{\text{atm}}^2}. \quad (6.124)$$

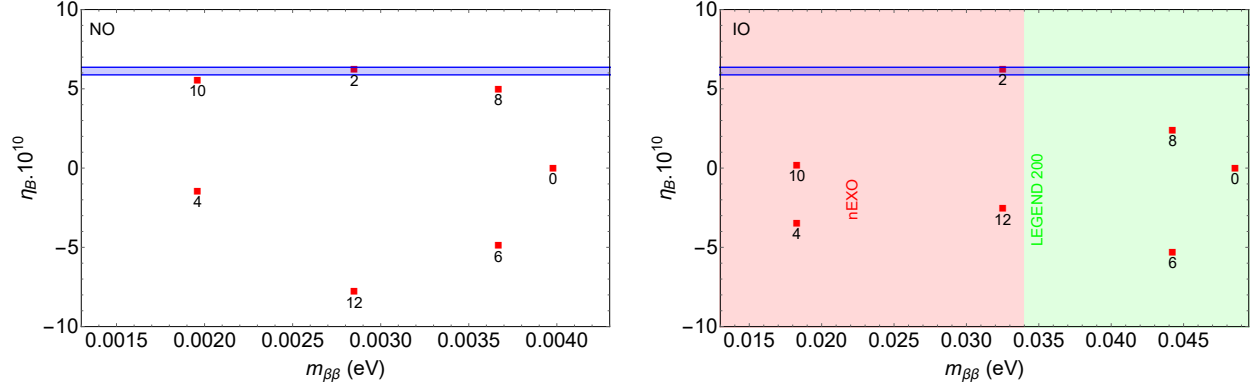


Fig. 6.19: Case 2 : Predictions for  $\eta_B$  as a function of effective neutrino mass  $m_{\beta\beta}$  for all values of  $t$  for  $u = 2s - t = 0$ ,  $n = 14$ ,  $M_N = 0.8(1.1)$  TeV with  $M_{Z'} = 4.3(4.3)$  TeV for strong NO(IO) in the left(right) panel. The shaded region indicates the  $m_{\beta\beta}$  range accessible to future  $0\nu\beta\beta$  experiments, LEGEND200 (green) and nEXO (red). Red points correspond to  $|\eta_B|$  in the  $5\sigma$  interval around  $\eta_B^{\text{obs}}$ .

The value of the effective Majorana neutrino mass  $m_{\beta\beta}$ , accessible in neutrinoless double beta decay experiments, crucially depends on the choice of the CP symmetry and is in this scenario considerably restricted [264]. For  $n = 26$ ,  $\vartheta_L \approx 0.18$  and strong NO, we get  $0.0018 \text{ eV} \lesssim m_{\beta\beta} \lesssim 0.0040 \text{ eV}$ , while for strong IO, we find  $0.015 \text{ eV} \lesssim m_{\beta\beta} \lesssim 0.048 \text{ eV}$ , using the best fit values for  $\Delta m_{\text{sol}}^2$  and  $\Delta m_{\text{atm}}^2$  [287]. For strong IO, most of the admitted values of  $m_{\beta\beta}$  can be tested with the proposed experiment LEGEND [288] and all of them can be explored with nEXO [289], whereas it is challenging to test the values of  $m_{\beta\beta}$  predicted for strong NO with current and future experiments. The corresponding values of  $\eta_B$  have been generated for  $M_N = 0.8(1.1)$  TeV for strong NO(IO). For NO, the  $M_{Z'}$  is set to 4.9 TeV and 5.0 TeV for the case of IO. These values of  $M_N$  and  $M_{Z'}$  have been chosen by analyzing red points in Fig. 6.15. As can be seen in Fig. 6.18, few values of  $s$  like  $s = 2, 4$  can explain experimentally observed  $\eta_B$  for strong NO. Note that while some values of  $s$  like  $s = 17$  can produce correct magnitude of  $\eta_B$  but the baryon asymmetry has a negative sign implying an anti-matter dominated Universe. It should also be pointed out that since inclusion of  $Z'$  only contributes to the washout of generated baryon asymmetry, increasing the value of  $M_{Z'}$  is akin to integrating out the  $Z'$  from the low-energy effective theory which leads to higher values of  $\eta_B$ .

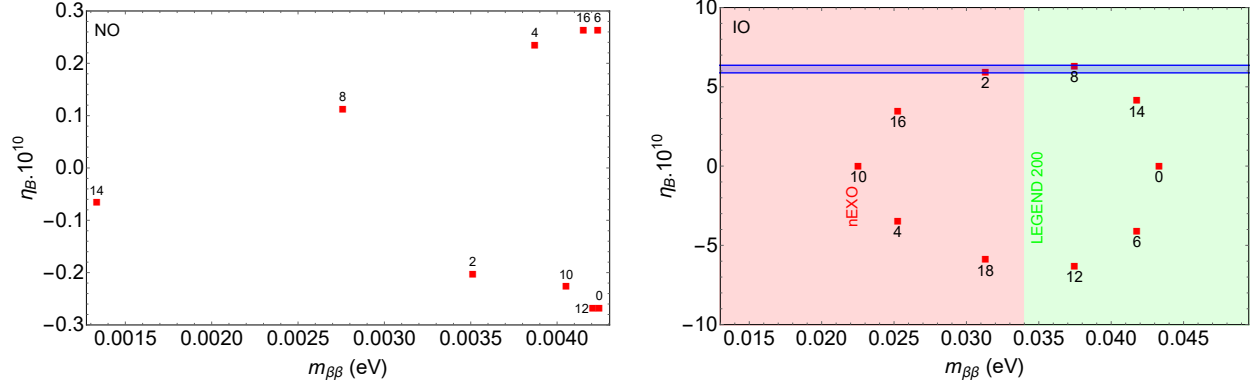


Fig. 6.20: Case 3a (left panel) and Case 3b.1 (right panel) : Predictions for  $\eta_B$  as a function of effective neutrino mass  $m_{\beta\beta}$  for all even values of  $s$  for  $n = 17(20)$ ,  $m = 16(10)$ ,  $M_N = 2.8(1.2)$  TeV with  $M_{Z'} = 5.8(5.6)$  TeV for strong NO(IO) in the left(right) panel. The shaded region indicates the  $m_{\beta\beta}$  range accessible to future  $0\nu\beta\beta$  experiments, LEGEND200 (green) and nEXO (red). Red points correspond to  $|\eta_B|$  in the  $5\sigma$  interval around  $\eta_B^{\text{obs}}$ .

### 6.7.2 Case 2

$$m_{ee}^{NO} \approx \frac{1}{3} \left| \sqrt{\Delta m_{\text{sol}}^2} - 2(-1)^{k_1+k_2} e^{i\phi_\nu} \left( \cos\theta \sin\frac{\phi_u}{2} - i \sin\theta \cos\frac{\phi_u}{2} \right)^2 \sqrt{\Delta m_{\text{atm}}^2} \right|, \quad (6.125)$$

$$m_{ee}^{IO} \approx \frac{1}{3} \left| 1 + (-1)^{k_1} e^{i\phi_\nu} (\cos\phi_u + \cos 2\theta - i \sin 2\theta \sin\phi_u) \right| \sqrt{\Delta m_{\text{atm}}^2}. \quad (6.126)$$

In this case, we set  $n = 14$ ,  $\vartheta_L \approx 2.96$  and  $u = 2s - t$  to 0 implying only even values of  $t$  are allowed. For strong NO, we get  $0.0020 \text{ eV} \lesssim m_{\beta\beta} \lesssim 0.0039 \text{ eV}$ , while for strong IO, we find  $0.018 \text{ eV} \lesssim m_{\beta\beta} \lesssim 0.048 \text{ eV}$ . The corresponding values of  $\eta_B$  have been generated for  $M_{Z'} = 4.3$  TeV in both cases. For NO, the  $M_N$  is set to 0.8 TeV and 1.1 TeV for the case of IO. Similar to case 1, these values of  $M_N$  and  $M_{Z'}$  have been chosen by analyzing red points in Fig. 6.16. As can be seen in Fig. 6.19,  $s = 2$  can nearly explain experimentally observed  $\eta_B$  for both orderings.

### 6.7.3 Case 3 a and 3b.1

$$(m_{ee}^{NO})_{3a} \approx \frac{1}{3} \left| \sin^2 \theta \sqrt{\Delta m_{\text{sol}}^2} + (-1)^{k_1} \cos^2 \theta \sqrt{\Delta m_{\text{atm}}^2} \right|, \quad (6.127)$$

$$(m_{ee}^{IO})_{3b.1} \approx \frac{1}{3} \left| \sqrt{2} \sin \theta + \cos \theta e^{-3i\phi_s} \right|^2 \sqrt{\Delta m_{\text{atm}}^2}. \quad (6.128)$$

In case 3a for a given  $n$ , only certain values of  $m \sim 0, n$  reproduce the observed neutrino mixing angles with allowed ordering restricted to NO. Thus, we set  $n = 17$ ,  $m = 16$  with  $\vartheta_L$  computed separately for each value of  $s/n$ . In case 3b for a given  $n$ , values of  $m$  which reproduce the observed neutrino mixing angles are  $m \sim n/2$  with allowed ordering restricted to IO. Thus, we set  $n = 20$ ,  $m = 10$  with  $\vartheta_L = 1.83$ . For case 3a with strong NO, we get  $0.0013 \text{ eV} \lesssim m_{\beta\beta} \lesssim 0.0042 \text{ eV}$ , while for case 3b with strong IO, we find  $0.023 \text{ eV} \lesssim m_{\beta\beta} \lesssim 0.043 \text{ eV}$ .

The corresponding values of  $\eta_B$  have been generated for  $M_N = 2.8(1.2) \text{ TeV}$  for Case 3a(3b.1). For case 3a, the  $M_{Z'}$  is set to 5.8 TeV and 5.6 TeV for case 3b. Similar to previous cases, these values of  $M_N$  and  $M_{Z'}$  have been chosen by analyzing red points in Fig. 6.17. As can be seen in Fig. 6.19,  $s = 2, 8$  can explain experimentally observed  $\eta_B$  for case 3b.1 (right panel) while none of the  $s$  values for case 3a (left panel) satisfy the criteria. The maximum  $\eta_B$  that can be produced in the case of strong NO Case 3a is only around  $2.8 \times 10^{-11}$ .

## 6.8 Conclusion

We have presented a type-I seesaw scenario with a flavour and CP symmetry as well as three RH neutrinos with almost degenerate masses in the few hundred GeV to TeV range. One of the RH neutrinos can be long-lived enough in order to be tested with the MATHUSLA detector, whereas the other two can be searched for at the LHC. Requiring  $\eta_B$  to be generated via resonant leptogenesis constrains the prospects for detecting RH neutrinos at colliders, if light neutrino masses follow strong IO. In this case, however, future neutrinoless double beta

## **Chapter 6. Resonant Leptogenesis in a Model of Discrete Flavor and CP Symmetries**

decay experiments can fully probe our scenario and thus provide complementary information to collider experiments.

## Chapter 7

# Conclusions

*“The answer is out there, Neo. It’s looking for you. And it will find you if you want it to.”*

- Trinity, The Matrix (1999)

SM is a highly successful theory which has been tested to great precision in experiments. It describes the fundamental particle interactions at the energy scales being probed today  $\sim 14$  TeV. Although we can predict the outcome for most processes in particle physics with SM, there have been few theoretical and experimental indications that points us towards physics beyond the SM. One of the major clear indicator is the non-zero neutrino masses, which leads to flavor eigenstate conversions during their propagation. The SM only features left-handed neutrinos interacting only through the weak nuclear force, which renders them massless. Since, this is in conflict with the observations, we need a BSM paradigm to explain neutrino masses. All proposed extensions of SM feature new particles species or extended gauge sector, which leads to new interactions for SM neutrinos. These new interactions might play a pivotal role in the discovery of BSM physics. Hence, it becomes highly crucial to probe and quantify the effect of these interaction in the current and future planned experiments. For this endeavour, even theoretical inconsistencies of the SM can help us point in the right direction.

In the second chapter, we find that in the extensions of the electroweak gauge group which contribute to the electric charge, there are strong limits on the new gauge couplings from the requirement that the couplings remain perturbative till the GUT scale. We obtain those

limits for the minimal versions of  $U(1)_{B-L}$  and LRSM models and study their implications for collider phenomenology.

In the third chapter, we develop a method to extract necessary and sufficient conditions to ensure vacuum stability in LRSM by using the application of gauge orbit parameters in two-Higgs fields case. We also show application of copositivity criteria and its usefulness in simplifying the analysis for vacuum stability. We show that vacuum stability constraints along with other theoretical constraints (perturbativity, unitarity, scalar mass spectrum) coupled with RGE analysis can help us narrow down the allowed parameter space for the quartic couplings in the potential of a BSM candidate.

In the fourth chapter, we perform a general field-theoretic study of scalar NSI of neutrinos with matter due to a light scalar mediator, which is valid at arbitrary temperature and density. We find that sizable scalar NSI effects although precluded in terrestrial experiments are still possible in the Sun, supernovae and early Universe environments, which may be detected in future solar and supernova neutrino data, as well as in the form of extra relativistic species ( $\Delta N_{\text{eff}}$ ) and neutrino self-interactions in cosmological observations.

In the fifth chapter, we probe the consequences of a hidden  $U(1)$  sector which interacts with the SM neutrinos through mixing with the RH neutrinos. While for other SM particles, it interacts only through loop effects. Assuming the most general Dirac and Majorana mass matrices, we have derived loop-induced couplings of  $Z$  to charged leptons and quarks. We find that future beam dump experiments like SHiP and FASER together with upgraded collider searches will have substantially improved sensitivity on such a dark photon. Thus, we conclude that hidden sectors might not be totally dark as previously expected.

In the sixth chapter, we present a type-I seesaw scenario embedded with a flavour and CP symmetry. We study the prospects of baryon asymmetry production through resonant leptogenesis as well as probe the signatures in colliders (LHC, 100TeV future) and long-lived particle searches such as MATHUSLA. We find that neutrinoless double beta decay experiments can fully probe our scenario and thus provide complementary information to

collider experiments.

In summary, we discover that well motivated BSM scenarios with new neutrino interactions - general neutrino interactions with scalar, type-I seesaw scenario, hidden sector models - have experimentally testable consequences. Most of these scenarios though not UV-complete models, but can provide the necessary bedrock to probe novel signatures and future observations to help push our understanding into the unknown.

## Appendix A

# Two-loop RGEs for the minimal LRSM

Here we list the  $\beta$ -functions for the gauge couplings  $g_{S,L,R,BL}$ , the quartic couplings  $\lambda_{1,2,3,4}$ ,  $\rho_{1,2}$  and  $\alpha_{1,2,3}$  in the scalar potential (2.17) and the Yukawa coupling  $h_t$  in the minimal LRSM up to two-loop level, which are obtained by using PyR@TE [93, 94].<sup>36</sup>

$$\beta(g_S) = \frac{1}{16\pi^2} [-7g_S^3] + \frac{1}{(16\pi^2)^2} \left[ \frac{1}{6}g_S^3 (2g_{BL}^2 + 3(9g_L^2 + 9g_R^2 - 52g_S^2 - 8h_t^2)) \right], \quad (\text{A.1})$$

$$\beta(g_L) = \frac{1}{16\pi^2} [-3g_L^3] + \frac{1}{(16\pi^2)^2} \left[ g_L^3 (g_{BL}^2 + 3(g_R^2 + 4g_S^2 - h_t^2) + 8g_L^2) \right], \quad (\text{A.2})$$

$$\beta(g_R) = \frac{1}{16\pi^2} \left[ -\frac{7}{3}g_R^3 \right] + \frac{1}{(16\pi^2)^2} \left[ \frac{1}{3}g_R^3 (27g_{BL}^2 + 9g_L^2 + 80g_R^2 + 36g_S^2 - 9h_t^2) \right], \quad (\text{A.3})$$

$$\beta(g_{BL}) = \frac{1}{16\pi^2} \left[ \frac{11}{3}g_{BL}^3 \right] + \frac{1}{(16\pi^2)^2} \left[ \frac{1}{9}g_{BL}^3 (122g_{BL}^2 + 3(9g_L^2 + 81g_R^2 + 8g_S^2 - 2h_t^2)) \right], \quad (\text{A.4})$$

---

<sup>36</sup> Note that some of the one-loop coefficients obtained here are different from those in Refs. [113, 114]. In particular, the coefficient for  $g_R$  in these references is  $-5/2$ , while, with the same matter and scalar fields that contribute to the running of  $g_R$ , we found it is  $-7/3$ .

$$\begin{aligned}
 \beta(\lambda_1) = & \frac{1}{16\pi^2} \left[ \frac{3}{8} (3g_L^4 + 2g_L^2 g_R^2 + 3g_R^4) + 16(2\lambda_1^2 + 4\lambda_2^2 + \lambda_3^2 + 3\lambda_4^2) \right. \\
 & + 3\alpha_1^2 + 3\alpha_1\alpha_3 + \frac{5}{4}\alpha_3^2 - 6h_t^4 - 9\lambda_1 (g_L^2 + g_R^2) + 16\lambda_1\lambda_3 + 12\lambda_1 h_t^2 \left. \right] \\
 & + \frac{1}{(16\pi^2)^2} \left[ \frac{291g_L^6}{16} + \frac{235g_R^6}{16} + g_L^4 \left( -\frac{191g_R^2}{16} - \frac{9h_t^2}{4} + \frac{69\lambda_1}{8} + 15\lambda_3 \right) \right. \\
 & + g_{BL}^2 \left( 24\alpha_1^2 + 10\alpha_3^2 + 24\alpha_1\alpha_3 + \frac{5}{3}\lambda_1 h_t^2 - \frac{2}{3}h_t^4 \right) \\
 & - \frac{1}{48} g_R^2 (12g_R^2 (30h_t^2 - 69\lambda_1 - 56\lambda_3) + 629g_R^4 \\
 & - 72 (15\lambda_1 h_t^2 + 8 (13\lambda_1^2 + 8\lambda_3\lambda_1 + 4\lambda_3^2 + 18\lambda_4^2))) \\
 & + g_R^4 \left( 30\alpha_1 + 15\alpha_3 - \frac{9h_t^2}{4} + \frac{157\lambda_1}{8} + 15\lambda_3 \right) \\
 & + g_R^2 \left( 48\alpha_1^2 + 17\alpha_3^2 + 48\alpha_1\alpha_3 + \frac{45}{2}\lambda_1 h_t^2 + 156\lambda_1^2 + 48\lambda_3^2 + 216\lambda_4^2 + 96\lambda_1\lambda_3 \right) \\
 & - 30\alpha_1^2\lambda_1 - 24\alpha_2^2\lambda_1 - \frac{29}{2}\alpha_3^2\lambda_1 - 30\alpha_1\alpha_3\lambda_1 - 192\alpha_2^2\lambda_2 - 96\alpha_2^2\lambda_3 - 144\alpha_1\alpha_2\lambda_4 \\
 & - 72\alpha_2\alpha_3\lambda_4 - 12\alpha_1^3 - \frac{13\alpha_3^3}{2} - 48\alpha_1\alpha_2^2 - 19\alpha_1\alpha_3^2 - 18\alpha_1^2\alpha_3 - 24\alpha_2^2\alpha_3 \\
 & + 16g_S^2 h_t^2 (5\lambda_1 - 2h_t^2) + 36h_t^6 - 12\lambda_1 h_t^4 - 96h_t^2 (2\lambda_1^2 + 4\lambda_2^2 + \lambda_3^2 + 3\lambda_4^2 + \lambda_1\lambda_3) \\
 & - 456\lambda_1^3 - 384\lambda_3^3 - 3456\lambda_1\lambda_2^2 - 704\lambda_1\lambda_3^2 - 2208\lambda_1\lambda_4^2 - 3328\lambda_2\lambda_4^2 \\
 & \left. - 1792\lambda_3\lambda_4^2 - 352\lambda_1^2\lambda_3 - 5632\lambda_2^2\lambda_3 \right], \tag{A.5}
 \end{aligned}$$

$$\begin{aligned}
 \beta(\lambda_2) = & \frac{1}{16\pi^2} \left[ 12\lambda_4^2 + 3\alpha_2^2 + \frac{3}{16}h_t^4 - 9\lambda_2(g_L^2 + g_R^2) + 24\lambda_2(\lambda_1 + 2\lambda_3) + 12\lambda_2 h_t^2 \right] \\
 & + \frac{1}{(16\pi^2)^2} \left[ -24\alpha_2^2\lambda_1 - 30\alpha_1^2\lambda_2 + 24\alpha_2^2\lambda_2 + \frac{3}{2}\alpha_3^2\lambda_2 - 30\alpha_1\alpha_3\lambda_2 - 24\alpha_2^2\lambda_3 \right. \\
 & - 36\alpha_1\alpha_2\lambda_4 - 18\alpha_2\alpha_3\lambda_4 - 24\alpha_1\alpha_2^2 - 12\alpha_2^2\alpha_3 + 24\alpha_2^2 g_{BL}^2 + \frac{5}{3}\lambda_2 g_{BL}^2 h_t^2 \\
 & + g_L^2 \left( \frac{57}{4}\lambda_2 g_R^2 + \frac{45}{2}\lambda_2 h_t^2 - \frac{9h_t^4}{32} + 54\lambda_4^2 + 72\lambda_1\lambda_2 + 288\lambda_2\lambda_3 \right) \\
 & + g_R^2 \left( 48\alpha_2^2 + \frac{45}{2}\lambda_2 h_t^2 - \frac{9h_t^4}{32} + 54\lambda_4^2 + 72\lambda_1\lambda_2 + 288\lambda_2\lambda_3 \right) \\
 & + 80\lambda_2 g_S^2 h_t^2 - \frac{231}{8}\lambda_2 g_L^4 - \frac{143}{8}\lambda_2 g_R^4 - 72\lambda_4^2 h_t^2 - 36\lambda_2 h_t^4 \\
 & - 144\lambda_1\lambda_2 h_t^2 - 288\lambda_2\lambda_3 h_t^2 + 384\lambda_2^3 - 512\lambda_2\lambda_3^2 - 432\lambda_1\lambda_4^2 \\
 & \left. - 1248\lambda_2\lambda_4^2 - 480\lambda_3\lambda_4^2 - 488\lambda_1^2\lambda_2 - 1312\lambda_1\lambda_2\lambda_3 \right], \tag{A.6}
 \end{aligned}$$

$$\begin{aligned}
 \beta(\lambda_3) = & \frac{1}{16\pi^2} \left[ \frac{27}{8} h_t^4 + 6\alpha_2^2 - \frac{1}{2}\alpha_3^2 + \frac{3}{2} g_L^2 g_R^2 - 9\lambda_3 (g_L^2 + g_R^2) \right. \\
 & \left. + 12\lambda_3 h_t^2 + 8(3\lambda_1 \lambda_3 + 16\lambda_2^2 + 2\lambda_3^2 + 3\lambda_4^2) \right] \\
 & + \frac{1}{(16\pi^2)^2} \left[ \frac{291g_L^6}{32} - \frac{1}{32} (415g_R^2 + 6(6h_t^2 - 23\lambda_1 - 308\lambda_2 + 114\lambda_3)) g_L^4 \right. \\
 & - \frac{1}{96} (1525g_R^4 + 12(30h_t^2 - 165\lambda_1 + 228\lambda_2 - 298\lambda_3)) g_R^2 \\
 & - 72(15(\lambda_1 - 4\lambda_2 + 2\lambda_3) h_t^2 + 8(13\lambda_1^2 - 4(6\lambda_2 - 5\lambda_3) \lambda_1 \\
 & \left. + 2(72\lambda_2^2 - 48\lambda_3 \lambda_2 + 8\lambda_3^2 + 9\lambda_4^2))) g_L^2 \right. \\
 & + \frac{235g_R^6}{32} + 6h_t^6 - 6\alpha_1^3 - \frac{5\alpha_3^3}{4} - 228\lambda_1^3 - 768\lambda_2^3 - 192\lambda_3^3 + 12g_{BL}^2 \alpha_1^2 \\
 & - 24\alpha_1 \alpha_2^2 + g_{BL}^2 \alpha_3^2 - \frac{11}{2} \alpha_1 \alpha_3^2 - 96h_t^2 \lambda_1^2 - 960h_t^2 \lambda_2^2 \\
 & - 4800\lambda_1 \lambda_2^2 - 144h_t^2 \lambda_3^2 - 896\lambda_1 \lambda_3^2 + 1024\lambda_2 \lambda_3^2 - 36\alpha_2 \alpha_3 \lambda_4 \\
 & - 144h_t^2 \lambda_4^2 - 1104\lambda_1 \lambda_4^2 - 1216\lambda_2 \lambda_4^2 - 1120\lambda_3 \lambda_4^2 - 9\alpha_1^2 \alpha_3 \\
 & - 12\alpha_2^2 \alpha_3 + 12g_{BL}^2 \alpha_1 \alpha_3 - 18h_t^4 \lambda_1 + \frac{5}{6} g_{BL}^2 h_t^2 \lambda_1 - 72\alpha_1 \alpha_2 \lambda_4 \\
 & + 40g_S^2 h_t^2 \lambda_1 - 15\alpha_1^2 \lambda_1 - 12\alpha_2^2 \lambda_1 - \frac{13}{4} \alpha_3^2 \lambda_1 - 15\alpha_1 \alpha_3 \lambda_1 \\
 & + 72h_t^4 \lambda_2 - \frac{10}{3} g_{BL}^2 h_t^2 \lambda_2 - 160g_S^2 h_t^2 \lambda_2 + 60\alpha_1^2 \lambda_2 - 240\alpha_2^2 \lambda_2 \\
 & - 3\alpha_3^2 \lambda_2 + 976\lambda_1^2 \lambda_2 + 60\alpha_1 \alpha_3 \lambda_2 + 288h_t^2 \lambda_1 \lambda_2 - 60h_t^4 \lambda_3 \\
 & + \frac{5}{3} g_{BL}^2 h_t^2 \lambda_3 + 80g_S^2 h_t^2 \lambda_3 - 30\alpha_1^2 \lambda_3 + 24\alpha_2^2 \lambda_3 + \frac{3}{2} \alpha_3^2 \lambda_3 - 664\lambda_1^2 \lambda_3 \\
 & - 4480\lambda_2^2 \lambda_3 - 30\alpha_1 \alpha_3 \lambda_3 - 192h_t^2 \lambda_1 \lambda_3 + 576h_t^2 \lambda_2 \lambda_3 + 2624\lambda_1 \lambda_2 \lambda_3 \\
 & - \frac{1}{16} g_R^4 (18h_t^2 - 240\alpha_1 - 120\alpha_3 - 157\lambda_1 - 572\lambda_2 + 166\lambda_3) \\
 & + g_R^2 \left( \frac{45}{4} \lambda_1 h_t^2 - 45\lambda_2 h_t^2 + \frac{45}{2} \lambda_3 h_t^2 + 24\alpha_1^2 + \frac{7\alpha_3^2}{2} + 78\lambda_1^2 + 864\lambda_2^2 \right. \\
 & \left. + 96\lambda_3^2 + 108\lambda_4^2 + 24\alpha_1 \alpha_3 - 144\lambda_1 \lambda_2 + 120\lambda_1 \lambda_3 - 576\lambda_2 \lambda_3 \right) \Bigg], \quad (A.7)
 \end{aligned}$$

$$\begin{aligned}
 \beta(\lambda_4) = & \frac{1}{16\pi^2} \left[ 3\alpha_2(2\alpha_1 + \alpha_3) + \frac{3}{2}h_t^4 - 9\lambda_4(g_L^2 + g_R^2) + 48(\lambda_1 + 2\lambda_2 + \lambda_3)\lambda_4 + 12\lambda_4h_t^2 \right] \\
 & + \frac{1}{(16\pi^2)^2} \left[ -72\alpha_1\alpha_2\lambda_1 - 36\alpha_2\alpha_3\lambda_1 - 144\alpha_1\alpha_2\lambda_2 - 72\alpha_2\alpha_3\lambda_2 - 72\alpha_1\alpha_2\lambda_3 \right. \\
 & - 36\alpha_2\alpha_3\lambda_3 - 30\alpha_1^2\lambda_4 - 120\alpha_2^2\lambda_4 - \frac{9}{2}\alpha_3^2\lambda_4 - 30\alpha_1\alpha_3\lambda_4 - 48\alpha_3^3 \\
 & - 15\alpha_2\alpha_3^2 - 36\alpha_1^2\alpha_2 - 36\alpha_1\alpha_2\alpha_3 + g_{BL}^2 \left( 48\alpha_1\alpha_2 + 24\alpha_2\alpha_3 + \frac{5}{3}\lambda_4h_t^2 \right) \\
 & + \frac{3}{4}g_R^2 \left( 128\alpha_1\alpha_2 + 64\alpha_3\alpha_2 + 3\lambda_4 \left( 13g_L^2 + 2 \left( 5h_t^2 + 48(\lambda_1 + 2\lambda_2 + \lambda_3) \right) \right) \right) \\
 & + \frac{45}{2}\lambda_4g_L^2h_t^2 + 80\lambda_4g_S^2h_t^2 - \frac{51}{8}\lambda_4g_L^4 + 216\lambda_1\lambda_4g_L^2 + 432\lambda_2\lambda_4g_L^2 + 216\lambda_3\lambda_4g_L^2 \\
 & + \left( 30\alpha_2 + \frac{37\lambda_4}{8} \right) g_R^4 - 36\lambda_4h_t^4 - 288\lambda_1\lambda_4h_t^2 - 576\lambda_2\lambda_4h_t^2 - 288\lambda_3\lambda_4h_t^2 \\
 & - 1248\lambda_4^3 - 1064\lambda_1^2\lambda_4 - 4992\lambda_2^2\lambda_4 - 1088\lambda_3^2\lambda_4 \\
 & \left. - 3456\lambda_1\lambda_2\lambda_4 - 1888\lambda_1\lambda_3\lambda_4 - 3840\lambda_2\lambda_3\lambda_4 \right], \tag{A.8}
 \end{aligned}$$

$$\begin{aligned}
 \beta(\rho_1) = & \frac{1}{16\pi^2} \left[ 3 \left( 3g_R^4 + 4g_R^2g_{BL}^2 + 2g_{BL}^4 \right) + 2 \left( 2\alpha_1^2 + 8\alpha_2^2 + 2\alpha_1\alpha_3 + \alpha_3^2 \right) \right. \\
 & \left. + 28\rho_1^2 + 16\rho_2^2 - 12\rho_1 \left( 2g_R^2 + g_{BL}^2 \right) + 16\rho_1\rho_2 \right] \\
 & + \frac{1}{(16\pi^2)^2} \left[ -\frac{2}{3} \left( 2g_{BL}^4 \left( 233g_R^2 - 170\rho_1 - 60\rho_2 \right) + 4g_{BL}^2 \left( 3(-17\rho_1 + 20\rho_2) g_R^2 \right. \right. \right. \\
 & \left. \left. + 118g_R^4 - 6 \left( 11\rho_1^2 + 4(2\rho_2)\rho_1 + 8\rho_2^2 \right) \right) + 196g_{BL}^6 \right. \\
 & + 3 \left( 20\alpha_1^2\rho_1 + 20\alpha_3\alpha_1\rho_1 + 80\alpha_2^2\rho_1 + 11\alpha_3^2\rho_1 + 8\alpha_1^3 + 12\alpha_3\alpha_1^2 \right. \\
 & \left. + 96\alpha_2^2\alpha_1 + 14\alpha_3^2\alpha_1 + 5\alpha_3^3 + 48\alpha_2^2\alpha_3 - 6 \left( 2\alpha_1^2 + 2\alpha_3\alpha_1 + 8\alpha_2^2 + \alpha_3^2 \right) g_L^2 \right. \\
 & \left. + 6 \left( 2\alpha_1^2 + 2\alpha_3\alpha_1 + 8\alpha_2^2 + \alpha_3^2 \right) h_t^2 + 192\rho_1^3 + 160\rho_2^3 + 312\rho_1\rho_2^2 + 176\rho_1^2\rho_2 \right) \\
 & - 2 \left( 30\alpha_1 + 15\alpha_3 + 154\rho_1 + 96\rho_2 \right) g_R^4 - 3 \left( 12\alpha_1^2 + 12\alpha_3\alpha_1 + 48\alpha_2^2 \right. \\
 & \left. \left. + 3\alpha_3^2 + 176\rho_1^2 + 80\rho_2^2 + 128\rho_1\rho_2 \right) g_R^2 + 33g_R^6 \right], \tag{A.9}
 \end{aligned}$$

$$\begin{aligned}
 \beta(\rho_2) = & \frac{1}{16\pi^2} \left[ 3g_R^2 (g_R^2 - 4g_{BL}^2) - \alpha_3^2 + 12\rho_2(2\rho_1 + \rho_2) - 12\rho_2 (2g_R^2 + g_{BL}^2) \right] \\
 & + \frac{1}{(16\pi^2)^2} \left[ \frac{2}{3} (2g_{BL}^4 (143g_R^2 + 50\rho_2) + 4g_{BL}^2 (9(-4\rho_1 + 7\rho_2)g_R^2 + 73g_R^4 \right. \\
 & + 18(2\rho_1 - \rho_2)\rho_2) - 3(-4\alpha_3^2\rho_1 - \alpha_3^2\rho_2 + 20\alpha_1\alpha_3\rho_2 + 20\alpha_1^2\rho_2 \\
 & + 80\alpha_2^2\rho_2 - 2\alpha_3^3 - 4\alpha_1\alpha_3^2 + 3\alpha_3^2g_L^2 - 3\alpha_3^2h_t^2 + 8\rho_2^3 + 224\rho_1\rho_2^2 + 224\rho_1^2\rho_2) \\
 & \left. + 4(9\rho_1 + 8\rho_2)g_R^4 + 144\rho_2(2\rho_1 + \rho_2)g_R^2 - 119g_R^6 \right], \tag{A.10}
 \end{aligned}$$

$$\begin{aligned}
 \beta(\alpha_1) = & \frac{1}{16\pi^2} \left[ 6g_R^4 + 4\alpha_1^2 + 16\alpha_2^2 + \alpha_3^2 + 4\alpha_1(5\lambda_1 + 2\lambda_3) + 48\alpha_2\lambda_4 + 8\alpha_3(\lambda_1 + \lambda_3) \right. \\
 & \left. + 8\alpha_1(2\rho_1 + \rho_2) + 2\alpha_3(3\rho_1 + 4\rho_2) - \frac{3}{2}\alpha_1(3g_L^2 + 11g_R^2 + 4g_{BL}^2) + 6\alpha_1h_t^2 \right] \\
 & + \frac{1}{(16\pi^2)^2} \left[ \frac{245g_R^6}{6} - 30g_R^4g_{BL}^2 - 2g_R^2g_{BL}^2(6h_t^2 - 10\alpha_1 + 19\alpha_3) \right. \\
 & - \frac{3}{16}g_L^4(\alpha_1 - 40\alpha_3) + g_{BL}^4 \left( -4h_t^2 + \frac{268\alpha_1}{3} + 30\alpha_3 \right) \\
 & + g_R^4 \left( -6h_t^2 + \frac{3647}{48}\alpha_1 + 50\alpha_3 + 100\lambda_1 + 40\lambda_3 + 80\rho_1 + 40\rho_2 \right) \\
 & - \frac{3}{8}g_L^2(60g_R^4 - (15\alpha_1 + 4\alpha_3)g_R^2 - 2(15\alpha_1h_t^2 + 4\alpha_1^2 + 16\alpha_2^2 + \alpha_3^2 \\
 & + 64\alpha_3\lambda_1 + 64\alpha_3\lambda_3 + 32\alpha_1(5\lambda_1 + 2\lambda_3) + 384\alpha_2\lambda_4)) \\
 & + g_R^2 \left( 11\alpha_1^2 + 44\alpha_2^2 + \frac{11}{4}\alpha_3^2 + \frac{45}{4}h_t^2\alpha_1 + 120\alpha_1\lambda_1 + 60\alpha_3\lambda_1 \right. \\
 & \left. + 48\alpha_1\lambda_3 + 24\alpha_3\lambda_3 + 288\alpha_2\lambda_4 + 256\alpha_1\rho_1 + 108\alpha_3\rho_1 + 128\alpha_1\rho_2 + 104\alpha_3\rho_2 \right) \\
 & + g_{BL}^2 \left( 4\alpha_1^2 + 16\alpha_2^2 + \alpha_3^2 + 48\alpha_3\rho_1 + 64\alpha_3\rho_2 \right. \\
 & \left. + \alpha_1 \left( \frac{5h_t^2}{6} + 32(4\rho_1 + 2\rho_2) \right) \right) - 64\alpha_1\alpha_3\rho_2 - 80\alpha_1\rho_1\rho_2 - 64\alpha_3\rho_1\rho_2 \\
 & - 15\alpha_1^3 - 6\alpha_3^3 - 12h_t^2\alpha_1^2 - 48h_t^2\alpha_2^2 - 172\alpha_1\alpha_2^2 - 3h_t^2\alpha_3^2 - \frac{45}{4}\alpha_1\alpha_3^2 \\
 & - 100\alpha_1\lambda_1^2 - 32\alpha_3\lambda_1^2 - 960\alpha_1\lambda_2^2 - 768\alpha_3\lambda_2^2 - 160\alpha_1\lambda_3^2 - 128\alpha_3\lambda_3^2 \\
 & - 240\alpha_1\lambda_4^2 - 144\alpha_3\lambda_4^2 - 80\alpha_1\rho_1^2 - 24\alpha_3\rho_1^2 - 120\alpha_1\rho_2^2 - 96\alpha_3\rho_2^2 \\
 & \left. \right) \tag{A.11}
 \end{aligned}$$

$$\begin{aligned}
 & -18h_t^4\alpha_1 + 40g_S^2h_t^2\alpha_1 - 7\alpha_1^2\alpha_3 - 80\alpha_2^2\alpha_3 - 120\alpha_1^2\lambda_1 - 224\alpha_2^2\lambda_1 \\
 & -30\alpha_3^2\lambda_1 - 120h_t^2\alpha_1\lambda_1 - 48h_t^2\alpha_3\lambda_1 - 64\alpha_1\alpha_3\lambda_1 - 768\alpha_2^2\lambda_2 - 48\alpha_1^2\lambda_3 \\
 & -320\alpha_2^2\lambda_3 - 12\alpha_3^2\lambda_3 - 48h_t^2\alpha_1\lambda_3 - 48h_t^2\alpha_3\lambda_3 - 64\alpha_1\alpha_3\lambda_3 - 80\alpha_1\lambda_1\lambda_3 \\
 & -64\alpha_3\lambda_1\lambda_3 - 288h_t^2\alpha_2\lambda_4 - 576\alpha_1\alpha_2\lambda_4 - 192\alpha_2\alpha_3\lambda_4 - 576\alpha_2\lambda_1\lambda_4 \\
 & -1152\alpha_2\lambda_2\lambda_4 - 576\alpha_2\lambda_3\lambda_4 - 96\alpha_1^2\rho_1 - 384\alpha_2^2\rho_1 - 24\alpha_3^2\rho_1 - 48\alpha_1\alpha_3\rho_1 \\
 & -48\alpha_1^2\rho_2 - 192\alpha_2^2\rho_2 - 12\alpha_3^2\rho_2 \Big], \tag{A.12}
 \end{aligned}$$

$$\begin{aligned}
 \beta(\alpha_2) = & \frac{1}{16\pi^2} \left[ -\frac{3}{2}\alpha_2(3g_L^2 + 11g_R^2 + 4g_{BL}^2) + 6(2\alpha_1 + \alpha_3)\lambda_4 + 4\alpha_2(\lambda_1 + 12\lambda_2 + 4\lambda_3) \right. \\
 & \left. + 8\alpha_2(2\rho_1 + \rho_2) + 4\alpha_2(2\alpha_1 + \alpha_3) + 6\alpha_2h_t^2 \right] \\
 & + \frac{1}{(16\pi^2)^2} \left[ -\frac{243}{16}\alpha_2g_L^4 + \frac{45}{8}\alpha_2g_L^2g_R^2 + g_R^4 \left( \frac{2927}{48}\alpha_2 + 60\lambda_4 \right) + \frac{268}{3}\alpha_2g_{BL}^4 \right. \\
 & + 40\alpha_2g_S^2h_t^2 + \frac{3}{8}g_L^2(2(4(\alpha_2(\alpha_3 + 8\lambda_1 + 96\lambda_2 + 32\lambda_3) \\
 & + 12\alpha_3\lambda_4 + 2\alpha_1(\alpha_2 + 12\lambda_4)) + 15\alpha_2h_t^2)) \\
 & + g_R^2 \left( 24\alpha_2\lambda_1 + 288\alpha_2\lambda_2 + 96\alpha_2\lambda_3g_R^2 + 72\alpha_1\lambda_4 + 36\alpha_3\lambda_4 + 256\alpha_2\rho_1 \right. \\
 & \left. + 128\alpha_2\rho_2 + 22\alpha_1\alpha_2 + 11\alpha_2\alpha_3 + \frac{45}{4}\alpha_2h_t^2 \right) \\
 & + \frac{1}{6}\alpha_2g_{BL}^2(24(2\alpha_1 + \alpha_3 + 32\rho_1 + 16\rho_2) + 120g_R^2 + 5h_t^2) \\
 & - 36\alpha_2\lambda_1^2 + 192\alpha_2\lambda_2^2 - 240\alpha_2\lambda_4^2 - 112\alpha_1\alpha_2\lambda_1 - 56\alpha_2\alpha_3\lambda_1 - 384\alpha_1\alpha_2\lambda_2 \\
 & - 192\alpha_2\alpha_3\lambda_2 - 384\alpha_2\lambda_1\lambda_2 - 160\alpha_1\alpha_2\lambda_3 - 80\alpha_2\alpha_3\lambda_3 - 144\alpha_2\lambda_1\lambda_3 \\
 & - 384\alpha_2\lambda_2\lambda_3 - 72\alpha_1^2\lambda_4 - 288\alpha_2^2\lambda_4 - 30\alpha_3^2\lambda_4 - 72\alpha_1\alpha_3\lambda_4 - 144\alpha_1\lambda_1\lambda_4 \\
 & - 72\alpha_3\lambda_1\lambda_4 - 288\alpha_1\lambda_2\lambda_4 - 144\alpha_3\lambda_2\lambda_4 - 144\alpha_1\lambda_3\lambda_4 \\
 & - 72\alpha_3\lambda_3\lambda_4 - 80\alpha_2\rho_1^2 - 120\alpha_2\rho_2^2 - 192\alpha_1\alpha_2\rho_1 - 96\alpha_2\alpha_3\rho_1 - 96\alpha_1\alpha_2\rho_2 \\
 & - 48\alpha_2\alpha_3\rho_2 - 80\alpha_2\rho_1\rho_2 - 60\alpha_2^3 - \frac{49}{4}\alpha_2\alpha_3^2 - 43\alpha_1^2\alpha_2 - 43\alpha_1\alpha_2\alpha_3 - 30\alpha_2h_t^4 \\
 & \left. - 12h_t^2(2\alpha_2\lambda_1 + 24\alpha_2\lambda_2 + 8\alpha_2\lambda_3 + 6\alpha_1\lambda_4 + 3\alpha_3\lambda_4 + 2\alpha_1\alpha_2 + \alpha_2\alpha_3) \right], \tag{A.13}
 \end{aligned}$$

$$\tag{A.14}$$

$$\begin{aligned}
 \beta(\alpha_3) = & \frac{1}{16\pi^2} \left[ 4\alpha_3^2 - \frac{3}{2}\alpha_3 (3g_L^2 + 11g_R^2 + 4g_{BL}^2) + 8\alpha_1\alpha_3 + 4\alpha_3(\lambda_1 - 2\lambda_3) \right. \\
 & \left. + 4\alpha_3(\rho_1 - 2\rho_2) + 6\alpha_3 h_t^2 \right] \\
 & + \frac{1}{(16\pi^2)^2} \left[ \frac{88}{3}\alpha_3 g_{BL}^4 + \frac{1}{6}g_{BL}^2 (144g_R^2 (4\alpha_3 + h_t^2) \right. \\
 & \left. + \alpha_3 (24(2\alpha_1 + \alpha_3 + 8(\rho_1 - 2\rho_2)) + 5h_t^2)) \right. \\
 & - \frac{1}{48}\alpha_3 (-18g_L^2 (16\alpha_1 + 8\alpha_3 + 7g_R^2 + 30h_t^2 + 64\lambda_1 - 128\lambda_3) \\
 & - 12g_R^2 (88\alpha_1 + 44\alpha_3 + 45h_t^2 + 160\rho_1 - 320\rho_2) \\
 & - 12(-448\alpha_1\lambda_1 - 224\alpha_3\lambda_1 + 128\alpha_1\lambda_3 + 64\alpha_3\lambda_3 - 768\alpha_2\lambda_4 \\
 & - 384\alpha_1\rho_1 - 192\alpha_3\rho_1 + 128\alpha_1\rho_2 + 64\alpha_3\rho_2 - 124\alpha_1^2 \\
 & - 48\alpha_2^2 - 29\alpha_3^2 - 124\alpha_1\alpha_3 + 160g_S^2 h_t^2 + 384\lambda_3^2 + 192\lambda_4^2 \\
 & - 48(2\alpha_1 + \alpha_3 + 2\lambda_1 - 4\lambda_3) h_t^2 - 72h_t^4 - 144\lambda_1^2 + 2304\lambda_2^2 \\
 & \left. \left. + 192\lambda_1\lambda_3 - 128\rho_1^2 + 288\rho_2^2 + 192\rho_1\rho_2) + 729g_L^4 + 1153g_R^4 \right) \right], \quad (\text{A.15})
 \end{aligned}$$

$$\begin{aligned}
 \beta(h_t) = & \frac{1}{16\pi^2} \left[ -h_t \left( 8g_S^2 + \frac{9}{4}g_L^2 + \frac{9}{4}g_R^2 + \frac{1}{6}g_{BL}^2 \right) + 5h_t^3 \right] \\
 & + \frac{1}{(16\pi^2)^2} \left[ -\frac{1}{144}h_t \left( -g_{BL}^2 (4(-8g_S^2 + 31h_t^2) + 27g_L^2 + 27g_R^2) \right. \right. \\
 & - 97g_{BL}^4 + 3(9g_L^2 (27g_R^2 - 48g_S^2 - 86h_t^2) \\
 & + 2(-9g_R^2 (24g_S^2 + 43h_t^2) - 992g_S^2 h_t^2 + 78g_R^4 + 2592g_S^4 \\
 & + 3(-12\alpha_1^2 - 48\alpha_2^2 - 9\alpha_3^2 - 12\alpha_1\alpha_3 + 64(2\lambda_1 - \lambda_3) h_t^2 \\
 & \left. \left. + 136h_t^4 - 80\lambda_1^2 - 768\lambda_2^2 - 128\lambda_3^2 - 192\lambda_4^2 - 64\lambda_1\lambda_3)) + 252g_L^4 \right) \right] \quad (\text{A.16})
 \end{aligned}$$

To see how the fermions get their masses in the LRSM, we write down the Yukawa Lagrangian:

$$\begin{aligned} \mathcal{L}_Y = & h^q \bar{Q}_L \Phi Q_R + \tilde{h}^q \bar{Q}_L \tilde{\Phi} Q_R + h^\ell \bar{\psi}_L \Phi \psi_R + \tilde{h}^\ell \bar{\psi}_L \tilde{\Phi} \psi_R \\ & + f_R \psi_R^\top C i \tau_2 \Delta_R \psi_R + \text{H.c.} \end{aligned} \quad (\text{A.17})$$

where  $\tilde{\Phi} = \sigma_2 \Phi^* \sigma_2$  ( $\sigma_2$  being the second Pauli matrix) and  $C = i \gamma_2 \gamma_0$  is the charge conjugation operator ( $\gamma_\mu$  being the Dirac matrices). After symmetry breaking, the quark and charged lepton masses are given by the generic formulas  $M_u = h^q \kappa + \tilde{h}^q \kappa'$  for up-type quarks,  $M_d = h^q \kappa' + \tilde{h}^q \kappa$  for down-type quarks, and similarly for the charged leptons, where we have neglected CP violation in the fermion matrices. To account for the SM fermion hierarchy, we set  $\kappa'/\kappa \simeq m_b/m_t \simeq 1/60$ , then the top and bottom quark masses are respectively

$$m_t \simeq h_{33}^q \kappa \simeq h_{33}^q v_{\text{EW}}, \quad m_b \simeq h_{33}^q \kappa' + \tilde{h}_{33}^q \kappa, \quad (\text{A.18})$$

with  $h_{33}^q$  and  $\tilde{h}_{33}^q$  the (3, 3) elements of the  $h^q$  and  $\tilde{h}^q$  matrices. It is expected that for the bottom quark mass  $\tilde{h}_{33}^q \ll h_{33}^q \sim \mathcal{O}(1)$ . With the first two generation quarks much lighter than the third generation in the SM, we consider only the RG running of  $h_t = h_{33}^q$  in the quark sector, as shown in Eq. (A.16).

In the lepton sector, the tauon mass  $m_\tau \simeq h_{33}^\ell \kappa' + \tilde{h}_{33}^\ell \kappa$  ( $h_{33}^\ell$  and  $\tilde{h}_{33}^\ell$  are respectively the (3, 3) elements of the  $h^\ell$  and  $\tilde{h}^\ell$  matrices), which is closely related to the Dirac mass matrix for neutrinos  $m_D = h^\ell \kappa + \tilde{h}^\ell \kappa'$ . The elements  $h_{33}^\ell$  and  $\tilde{h}_{33}^\ell$  cannot be very large for TeV-scale RHNs, or we need fine-tuning or large cancellation in fitting the charged lepton masses and the tiny neutrino masses. Thus we have neglected also the matrices  $h^\ell$  and  $\tilde{h}^\ell$  in the  $\beta$ -functions above. For the RH scale  $v_R \gtrsim 10$  TeV, as implied by the scalar perturbativity constraints in Figs. 2.7 and 2.8, if the RHNs are all the TeV-scale, say  $M_N \simeq 1$  TeV, the Yukawa coupling  $f_R \sim M_N/v_R \lesssim 0.1$ , and we do not include it either in the  $\beta$ -functions above.

## Appendix B

# Limiting cases for scalar NSI expression

### B.1 Limiting cases for scalar NSI expression

In this Appendix we evaluate the self-energy given in Eq. (4.14) corresponding to the tadpole diagram of Fig. 4.1. We shall evaluate only the fermionic contribution to Eq. (4.14), from which it is easy to read off the anti-fermionic background contribution as well. We also provide an exact expression for the medium-dependent neutrino mass, which can be evaluated numerically.

#### B.1.1 Case 1: $\mu > m_f \gg T$

Breaking the integration limits and expanding the occupation number as an infinite series, we can write Eq. (4.14) as follows:

$$\begin{aligned} \Delta m_{\nu, \alpha\beta} = & \frac{m_f y_{\alpha\beta} y_f}{2\pi^2 m_\phi^2} \left( \left[ \mu \sqrt{\mu^2 - m_f^2} + m_f^2 \ln \left( \frac{m_f}{\mu + \sqrt{\mu^2 - m_f^2}} \right) \right] \right. \\ & \left. + \sum_{n=1}^{\infty} (-1)^n \left[ \int_{m_f}^{\mu} dE e^{n(E-\mu)/T} \sqrt{E^2 - m_f^2} + \int_{\mu}^{\infty} dE e^{-n(E-\mu)/T} \sqrt{E^2 - m_f^2} \right] \right) . \end{aligned} \tag{B.1}$$

As  $T \rightarrow 0$ , the first term in the series dominates the result. We know that sum over all momentum states weighted by occupation number yields the number density. Inverting the relation to obtain  $\mu$ , we get:

$$\mu^2 = (3\pi^2 N_f)^{\frac{2}{3}} + m_f^2 \simeq (3\pi^2 N_f)^{\frac{2}{3}}, \quad (\text{B.2})$$

where in the second relation we assumed  $\mu^2 \gg m_f^2$ . Thus, for  $\mu \gg m_f$  we have

$$\Delta m_{\nu,\alpha\beta} \simeq \frac{y_{\alpha\beta} y_f m_f}{m_\phi^2} \frac{m_f}{2} \left( \frac{3N_f}{\pi} \right)^{\frac{2}{3}}, \quad (\text{B.3})$$

as given in Eq. (4.16).

### B.1.2 Case 2: $T \ll \mu < m_f$

When  $\mu < m_f$ , the expression for  $\Sigma$  of Eq. (4.14) can be written as a weighted series of modified Bessel function of the second kind:

$$\Delta m_{\nu,\alpha\beta} = \frac{m_f y_{\alpha\beta} y_f}{\pi^2 m_\phi^2} \sum_{n=1}^{\infty} (-1)^{n+1} \frac{m_f T}{n} e^{n\mu/T} K_1 \left( \frac{nm_f}{T} \right). \quad (\text{B.4})$$

For  $z \rightarrow \infty$ , we can use the asymptotic form for  $K_\nu(z)$  :

$$K_\nu(z) \simeq e^{-z} \sqrt{\frac{\pi}{2z}} \left( 1 + \frac{4\nu^2 - 1}{8z} + \dots \right). \quad (\text{B.5})$$

Due to the exponential suppression, the  $n = 1$  term in the sum will be dominant in Eq. (B.4).

This yields:

$$\Delta m_{\nu,\alpha\beta} \simeq \frac{2y_f y_{\alpha\beta}}{m_\phi^2} \left( \frac{m_f T}{2\pi} \right)^{\frac{3}{2}} e^{-(m_f - \mu)/T}. \quad (\text{B.6})$$

To relate the above function to the number density  $N_f$ , we use

$$\begin{aligned}
 N_f &= 2 \int \frac{d^3k}{(2\pi)^3} \frac{1}{e^{(E-\mu)/T} + 1} \\
 &= \frac{1}{\pi^2} \int_{m_f}^{\infty} dE \frac{E \sqrt{E^2 - m_f^2}}{e^{(E-\mu)/T} + 1} \\
 &= \frac{1}{\pi^2} \sum_{n=1}^{\infty} \int_{m_f}^{\infty} dE E \sqrt{E^2 - m_f^2} e^{-n(E-\mu)/T} (-1)^{n+1} \\
 &= \frac{1}{\pi^2} \sum_{n=1}^{\infty} (-1)^{n+1} \frac{m_f^2 T}{n} e^{n\mu/T} K_2 \left( \frac{nm_f}{T} \right). \tag{B.7}
 \end{aligned}$$

Using Eq. (B.5) in the expression above and retaining only the dominant  $n = 1$  term, we have

$$N_f \simeq 2 \left( \frac{m_f T}{2\pi} \right)^{\frac{3}{2}} e^{-(m_f - \mu)/T}. \tag{B.8}$$

Thus, the medium-induced neutrino mass in the limit  $T \ll \mu < m_f$  evaluates to:

$$\Delta m_{\nu, \alpha\beta} \simeq \frac{y_f y_{\alpha\beta}}{m_\phi^2} N_f, \tag{B.9}$$

as given in Eq. (4.15).

### B.1.3 Case 3: $\mu < m_f \ll T$

For  $z \rightarrow 0$ , the asymptotic form for  $K_\nu(z)$  is:

$$K_\nu(z) \simeq \frac{\Gamma(\nu)}{2} \left( \frac{z}{2} \right)^{-\nu}. \tag{B.10}$$

Using the above in Eq. (B.4), we can write the mass correction as:

$$\Delta m_{\nu, \alpha\beta} \simeq \frac{m_f y_{\alpha\beta} y_f}{\pi^2 m_\phi^2} \sum_{n=1}^{\infty} (-1)^{n+1} \frac{T^2}{n^2} e^{n\mu/T} \tag{B.11}$$

$$= -\frac{m_f y_{\alpha\beta} y_f T^2}{\pi^2 m_\phi^2} \text{Li}_2(-e^{\mu/T}), \tag{B.12}$$

where  $\text{Li}_\nu(z)$  is the polylogarithm. In the case  $|z| \rightarrow 0$ ,  $\text{Li}_n(-e^z) \simeq -(1 - 2^{1-n})\zeta(n)$ . Using this one obtains:

$$\Delta m_{\nu,\alpha\beta} \simeq \frac{y_f y_{\alpha\beta} m_f T^2}{12 m_\phi^2}. \quad (\text{B.13})$$

Again using Eq. (B.10) in Eq. (B.7) and retaining only the  $n = 1$  term we get:

$$N_f \simeq -\frac{2T^3}{\pi^2} \text{Li}_3(-e^{\mu/T}) = \frac{3T^3}{2\pi^2} \zeta(3). \quad (\text{B.14})$$

Thus, the scalar NSI expression for  $\mu < m_f \ll T$  evaluates to:

$$\Delta m_{\nu,\alpha\beta} \simeq \frac{y_{\alpha\beta} y_f m_f}{3 m_\phi^2} \left( \frac{\pi^2 N_f}{12 \zeta(3)} \right)^{\frac{2}{3}}, \quad (\text{B.15})$$

as given in Eq. (4.17).

## B.2 Calculation of neutrino self-energy in neutrino background

Here we evaluate the neutrino self-energy arising from a neutrino background as given in Eq. (4.31). We can rewrite the delta function in Eq. (4.31) as follows:

$$\delta \left[ \left( k + \frac{p}{2} \right)^2 - m_\phi^2 \right] = \frac{1}{|\mathbf{k}||\mathbf{p}|} \delta(\cos \theta - \cos \theta_0), \quad (\text{B.16})$$

where

$$\cos \theta_0 = \frac{k_0^2 - |\mathbf{k}|^2 + \frac{p^2}{4} - m_\phi^2 + k_0 p_0}{|\mathbf{k}||\mathbf{p}|}. \quad (\text{B.17})$$

Using kinematical arguments and  $|\cos \theta_0| \leq 1$ , we find the range for  $k_0$  and  $|\mathbf{k}|^2$ :

$$k_0 : \left\{ \frac{-p_0}{2} + m_\nu, \infty \right\}, \quad |\mathbf{k}|^2 : \left\{ |\mathbf{k}|_-^2, |\mathbf{k}|_+^2 \right\} \quad (\text{B.18})$$

where

$$|\mathbf{k}|_{\pm}^2 = \frac{1}{4} \left( |\mathbf{p}| \pm \sqrt{|\mathbf{p}|^2 + 4k_0 p_0 - 4m_\nu^2 + 4k_0^2 + p^2} \right)^2. \quad (\text{B.19})$$

Changing the integration variables to spherical coordinates and integrating over  $\cos\theta$  we obtain:

$$\Sigma_{\alpha\beta}^\nu = -\frac{y_{\alpha\gamma} y_{\gamma\beta}}{16\pi^2 |\mathbf{p}|} \int_{k_0^{\min}}^{k_0^{\max}} dk_0 \int_{|\mathbf{k}|_-^2}^{|\mathbf{k}|_+^2} d|\mathbf{k}|^2 \frac{(k + \frac{p}{2} + m_\nu)}{k_0^2 - |\mathbf{k}|^2 + \frac{p^2}{4} - \frac{m_\phi^2 + m_\nu^2}{2}} n_\nu \left( k_0 + \frac{p_0}{2} \right). \quad (\text{B.20})$$

This contribution can be decomposed as given in Eq. (4.22). By defining

$$\mathcal{I} = \int_{m_\nu}^{\infty} dk_0 n_\nu(k_0) \ln \left[ \frac{k_0 p_0 - p^2 + \frac{m_\phi^2 - m_\nu^2}{2} + |\mathbf{p}| \sqrt{k_0^2 - m_\nu^2}}{k_0 p_0 - p^2 + \frac{m_\phi^2 - m_\nu^2}{2} - |\mathbf{p}| \sqrt{k_0^2 - m_\nu^2}} \right], \quad (\text{B.21})$$

the quantities  $J_u, J_m, J_p$  in Eq. (4.24) can be written succinctly as:

$$J_m = -2m_\nu \mathcal{I}, \quad (\text{B.22})$$

$$J_p = -(p^2 + m_\nu^2 - m_\phi^2) \mathcal{I} - 2|\mathbf{p}| \int_{m_\nu}^{\infty} dk_0 n_\nu(k_0) \sqrt{k_0^2 - m_\nu^2}, \quad (\text{B.23})$$

$$J_u = -2 \int_{m_\nu}^{\infty} dk_0 k_0 n_\nu(k_0) \ln \left[ \frac{k_0 p_0 - p^2 + \frac{m_\phi^2 - m_\nu^2}{2} + |\mathbf{p}| \sqrt{k_0^2 - m_\nu^2}}{k_0 p_0 - p^2 + \frac{m_\phi^2 - m_\nu^2}{2} - |\mathbf{p}| \sqrt{k_0^2 - m_\nu^2}} \right]. \quad (\text{B.24})$$

These integrals ( $J_m, J_p, J_u$ ) cannot be evaluated analytically in general. However, they may be evaluated in the high temperature limit. For this purpose we set  $m_\nu$  to zero and assume the chemical potential  $\mu$  is small. This condition should be realized when the results are applied to early Universe. The integrals in this limit are evaluated to be:

$$J_m \simeq -2m_\nu T \ln 2 \ln \left( \frac{2\sqrt{2}|\mathbf{p}|T}{m_\phi^2} \right), \quad (\text{B.25})$$

$$J_p \simeq \frac{\pi^2 T^2 |\mathbf{p}|}{3} + |\mathbf{p}|^2 T \ln 2 \ln \left( \frac{2\sqrt{2}|\mathbf{p}|T}{m_\phi^2} \right), \quad (\text{B.26})$$

$$J_u \simeq \frac{\pi^2 T^2}{6} \left( 12\zeta'(-1) + \ln \left( \frac{16\pi|\mathbf{p}|T}{m_\phi^2} \right) \right). \quad (\text{B.27})$$

These results have been applied to derive the energy shift for neutrinos and antineutrinos in Sec. 4.2.2, see Eq. (4.33).

Similar calculation can be performed for the case of thermalized scalar field  $\phi$ . By defining :

$$\mathcal{I}^\phi = \int_{m_\phi}^{\infty} dk_0 n_\phi(k_0) \ln \left[ \frac{k_0 p_0 + p^2 + |\mathbf{p}| \sqrt{k_0^2 - m_\phi^2}}{k_0 p_0 + p^2 - |\mathbf{p}| \sqrt{k_0^2 - m_\phi^2}} \right], \quad (\text{B.28})$$

the contribution from thermal  $\phi$  to Eq. (4.24) can be labeled as  $J_m^\phi, J_p^\phi, J_u^\phi$  and given by:

$$J_m^\phi = -2m_\nu \mathcal{I}^\phi, \quad (\text{B.29})$$

$$J_p^\phi = -p^2 \mathcal{I}^\phi + 2|\mathbf{p}| \int_{m_\phi}^{\infty} dk_0 n_\phi(k_0) \sqrt{k_0^2 - m_\phi^2}, \quad (\text{B.30})$$

$$J_u^\phi = -2 \int_{m_\phi}^{\infty} dk_0 (k_0 + p_0) n_\phi(k_0) \ln \left[ \frac{k_0 p_0 + p^2 + |\mathbf{p}| \sqrt{k_0^2 - m_\phi^2}}{k_0 p_0 + p^2 - |\mathbf{p}| \sqrt{k_0^2 - m_\phi^2}} \right]. \quad (\text{B.31})$$

These terms should be added to the terms  $J_p, J_u, J_m$  of Eq. (4.24) so that they become  $J_p + J_p^\phi, J_u + J_u^\phi, J_m + J_m^\phi$ . The results of the matter-dependent neutrino mass will go through with these replacements.

## B.3 Examples for finite medium effects in relativistic cases

Here we work out Eq. (4.46) in the relativistic limit for two different density profile distributions.

### B.3.1 Constant density distribution

For a relativistic medium like electron background in supernovae, the quantity  $\langle \bar{f} f \rangle$  in Eq. (4.46) takes the form:

$$\langle \bar{f} f \rangle_{\text{SN}} = \frac{m_f}{2} \left( \frac{3N_f}{\pi} \right)^{\frac{2}{3}}. \quad (\text{B.32})$$

## Appendix B. Limiting cases for scalar NSI expression

---

Consider a constant density distribution such that

$$N_f(r) = N_f(0) \Theta(R - r), \quad (\text{B.33})$$

where  $R$  is the radius of the constant-density spherical body. Plugging the  $\langle \bar{f} f \rangle$  in Eq. (4.46) yields a general form for scalar NSI in relativistic media with  $\mu > m_f \gg T$ :

$$\begin{aligned} \Delta m_{\nu, \alpha\beta}(r) = & \frac{y_{\alpha\beta} y_f m_f}{m_\phi r} \frac{1}{2} \left( \frac{3}{\pi} \right)^{\frac{2}{3}} \left( e^{-m_\phi r} \int_0^r x N_f^{2/3} \sinh(m_\phi x) dx \right. \\ & \left. + \sinh(m_\phi r) \int_r^\infty x N_f^{2/3} e^{-m_\phi x} dx \right). \end{aligned} \quad (\text{B.34})$$

For number density profile in consideration, the above equation yields:

$$\Delta m_{\nu, \alpha\beta}(r) = \frac{y_{\alpha\beta} y_f m_f}{2m_\phi r} \left( \frac{3N_f(0)}{\pi} \right)^{\frac{2}{3}} \times \begin{cases} F_{<} & (r \leq R) \\ F_{>} & (r > R) \end{cases}, \quad (\text{B.35})$$

$$(\text{B.36})$$

where

$$F_{<} = 1 - \frac{m_\phi R + 1}{m_\phi r} e^{-m_\phi R} \sinh(m_\phi r), \quad (\text{B.37})$$

$$F_{>} = \frac{e^{-m_\phi r}}{m_\phi r} [m_\phi R \cosh(m_\phi R) - \sinh(m_\phi R)]. \quad (\text{B.38})$$

Note that the pre-factor in Eq. (B.34) matches the scalar NSI contribution calculated in Eq. (4.16) assuming point contact interaction.

For the non-relativistic case our formalism gives the same result derived in Ref. [158] and given below:

$$\Delta m_{\nu, \alpha\beta}(r) = \frac{y_{\alpha\beta} y_f N_f(0)}{m_\phi^2} \times \begin{cases} F_{<} & (r \leq R) \\ F_{>} & (r > R) \end{cases} \quad (\text{B.39})$$

$$(\text{B.40})$$

where the functions ( $F_{<}$ ,  $F_{>}$ ) are identical to the ones in Eqs. (B.37) and (B.38).

### B.3.2 Exponential density distribution

Given a relativistic medium ( $\mu > m_f \gg T$ ) with the following number density profile:

$$N_f(r) = N_f(0) e^{-\lambda r} \Theta(R - r) \quad (\text{B.41})$$

where  $R$  is the radius of the spherical body in consideration, Eq. (B.34) yields:

$$\Delta m_{\nu,\alpha\beta}(r) = \frac{y_{\alpha\beta} y_f}{2m_\phi r} \left( \frac{3N_f(0)}{\pi} \right)^{\frac{2}{3}} \times \begin{cases} G_{<} & (r \leq R) \quad , \\ G_{>} & (r > R) \quad , \end{cases} \quad (\text{B.42})$$

where

$$G_{<} = \frac{2\lambda m_\phi}{3} \left( \frac{e^{m_\phi r} \left( \frac{3m_\phi^2 r}{2\lambda} - \frac{2\lambda r}{3} - 2 \right) + 2e^{\frac{2\lambda r}{3}}}{(m_\phi^2 - \frac{4\lambda^2}{9})^2} \right) e^{-r(\frac{2\lambda}{3} + m_\phi)} - \left( \frac{\sinh(m_\phi r)(m_\phi R + \frac{2\lambda R}{3} + 1)}{(m_\phi + \frac{2\lambda}{3})^2} \right) e^{-R(\frac{2\lambda}{3} + m_\phi)} \quad , \quad (\text{B.44})$$

$$G_{>} = \sinh(m_\phi R) \left( \frac{m_\phi^2 (\frac{2\lambda R}{3} - 1) - \frac{4\lambda^2}{9} (\frac{2\lambda R}{3} + 1)}{(m_\phi^2 - \frac{4\lambda^2}{9})^2} \right) e^{-(m_\phi R + \frac{2\lambda R}{3})} + \frac{4\lambda m_\phi}{3 (m_\phi^2 - \frac{4\lambda^2}{9})^2} e^{-m_\phi R} + \cosh(m_\phi R) \left( \frac{m_\phi^3 R - \frac{4\lambda^2 R m_\phi}{9} - \frac{4\lambda m_\phi}{3}}{(m_\phi^2 - \frac{4\lambda^2}{9})^2} \right) e^{-(m_\phi R + \frac{2\lambda R}{3})} \quad . \quad (\text{B.45})$$

Similar analyses can be done for other relativistic cases such as for early Universe cosmology ( $\mu < m_f < T$ ) albeit with a different pre-factor.

For an exponential density distribution with a cut-off in the non-relativistic case we obtain:

$$\Delta m_{\nu,\alpha\beta}(r) = \frac{y_{\alpha\beta} y_f N_f(0)}{m_\phi r} \times \begin{cases} K_{<} & (r \leq R) \quad , \\ K_{>} & (r > R) \quad , \end{cases} \quad (\text{B.46})$$

where we can obtain the functions  $K_{<}$  and  $K_{>}$  by replacing  $\lambda \rightarrow \frac{3\lambda}{2}$  in  $G_{<}$  and  $G_{>}$  respectively, i.e.,  $K(\lambda)_{>(<)} = G(3\lambda/2)_{>(<)}$ . This expression is in full agreement with the result of

Ref. [158].

## B.4 Calculation of thermal mass for the scalar field

Here we carry out the evaluation of the self-energy diagram of  $\phi$  to calculate its thermal mass. As shown in Sec. 4.5,  $\phi$  can develop a medium-dependent mass, which is given by Eq. (4.66). This contribution can be written as:

$$\mathcal{M} = \mathcal{M}_1 + \mathcal{M}_2, \quad (\text{B.48})$$

where

$$\mathcal{M}_1 = 4y_f^2 \int \frac{d^4p}{(2\pi)^4} \left( k^2 - \frac{p^2}{4} + m_f^2 \right) \frac{\Gamma_f(k + p/2)}{(k - p/2)^2 - m_f^2}, \quad (\text{B.49})$$

$$\mathcal{M}_2 = 4y_f^2 \int \frac{d^4p}{(2\pi)^4} \left( k^2 - \frac{p^2}{4} + m_f^2 \right) \frac{\Gamma_f(k - p/2)}{(k + p/2)^2 - m_f^2}. \quad (\text{B.50})$$

Since  $\mathcal{M}_1 \rightarrow \mathcal{M}_2$  with the replacement  $p \rightarrow -p$ , we will focus only on simplifying the expression for  $\mathcal{M}_1$ .

$$\mathcal{M}_1 = 4y_f^2 \int_{\frac{-p_0}{2}}^{\infty} dk_0 \int \frac{d^3p}{(2\pi)^3} \left( k^2 - \frac{p^2}{4} + m_f^2 \right) \frac{\delta((k + p/2)^2 - m_f^2)}{(k - p/2)^2 - m_f^2} n_f \left( k_0 + \frac{p_0}{2} \right). \quad (\text{B.51})$$

The delta function can be written as

$$\delta \left[ \left( k + \frac{p}{2} \right)^2 - m_f^2 \right] = \frac{1}{|\mathbf{k}||\mathbf{p}|} \delta(\cos \theta - \cos \theta_0), \quad (\text{B.52})$$

where

$$\cos \theta_0 = \frac{k_0^2 - |\mathbf{k}|^2 + \frac{p^2}{4} - m_f^2 + k_0 p_0}{|\mathbf{k}||\mathbf{p}|}. \quad (\text{B.53})$$

## Appendix B. Limiting cases for scalar NSI expression

---

Using kinematical arguments and  $|\cos\theta_0| \leq 1$ , we find the range for  $k_0$  and  $|\mathbf{k}|^2$ :

$$k_0 : \left\{ \frac{-p_0}{2} + m_f, \infty \right\}, \quad |\mathbf{k}|^2 : \left\{ |\mathbf{k}|_-^2, |\mathbf{k}|_+^2 \right\}, \quad (\text{B.54})$$

where

$$|\mathbf{k}|_\pm^2 = \frac{1}{4} \left( |\mathbf{p}| \pm \sqrt{|\mathbf{p}|^2 + 4k_0 p_0 - 4m_f^2 + 4k_0^2 + p^2} \right)^2. \quad (\text{B.55})$$

Thus, changing the integration variables to spherical coordinates and integrating over  $\cos\theta$  we get:

$$\mathcal{M}_1 = -\frac{y_f^2}{4\pi^2 |\mathbf{p}|} \int_{k_0^{\min}}^{k_0^{\max}} dk_0 \int_{|\mathbf{k}|_-^2}^{|\mathbf{k}|_+^2} d|\mathbf{k}|^2 \frac{k_0^2 - |\mathbf{k}|^2 - \frac{p^2}{4} + m_f^2}{k_0^2 - |\mathbf{k}|^2 + \frac{p^2}{4} + m_f^2} n_f \left( k_0 + \frac{p_0}{2} \right). \quad (\text{B.56})$$

Integrating the above integral with respect to  $|\mathbf{k}|^2$  and adding the contribution from both  $\mathcal{M}_1$  and  $\mathcal{M}_2$  yields:

$$\begin{aligned} \mathcal{M} &= \frac{y_f^2}{\pi^2} \int_{m_f}^{\infty} dk_0 n_f(k_0) \sqrt{k_0^2 - m_f^2} \\ &\quad - \frac{y_f^2}{2\pi^2 |\mathbf{p}|} \left( m_f^2 - \frac{m_\phi^2}{4} \right) \int_{m_f}^{\infty} dk_0 n_f(k_0) \ln \left( \frac{\left( |\mathbf{p}| \sqrt{k_0^2 - m_f^2} - \frac{m_\phi^2}{2} \right)^2 - k_0^2 p_0^2}{\left( |\mathbf{p}| \sqrt{k_0^2 - m_f^2} + \frac{m_\phi^2}{2} \right)^2 - k_0^2 p_0^2} \right). \end{aligned} \quad (\text{B.57})$$

In the limit  $m_\phi \rightarrow 0$ , the mass correction for scalar reduces to Eq. (4.67).

## Appendix C

# Explicit calculation of loop diagrams

### C.1 Explicit calculation of loop diagrams

In this appendix, we compute loop diagrams presented in Fig. 5.1 in the mass basis. In the main text, we use two-component Weyl spinors for conceptual simplicity. However, technically it is more convenient to convert them to four-component Dirac/Majorana spinors so that the standard trace technology can be employed. Following the same convention as Ref. [207], we rewrite Eq. (5.6) as

$$\mathcal{L} \supset (G_Z)^{ij} Z_\mu \bar{\psi}_i \gamma_L^\mu \psi_j + (G_R)^{ij} Z'_\mu \bar{\psi}_i \gamma_L^\mu \psi_j + [(G_W)^{\alpha i} W_\mu^- \bar{\psi}_\alpha \gamma_L^\mu \psi_i + \text{h.c.}], \quad (\text{C.1})$$

where  $P_L = \frac{1}{2}(1 - \gamma_5)$ ,  $\gamma_L^\mu \equiv \gamma^\mu P_L$ , and

$$\psi_\alpha = \begin{pmatrix} \ell_{L,\alpha} \\ \ell_{R,\alpha}^\dagger \end{pmatrix}, \quad \psi_i \equiv \begin{pmatrix} \nu_i \\ \nu_i^\dagger \end{pmatrix}. \quad (\text{C.2})$$

For simplicity, we symbolically denote the relevant product of neutrino-gauge couplings by  $G_X$  (it may stand for different quantities in different diagrams), which will be replaced by specific couplings when actually used.

### C.1.1 The $Z$ diagram

The diagram is presented in the upper right panel in Fig. 5.1. We first compute the vacuum polarization part of the diagram (i.e. without the external fermion lines):

$$i\mathcal{M}_{\mu\nu} = G_X \int \frac{d^4k}{(2\pi)^4} \text{Tr} [ \gamma_\mu P_L \Delta_j(q-k) \gamma_\nu P_L \Delta_i(k) ], \quad (\text{C.3})$$

where  $q$  is the momentum of  $Z'$  and

$$\Delta_i(p) = \frac{i}{\not{p} - m_i}. \quad (\text{C.4})$$

Taking into account the Lorentz structure of the amplitude, this can be further decomposed as :

$$i\mathcal{M}_{\mu\nu} = -\frac{iG_X}{16\pi^2} [ \mathcal{F}_1(m_i, m_j, q^2) q_\mu q_\nu + \mathcal{F}_2(m_i, m_j, q^2) g_{\mu\nu} ], \quad (\text{C.5})$$

where

$$\begin{aligned} \mathcal{F}_1(m_i, m_j, q^2) &= \frac{5m_i^4 - 22m_i^2 m_j^2 + 5m_j^4}{9(m_i^2 - m_j^2)^2} + \frac{2m_j^4(3m_i^2 - m_j^2)}{3(m_i^2 - m_j^2)^3} \log\left(\frac{m_i^2}{m_j^2}\right) \\ &\quad + \frac{2}{3} \left[ \frac{1}{\epsilon} + \log\left(\frac{\mu^2}{m_i^2}\right) \right] + \mathcal{O}(q^2), \end{aligned} \quad (\text{C.6})$$

$$\begin{aligned} \mathcal{F}_2(m_i, m_j, q^2) &= \frac{m_i^2 + m_j^2}{2} - \frac{m_j^4}{(m_i^2 - m_j^2)} \log\left(\frac{m_i^2}{m_j^2}\right) \\ &\quad + (m_i^2 + m_j^2) \left[ \frac{1}{\epsilon} + \log\left(\frac{\mu^2}{m_i^2}\right) \right] + \mathcal{O}(q^2). \end{aligned} \quad (\text{C.7})$$

The full amplitude of the  $Z$  diagram can be written as

$$i\mathcal{M}_Z = -i G_X \int \frac{d^4k}{(2\pi)^4} \text{Tr} [ \gamma_\mu P_L \Delta_j(q-k) \gamma_\rho P_L \Delta_i(k) ] \Delta_Z^{\rho\nu}(q) \overline{u(p_1)} \gamma_\nu P_{L/R} u(p_2), \quad (\text{C.8})$$

where the most general form of  $\Delta_Z^{\mu\nu}(q)$  in  $R_\xi$  gauges is

$$\Delta_Z^{\mu\nu}(q) = \frac{-i}{q^2 - m_Z^2} \left[ g^{\mu\nu} - \frac{q^\mu q^\nu}{q^2 - \xi m_Z^2} (1 - \xi) \right]. \quad (\text{C.9})$$

We proceed with the unitarity gauge corresponding to  $\xi \rightarrow \infty$ , and the soft-scattering limit  $q \ll m_Z$ :

$$\Delta_Z^{\mu\nu}(k) \xrightarrow{\xi \rightarrow \infty, q \ll m_Z} \frac{i g^{\mu\nu}}{m_Z^2}. \quad (\text{C.10})$$

By applying the result of Eq. (C.3) to Eq. (C.8), we obtain

$$i\mathcal{M}_Z = -i \frac{G_X}{16\pi^2 m_Z^2} \left[ \mathcal{F}_1(m_i, m_j, q^2) q_\mu q_\nu + \mathcal{F}_2(m_i, m_j, q^2) g_{\mu\nu} \right] \overline{u(p_1)} \gamma^\nu P_{L/R} u(p_2), \quad (\text{C.11})$$

where  $\mathcal{F}_1$  and  $\mathcal{F}_2$  were already given in Eqs. (C.6) and (C.7), respectively.

### C.1.2 The $W$ diagram

The diagram is presented in the upper left panel in Fig. 5.1. The amplitude reads:

$$i\mathcal{M}_W = -i G_X \int \frac{d^4 k}{(2\pi)^4} \overline{u(p_1)} \gamma^\nu P_L \Delta_j(k - p_1) \gamma^\rho P_L \Delta_i(p_2 - k) \gamma^\mu P_L u(p_2) \Delta_{\mu\nu}^W(k), \quad (\text{C.12})$$

where

$$\Delta_i(p) = \frac{i}{\not{p} - m_i}, \quad (\text{C.13})$$

$$\Delta_{\mu\nu}^W(k) = \frac{-i}{k^2 - m_W^2} \left[ g_{\mu\nu} - \frac{k_\mu k_\nu}{k^2 - \xi m_W^2} (1 - \xi) \right]. \quad (\text{C.14})$$

Similar to the  $Z$  diagram, we take the unitarity gauge ( $\xi \rightarrow \infty$ ) and the soft-scattering limit ( $q \rightarrow 0$ ). The quantity in the loop integral is proportional to

$$\int \frac{d^4 k}{(2\pi)^4} \gamma^\nu P_L \Delta_j(k - p_1) \gamma^\rho P_L \Delta_i(p_2 - k) \gamma^\mu P_L \Delta_{\mu\nu}^W(k) \equiv C_a \gamma^\rho P_L + C_b P_L p_1^\rho + C_c P_L p_2^\rho. \quad (\text{C.15})$$

## Appendix C. Explicit calculation of loop diagrams

---

Here  $(C_a, C_b, C_c)$  are functions of scalar invariants  $p_1^2$  and  $p_2^2$ . The last two terms are suppressed when imposing the on-shell conditions. Focusing only on the  $\gamma^\rho P_L$  term, we obtain

$$i\mathcal{M}_W = i\frac{G_X}{16\pi^2}\mathcal{F}(m_i, m_j)\overline{u(p_1)}\gamma^\rho P_L u(p_2), \quad (\text{C.16})$$

where

$$\begin{aligned} \mathcal{F}(m_i, m_j) = & \frac{2m_i^2 + 2m_j^2 + 3m_W^2}{2m_W^2} + \frac{m_j^4 \log(m_j^2/m_W^2) - m_i^4 \log(m_i^2/m_W^2)}{(m_i^2 - m_j^2)m_W^2} \\ & + \frac{m_i^2 + m_j^2}{m_W^2} \left[ \frac{1}{\epsilon} + \log\left(\frac{\mu^2}{m_W^2}\right) \right]. \end{aligned} \quad (\text{C.17})$$

## Appendix D

# Group Theory of $\Delta(6n^2)$ and Representation Matrices

## D.1 Group Theory of $\Delta(6n^2)$ and Representation Matrices

As discussed in [290], the discrete groups  $\Delta(3n^2)$ ,  $n \geq 2$  integer, can be described in terms of three generators  $a$ ,  $c$  and  $d$  fulfilling the relations

$$a^3 = e, \quad c^n = e, \quad d^n = e, \quad cd = dc, \quad aca^{-1} = c^{-1}d^{-1}, \quad ada^{-1} = c \quad (\text{D.1})$$

with  $e$  being the neutral element of the group. The discrete groups  $\Delta(6n^2)$ ,  $n \geq 2$  integer, are obtained by adding a fourth generator  $b$  to the set of  $a$ ,  $c$  and  $d$ . The relations involving  $b$  are

$$b^2 = e, \quad (ab)^2 = e, \quad bcb^{-1} = d^{-1}, \quad bdb^{-1} = c^{-1}. \quad (\text{D.2})$$

In the trivial representation  $\mathbf{1}$  all elements of the group are represented by the character 1. The explicit representation matrices  $g(\mathbf{3})$  for  $a$ ,  $b$ ,  $c$  and  $d$  can be chosen in the irreducible,

faithful, complex three-dimensional representation  $\mathbf{3}$  as

$$\begin{aligned}
 a(\mathbf{3}) &= \begin{pmatrix} 1 & 0 & 0 \\ 0 & \omega & 0 \\ 0 & 0 & \omega^2 \end{pmatrix}, \quad b(\mathbf{3}) = \begin{pmatrix} 1 & 0 & 0 \\ 0 & 0 & \omega^2 \\ 0 & \omega & 0 \end{pmatrix}, \\
 c(\mathbf{3}) &= \frac{1}{3} \begin{pmatrix} 1 + 2 \cos \phi_n & 1 - \cos \phi_n - \sqrt{3} \sin \phi_n & 1 - \cos \phi_n + \sqrt{3} \sin \phi_n \\ 1 - \cos \phi_n + \sqrt{3} \sin \phi_n & 1 + 2 \cos \phi_n & 1 - \cos \phi_n - \sqrt{3} \sin \phi_n \\ 1 - \cos \phi_n - \sqrt{3} \sin \phi_n & 1 - \cos \phi_n + \sqrt{3} \sin \phi_n & 1 + 2 \cos \phi_n \end{pmatrix}
 \end{aligned} \tag{D.3}$$

with  $\omega = e^{2\pi i/3}$  and  $\phi_n = \frac{2\pi}{n}$  and  $d$  can be computed via  $d(\mathbf{3}) = a(\mathbf{3})^2 c(\mathbf{3}) a(\mathbf{3})$ .

The existence of an irreducible, in general unfaithful, real three-dimensional representation  $\mathbf{3}'$  requires that all its characters are real. This cannot be fulfilled in all groups  $\Delta(6n^2)$ , but only, if the index  $n$  is even. In this case the form of the representation matrices  $g(\mathbf{3}')$  is

$$a(\mathbf{3}') = a(\mathbf{3}), \quad b(\mathbf{3}') = b(\mathbf{3}), \quad c(\mathbf{3}') = \frac{1}{3} \begin{pmatrix} -1 & 2 & 2 \\ 2 & -1 & 2 \\ 2 & 2 & -1 \end{pmatrix} \tag{D.4}$$

and  $d(\mathbf{3}') = a(\mathbf{3}')^2 c(\mathbf{3}') a(\mathbf{3}')$ . Note that the representation matrices  $g(\mathbf{3}')$  do not depend on the index  $n$  of the group and thus lead to the same representation for all groups  $\Delta(6n^2)$  with even  $n$ . Indeed, we can observe that the group generated by the representation matrices  $g(\mathbf{3}')$  has 24 elements and thus corresponds to the group  $\Delta(6 \cdot 2^2) = \Delta(24)$ . This group is isomorphic to the permutation group  $S_4$ . This representation together with the one generated by the representation matrices  $a(\mathbf{3}')$ ,  $c(\mathbf{3}')$ ,  $d(\mathbf{3}')$  and  $-b(\mathbf{3}')$  (i.e. the representation matrix  $b(\mathbf{3}')$  acquires an overall sign, see [261]) are the only real three-dimensional representations in a generic group  $\Delta(6n^2)$  with even  $n$  and  $3 \nmid n$ . To see this we inspect the characters of the three-dimensional representations. Following [261] we see that the characters  $\chi(\mathbf{3}_{\text{gen}})$  of a generic irreducible three-dimensional representation  $\mathbf{3}_{\text{gen}}$  for a certain type of classes is given

by  $\eta^{-\rho l}$  with  $\eta = e^{2\pi i/n}$ ,  $\rho = 0, \dots, n-1$  (labelling this type of class of the group  $\Delta(6n^2)$ ) and  $l = 1, \dots, n-1$  ( $l$  labels the different pairs of three-dimensional representations). We have to require that all  $\eta^{-\rho l}$  for a certain representation labeled by  $l$  are real. This is ensured, if  $\eta^{-l}$  is real for all powers  $\rho$  with  $\rho = 0, \dots, n-1$ , meaning  $\eta^{-l}$  should be real itself. Hence,  $2l/n$  must be an integer. With the constraint on  $l$ ,  $1 \leq l \leq n-1$ , we know that there is a single solution to  $2l/n$  being an integer, namely  $l = n/2$ , i. e. there is a single pair of irreducible three-dimensional representations that are real. In this case their characters are real for all classes, as can be explicitly checked with the help of the character table, shown in [261].

## D.2 Form of the Representation Matrices for Residual Symmetries

In the following, we list the form of the representation matrices in the representations **3** and **3'** for the different residual symmetries, used in the discussion of Case 1, Case 2 and Case 3a and Case 3b.1.

In all these cases, the residual flavor symmetry in the charged lepton sector is generated by  $a$  which corresponds to the representation matrices

$$a(\mathbf{3}) = \begin{pmatrix} 1 & 0 & 0 \\ 0 & \omega & 0 \\ 0 & 0 & \omega^2 \end{pmatrix}. \quad (\text{D.5})$$

The residual flavor symmetry in the neutrino sector is generated by  $Z$ .

In Case 1 and Case 2,  $Z$  is chosen as  $e^{n/2}$  which is in the representation **3** of the form

$$Z(\mathbf{3}) = \frac{1}{3} \begin{pmatrix} -1 & 2 & 2 \\ 2 & -1 & 2 \\ 2 & 2 & -1 \end{pmatrix} \quad (\text{D.6})$$

independent of the index  $n$ , while the form of  $Z = c^{n/2}$  in  $\mathbf{3}'$  reads either

$$Z(\mathbf{3}') = \begin{pmatrix} 1 & 0 & 0 \\ 0 & 1 & 0 \\ 0 & 0 & 1 \end{pmatrix} \quad \text{for } n/2 \text{ even} \quad (\text{D.7})$$

or

$$Z(\mathbf{3}') = \frac{1}{3} \begin{pmatrix} -1 & 2 & 2 \\ 2 & -1 & 2 \\ 2 & 2 & -1 \end{pmatrix} = Z(\mathbf{3}) \quad \text{for } n/2 \text{ odd.} \quad (\text{D.8})$$

In Case 3a and Case 3b.1,  $Z$  is chosen as  $b c^m d^m$  with  $m = 0, \dots, n-1$ . In the representation  $\mathbf{3}$  it is of the form [9]

$$Z(m)(\mathbf{3}) = \frac{1}{3} \begin{pmatrix} 1 + 2 \cos \gamma_m & \omega^2 (1 - \cos \gamma_m + \sqrt{3} \sin \gamma_m) & \omega (1 - \cos \gamma_m - \sqrt{3} \sin \gamma_m) \\ \omega (1 - \cos \gamma_m + \sqrt{3} \sin \gamma_m) & 1 - \cos \gamma_m - \sqrt{3} \sin \gamma_m & \omega^2 (1 + 2 \cos \gamma_m) \\ \omega^2 (1 - \cos \gamma_m - \sqrt{3} \sin \gamma_m) & \omega (1 + 2 \cos \gamma_m) & 1 - \cos \gamma_m + \sqrt{3} \sin \gamma_m \end{pmatrix} \quad (\text{D.9})$$

with  $\gamma_m = 2\pi m/n$ . For the special values,  $m = 0$ ,  $m = n$  and  $m = n/2$ , the form of  $Z(m)(\mathbf{3})$  simplifies and we find

$$Z(m=0)(\mathbf{3}) = Z(m=n)(\mathbf{3}) = \begin{pmatrix} 1 & 0 & 0 \\ 0 & 0 & \omega^2 \\ 0 & \omega & 0 \end{pmatrix}, \quad (\text{D.10})$$

and

$$Z(m=n/2)(\mathbf{3}) = \frac{1}{3} \begin{pmatrix} -1 & 2\omega^2 & 2\omega \\ 2\omega & 2 & -\omega^2 \\ 2\omega^2 & -\omega & 2 \end{pmatrix}. \quad (\text{D.11})$$

Similarly, we can analyze the form of the representation matrix  $Z(m)(\mathbf{3}')$ . The decisive criterion for this form is whether  $m$  is even or odd and otherwise there is no further dependence

on the parameter  $m$  for  $Z(m)(\mathbf{3}')$ . So, for  $m$  being even we get

$$Z(m \text{ even})(\mathbf{3}') = \begin{pmatrix} 1 & 0 & 0 \\ 0 & 0 & \omega^2 \\ 0 & \omega & 0 \end{pmatrix}, \quad (\text{D.12})$$

while for  $m$  odd we have

$$Z(m \text{ odd})(\mathbf{3}') = \frac{1}{3} \begin{pmatrix} -1 & 2\omega^2 & 2\omega \\ 2\omega & 2 & -\omega^2 \\ 2\omega^2 & -\omega & 2 \end{pmatrix}. \quad (\text{D.13})$$

We note that  $Z(m \text{ even})(\mathbf{3}')$  coincides with  $Z(m = 0)(\mathbf{3}) = Z(m = n)(\mathbf{3})$  as well as  $Z(m \text{ odd})(\mathbf{3}')$  coincides with  $Z(m = n/2)(\mathbf{3})$ .

### D.3 CP symmetries and form of CP transformations

The CP symmetries correspond to automorphisms of the flavor group  $\Delta(6n^2)$ , see discussion in [9]. In the present analysis we employ the ones, as used in [264]. These can be obtained as follows: consider the automorphism

$$a \rightarrow a, \quad c \rightarrow c^{-1}, \quad d \rightarrow d^{-1} \quad \text{and} \quad b \rightarrow b \quad (\text{D.14})$$

The automorphism in Eq. (D.14) can be represented by  $X_0(\mathbf{1}) = 1$  in the trivial representation  $\mathbf{1}$  and by the matrix

$$X_0(\mathbf{3}) = X_0(\mathbf{3}') = \begin{pmatrix} 1 & 0 & 0 \\ 0 & 0 & 1 \\ 0 & 1 & 0 \end{pmatrix} \quad (\text{D.15})$$

in both three-dimensional representations  $\mathbf{3}$  and  $\mathbf{3}'$ . In Case 1, the CP transformation  $X(s)(\mathbf{3})$  has the explicit form  $a(\mathbf{3})b(\mathbf{3})c(\mathbf{3})d(\mathbf{3})^{2s} X_0$ . The form of the CP transformation  $X(s)(\mathbf{3}')$  in the representation  $\mathbf{3}'$  depends on whether  $s$  is even or odd, i. e.

$$X(s)(\mathbf{3}') = \begin{pmatrix} 1 & 0 & 0 \\ 0 & 1 & 0 \\ 0 & 0 & 1 \end{pmatrix} \text{ for } s \text{ even,} \quad (\text{D.16})$$

and

$$X(s)(\mathbf{3}') = \frac{1}{3} \begin{pmatrix} -1 & 2 & 2 \\ 2 & -1 & 2 \\ 2 & 2 & -1 \end{pmatrix} \text{ for } s \text{ odd.} \quad (\text{D.17})$$

In Case 2, the form of the CP transformation  $X(\mathbf{3})(s, t)$  in the representation  $\mathbf{3}$  can be chosen as  $c(\mathbf{3})^s d(\mathbf{3})^t X_0$ . and is more conveniently written in terms of the variables  $u = 2s - t$  and  $v = 3t$  with  $\phi_u = \frac{\pi u}{n}$  and  $\phi_v = \frac{\pi v}{n}$ . For the form of the CP transformation  $X(s, t)(\mathbf{3}')$  depends like the latter on whether  $s$  and  $t$  are even or odd. The explicit form of  $X(s, t)(\mathbf{3}')$ , however, does neither contain  $s$  nor  $t$  are parameters. For  $s$  and  $t$  even we have

$$X(s \text{ even}, t \text{ even})(\mathbf{3}') = \begin{pmatrix} 1 & 0 & 0 \\ 0 & 0 & 1 \\ 0 & 1 & 0 \end{pmatrix}, \quad (\text{D.18})$$

for  $s$  even and  $t$  odd we find

$$X(s \text{ even}, t \text{ odd})(\mathbf{3}') = \frac{1}{3} \begin{pmatrix} -1 & 2\omega^2 & 2\omega \\ 2\omega^2 & 2\omega & -1 \\ 2\omega & -1 & 2\omega^2 \end{pmatrix}, \quad (\text{D.19})$$

for  $s$  odd and  $t$  even we have

$$X(s \text{ odd}, t \text{ even})(\mathbf{3}') = \frac{1}{3} \begin{pmatrix} -1 & 2 & 2 \\ 2 & 2 & -1 \\ 2 & -1 & 2 \end{pmatrix}, \quad (\text{D.20})$$

and for  $s$  and  $t$  odd we find

$$X(s \text{ odd}, t \text{ odd})(\mathbf{3}')(\mathbf{3}') = \frac{1}{3} \begin{pmatrix} -1 & 2\omega & 2\omega^2 \\ 2\omega & 2\omega^2 & -1 \\ 2\omega^2 & -1 & 2\omega \end{pmatrix}. \quad (\text{D.21})$$

For Case 3a and Case 3b.1, the form of the CP transformation  $X(s, m)(\mathbf{3})$  is given as [9]

$$X(s)(\mathbf{3}) = \frac{1}{3} e^{-i\delta_s} \begin{pmatrix} 3 \cos 3\delta_s + i \sin 3\delta_s & -2i\omega \sin 3\delta_s & -2i\omega^2 \sin 3\delta_s \\ -2i\omega \sin 3\delta_s & \omega^2 (3 \cos 3\delta_s + i \sin 3\delta_s) & -2i \sin 3\delta_s \\ -2i\omega^2 \sin 3\delta_s & -2i \sin 3\delta_s & \omega (3 \cos 3\delta_s + i \sin 3\delta_s) \end{pmatrix} \quad (\text{D.22})$$

with  $\delta_s = \pi s/n$  and  $\omega = e^{\frac{2\pi i}{3}}$ . The form of the CP transformation  $X(s)(\mathbf{3}')$  only depends on whether  $s$  is even or odd. In particular, we can use for  $s$  even

$$X(s \text{ even})(\mathbf{3}') = \begin{pmatrix} 1 & 0 & 0 \\ 0 & \omega^2 & 0 \\ 0 & 0 & \omega \end{pmatrix}, \quad (\text{D.23})$$

and for  $s$  odd

$$X(s \text{ odd})(\mathbf{3}') = \frac{1}{3} \begin{pmatrix} -1 & 2\omega & 2\omega^2 \\ 2\omega & -\omega^2 & 2 \\ 2\omega^2 & 2 & -\omega \end{pmatrix}, \quad (\text{D.24})$$

# Bibliography

- [1] The Atlas Collaboration [ATLAS Collaboration], *Search for new high-mass resonances in the dilepton final state using proton-proton collisions at  $\sqrt{s} = 13$  tev with the atlas detector*, ATLAS-CONF- 2016–045.
- [2] CMS Collaboration [CMS Collaboration], *Search for a high-mass resonance decaying into a dilepton final state in  $13 \text{ fb}^{-1}$  of pp collisions at  $\sqrt{s} = 13\text{TeV}$* , CMS-PAS-EXO-16–031.
- [3] R. Diener, S. Godfrey and T. A. W. Martin, *Unravelling an extra neutral gauge boson at the lhc using third generation fermions*, *Phys. Rev. D* **83** (2011) 115008, [1006.2845].
- [4] S. Godfrey and T. Martin, *Z' Discovery Reach at Future Hadron Colliders: A Snowmass White Paper*. [hep-ph].
- [5] T. G. Rizzo, *Exploring new gauge bosons at a 100 tev collider*, *Phys. Rev. D* **89** (2014) 095022, [1403.5465].
- [6] M. A. et al. [ATLAS Collaboration], *Search for heavy majorana or dirac neutrinos and right-handed w gauge bosons in final states with two charged leptons and two jets at  $\sqrt{s} = 13$  tev with the atlas detector*, 1809.11105.
- [7] A. Ferrari, J. Collot, M. L. Andrieux, B. Belhorma, P. de Saintignon, J. Y. Hostachy et al., *Sensitivity study for new gauge bosons and right-handed majorana neutrinos in pp collisions at  $s = 14\text{-tev}$* , *Phys. Rev. D* **62** (2000) 013001.

- [8] M. Mitra, R. Ruiz, D. J. Scott and M. Spannowsky, *Neutrino jets from high-mass  $w_r$  gauge bosons in tev-scale left-right symmetric models*, *Phys. Rev. D* **94** (2016) 095016, [1607.03504].
- [9] C. Hagedorn, A. Meroni and E. Molinaro, *Lepton mixing from  $\Delta(3n^2)$  and  $\Delta(6n^2)$  and CP*, *Nucl. Phys. B* **891** (2015) 499–557, [1408.7118].
- [10] G. Chauhan, P. S. B. Dev, R. N. Mohapatra and Y. Zhang, *Perturbativity constraints on  $U(1)_{B-L}$  and left-right models and implications for heavy gauge boson searches*, *JHEP* **01** (2019) 208, [1811.08789].
- [11] G. Chauhan, *Vacuum Stability and Symmetry Breaking in Left-Right Symmetric Model*, *JHEP* **12** (2019) 137, [1907.07153].
- [12] K. S. Babu, G. Chauhan and P. S. Bhupal Dev, *Neutrino nonstandard interactions via light scalars in the Earth, Sun, supernovae, and the early Universe*, *Phys. Rev. D* **101** (2020) 095029, [1912.13488].
- [13] G. Chauhan and X.-J. Xu, *How dark is the  $\nu_R$ -philic dark photon?*, *JHEP* **04** (2021) 003, [2012.09980].
- [14] S. Weinberg, *A Model of Leptons*, *Phys. Rev. Lett.* **19** (1967) 1264–1266.
- [15] I. Esteban, M. C. Gonzalez-Garcia, M. Maltoni, T. Schwetz and A. Zhou, *The fate of hints: updated global analysis of three-flavor neutrino oscillations*, *JHEP* **09** (2020) 178, [2007.14792].
- [16] PLANCK collaboration, N. Aghanim et al., *Planck 2018 results. VI. Cosmological parameters*, 1807.06209.
- [17] G. Isidori, G. Ridolfi and A. Strumia, *On the metastability of the standard model vacuum*, *Nucl. Phys.* **B609** (2001) 387–409, [hep-ph/0104016].

- [18] H. Georgi, *The state of the art in gauge theories*, in *AIP Conf. Proc.* **23**, p. 575, 1975.
- [19] H. Fritzsch and P. Minkowski, *Unified interactions of leptons and hadrons*, *Annals Phys* **93** (1975) 193.
- [20] M. S. Chanowitz, J. R. Ellis and M. K. Gaillard, *The price of natural flavor conservation in neutral weak interactions*, *Nucl. Phys. B* **128** (1977) 506.
- [21] H. Georgi and D. V. Nanopoulos, *Ordinary predictions from grand principles:  $T$  quark mass in  $o(10)$* , *Nucl. Phys B* **155** (1979) 52.
- [22] K. S. Babu and R. N. Mohapatra, *Predictive neutrino spectrum in minimal  $so(10)$  grand unification*, *Phys. Rev. Lett.* **70** (1993) 2845, [9209215].
- [23] R. E. Marshak and R. N. Mohapatra, *Quark - lepton symmetry and  $b-l$  as the  $u(1)$  generator of the electroweak symmetry group*, *Phys. Lett.* **91B** (1980) 222.
- [24] R. N. Mohapatra and R. E. Marshak, *Local  $b-l$  symmetry of electroweak interactions, majorana neutrinos and neutron oscillations*, *Phys. Rev. Lett.* **44** (1980) 1316.
- [25] N. G. Deshpande and D. Iskandar, *Study of the gauge group  $su(2)_l \times t(3)_r \times u(1)_v$* , *Nucl. Phys. B* **167** (November, 1980) 223.
- [26] P. Galison and A. Manohar, *Two  $z$ 's or not two  $z$ 's?*, *Phys. Lett.* **136B** (1984) 279.
- [27] J. C. Pati and A. Salam, *Lepton number as the fourth color*, *Phys. Rev. D* **10** (1975) 275.
- [28] R. N. Mohapatra and J. C. Pati, *A natural left-right symmetry*, *Phys. Rev. D* **11** (1975) 2558.
- [29] G. Senjanovic and R. N. Mohapatra, *Exact left-right symmetry and spontaneous violation of parity*, *Phys. Rev. D* **12** (1975) 1502.

- [30] P. Minkowski,  $\mu \rightarrow e\gamma$  at a Rate of One Out of  $10^9$  Muon Decays?, *Phys. Lett.* **67B** (1977) 421–428.
- [31] R. N. Mohapatra and G. Senjanovic, *Neutrino masses and mixings in gauge models with spontaneous parity violation*, *Phys. Rev. D* **23** (1981) 165.
- [32] T. Yanagida, *Horizontal gauge symmetry and masses of neutrinos*, *Conf. Proc.* **C7902131** (1979) 95–99.
- [33] M. Gell-Mann, P. Ramond and R. Slansky, *Complex Spinors and Unified Theories*, *Conf. Proc.* **C790927** (1979) 315–321, [1306.4669].
- [34] S. L. Glashow, *The Future of Elementary Particle Physics*, *NATO Sci. Ser. B* **61** (1980) 687.
- [35] L. B. Okun, *Limits of electrodynamics: Paraphotons?*, *Sov. Phys. JETP* **56** (1982) 502.
- [36] B. Holdom, *Two  $u(1)$ 's and epsilon charge shifts*, *Phys. Lett.* **166B** (1986) 196.
- [37] R. Foot and X. G. He, *Comment on  $z$   $z'$ -prime mixing in extended gauge theories*, *Phys. Lett. B* **267** (1991) 509.
- [38] W. Buchmuller, C. Greub and P. Minkowski, *Neutrino masses, neutral vector bosons and the scale of  $b$ - $l$  breaking*, *Phys. Lett. B* **267** (1991) 35.
- [39] L. Basso, *Phenomenology of the minimal  $B$ - $L$  extension of the Standard Model at the LHC*. 2011.
- [40] T. Appelquist, B. A. Dobrescu and A. R. Hopper, *Nonexotic neutral gauge bosons*, *Phys. Rev* **68.035012** (2003) , [0212073].
- [41] M. Carena, A. Daleo, B. A. Dobrescu and T. M. P. Tait,  *$z'$  gauge bosons at the tevatron*, *Phys. Rev. D* **70.093009** (2004) , [0408098].

- [42] A. Das, S. Oda, N. Okada and D. S. Takahashi, *Classically conformal  $u(1)_j$  extended standard model, electroweak vacuum stability, and lhc run-2 bounds*, *Phys. Rev. D* **93** (2016) , [1605.01157].
- [43] S. Oda, N. Okada and D. S. Takahashi, *Right-handed neutrino dark matter in the classically conformal  $u(1)$  extended standard model*, *Phys. Rev. D* **96** (2017) 095032, [1704.05023].
- [44] J. Alexander, *Dark sectors workshop: Community report*, 1608.08632.
- [45] P. Langacker, *The physics of heavy  $z'$  gauge bosons*, *Rev. Mod. Phys.* **81** (2009) 1199, [0801.1345].
- [46] A. M. S. et al [CMS Collaboration], *Search for a heavy right-handed  $w$  boson and a heavy neutrino in events with two same-flavor leptons and two jets at  $\sqrt{s} = 13$  tev*, *JHEP* **1805** (2018) 148, [1803.11116].
- [47] P. S. B. Dev, D. Kim and R. N. Mohapatra, *Disambiguating seesaw models using invariant mass variables at hadron colliders*, *JHEP* **1601** (2016) 118, [1510.04328].
- [48] R. Ruiz, *Lepton number violation at colliders from kinematically inaccessible gauge bosons*, *Eur. Phys. J. C* **77** (November, 2017) 375, [1703.04669].
- [49] N. Arkani-Hamed, T. Han, M. Mangano and L. T. Wang, *Physics opportunities of a 100 tev proton-proton collider*, *Phys. Rept.* **652** (2016) 1, [1511.06495].
- [50] T. G. et al., *Physics at a 100 tev pp collider: beyond the standard model phenomena*, *CERN Yellow Report* **3** (2017) 441, [1606.00947].
- [51] M. T. et al. [Particle Data Group], *Review of particle physics*, *Phys. Rev. D* **98** (2018) 030001.
- [52] G. Ecker, W. Grimus and H. Neufeld, *Higgs induced flavor changing neutral interactions in  $su(2)_l \times su(2)_r \times u(1)$* , *Phys. Lett.* **127B** (1983) 365.

- [53] Y. Zhang, H. An, X. Ji and R. N. Mohapatra, *General cp violation in minimal left-right symmetric model and constraints on the right-handed scale*, *Nucl. Phys. B* **802** (2008) 247, [0712.4218].
- [54] A. Maiezza, M. Nemevsek, F. Nesti and G. Senjanovic, *Left-right symmetry at lhc*, *Phys. Rev. D* **82** (2010) 055022, [1005.5160].
- [55] S. Bertolini, A. Maiezza and F. Nesti, *Present and future k and b meson mixing constraints on tev scale left-right symmetry*, *Phys. Rev. D* **89** (2014) 095028, [1403.7112].
- [56] M. Singer, J. W. F. Valle and J. Schechter, *Canonical neutral current predictions from the weak electromagnetic gauge group  $su(3) \times u(1)$* , *Phys. Rev. D* **22** (1980) 738.
- [57] P. H. Frampton, *Chiral dilepton model and the flavor question*, *Phys. Rev. Lett.* **69** (1992) 2889.
- [58] F. Pisano and V. Pleitez, *An  $su(3) \times u(1)$  model for electroweak interactions*, *Phys. Rev. D* **46** (1992) 410, [9206242].
- [59] R. Foot, O. F. Hernandez, F. Pisano and V. Pleitez, *Lepton masses in an  $su(3)_l \times u(1)_n$  gauge model*, *Phys. Rev. D* **47** (1993) 4158, [9207264].
- [60] A. G. Dias, C. A. de S. Pires and P. S. R. da Silva, *The left-right  $su(3)_l \times su(3)_r \times u(1)_x$  model with light, kev and heavy neutrinos*, *Phys. Rev. D* **82** (2010) 035013, [1003.3260].
- [61] M. Reig, J. W. F. Valle and C. A. Vaquera-Araujo, *Unifying left-right symmetry and 331 electroweak theories*, *Phys. Lett. B* **766** (2017) 35, [1611.02066].
- [62] M. Reig, J. W. F. Valle and C. A. Vaquera-Araujo, *Three-family left-right symmetry with low-scale seesaw mechanism*, *JHEP* **1705** (2017) 100, [1611.04571].

- [63] D. Borah and S. Patra, *Universal seesaw and  $0\nu\beta\beta$  in new 3331 left-right symmetric model*, *Phys. Lett. B* **771** (2017) 318, [1701.08675].
- [64] C. Hati, S. Patra, M. Reig, J. W. F. Valle and C. A. Vaquera-Araujo, *Towards gauge coupling unification in left-right symmetric  $SU(3)_c \times SU(3)_L \times SU(3)_R \times U(1)_X$  theories*, *Phys. Rev. D* **96** (2017) 015004, [1703.09647].
- [65] Z. G. Berezhiani, *The weak mixing angles in gauge models with horizontal symmetry: A new approach to quark and lepton masses*, *Phys. Lett.* **129B** (1983) 99.
- [66] D. Chang and R. N. Mohapatra, *Small and calculable dirac neutrino mass*, *Phys. Rev. Lett.* **58** (1987) 1600.
- [67] S. Rajpoot, *See-saw masses for quarks and leptons in an ambidextrous electroweak interaction model*, *Mod. Phys. Lett. A* **2** (1987) 307.
- [68] A. Davidson and K. C. Wali, *Universal seesaw mechanism?*, *Phys. Rev. Lett.* **59** (1987) 393.
- [69] K. S. Babu and R. N. Mohapatra, *CP violation in seesaw models of quark masses*, *Phys. Rev. Lett.* **62** (1989) .
- [70] K. S. Babu and R. N. Mohapatra, *A solution to the strong CP problem without an axion*, *Phys. Rev. D* **41** (1990) 1286.
- [71] R. N. Mohapatra and Y. Zhang, *Tev scale universal seesaw, vacuum stability and heavy higgs*, *JHEP* **1406** (2014) 072, [1401.6701].
- [72] P. S. B. Dev, R. N. Mohapatra and Y. Zhang, *Quark seesaw, vectorlike fermions and diphoton excess*, *JHEP* **1602** (2016) 186, [1512.08507].
- [73] F. F. Deppisch, C. Hati, S. Patra, P. Pritimita and U. Sarkar, *Neutrinoless double beta decay in left-right symmetric models with a universal seesaw mechanism*, *Phys. Rev. D* **97** (2018) 035005, [1701.02107].

- [74] A. Patra and S. K. Rai, *Lepton-specific universal seesaw model with left-right symmetry*, *Phys. Rev. D* **98** (2018) 015033, [1711.00627].
- [75] P. S. B. Dev, R. N. Mohapatra and Y. Zhang, *Naturally stable right-handed neutrino dark matter*, *JHEP* **1611** (2016) 077, [1608.06266].
- [76] P. S. B. Dev, R. N. Mohapatra and Y. Zhang, *Heavy right-handed neutrino dark matter in left-right models*, *Mod. Phys. Lett. A* **32** (2017) 1740007, [1610.05738].
- [77] J. L. Hewett and T. G. Rizzo, *Low-energy phenomenology of superstring inspired  $e(6)$  models*, *Phys. Rept.* **183** (1989) 193.
- [78] H. Georgi and S. Weinberg, *Neutral currents in expanded gauge theories*, *Phys. Rev. D* **17** (1978) 275.
- [79] P. S. B. Dev, R. N. Mohapatra and Y. Zhang, *Probing the higgs sector of the minimal left-right symmetric model at future hadron colliders*, *JHEP* **1605** (2016) 174, [1602.05947].
- [80] J. Brehmer, J. Hewett, J. Kopp, T. Rizzo and J. Tattersall, *Symmetry restored in dibosons at the lhc?*, *JHEP* **1510** (2015) 182, [1507.00013].
- [81] P. S. B. Dev, R. N. Mohapatra and Y. Zhang, *Long lived light scalars as probe of low scale seesaw models*, *Nucl. Phys. B* **923** (2017) 179, [1703.02471].
- [82] P. S. B. Dev, R. N. Mohapatra and Y. Zhang, *Leptogenesis constraints on  $b-l$  breaking higgs boson in tev scale seesaw models*, *JHEP* **1803** (2018) 122, [1711.07634].
- [83] S. Patra, F. S. Queiroz and W. Rodejohann, *Stringent dilepton bounds on left-right models using lhc data*, *Phys. Lett. B* **752** (2016) 186, [1506.03456].

- [84] M. Lindner, F. S. Queiroz and W. Rodejohann, *Dilepton bounds on left-right symmetry at the lhc run ii and neutrinoless double beta decay*, *Phys. Lett. B* **762** (2016) 190, [1604.07419].
- [85] M. Magg and C. Wetterich, *Neutrino mass problem and gauge hierarchy*, *Phys. Lett.* **94B** (1980) 61.
- [86] J. Schechter and J. W. F. Valle, *Neutrino masses in  $su(2) \times u(1)$  theories*, *Phys. Rev. D* **2227** (1980) .
- [87] G. Lazarides, Q. Shafi and C. Wetterich, *Proton lifetime and fermion masses in an  $so(10)$  model*, *Nucl. Phys. B* **181** (1981) 287.
- [88] W. Konetschny and W. Kummer, *Nonconservation of total lepton number with scalar bosons*, *Phys. Lett.* **70B** (1977) 433.
- [89] T. P. Cheng and L. F. Li, *Neutrino masses, mixings and oscillations in  $su(2) \times u(1)$  models of electroweak interactions*, *Phys. Rev. D* **22** (1980) 2860.
- [90] F. F. Deppisch, T. E. Gonzalo, S. Patra, N. Sahu and U. Sarkar, *Double beta decay, lepton flavor violation, and collider signatures of left-right symmetric models with spontaneous d-parity breaking*, *Phys. Rev. D* **91** (2015) 015018, [1410.6427].
- [91] P. S. B. Dev and R. N. Mohapatra, *Unified explanation of the  $eejj$ , diboson and dijet resonances at the lhc*, *Phys. Rev. Lett.* **115** (2015) 181803, [1508.02277].
- [92] D. Chang, R. N. Mohapatra and M. K. Parida, *Decoupling parity and  $su(2)$ -r breaking scales: A new approach to left-right symmetric models*, *Phys. Rev. Lett.* **52** (1984) 1072.
- [93] F. Lyonnet, I. Schienbein, F. Staub and A. Wingerter, *Pyr@te: Renormalization group equations for general gauge theories*, *Comput. Phys. Commun.* **185** (2014) 1130, [1309.7030].

- [94] F. Lyonnet, *Automation of non-susy two-loop rges with pyr@te: latest developments*, 1510.08841.
- [95] W. Y. Keung and G. Senjanovic, *Majorana neutrinos and the production of the right-handed charged gauge boson*, *Phys. Rev. Lett.* **50** (1983) 1427.
- [96] C. Y. Chen, P. S. B. Dev and R. N. Mohapatra, *Probing heavy-light neutrino mixing in left-right seesaw models at the lhc*, *Phys. Rev. D* **88** (2013) 033014, [1306.2342].
- [97] F. F. Deppisch, P. S. B. Dev and A. Pilaftsis, *Neutrinos and collider physics*, *New J. Phys* **17** (2015) 075019, [1502.06541].
- [98] G. Senjanovic and V. Tello, *Right handed quark mixing in left-right symmetric theory*, *Phys. Rev. Lett.* **114** (2015) 071801, [1408.3835].
- [99] G. Beall, M. Bander and A. Soni, *Constraint on the mass scale of a left-right symmetric electroweak theory from the  $k(l)$   $k(s)$  mass difference*, *Phys. Rev. Lett.* **48** (1982) 848.
- [100] R. N. Mohapatra, G. Senjanovic and M. D. Tran, *Strangeness changing processes and the limit on the right-handed gauge boson mass*, *Phys. Rev. D* **28** (1983) 546.
- [101] G. Ecker and W. Grimus,  *$C_p$  violation and left-right symmetry*, *Nucl. Phys. B* **258** (1985) 328.
- [102] P. S. B. Dev, S. Goswami, M. Mitra and W. Rodejohann, *Constraining neutrino mass from neutrinoless double beta decay*, *Phys. Rev. D* **88** (2013) 091301, [1305.0056].
- [103] P. S. B. Dev, S. Goswami and M. Mitra, *Tev scale left-right symmetry and large mixing effects in neutrinoless double beta decay*, *Phys. Rev. D* **91** (2015) 113004, [1405.1399].
- [104] R. N. Mohapatra and J. D. Vergados, *A new contribution to neutrinoless double beta decay in gauge models*, *Phys. Rev. Lett.* **47** (1981) 1713.

- [105] M. Hirsch, H. V. Klapdor-Kleingrothaus and O. Panella, *Double beta decay in left-right symmetric models*, *Phys. Lett. B* **374** (1996) 7, [9602306].
- [106] V. Tello, M. Nemevsek, F. Nesti, G. Senjanovic and F. Vissani, *Left-right symmetry: from lhc to neutrinoless double beta decay*, *Phys. Rev. Lett.* **106** (2011) 151801, [1011.3522].
- [107] J. Chakraborty, H. Z. Devi, S. Goswami and S. Patra, *Neutrinoless double- $\beta$  decay in tev scale left-right symmetric models*, *JHEP* **1208** (2012) 008, [1204.2527].
- [108] J. Barry and W. Rodejohann, *Lepton number and flavour violation in tev-scale left-right symmetric theories with large left-right mixing*, *JHEP* **1309** (2013) 153, [1303.6324].
- [109] W. C. Huang and J. Lopez-Pavon, *On neutrinoless double beta decay in the minimal left-right symmetric model*, *Eur. Phys. J. C* **74** (2014) 2853, [1310.0265].
- [110] G. Bambhaniya, P. S. B. Dev, S. Goswami and M. Mitra, *The scalar triplet contribution to lepton flavour violation and neutrinoless double beta decay in left-right symmetric model*, *JHEP* **1604** (2016) 046, [1512.00440].
- [111] M. NemevÅjek, F. Nesti and G. Popara, *Keung-senjanović process at lhc: from lnu to displaced vertices to invisible decays*, *Phys. Rev. D* **97** (2018) 115018, [1801.05813].
- [112] A. Belyaev, N. D. Christensen and A. Pukhov, *Calchep 3.4 for collider physics within and beyond the standard model*, *Comput. Phys. Commun* **184** (2013) 1729, [1207.6082].
- [113] I. Z. Rothstein, *Renormalization group analysis of the minimal left-right symmetric model*, *Nucl. Phys. B* **358** (1991) 181.
- [114] J. Chakraborty, P. Konar and T. Mondal, *Constraining a class of b-l extended*

- models from vacuum stability and perturbativity, Phys. Rev. D* **89** (2014) 056014, [1308.1291].
- [115] J. Chakraborty, J. Gluza, T. Jelinski and T. Srivastava, *Theoretical constraints on masses of heavy particles in left-right symmetric models, Phys. Lett. B* **759** (2016) 361, [1604.06987].
- [116] A. Maiezza, G. Senjanović and J. C. Vasquez, *Higgs sector of the minimal left-right symmetric theory, Phys. Rev. D* **95** (2017) 095004, [1612.09146].
- [117] P. S. B. Dev, R. N. Mohapatra and Y. Zhang, *Displaced photon signal from a possible light scalar in minimal left-right seesaw model, Phys. Rev. D* **95** (2017) 115001, [1612.09587].
- [118] M. A. et al. [ATLAS Collaboration], *Search for doubly charged higgs boson production in multi-lepton final states with the atlas detector using proton-antiproton collisions at  $\sqrt{s} = 13$  tev, Eur. Phys. J. C* **78** (2018) 19, [1710.09748].
- [119] C. C. C. Collaboration], *A search for doubly-charged higgs boson production in three and four lepton final states at  $\sqrt{s} = 13$ TeV, CMS-PAS-HIG-* (2017) 16–036.
- [120] P. S. B. Dev and Y. Zhang, *Displaced vertex signatures of doubly charged scalars in the type-ii seesaw and its left-right extensions, JHEP* **1810** (2018) 199, [1808.00943].
- [121] G. A. et al. [ATLAS and C. Collaborations], *Combined measurement of the higgs boson mass in pp collisions at  $\sqrt{s} = 7$  and 8 tev with the atlas and cms experiments, Phys. Rev. Lett* **114** (2015) 191803, [1503.07589].
- [122] P. S. B. Dev, R. N. Mohapatra, W. Rodejohann and X. J. Xu, *Vacuum structure of the left-right symmetric model, 1811.06869.*
- [123] J. Chakraborty, P. Konar and T. Mondal, *Copositive criteria and boundedness of the scalar potential, Phys. Rev. D* **89** (2014) 095008, [1311.5666].

- [124] A. Davidson,  *$B^{-l}$  as the Fourth Color, Quark - Lepton Correspondence, and Natural Masslessness of Neutrinos Within a Generalized  $W_3$  Model*, *Phys. Rev.* **D20** (1979) 776.
- [125] R. N. Mohapatra and G. Senjanović, *Neutrino Mass and Spontaneous Parity Nonconservation*, *Phys. Rev. Lett.* **44** (1980) 912.
- [126] K. Kannike, *Vacuum Stability Conditions From Copositivity Criteria*, *Eur. Phys. J.* **C72** (2012) 2093, [1205.3781].
- [127] K. Kannike, *Vacuum Stability of a General Scalar Potential of a Few Fields*, *Eur. Phys. J.* **C76** (2016) 324, [1603.02680].
- [128] B. L. Sánchez-Vega, G. Gambini and C. E. Alvarez-Salazar, *Vacuum stability conditions of the economical 3-3-1 model from copositivity*, *Eur. Phys. J.* **C79** (2019) 299, [1811.00585].
- [129] J. Kim, *General Method for Analyzing Higgs Potentials*, *Nucl. Phys.* **B196** (1982) 285–300.
- [130] J. Kim,  *$SU(N)$  Higgs Problem With Adjoint Representation and Michel's Conjecture*, *Nucl. Phys.* **B197** (1982) 174–188.
- [131] S. C. Frautschi and J. Kim,  *$SU(5)$  Higgs Problem With Adjoint + Vector Representations*, *Nucl. Phys.* **B196** (1982) 301–327.
- [132] J. S. Kim, *Orbit Spaces of Low Dimensional Representations of Simple Compact Connected Lie Groups and Extrema of a Group Invariant Scalar Potential*, *J. Math. Phys.* **25** (1984) 1694.
- [133] M. Abud and G. Sartori, *The Geometry of Orbit Space and Natural Minima of Higgs Potentials*, *Phys. Lett.* **104B** (1981) 147–152.

- [134] M. Abud and G. Sartori, *The Geometry of Spontaneous Symmetry Breaking*, *Annals Phys.* **150** (1983) 307.
- [135] J. F. Gunion, J. Grifols, A. Mendez, B. Kayser and F. I. Olness, *Higgs Bosons in Left-Right Symmetric Models*, *Phys. Rev.* **D40** (1989) 1546.
- [136] N. G. Deshpande, J. F. Gunion, B. Kayser and F. I. Olness, *Left-right symmetric electroweak models with triplet Higgs*, *Phys. Rev.* **D44** (1991) 837–858.
- [137] A. W. El Kaffas, W. Khater, O. M. Ogreid and P. Osland, *Consistency of the two Higgs doublet model and CP violation in top production at the LHC*, *Nucl. Phys.* **B775** (2007) 45–77, [[hep-ph/0605142](#)].
- [138] I. P. Ivanov, *Minkowski space structure of the Higgs potential in 2HDM*, *Phys. Rev.* **D75** (2007) 035001, [[hep-ph/0609018](#)].
- [139] A. Arhrib, R. Benbrik, M. Chabab, G. Moulhaka, M. C. Peyranere, L. Rahili et al., *The Higgs Potential in the Type II Seesaw Model*, *Phys. Rev.* **D84** (2011) 095005, [[1105.1925](#)].
- [140] C. Bonilla, R. M. Fonseca and J. W. F. Valle, *Consistency of the triplet seesaw model revisited*, *Phys. Rev.* **D92** (2015) 075028, [[1508.02323](#)].
- [141] P. Duka, J. Gluza and M. Zralek, *Quantization and renormalization of the manifest left-right symmetric model of electroweak interactions*, *Annals Phys.* **280** (2000) 336–408, [[hep-ph/9910279](#)].
- [142] CMS COLLABORATION collaboration, *A search for doubly-charged Higgs boson production in three and four lepton final states at  $\sqrt{s} = 13$  TeV*, Tech. Rep. CMS-PAS-HIG-16-036, CERN, Geneva, 2017.
- [143] I. Rothstein, *Renormalisation group analysis of the minimal left-right symmetric model*, *Nuclear Physics B* **358** (1991) 181 – 194.

- [144] A. Kobakhidze and A. Spencer-Smith, *Neutrino Masses and Higgs Vacuum Stability*, *JHEP* **08** (2013) 036, [1305.7283].
- [145] L. Wolfenstein, *Neutrino Oscillations in Matter*, *Phys. Rev.* **D17** (1978) 2369–2374.
- [146] K. S. Babu, P. S. B. Dev, S. Jana and A. Thapa, *Non-Standard Interactions in Radiative Neutrino Mass Models*, 1907.09498.
- [147] P. Coloma, I. Esteban, M. C. Gonzalez-Garcia and M. Maltoni, *Improved global fit to Non-Standard neutrino Interactions using COHERENT energy and timing data*, 1911.09109.
- [148] Y. Farzan, *A model for large non-standard interactions of neutrinos leading to the LMA-Dark solution*, *Phys. Lett.* **B748** (2015) 311–315, [1505.06906].
- [149] Y. Farzan and I. M. Shoemaker, *Lepton Flavor Violating Non-Standard Interactions via Light Mediators*, *JHEP* **07** (2016) 033, [1512.09147].
- [150] K. S. Babu, A. Friedland, P. A. N. Machado and I. Mocioiu, *Flavor Gauge Models Below the Fermi Scale*, *JHEP* **12** (2017) 096, [1705.01822].
- [151] P. S. B. Dev et al., *Neutrino Non-Standard Interactions: A Status Report*, *SciPost Phys. Proc* **2** (2019) 001, [1907.00991].
- [152] S.-F. Ge and S. J. Parke, *Scalar Nonstandard Interactions in Neutrino Oscillation*, *Phys. Rev. Lett.* **122** (2019) 211801, [1812.08376].
- [153] A. K. Das, *Finite Temperature Field Theory*. World Scientific, New York, 1997.
- [154] D. Notzold and G. Raffelt, *Neutrino Dispersion at Finite Temperature and Density*, *Nucl. Phys.* **B307** (1988) 924–936.
- [155] P. B. Pal and T. N. Pham, *A Field Theoretic Derivation of Wolfenstein’s Matter Oscillation Formula*, *Phys. Rev.* **D40** (1989) 259.

- [156] P. Langacker and J. Liu, *Standard Model contributions to the neutrino index of refraction in the early universe*, *Phys. Rev.* **D46** (1992) 4140–4160, [hep-ph/9206209].
- [157] M. B. Wise and Y. Zhang, *Lepton Flavorful Fifth Force and Depth-dependent Neutrino Matter Interactions*, *JHEP* **06** (2018) 053, [1803.00591].
- [158] A. Y. Smirnov and X.-J. Xu, *Wolfenstein potentials for neutrinos induced by ultra-light mediators*, *JHEP* **12** (2019) 046, [1909.07505].
- [159] M. E. Peskin and D. V. Schroeder, *An Introduction to quantum field theory*. Addison-Wesley, Reading, USA, 1995.
- [160] J. Liu, C. E. M. Wagner and X.-P. Wang, *A light complex scalar for the electron and muon anomalous magnetic moments*, *JHEP* **03** (2019) 008, [1810.11028].
- [161] J. K. Hoskins, R. D. Newman, R. Spero and J. Schultz, *Experimental tests of the gravitational inverse-square law for mass separations from 2 to 105 cm*, *Phys. Rev. D* **32** (Dec, 1985) 3084–3095.
- [162] J. C. Long, H. W. Chan, A. B. Churnside, E. A. Gulbis, M. C. M. Varney and J. C. Price, *Upper limits to submillimeter-range forces from extra space-time dimensions*, hep-ph/0210004.
- [163] D. J. Kapner, T. S. Cook, E. G. Adelberger, J. H. Gundlach, B. R. Heckel, C. D. Hoyle et al., *Tests of the gravitational inverse-square law below the dark-energy length scale*, *Phys. Rev. Lett.* **98** (2007) 021101, [hep-ph/0611184].
- [164] A. A. Geraci, S. J. Smullin, D. M. Weld, J. Chiaverini and A. Kapitulnik, *Improved constraints on non-Newtonian forces at 10 microns*, *Phys. Rev.* **D78** (2008) 022002, [0802.2350].

- [165] S.-Q. Yang, B.-F. Zhan, Q.-L. Wang, C.-G. Shao, L.-C. Tu, W.-H. Tan et al., *Test of the gravitational inverse square law at millimeter ranges*, *Phys. Rev. Lett.* **108** (Feb, 2012) 081101.
- [166] W.-H. Tan, S.-Q. Yang, C.-G. Shao, J. Li, A.-B. Du, B.-F. Zhan et al., *New test of the gravitational inverse-square law at the submillimeter range with dual modulation and compensation*, *Phys. Rev. Lett.* **116** (Mar, 2016) 131101.
- [167] E. Adelberger, J. Gundlach, B. Heckel, S. Hoedl and S. Schlamminger, *Torsion balance experiments: A low-energy frontier of particle physics*, *Progress in Particle and Nuclear Physics* **62** (2009) 102 – 134.
- [168] E. Hardy and R. Lasenby, *Stellar cooling bounds on new light particles: plasma mixing effects*, *JHEP* **02** (2017) 033, [1611.05852].
- [169] S. Knapen, T. Lin and K. M. Zurek, *Light Dark Matter: Models and Constraints*, *Phys. Rev.* **D96** (2017) 115021, [1709.07882].
- [170] G. G. Raffelt, *Stars as laboratories for fundamental physics*. 1996.
- [171] N. Ishizuka and M. Yoshimura, *Axion and Dilaton Emissivity From Nascent Neutron Stars*, *Prog. Theor. Phys.* **84** (1990) 233–250.
- [172] B. Batell, A. Freitas, A. Ismail and D. Mckeen, *Probing Light Dark Matter with a Hadrophilic Scalar Mediator*, *Phys. Rev.* **D100** (2019) 095020, [1812.05103].
- [173] C. Alexandrou et al., *Nucleon scalar and tensor charges using lattice QCD simulations at the physical value of the pion mass*, *Phys. Rev.* **D95** (2017) 114514, [1703.08788].
- [174] LEP, ALEPH, DELPHI, L3, LEP ELECTROWEAK WORKING GROUP, SLD ELECTROWEAK GROUP, SLD HEAVY FLAVOUR GROUP, OPAL collaboration, *A*

*Combination of preliminary electroweak measurements and constraints on the standard model*, hep-ex/0412015.

- [175] M. Escudero and M. Fairbairn, *Cosmological Constraints on Invisible Neutrino Decays Revisited*, *Phys. Rev.* **D100** (2019) 103531, [1907.05425].
- [176] F. Forastieri, M. Lattanzi and P. Natoli, *Cosmological constraints on neutrino self-interactions with a light mediator*, *Phys. Rev.* **D100** (2019) 103526, [1904.07810].
- [177] CMB-S4 collaboration, K. N. Abazajian et al., *CMB-S4 Science Book, First Edition*, 1610.02743.
- [178] S. Shalgar, I. Tamborra and M. Bustamante, *Core-collapse supernovae stymie secret neutrino interactions*, 1912.09115.
- [179] H. A. Bethe and J. R. Wilson, *Revival of a stalled supernova shock by neutrino heating*, *Astrophys. J.* **295** (1985) 14–23.
- [180] E. W. Kolb and M. S. Turner, *Supernova SN 1987a and the Secret Interactions of Neutrinos*, *Phys. Rev.* **D36** (1987) 2895.
- [181] Y. Farzan, M. Lindner, W. Rodejohann and X.-J. Xu, *Probing neutrino coupling to a light scalar with coherent neutrino scattering*, *JHEP* **05** (2018) 066, [1802.05171].
- [182] C. D. Kreisch, F.-Y. Cyr-Racine and O. Doré, *The Neutrino Puzzle: Anomalies, Interactions, and Cosmological Tensions*, 1902.00534.
- [183] J. H. Hubbell and Overboi, *Relativistic atomic form factors and photon coherent scattering cross sections*, *Journal of Physical and Chemical Reference Data* **8** (1979) 69–106.
- [184] A. M. Dziewonski and D. L. Anderson, *Preliminary reference Earth model*, *Physics of the Earth and Planetary Interiors* **25** (Jun, 1981) 297–356.

- [185] “Standard solar model.”  
<http://www.sns.ias.edu/~jnb/SNdata/solarmodels.html>.
- [186] J. N. Bahcall, S. Basu and M. H. Pinsonneault, *How uncertain are solar neutrino predictions?*, *Phys. Lett.* **B433** (1998) 1–8, [astro-ph/9805135].
- [187] J. N. Bahcall, A. M. Serenelli and S. Basu, *New solar opacities, abundances, helioseismology, and neutrino fluxes*, *The Astrophysical Journal* **621** (Jan, 2005) L85–L88.
- [188] N. Arkani-Hamed, L. Motl, A. Nicolis and C. Vafa, *The String landscape, black holes and gravity as the weakest force*, *JHEP* **06** (2007) 060, [hep-th/0601001].
- [189] J. H. Chang, R. Essig and S. D. McDermott, *Revisiting supernova 1987a constraints on dark photons*, *Journal of High Energy Physics* **2017** (Jan, 2017) .
- [190] T. Asaka and M. Shaposhnikov, *The  $\nu$ MSM, dark matter and baryon asymmetry of the universe*, *Phys. Lett. B* **620** (2005) 17–26, [hep-ph/0505013].
- [191] T. Asaka, S. Blanchet and M. Shaposhnikov, *The  $\nu$ MSM, dark matter and neutrino masses*, *Phys. Lett. B* **631** (2005) 151–156, [hep-ph/0503065].
- [192] E. Ma, *Verifiable radiative seesaw mechanism of neutrino mass and dark matter*, *Phys. Rev.* **D73** (2006) 077301, [hep-ph/0601225].
- [193] M. Fukugita and T. Yanagida, *Baryogenesis Without Grand Unification*, *Phys. Lett.* **B174** (1986) 45–47.
- [194] B. Batell, *Dark Discrete Gauge Symmetries*, *Phys. Rev.* **D83** (2011) 035006, [1007.0045].
- [195] W.-F. Chang and C.-F. Wong, *A Model for Neutrino Masses and Dark Matter with the Discrete Gauge Symmetry*, *Phys. Rev.* **D85** (2012) 013018, [1104.3934].

- [196] E. Ma, I. Picek and B. Radovicic, *New Scotogenic Model of Neutrino Mass with  $U(1)_D$  Gauge Interaction*, *Phys. Lett.* **B726** (2013) 744–746, [1308.5313].
- [197] M. Lindner, D. Schmidt and A. Watanabe, *Dark matter and  $U(1)'$  symmetry for the right-handed neutrinos*, *Phys. Rev.* **D89** (2014) 013007, [1310.6582].
- [198] P. Ballett, M. Hostert and S. Pascoli, *Dark Neutrinos and a Three Portal Connection to the Standard Model*, *Phys. Rev. D* **101** (2020) 115025, [1903.07589].
- [199] M. Berbig, S. Jana and A. Trautner, *The Hubble tension and a renormalizable model of gauged neutrino self-interactions*, 2004.13039.
- [200] A. Abdullahi, M. Hostert and S. Pascoli, *A Dark Seesaw Solution to Low Energy Anomalies: MiniBooNE, the muon  $(g - 2)$ , and BaBar*, 2007.11813.
- [201] Lowski and S. Trojanowski, *Neutrino beam-dump experiment with FASER at the LHC*, 2011.04751.
- [202] A. Pilaftsis, *Radiatively induced neutrino masses and large Higgs neutrino couplings in the standard model with Majorana fields*, *Z. Phys. C* **55** (1992) 275–282, [hep-ph/9901206].
- [203] R. Essig et al., *Working Group Report: New Light Weakly Coupled Particles*, in *Community Summer Study 2013: Snowmass on the Mississippi*, 10, 2013. 1311.0029.
- [204] P. Ilten, Y. Soreq, M. Williams and W. Xue, *Serendipity in dark photon searches*, *JHEP* **06** (2018) 004, [1801.04847].
- [205] M. Bauer, P. Foldenauer and J. Jaeckel, *Hunting All the Hidden Photons*, *JHEP* **18** (2020) 094, [1803.05466].
- [206] M. Fabbrichesi, E. Gabrielli and G. Lanfranchi, *The Dark Photon*, 2005.01515.

- [207] X.-J. Xu, *The  $\nu_R$ -philic scalar: its loop-induced interactions and Yukawa forces in LIGO observations*, *JHEP* **09** (2020) 105, [2007.01893].
- [208] J. Kersten and A. Y. Smirnov, *Right-Handed Neutrinos at CERN LHC and the Mechanism of Neutrino Mass Generation*, *Phys. Rev. D* **76** (2007) 073005, [0705.3221].
- [209] G. 't Hooft, *Naturalness, chiral symmetry, and spontaneous chiral symmetry breaking*, *NATO Sci. Ser. B* **59** (1980) 135–157.
- [210] R. Harnik, J. Kopp and P. A. Machado, *Exploring  $\nu\mu$  Signals in Dark Matter Detectors*, *JCAP* **07** (2012) 026, [1202.6073].
- [211] J. Heeck, *Unbroken  $B - L$  symmetry*, *Phys. Lett. B* **739** (2014) 256–262, [1408.6845].
- [212] D. Curtin, R. Essig, S. Gori and J. Shelton, *Illuminating Dark Photons with High-Energy Colliders*, *JHEP* **02** (2015) 157, [1412.0018].
- [213] LHCb collaboration, R. Aaij et al., *Search for Dark Photons Produced in 13 TeV  $pp$  Collisions*, *Phys. Rev. Lett.* **120** (2018) 061801, [1710.02867].
- [214] BABAR collaboration, J. Lees et al., *Search for a Dark Photon in  $e^+e^-$  Collisions at BaBar*, *Phys. Rev. Lett.* **113** (2014) 201801, [1406.2980].
- [215] ALEPH, DELPHI, L3, OPAL, LEP ELECTROWEAK collaboration, S. Schael et al., *Electroweak Measurements in Electron-Positron Collisions at  $W$ -Boson-Pair Energies at LEP*, *Phys. Rept.* **532** (2013) 119–244, [1302.3415].
- [216] S. Andreas, C. Niebuhr and A. Ringwald, *New Limits on Hidden Photons from Past Electron Beam Dumps*, *Phys. Rev. D* **86** (2012) 095019, [1209.6083].
- [217] CHARM-II collaboration, P. Vilain et al., *Measurement of differential cross-sections for muon-neutrino electron scattering*, *Phys. Lett.* **B302** (1993) 351–355.

- [218] CHARM-II collaboration, P. Vilain et al., *Precision measurement of electroweak parameters from the scattering of muon-neutrinos on electrons*, *Phys. Lett.* **B335** (1994) 246–252.
- [219] TEXONO collaboration, M. Deniz et al., *Measurement of  $\bar{\nu}(e)$ -Electron Scattering Cross-Section with a CsI(Tl) Scintillating Crystal Array at the Kuo-Sheng Nuclear Power Reactor*, *Phys. Rev.* **D81** (2010) 072001, [0911.1597].
- [220] A. G. Beda, V. B. Brudanin, V. G. Egorov, D. V. Medvedev, V. S. Pogosov, M. V. Shirchenko et al., *Upper limit on the neutrino magnetic moment from three years of data from the GEMMA spectrometer*, 1005.2736.
- [221] G. Bellini et al., *Precision measurement of the  $^7\text{Be}$  solar neutrino interaction rate in Borexino*, *Phys. Rev. Lett.* **107** (2011) 141302, [1104.1816].
- [222] COHERENT collaboration, D. Akimov et al., *Observation of Coherent Elastic Neutrino-Nucleus Scattering*, *Science* **357** (2017) 1123–1126, [1708.01294].
- [223] S. Bilmis, I. Turan, T. Aliev, M. Deniz, L. Singh and H. Wong, *Constraints on Dark Photon from Neutrino-Electron Scattering Experiments*, *Phys. Rev. D* **92** (2015) 033009, [1502.07763].
- [224] M. Lindner, F. S. Queiroz, W. Rodejohann and X.-J. Xu, *Neutrino-electron scattering: general constraints on  $Z'$  and dark photon models*, *JHEP* **05** (2018) 098, [1803.00060].
- [225] DUNE collaboration, B. Abi et al., *Prospects for Beyond the Standard Model Physics Searches at the Deep Underground Neutrino Experiment*, 2008.12769.
- [226] P. Ballett, M. Hostert, S. Pascoli, Y. F. Perez-Gonzalez, Z. Tabrizi and R. Zukanovich Funchal,  *$Z'$ s in neutrino scattering at DUNE*, *Phys. Rev. D* **100** (2019) 055012, [1902.08579].

- [227] J. Redondo and G. Raffelt, *Solar constraints on hidden photons re-visited*, *JCAP* **08** (2013) 034, [1305.2920].
- [228] J. B. Dent, F. Ferrer and L. M. Krauss, *Constraints on Light Hidden Sector Gauge Bosons from Supernova Cooling*, 1201.2683.
- [229] B. Dutta, S. Ghosh and J. Kumar, *Contributions to  $\Delta N_{eff}$  from the dark photon of  $U(1)_{T3R}$* , *Phys. Rev. D* **102** (2020) 015013, [2002.01137].
- [230] X. Luo, W. Rodejohann and X.-J. Xu, *Dirac neutrinos and  $N_{eff}$* , *JCAP* **06** (2020) 058, [2005.01629].
- [231] B. Dutta, S. Ghosh and J. Kumar, *Opportunities for probing  $U(1)_{T3R}$  with light mediators*, *Phys. Rev. D* **102** (2020) 075041, [2007.16191].
- [232] X. Luo, W. Rodejohann and X.-J. Xu, *Dirac neutrinos and  $N_{eff}$  II: the freeze-in case*, 2011.13059.
- [233] P. Langacker and M. Plumacher, *Flavor changing effects in theories with a heavy  $Z'$  boson with family nonuniversal couplings*, *Phys. Rev. D* **62** (2000) 013006, [hep-ph/0001204].
- [234] SINDRUM II collaboration, J. Kaulard et al., *Improved limit on the branching ratio of  $\mu^- \rightarrow e^+$  conversion on titanium*, *Phys. Lett. B* **422** (1998) 334–338.
- [235] L. Willmann et al., *New bounds from searching for muonium to anti-muonium conversion*, *Phys. Rev. Lett.* **82** (1999) 49–52, [hep-ex/9807011].
- [236] J. Casas and A. Ibarra, *Oscillating neutrinos and  $\mu \rightarrow e, \gamma$* , *Nucl. Phys. B* **618** (2001) 171–204, [hep-ph/0103065].
- [237] E. G. Adelberger, B. R. Heckel, S. A. Hoedl, C. D. Hoyle, D. J. Kapner and A. Upadhye, *Particle Physics Implications of a Recent Test of the Gravitational Inverse Square Law*, *Phys. Rev. Lett.* **98** (2007) 131104, [hep-ph/0611223].

- [238] E. Adelberger, J. Gundlach, B. Heckel, S. Hoedl and S. Schlamminger, *Torsion balance experiments: A low-energy frontier of particle physics*, *Prog. Part. Nucl. Phys.* **62** (2009) 102–134.
- [239] T. Wagner, S. Schlamminger, J. Gundlach and E. Adelberger, *Torsion-balance tests of the weak equivalence principle*, *Class. Quant. Grav.* **29** (2012) 184002, [1207.2442].
- [240] S. G. Turyshev and J. G. Williams, *Space-based tests of gravity with laser ranging*, *Int. J. Mod. Phys. D* **16** (2007) 2165–2179, [gr-qc/0611095].
- [241] M. Bordag, U. Mohideen and V. Mostepanenko, *New developments in the Casimir effect*, *Phys. Rept.* **353** (2001) 1–205, [quant-ph/0106045].
- [242] M. Baryakhtar, R. Lasenby and M. Teo, *Black Hole Superradiance Signatures of Ultralight Vectors*, *Phys. Rev.* **D96** (2017) 035019, [1704.05081].
- [243] M. Bustamante and S. K. Agarwalla, *Universe’s Worth of Electrons to Probe Long-Range Interactions of High-Energy Astrophysical Neutrinos*, *Phys. Rev. Lett.* **122** (2019) 061103, [1808.02042].
- [244] A. Y. Smirnov and X.-J. Xu, *Wolfenstein potentials for neutrinos induced by ultra-light mediators*, *JHEP* **12** (2019) 046, [1909.07505].
- [245] J. L. Feng, I. Galon, F. Kling and S. Trojanowski, *ForwArd Search ExpeRiment at the LHC*, *Phys. Rev. D* **97** (2018) 035001, [1708.09389].
- [246] J. P. Chou, D. Curtin and H. Lubatti, *New Detectors to Explore the Lifetime Frontier*, *Phys. Lett. B* **767** (2017) 29–36, [1606.06298].
- [247] J. A. Evans, *Detecting Hidden Particles with MATHUSLA*, *Phys. Rev. D* **97** (2018) 055046, [1708.08503].

- [248] V. V. Gligorov, S. Knapen, M. Papucci and D. J. Robinson, *Searching for Long-lived Particles: A Compact Detector for Exotics at LHCb*, *Phys. Rev. D* **97** (2018) 015023, [1708.09395].
- [249] SHiP collaboration, M. Anelli et al., *A facility to Search for Hidden Particles (SHiP) at the CERN SPS*, 1504.04956.
- [250] S. Alekhin et al., *A facility to Search for Hidden Particles at the CERN SPS: the SHiP physics case*, *Rept. Prog. Phys.* **79** (2016) 124201, [1504.04855].
- [251] BELLE-II collaboration, T. Abe et al., *Belle II Technical Design Report*, 1011.0352.
- [252] NA64 collaboration, D. Banerjee et al., *Search for invisible decays of sub-GeV dark photons in missing-energy events at the CERN SPS*, *Phys. Rev. Lett.* **118** (2017) 011802, [1610.02988].
- [253] S. Gninenko and N. Krasnikov, *Probing the muon  $g_\mu - 2$  anomaly,  $L_\mu - L_\tau$  gauge boson and Dark Matter in dark photon experiments*, *Phys. Lett. B* **783** (2018) 24–28, [1801.10448].
- [254] FASER collaboration, A. Ariga et al., *FASER’s physics reach for long-lived particles*, *Phys. Rev. D* **99** (2019) 095011, [1811.12522].
- [255] R. N. Mohapatra and J. W. F. Valle, *Neutrino Mass and Baryon Number Nonconservation in Superstring Models*, *Phys. Rev. D* **34** (1986) 1642.
- [256] F. Feruglio, C. Hagedorn and R. Ziegler, *Lepton Mixing Parameters from Discrete and CP Symmetries*, *JHEP* **07** (2013) 027, [1211.5560].
- [257] A. Pilaftsis, *CP violation and baryogenesis due to heavy Majorana neutrinos*, *Phys. Rev. D* **56** (1997) 5431–5451, [hep-ph/9707235].
- [258] A. Pilaftsis and T. E. J. Underwood, *Resonant leptogenesis*, *Nucl. Phys. B* **692** (2004) 303–345, [hep-ph/0309342].

- [259] F. F. Deppisch, N. Desai and J. W. F. Valle, *Is charged lepton flavor violation a high energy phenomenon?*, *Phys. Rev. D* **89** (2014) 051302, [1308.6789].
- [260] J. C. Helo, M. Hirsch and S. Kovalenko, *Heavy neutrino searches at the LHC with displaced vertices*, *Phys. Rev. D* **89** (2014) 073005, [1312.2900].
- [261] J. A. Escobar and C. Luhn, *The Flavor Group  $\Delta(6n^{**}2)$* , *J. Math. Phys.* **50** (2009) 013524, [0809.0639].
- [262] M. Holthausen, M. Lindner and M. A. Schmidt, *CP and Discrete Flavour Symmetries*, *JHEP* **04** (2013) 122, [1211.6953].
- [263] M.-C. Chen, M. Fallbacher, K. T. Mahanthappa, M. Ratz and A. Trautner, *CP Violation from Finite Groups*, *Nucl. Phys. B* **883** (2014) 267–305, [1402.0507].
- [264] C. Hagedorn and E. Molinaro, *Flavor and CP symmetries for leptogenesis and  $0\nu\beta\beta$  decay*, *Nucl. Phys. B* **919** (2017) 404–469, [1602.04206].
- [265] S. F. King and C. Luhn, *Neutrino Mass and Mixing with Discrete Symmetry*, *Rept. Prog. Phys.* **76** (2013) 056201, [1301.1340].
- [266] F. Feruglio, C. Hagedorn and R. Ziegler, *A realistic pattern of lepton mixing and masses from  $S_4$  and CP*, *Eur. Phys. J. C* **74** (2014) 2753, [1303.7178].
- [267] P. S. Bhupal Dev, P. Millington, A. Pilaftsis and D. Teresi, *Flavour Covariant Transport Equations: an Application to Resonant Leptogenesis*, *Nucl. Phys. B* **886** (2014) 569–664, [1404.1003].
- [268] D. Curtin and M. E. Peskin, *Analysis of Long Lived Particle Decays with the MATHUSLA Detector*, *Phys. Rev. D* **97** (2018) 015006, [1705.06327].
- [269] A. Atre, T. Han, S. Pascoli and B. Zhang, *The Search for Heavy Majorana Neutrinos*, *JHEP* **05** (2009) 030, [0901.3589].

- [270] N. Okada and S. Okada, *Z'-portal right-handed neutrino dark matter in the minimal  $U(1)_X$  extended Standard Model*, *Phys. Rev. D* **95** (2017) 035025, [1611.02672].
- [271] A. Das, N. Okada and D. Raut, *Enhanced pair production of heavy Majorana neutrinos at the LHC*, *Phys. Rev. D* **97** (2018) 115023, [1710.03377].
- [272] A. E. Faraggi and M. Masip, *Leptophobic Z-prime from superstring derived models*, *Phys. Lett. B* **388** (1996) 524–531, [hep-ph/9604302].
- [273] D. Gomez Dumm, *Leptophobic character of the Z-prime in an  $SU(3)(C) \times SU(3)(L) \times U(1)(X)$  model*, *Phys. Lett. B* **411** (1997) 313–320, [hep-ph/9709245].
- [274] M. Malinsky, J. C. Romao and J. W. F. Valle, *Novel supersymmetric  $SO(10)$  seesaw mechanism*, *Phys. Rev. Lett.* **95** (2005) 161801, [hep-ph/0506296].
- [275] M. R. Buckley, D. Hooper and J. L. Rosner, *A Leptophobic Z' And Dark Matter From Grand Unification*, *Phys. Lett. B* **703** (2011) 343–347, [1106.3583].
- [276] L. Basso, A. Belyaev, S. Moretti and C. H. Shepherd-Themistocleous, *Phenomenology of the minimal B-L extension of the Standard model: Z' and neutrinos*, *Phys. Rev. D* **80** (2009) 055030, [0812.4313].
- [277] S. Amrith, J. M. Butterworth, F. F. Deppisch, W. Liu, A. Varma and D. Yallup, *LHC Constraints on a B – L Gauge Model using Contur*, *JHEP* **05** (2019) 154, [1811.11452].
- [278] F. F. Deppisch, W. Liu and M. Mitra, *Long-lived Heavy Neutrinos from Higgs Decays*, *JHEP* **08** (2018) 181, [1804.04075].
- [279] A. Pilaftsis and T. E. J. Underwood, *Electroweak-scale resonant leptogenesis*, *Phys. Rev. D* **72** (2005) 113001, [hep-ph/0506107].
- [280] S. Blanchet, Z. Chacko, S. S. Granor and R. N. Mohapatra, *Probing Resonant Leptogenesis at the LHC*, *Phys. Rev. D* **82** (2010) 076008, [0904.2174].

- [281] S. Blanchet, P. S. B. Dev and R. N. Mohapatra, *Leptogenesis with TeV Scale Inverse Seesaw in  $SO(10)$* , *Phys. Rev. D* **82** (2010) 115025, [1010.1471].
- [282] GERDA collaboration, M. Agostini et al., *Final Results of GERDA on the Search for Neutrinoless Double- $\beta$  Decay*, *Phys. Rev. Lett.* **125** (2020) 252502, [2009.06079].
- [283] KAMLAND-ZEN collaboration, A. Gando et al., *Search for Majorana Neutrinos near the Inverted Mass Hierarchy Region with KamLAND-Zen*, *Phys. Rev. Lett.* **117** (2016) 082503, [1605.02889].
- [284] EXO-200 collaboration, J. B. Albert et al., *Searches for double beta decay of  $^{134}\text{Xe}$  with EXO-200*, *Phys. Rev. D* **96** (2017) 092001, [1704.05042].
- [285] CUORE collaboration, D. Q. Adams et al., *High sensitivity neutrinoless double-beta decay search with one tonne-year of CUORE data*, 2104.06906.
- [286] NEMO-3 collaboration, R. Arnold et al., *Detailed studies of  $^{100}\text{Mo}$  two-neutrino double beta decay in NEMO-3*, *Eur. Phys. J. C* **79** (2019) 440, [1903.08084].
- [287] I. Esteban, M. C. Gonzalez-Garcia, M. Maltoni, I. Martinez-Soler and T. Schwetz, *Updated fit to three neutrino mixing: exploring the accelerator-reactor complementarity*, *JHEP* **01** (2017) 087, [1611.01514].
- [288] LEGEND collaboration, N. Abgrall et al., *The Large Enriched Germanium Experiment for Neutrinoless Double Beta Decay (LEGEND)*, *AIP Conf. Proc.* **1894** (2017) 020027, [1709.01980].
- [289] NEXO collaboration, J. B. Albert et al., *Sensitivity and Discovery Potential of nEXO to Neutrinoless Double Beta Decay*, *Phys. Rev. C* **97** (2018) 065503, [1710.05075].
- [290] C. Luhn, S. Nasri and P. Ramond, *The Flavor group  $\Delta(3n^{**}2)$* , *J. Math. Phys.* **48** (2007) 073501, [hep-th/0701188].